Theoretical study of spermatozoa sorting by dielectrophoresis or magnetophoresis with supervised learning

Koh, James Boon Yong

2018

Koh, J. B. Y. (2018). Theoretical study of spermatozoa sorting by dielectrophoresis or magnetophoresis with supervised learning. Doctoral thesis, Nanyang Technological University, Singapore.

https://hdl.handle.net/10356/82937

https://doi.org/10.32657/10220/47538

Theoretical Study of Sperm Sorting with Supervised Learning

Koh Boon Yong James 2019

THEORETICAL STUDY OF SPERMATOZOA SORTING BY DIELECTROPHORESIS OR MAGNETOPHORESIS WITH SUPERVISED LEARNING

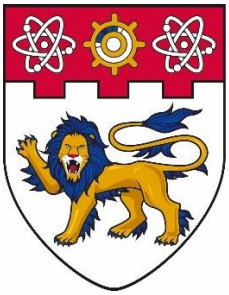

NANYANG TECHNOLOGICAL UNIVERSITY
SINGAPORE

KOH BOON YONG JAMES

SCHOOL OF MECHANICAL AND AEROSPACE ENGINEERING
NANYANG TECHNOLOGICAL UNIVERSITY, SINGAPORE

Year 2019

THEORETICAL STUDY OF SPERMATOZOA SORTING BY DIELECTROPHORESIS OR MAGNETOPHORESIS WITH SUPERVISED LEARNING

KOH BOON YONG JAMES

SCHOOL OF MECHANICAL AND AEROSPACE ENGINEERING

A thesis submitted to the Nanyang Technological University, Singapore
in partial fulfilment of the requirements for the degree of
Doctor of Philosophy

Jan 2019

Statement of Originality

I hereby certify that the work embodied in this thesis is the result of original research, is free of plagiarised materials, and has not been submitted for a higher degree to any other University or Institution.

19 January 2019
. . . . . .
Date

. . . . . .
Koh Boon Yong James

Supervisor Declaration Statement

I have reviewed the content and presentation style of this thesis and declare it is free of plagiarism and of sufficient grammatical clarity to be examined. To the best of my knowledge, the research and writing are those of the candidate except as acknowledged in the Author Attribution Statement. I confirm that the investigations were conducted in accord with the ethics policies and integrity standards of Nanyang Technological University and that the research data are presented honestly and without prejudice.

19 January 2019

. . . . . .

Date

. . . . . .

Assistant Professor Marcos

Authorship Attribution Statement

This thesis contains material from six paper published in the following peer-reviewed journals where I was the first and/or corresponding author.

Chapter 2.1 and 2.3 is published as Koh JBY and Marcos (2015) The study of spermatozoa and sorting in relation to human reproduction. *Microfluidics and Nanofluidics* 18(5-6):755-774. DOI: 10.1007/s10404-014-1520-x.

The contributions of the co-authors are as follows:

- Asst. Prof Marcos provided the initial project direction and edited the manuscript drafts.
- I carried out the literature reviews, organized the materials and prepared the manuscript.

Chapter 2.2 is published as Koh JBY, Shen X and Marcos (2016) Theoretical modeling in microscale locomotion. *Microfluidics and Nanofluidics* 20(7):1-27. DOI: 10.1007/s10404-016-1761-y.

The contributions of the co-authors are as follows:

- I provided the initial project direction.
- Asst. Prof Marcos provided guidance and edited the manuscript drafts.
- Dr Shen and I carried out the literature reviews, organized the materials and prepared the manuscript.

Chapter 3 is published as Koh JBY and Marcos (2014) Effect of dielectrophoresis on spermatozoa. *Microfluidics and Nanofluidics* 17(4):613-622. DOI: 10.1007/s10404-014-1342-x.

The contributions of the co-authors are as follows:

- Asst. Prof provided the initial project direction, provided guidance in interpreting the results and edited the manuscript drafts.
- I performed the modelling, obtained the results, proposed the application and prepared the manuscript.

Chapter 4 is published as Koh JBY and Marcos (2015) Dielectrophoresis of spermatozoa in viscoelastic medium. *Electrophoresis* 36(13):1514-1521. DOI: 10.1002/elps.201400326.

The contributions of the co-authors are as follows:

- Asst. Prof provided the initial project direction, provided guidance in interpreting the results and edited the manuscript drafts.
- I performed the modelling, wrote the code, obtained the results and prepared the manuscript.

Chapter 5 is published as Koh JBY and Marcos (2017) Sorting spermatozoa by morphology using magnetophoresis. *Microfluidics and Nanofluidics* 21(4):75. DOI: 10.1007/s10404-017-1911-x.

The contributions of the co-authors are as follows:

- Asst. Prof provided the initial project direction and edited the manuscript drafts.
- I performed the modelling, wrote the code, obtained the results, proposed the application and prepared the manuscript.

Chapter 6 is published as Koh JBY, Shen X and Marcos (2018) Supervised learning to predict sperm sorting by magnetophoresis. *Magnetochemistry* 4(3):31. DOI: 10.3390/magnetochemistry4030031.

The contributions of the co-authors are as follows:

- I provided the initial project direction.
- Dr Shen and I performed the modelling, wrote the code, obtained the results, and prepared the manuscript.
- Asst. Prof Marcos provided guidance and edited the manuscript drafts.

19 January 2019

. . . . . .

Date

. . . . . .

Koh Boon Yong James

Acknowledgements

The author would like to express his heartfelt gratitude to all the professors and teachers who have taught him in one way or another during his years of education. In particular, the author is extremely grateful to his advisor, Prof. Marcos, for his close guidance throughout the years. Prof. Marcos has been very generous in sharing his knowledge and experience, and has dedicated much time in mentoring the author.

The author would like to sincerely thank Nanyang Technological University, Singapore for providing him with the Nanyang Scholarship from year 2010 to 2014 and Nanyang President Graduate Scholarship from year 2014 to 2018, and the School of Mechanical and Aerosapce Engineering for providing a condusive environment to carry out research. The author also thanks the Ministry of Education, Singapore for heavily subsidising all levels of education beginning from preschool up to graduate programmes.

The author values the friendship and intellectual discussions with Dr. Kong Tian Fook, Dr. Yao Xin, Dr. Tran Ngoc Phu, Dr. Tran Duc Quang, Dr. Shen Xinhui, Mr. Tan Pei Yen, Mr. Benjamin Tay Zikai and Mr. Teo Ting Wei. Last but not least, the author is very grateful to his family for their unwavering love and support.

Abstract

Assisted reproduction currently accounts for over one in every hundred births in developed countries. The chances of successful conception are closely related to the morphology of sperm used. Despite well-established microfluidic sorting techniques, and reliable mathematical models to quantify the swimming of microorganisms, research on sperm sorting via dielectrophoresis or magnetophoresis lacks theoretical and statistical support. In this thesis, the kinematics of sperm subjected to an external electric or magnetic field is investigated to provide a theoretical framework for computing the resultant velocity. The flagellum waveform is prescribed analytically, and subsequently solved from force and moment balance. The hydrodynamic force acting on the sperm is computed using Resistive Force Theory as well as Slender Body Theory, and the resulting velocity is compared qualitatively and quantitatively. As normal and abnormal sperm cells have different morphological parameters, their velocities under the influence of dielectrophoresis or magnetophoresis are altered to varying extents. This effect is more prominent in a viscoelastic Oldroyd-B fluid than in a Newtonian fluid medium.

To account for the natural variations in sperm morphology and beating characteristics, pseudo-random data are generated from a normal distribution. The cross-section of the microchannel is assumed to be much larger than the sperm, such that boundary effects can be ignored. A large number of velocity computations is performed to obtain statistically meaningful results. The difference in velocity distribution between normal and abnormal sperm cells can be widened using an external field to double the proportion of normal ones, with at least half the number of normal spermatozoa in the original sample retained. This sorting has potential to improve the probability of success for intrauterine insemination, given that pregnancy rates are similar as long as the percentage of normal cells exceed a minimum threshold, even if the initial motile sperm count is under a million. Supervised learning is proposed to reduce the computational costs by making predictions after a subset of the data is computed and used for training. By fitting the model to a tenth of the sample size required for statistical convergence, predicted results are precise and accurate to a handful of percentage points. This framework can be adopted to shortlist feasible designs of microfluidic devices before fabrication, as well as assess a wider variety of scenarios in preliminary hypotheses.

Contents

List of Figures

List of Tables

List of Symbols

a	Radius of spermatozoon head
b	Beat amplitude of spermatozoon flagellum
$\mathbf{B}$	Magnetic field strength
C_i	Constants in solution to homogeneous equation
C_0	Force density due to magnetophoresis
d_sep	Electrode separation distance
D_0	DEP force density
D_1	DEP force density per unit length in x-direction
D_2	DEP force density per unit length in y-direction
De	Deborah number
De_2	Deborah number multiplied by viscosity ratio
$\mathbf{e}$	Unit vector
$\mathbf{E}$	Electric field strength
E	Young's modulus
F_i	Force along the i-direction
$\mathbf{F}$	Force vector
$\mathbf{F}_{DEP}$	Force due to DEP
$\mathbf{F}_B$	Force due to magnetophoresis
f_{CM}	Clausius-Mossotti factor
f_m	Internal sliding force per unit length within flagellum
$\overline{f}_m$	Dimensionless f_m independent of space and time
$\mathbf{f}_\mathrm{oldroyd}$	Hydrodynamic force in an Oldroyd-B fluid
$\mathbf{f}_\mathrm{viscous}$	Hydrodynamic force in a viscous fluid
h	Deflection of flagellum as a function of space
i	Imaginary number $\sqrt{-1}$
I	Second moment of area
k	Spatial distribution of internal force within flagellum
K	Resistive force coefficient
M_i	Moment along the i-direction
M_bend	Internal bending moment within flagellum

$\mathbf{M}$	Moment vector
n	Sample size
N	Number of segments flagellum is discretized into
p	Radius of spermatozoon flagellum
q	Half segment length of flagellum in Slender Body Theory
Q	Internal shear force within flagellum
r_i	Roots to homogeneous equation
$\mathbf{r}$	Radial position vector in body-frame
$\mathbf{R}$	Radial position vector in inertial-frame
R_i	Surface force per unit area
Re	Reynolds number
s	Curvilinear position along flagellum
Sp	Sperm number
St	Strouhal number
t	Time
T	Internal tension within flagellum
u_i	Velocity along i-axis in body-frame
U_i	Velocity along i-axis in inertial-frame
$\mathbf{v}_{\text{wiggling}}$	Velocity of infinitesimal segment of flagellum in body-frame
$\mathbf{v}_{\text{swim}}$	Velocity of sperm head in body-frame
$\mathbf{v}_{\text{rel}}$	Relative fluid velocity in body-frame
$\mathbf{V}$	Velocity vector
V	Voltage across electrodes
$\forall$	Particle volume
$\mathbf{x}$	Position vector in cartesian coordinates
$\mathbf{X}$	Position vector of Stokeslet
y	Deflection of flagellum as a function of space and time
Z	Shear
α	Ratio of the wavelength to the arc length of the flagellum
β	Angle between fluid velocity and cylinder
Γ	Shape factor
δ_{ij}	Kronecker delta

$\varepsilon_{\text{medium}}$	Medium permittivity
ζ_{ij}	Function of parameters relating force to velocity
η	Yield
θ	Angular displacement between local-frame and body-frame
λ	Wavelength of flagellum waveform
Λ	Length of flagellum
μ	Fluid viscosity
ξ_i	Function of parameters relating force to velocity
ρ	Density
τ	Fluid relaxation time
τ_{ij}	Stress tensor
ϕ	Angular displacement between body-frame and inertial-frame
$\dot{\phi}$	Angular velocity
Θ	Transformation matrix that maps to local coordinates
χ	Purity
ψ	Normalised statistic
ω_{wave}	Beating frequency of flagellum
$^{\text{L}}$	Superscript denoting parameter in local coordinate frame
$_x$	Subscript denoting parameter in *x*-direction
$_y$	Subscript denoting parameter in *y*-direction
$_T$	Subscript denoting parameter in tangential direction
$_N$	Subscript denoting parameter in normal direction
$\sim$	Non-dimensionalised parameter
$\langle\ \rangle$	Time-average parameter

Chapter 1
Introduction

1.1 Significance of study

The study of human spermatozoa has significant medical applications relating to fertility and assisted reproduction, as well as social implications. Singapore has one of the lowest fertility rates in the world, with an average of 1.2 births per woman (Singapore Department of Statistics). Many other countries, such as Japan and South Korea, also have a birth rate much lower than what is required for the population to replace itself (The World Bank). Apart from encouraging the setting up of families, it is also important that assistance is provided to couples who wish to conceive but face medical difficulties, and minimise the social stigma that some may experience. Fertility issues are actually commonplace, with about 10% of the couples worldwide (World Health Organisation 2002) and 16% of the couples in Singapore (NUH Women's Centre, Singapore) experiencing difficulties conceiving, where male infertility accounts for half of the cases (Cui 2010). In 2012, a population-based study on nearly 5,000 men found that one in four will experience prolonged waiting time if they intend to father a child, while another 15% are likely to require medical assistance in order to have biological children (Jørgensen *et al*. 2012).

Assisted reproduction techniques account for over 1% of the infants born in developed countries today (Sutcliffe and Ludwig 2007). Despite advancements in medical technology, each cycle of fertility procedure is likely to turn out futile. An IUI cycle costs over SGD700 in Singapore, excluding medications or consultation fees, and comes with a success rate of only 9% (NUH Women's Centre, Singapore). Therefore, it is important to maximise the success rate by tapping on the knowledge from research and putting the information together. One way is to select healthy spermatozoa, or increase the likelihood of a healthy one fertilising the oocyte, so as to improve the chances of a successful pregnancy. Research has found that the chances of successful conception is significantly dependent on sperm morphology, both in natural fertilisation (Bartoov *et al*. 1994) as well as the various forms of assisted reproduction (Berkovitz *et al*. 1999, De Vos *et al*. 2003, Cassuto *et al*. 2009). While desirable sperm cells are

manually selected for IVF or ICSI, this is not feasible for IUI where a large number of sperm is used. Therefore, it will be advantageous to have a passive sorting procedure that gives a higher proportion of morphologically normal sperm, thus reducing the likelihood of morphologically abnormal sperm reaching the oocyte and competing for fertilisation.

From an applied engineering perspective, we first need to understand the mechanics of sperm locomotion, before looking into techniques for sorting them. The physical dimensions of the flagellum (Dresdner and Katz 1981, Serres *et al*. 1984) and head (Katz *et al*. 1982), as well as kinematic properties such as flagellum waveform (Ishijima *et al*. 1986), beat frequency (Katz *et al*. 1978) and progressive velocity (Mortimer *et al*. 1986) were measured decades ago. Due to the small characteristic length and velocity of a swimming sperm with respect to the kinematic viscosity of its fluid environment, the associated Reynolds number is many orders of magnitude smaller than unity. In this regime, viscous force dominates over inertia force, and motion is governed by the Stokes equation (Nguyen *et al*. 2014). Force scales linearly with relative velocity (Happel and Brenner 2012) rather than the square of it, and organisms are unable to swim by reciprocal motion due to kinematic reversibility (Purcell 1977).

With knowledge of how microorganisms behave (Lauga and Powers 2009), the desire for applications follow. Microfluidics allows researchers to investigate and manipulate particles as well as living cells (Lam *et al*. 2012, Nguyen 2012). Sperm cells have been sorted by the motility, morphology or chromosome contents using flow cytometry (Johnson *et al*. 1987), optics (Shi *et al*. 2009), magnetophoresis (Said *et al*. 2008), filtration (Henkel *et al*. 1994), density gradient centrifugation (Bolton and Braude 1984), boundary attraction (Guidobaldi *et al*. 2014), or the sperm's own motility in a microfluidic channel (Cho *et al*. 2003, Seo *et al*. 2007). A few years ago, the first paper on subjecting sperm to dielectrophoresis was published (Rosales-Cruzaley *et al*. 2013).

A literature review on the different disciplines led the author to see an area for improvement with far-reaching effects on society (which is the success rate of ART), know the objectives that should be worked towards (which is to acquire motile and normal sperm), understand the physics behind what influences the behaviour of sperm, as well as recognise the variety of established microfluidic procedures which may potentially be applied to achieve the objectives. The author then narrowed down the

choices to using dielectrophoresis or magnetophoresis. Both fields of research have led to the effective sorting of cells. Dielectrophoresis have been used to concentrate rat sperm and distinguish between mature and spermatogenic cells (Rosales-Cruzaley *et al*. 2013), while magnetic activated cell sorting even led to the birth of a healthy human baby (Rawe *et al*. 2010).

The known published studies on sperm sorting by dielectrophoresis or magnetophoresis have been confined to experimental work. Without a theoretical framework, future studies exploring new set-ups are likely to be associated with trial-and-error. While there are comprehensive theoretical studies on modelling sperm motion (Gaffney *et al*. 2011, Lauga and Powers 2009), these are focused on the hydrodynamics and do not include the effects of an external electrical or magnetic field. Morever, statistical uncertainties are not incorporated. Given that morphometric parameters of sperm vary substantially (Katz *et al*. 1986), each cell responds differently under the same environment, and this should be accounted for in cell sorting. The author is interested to explore the sorting of sperm using an external field from a theoretical approach coupled with statistical analysis. In addition, the use of machine learning to reduce computational costs will be explored.

The contents in this thesis are written with the aim of improving our knowledge of sperm subjected to external fields, providing a framework which may be built upon by follow-up studies to develop applications that enhance the success rate of assisted reproduction. Every contribution towards this field of research can potentially lead to future breakthroughs, and even a slight improvement in the odds can help thousands of families realise their dreams of parenthood.

1.2 Research gap

There are numerous microfluidic sorting techniques, of which many have been applied to sort sperm using different concepts. However, the published information typically contains information to replicate the experiment, but lack equations for other researchers to adopt the experiment to their own specific research objectives. If a different outcome is desired, the experiment set-up may have to be tuned by trial-and-error before a trend can be observed, thus taking up precious resources which could have been put to better use.

The mathematical models available allow the locomotion of micro-organisms to be described with high accuracy. With the advancement in computation power, numerical simulations which would have been impossible to solve by hand decades ago can now be performed by moderately-priced personal computers. However, these models often describe the response of a single cell rather than provide a distribution-based response of the entire cell population in the sample. A full detailed computation taking into account all the cells would undoubtedly be mathematically complicated and resource-intesive. Nonetheless, distributions in response ought to be taken into account for applications such as cell sorting, and making approximations would be better than ignoring the need to take variations into account.

It has been over 40 years since the birth of the world's first baby conceived by IVF. Despite tremendous technological progress in many areas of science, the success rate of IVF is still barely over 30%, while IUI is like a roll of the die given its one in six chance of leading to pregnancy. The community has a thorough understanding of the factors influencing the outcome of successful reproduction, but is still unable to control the fertilisation outcome as desired. There is much emphasis placed on the biological and chemical aspects of assisted reproduction, and rightly so, but perhaps adding an engineering perspective might contribute to breakthroughs.

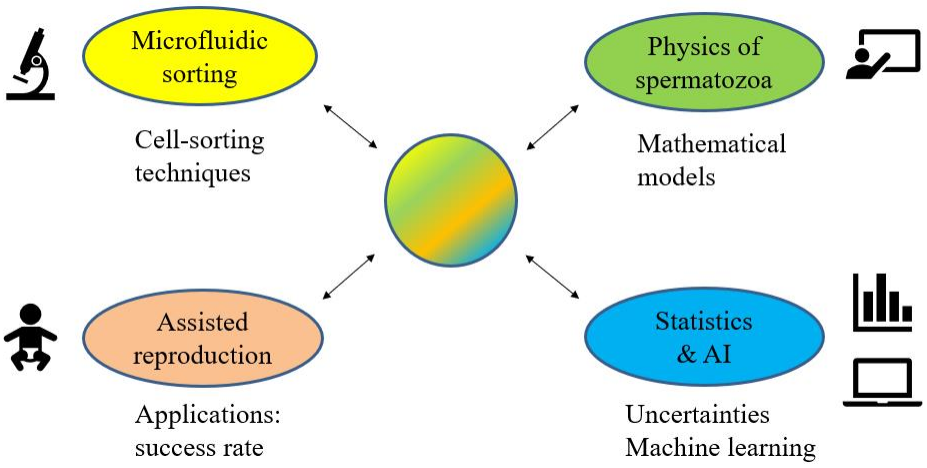

Figure 1-1 – Illustration of different fields which can be combined for inter-displinary research.

Data science, which encompasses statistical analysis and machine learning, has seen a boom in popularity over the past few years. Supervised learning has already led to human-level performance in image recognition, while the use of reinforcement

learning has led to computers which defeated world masters in chess and Go. Corporations of all sizes are looking to join the wave and improve their workflow or profits. Surprisingly, the benefits of data science are not widely tapped by the fluid dynamics community.

Each field described above (Figure 1-1) has a vast amount of knowledge which can be applied. However, partnerships encompassing all the above disciplines are rare. There is tremendous potential for progress if multi-disciplinary synergy can be established, and the benefits can be more than just the sum of its parts.

1.3 Objectives and scope

The key objective of this thesis is to study the feasibility of sperm sorting by an external field to increase the proportion of morphologically normal sperm cells for use in assisted reproduction. First, the factors influencing the success rates of assisted reproduction, and the existing sperm sorting techniques, will be identified. Second, the mathematics behind sperm locomotion in an external field will be studied, so that experimentalists can have a clearer picture of the relative contribution from each variable involved. Third, the effect of sperm manipulation in a Newtonian and non-Newtonian fluid will be investigated, to understand the significance of the fluid environment on the sperm velocity and flagellum waveform. Fourth, the velocity distribution of a sample population of sperm will be computed to account for variations in morphology which may result in overlapping response between normal and abnormal sperm. Finally, the use of supervise learning to make predictions will be assessed to determine the conditions upon which supervised learning may be applied to predict the outcome of sperm sorting.

The studies will be theoretical, although comparisons are made to experimental observations for specific cases. Hydrodynamic force will be modelled using Resistive Force Theory or Slender Body Theory. Boundary effects and interactions between cells are ignored in the context of a dilute sample in a large microchannel, and the electric or magnetic field is assumed to be unaltered by the presence of cells or fluid. Biological responses of spermatozoa are also neglected.

1.4 Overview of thesis

With an understanding of the rational for carrying out research in this field, the rest of this thesis will be presented systematically as follows. The literature review in Chapter 2 provides a broad knowledge on available assisted reproduction techniques and the physical aspects of sperm, followed by the theory and supporting experiments regarding hydrodynamic forces and interesting phenomena present in microfluidics. Thereafter, readers will be introduced to a variety of established methods to sort sperm by different properties.

Chapter 3 contains a simplified analytical study on the effects of dielectrophoresis on the velocity of sperm. Using an approximate analytical relation between the velocity and electric field gradient, it will be shown that larger sperm will be more strongly influenced by an applied field. Given the difference in morphology between the X- and Y-sperm, the results provide proof-of-concept that sperm may be sorted by gender using a non-uniform electric field.

Chapter 4 treats the flagellum as a flexible filament and solves for beating pattern analytically as a function of the Sperm number, internal force distribution, as well as fluid properties. The extent to which dielectrophoresis modifies the flagellum waveform will be considered, and subsequently shown to be insignificant within the range of conditions sufficient for sorting. The induced velocity in a Newtonian fluid and viscoelastic fluid according to this model will be studied.

Chapter 5 delves deeper into theoretical aspects of hydrodynamics and looks into the mathematical framework of Slender Body Theory (SBT), which has an improved accuracy over Resistive Force Theory (RFT). The force-velocity relation given by these two theories will be compared, and the sources of deviation will be discussed. Thereafter, SBT will be applied to solve for the beating pattern of a flexible flagellum, and the rationale for choosing a prescribed waveform for subsequent statistical analysis will be given.

Chapter 6 explores the feasibility of sorting sperm to obtain a higher proportion of morphologically normal sperm, with the objective being to increase the success rate of assisted reproduction. Recognising that the physical dimensions of sperm are widely distributed, a statistical approach will be taken, and the results will be interpreted in

terms of probabilities and confidence intervals. This framework is a novel improvement to existing sperm studies which involve deterministic computations and lacks the accountability for random distributions. Supervised learning will also be implemented in a bid to reduce computational costs.

Chapter 7 provides a summary of the research carried out and key findings to take away from this thesis, and concludes with suggestions on possible future directions on how studies on sperm sorting may be furthered.

Chapter 2
Literature Review

In this chapter, a review is done on the principles and effectiveness of various assisted reproduction procedures available. Thereafter, the fluid mechanics and various phenomena in microscale locomotion are discussed. This is followed by a review of established sorting techniques used to sort microparticles and sperm cells. Finally, the author concludes this chapter by highlighting the key points and discussing how the existing literature may be built upon to fill the research gap and serve as a foundation for practical applications.

Roosen-Runge (1977) has described the process of how primordial germ cells develop into spermatogonia, spermatocytes, spermatids and finally completing the differentiation process to become spermatozoa. In this thesis, the word 'spermatozoa' and 'sperm' is used interchangably for convenience, as is the common practice among the general public.

2.1 Assisted Reproduction Techniques

It is estimated that 10% of the couples globally experience some degree of infertility (World Health Organisation 2002), and assisted reproduction techniques account for at least 1% of the infants born in developed countries (Sutcliffe and Ludwig 2007). Infertility could be attributed to the sperm (Agarwal and Said 2003; Fisch and Lipshultz 1992), or various other factors such as immunologic (Schwimmer *et al*. 1967), uterine (Hunt and Wallach 1974), environmental (Hruska *et al*. 2000), and psychological factors (Edelmann and Connolly 1986). Assisted reproductive techniques are procedures which increase the chance of a woman conceiving through the use of scientific methods. Couples who are unable to conceive will first be asked to undergo further tests for male infertility (Sharma *et al*. 2010) and female infertility (Smith *et al*. 2003) before doctors recommend appropriate actions. In this section, the three most widely-used methods will be presented.

2.1.1 In vitro fertilisation (IVF)

The term IVF is synonymous with assisted reproduction to many people, despite being neither the first approach recommended by doctors, nor the procedure with the highest chance of conception. As evident from the name, this technique involves fertilisation outside the female body. This idea was introduced in the 1950s, and the advancement as well as acceptance of this technology over the decades are discussed by one of the pioneers who won the Nobel Prize for IVF (Edwards 2001). IVF begins with the patient given ovarian stimulation, after which the oocytes were collected and inseminated, then placed in an incubator (Edwards 2000). After fertilisation, a zygote is formed, and the cell multiplies to form an embryo, which is then transferred to the uterus. It has been found that the success rate is dependent on the spermatozoa motility (Verheyen *et al*. 1999) and morphology (Grow *et al*. 1994). The first baby conceived by IVF was borned in 1978, and since then, IVF had led to the birth of over 5 million infants (National University Hospital, Singapore).

According to a review (Henkel and Schill 2003) of sperm preparation techniques used in ART, the three common classes of methods are migration, density gradient centrifugation and filtration. The migration technique, which includes swim-up (Sakkas *et al*. 2000) and migration-sedimentation (Tea *et al*. 1984), are low-cost methods suitable only when female factor infertility is involved. Although a clean fraction of highly motile sperm can be recovered, this method has a low yield, and hence it requires both a high sperm count and motility. A second category is density gradient centrifugation, which gives a clean fraction of highly motile sperm and is suitable for low sperm density samples (Mortimer 1994). Lastly, filtration may be done using glass wool (Henkel *et al*. 1994), fibrous polyester L4 membranes (Agarwal *et al*. 1992) or Sephadex beads (Drobnis *et al*. 1991) which are synthetic cross-linked polymers. Filtration gives a high yield and reduces the level of reactive oxygen species, which are shunned as they oxidise sperm plasma membrane and impair sperm functions. More details of sperm preparation techniques are given in section 2.3.

IVF involves the transfer of multiple embryos to the womb, and couples could get more than they asked for. Approximately a quarter of the successful cases resulting in live birth are multiple gestations (Land and Evers 2003), as compared to less than 2% in a natural conception (National University Hospital, Singapore), hence increasing the

risk of premature birth or delivery complications. Therefore, elective single embryo transfer (eSET), where only one good-quality embryo is transferred, is encouraged for the initial treatment cycles (van Montfoort *et al*. 2005). This mitigates the risks of twin pregnancies, at the expense of a slightly lower but still comparable rate of successful conception (National University Hospital, Singapore).

Apart from couples facing limited success in achieving pregnancy, some opt for IVF along with preimplantation genetic diagnosis (PGD) to avoid transmitting a genetic disorder or disease to their child. In a bid to support parenthood and mitigate the aging-population, the Singapore government not only provides a basket of monetary and non-monetary incentives for parents, but also supports couples with difficulties conceiving by co-funding up to 75% of the costs involved in IVF or other approved assisted reproduction treatments (Ministry of Health, Singapore).

2.1.2 Intracytoplasmic sperm injection (ICSI)

ICSI can be deemed as a modification to IVF. A single spermatozoon is selected and placed using an injection pipette into the plasma membrane of the oocyte, which is then left for fertilisation to occur (Malter and Cohen 2002). The subsequent procedure is similar to IVF, where the embryo is transferred to the uterus a few days later. ICSI has the highest pregnancy rate and is well-suited for cryptozoospermia, that is, the condition of extremely low number of viable spermatozoa (Van Steirteghem 2002).

It may appear as though the motility and health of the spermatozoa can now be neglected, given that the spermatozoon is selected and placed into the oocyte without its own efforts. However, a study done on 1000 ICSI cycles proved otherwise (De Vos *et al*. 2003). The fertilisation rate was about 11 percentage points higher when spermatozoon with a normal morphology was selected, as compared to spermatozoon with an abnormal morphology. To address concerns raised over the lack of natural selection, Takeda *et al*. (2012) proposed using spermatozoa sorted by cervical mucus-penetration for ICSI. They highlighted that the procedure is simple, and gives a higher percentage of morphologically normal spermatozoa compared to those obtained from density gradient centrifuge with swim-up technique, without the need for centrifugation.

Bartoov *et al*. (2001) introduced the motile-sperm organelle-morphology examination (MSOME), in which inverted light microscope and digital imaging allows the nuclear contents to be examined at 6600×, improving the pregnancy rate of ICSI from 30% to 58%. MSOME allows spermatozoa with large nuclear vacuoles to be identified and avoided, with subsequent research finding that large nuclear vacuoles is correlated with DNA fragmentation (Utsuno *et al*. 2013). A review by Komiya *et al*. (2014) has summarised how 'large vacuoles' is defined in various studies. This improvisation to ICSI is termed Intracytoplasmic morphologically-selected sperm injection (IMSI), and follow-up studies bear testament to the improved pregnancy rate (Antinori *et al*. 2008, Balaban *et al*. 2011, Bartoov *et al*. 2003).

2.1.3 Intrauterine insemination (IUI)

For IUI, fertilisation occurs inside the female body, unlike IVF and ISCI. In this procedure, semen from the male partner or a donor is washed and centrifuged, and the motile spermatozoa is then deposited by means of a catheter into the uterus during the ovulation period (Human Fertilisation Embryology Authority), and what happens after is left to nature. It was found that age was the most important factor in determining the success of IUI, followed by the number of motile spermatozoa (Campana *et al*. 1996). The cumulative ongoing pregnancy rate after three IUI cycles is comparable to one IVF cycle (Ombelet *et al*. 2003). Since IUI is a simpler and less invasive procedure, with the cost-per-maternity being around half compared to IVF and ICSI, it is promoted as a good first approach for cases of mild male infertility (Zayed *et al*. 1997).

A review of 55 studies which investigated sperm parameters in relation to IUI success found that initial motile count (IMC) was deemed the most important (Ombelet *et al*. 2014), with the majority citing a threshold value of between 1 and 2 million. Sperm morphology using the strict criteria was deemed the second most important parameter, with the majority citing a threshold of 5%. If these criteria are not met, the success rate is significantly lower, but meeting these criteria still does not come close to guaranteeing success. Another review reported that two-thirds of the studies set the benchmark for IMC at 5 million (Tomlinson *et al*. 2013). Ombelet *et al*. (2003) reported that as long as the morphologically normal sperm exceeds 4%, the cumulative ongoing pregnancy rate after three IUI cycles with clomiphene citrate ovarian stimulation is similar regardless

of the initial motile sperm count (Figure 2-1). Since a morphologically satisfactory sample is a sufficient condition for infertile couples without tubal factor to undergo their desired choice of treatment, it is apparent that a preparation procedure which improves the morphology of the sperm sample will be highly valued, and one which improves motility at the same time will be an added bonus.

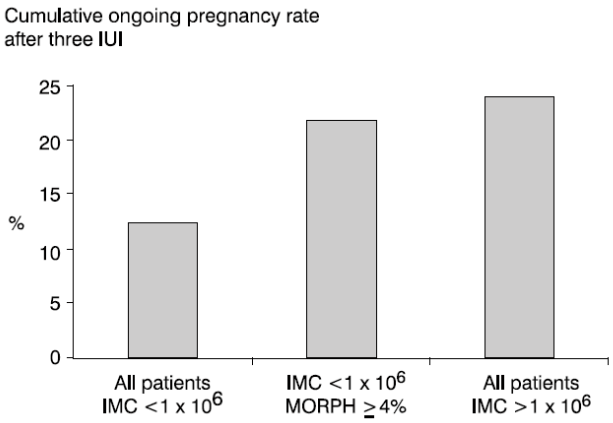

Figure 2-1 – Cumulative ongoing pregnancy rate after three CC-IUI cycles. Reprinted from Ombelet *et al.* (2003).

2.1.4 Risks involved

The price of assisted reproduction techniques to infertile couples is not just on the financial aspect. Even after a successful pregnancy and live birth, the health of their offspring is of another concern, such as the higher likelihood of low birth weight (Schieve *et al*. 2002) and risk of major birth defects (Olson *et al*. 2005). Hansen *et al*. (2005) reviewed 25 published papers on the prevalence of birth defects associated with assisted reproduction techniques and cited that two-thirds of the studies showed an increased risk of at least 25%.

On the flip side, one should keep in mind that the age of couples who undergo assisted reproduction is generally higher than those who conceive naturally, as couples would not choose this option at the first instance. Statistics showed that the age of the mother (Andersen *et al*. 2000) and father (Kidd *et al*. 2001) have a significant effect on the chances of a successful pregnancy. According to the Human Fertilisation Embryology Authority of the United Kingdom, 32% of IVF/ICSI cycles and 16% of the IUI cycles resulted in a live birth for women under 35 years of age, and the success rate declined steadily and rapidly as the age increase. This explains why some studies

looking into the risks of assisted reproduction give a corrected result taking into account such factors. The odds ratio of congenital malformation for children conceived by IVF is 1.20 times that of children conceived naturally, but after correction for different factors such maternal age, the odds ratio is reported to be a mere 1.03 (Anthony *et al*. 2002). Another study found the odds ratio of major malformation for children conceived by ICSI to be 1.44, and after correction for risk factors, to be 1.24, hence concluding that while much risk can be attributed to parental factors, technique-related risk is still not negligible (Katalinic *et al*. 2004).

In spite of the concerns discussed, the risks could be worth taking as long as a well-informed and careful decision is made with the expected benefits outweighing the expected costs, and with parents prepared to care for their children regardless of possible medical complications. Given that spermatozoa play a direct role in reproduction, we need to understand it not just biologically but also physically, and seek to apply this knowledge for the betterment of related fields in reproduction.

2.2 Theory on microscale fluid mechanics and spermatozoa[1]

In light of the earlier discussions on assisted reproduction, there is much to be contributed by physicists and engineers as new applications can be created with an understanding of what influences the sperm behaviour. In this section, an overview of the physics in low Reynolds number locomotion will be explored.

2.2.1 Resistive Force Theory

It is widely accepted that inertial effects can be ignored when dealing with microorganisms (Pedley and Kessler 1992). As such, their motion is governed by Stokes equation. Self-propulsion due to a purely viscous force is first discussed by Taylor (1951) in the form of a waving sheet with small amplitude, and subsequently Hancock (1953) considered the propulsion of an infinite filament. This leads to RFT, in which a "suboptimal" resistive coefficient (Lighthill 1976) is used to linearly relate the viscous force to the fluid viscosity, relative fluid velocity, and the object's length scale. In RFT,

[1] Published in Koh JBY, Shen X, Marcos (2016) Theoretical modeling in microscale locomotion. *Microfluidics and Nanofluidics* 20:1-27

the flow field is assumed to be uninfluenced by other parts of the filament (or flagellum), and ignores the presence of any cell body. The first application of RFT on microorganisms was by Gray and Hancock (1955), who modelled the force acting on a sperm as the summation of independently determined viscous force acting on each infinitesimal segment of the flagellum in the normal direction, denoted subscript *N*, as well as tangential direction, denoted by subscript *T*:

$$\mathbf{F} = \int \left[K_N V_N \mathbf{e}_N + K_T V_T \mathbf{e}_T \right] ds \,, \tag{2.1}$$

where s is the curvilinear position along the flagellum, K_N and K_T are the resistive force coefficients, V_N and V_T are the velocity components, while $\mathbf{e}_N$ and $\mathbf{e}_T$ are the unit vectors in the normal and tangential directions, respectively. Gray and Hancock (1955) proposed an analytical relation for K_N and K_T, which was subsequently refined by Lighthill (1976) to be

$$K_{N(Lighthill)} = \frac{4\pi\mu}{\ln\left(0.18\lambda / p\right) + 0.5} \,, \tag{2.2}$$

$$K_{T(Lighthill)} = \frac{2\pi\mu}{\ln\left(0.18\lambda / p\right)} \,, \tag{2.3}$$

where μ is the fluid viscosity, λ is the wavelength, and p is the radius of the flagellum. The procedure in which Lighthill derived RFT is presented in the Appendix A, with the intermediate steps filled by the author.

The solutions to analytical models depend on the dimensionless ratio K_N / K_T. In the limit of infinitely long filaments, the ratio approaches 2, which is the approximation used in some studies (Fu *et al*. 2008; Koh and Marcos 2014; Tournus *et al*. 2015). However, any real finite filament will have K_N less than twice the value of K_T. Experimental investigations have led to varying conclusions regarding the measured and computed ratio. Friedrich *et al*. (2010) used high-precision tracking of bull spermatozoa to measure the instantaneous velocities as well as flagella beat pattern, after which RFT was used to reconstruct the instantaneous velocities. Using a least square fit, the ratio between the normal and tangential resistive force coefficient was determined to be 1.81 ± 0.07. Using this model, the team found that RFT can be used to predict instantaneous velocities with an error of 6% on average (Friedrich *et al*. 2010).

Bayly *et al*. (2011) analysed the images of three phenotypes of uniflagellate *Chlamydomonas* cells under high speed video microscopy, and plotted the observations against analytical predictions using coefficients which give the smallest mean-squared error. They concluded "good qualitative agreement" between measured velocities and those predicted by RFT. However, the values of resistive coefficients determined experimentally differ by a factor of two as compared to the theoretical values computed using Lighthill's coefficients. They proposed that the deviations may have resulted from long-range interactions being neglected. It is worthy to note that *Chlamydomonas* has a flagellum length of only 12 μm, and is a pulling cell which generates a different flow field (Elgeti *et al*. 2015) compared to that generated by a pushing cell like spermatozoa.

The nematode *C. elegans*, although not a microscopic cell, is used in some experiments as a swimmer in low Re, with justifications being made by Sznitman *et al*. (2010). Being in the scale of 10^{-3} m, *C. elegans* generate a force which can be measured more conveniently than microscopic cells. Measurements revealed that the resistive force coefficient ratio is 1.4 and swimming speed is 0.36 mm/s, while calculations from RFT predicted the ratio to be 1.5 and the speed to be 0.43 mm/s. Also dealing with *C. elegans*, Schulman *et al*. (2014) found that variations in drag coefficients vary little for nematodes of all sizes ranging from 0.4 to 1.2 mm. They measured the normal and tangential force coefficients to be $(5.1\pm0.3)\mu$ and $(3.4\pm0.2)\mu$, as compared to theoretical predictions of $(4.9\pm0.4)\mu$ and $(3.0\pm0.3)\mu$, respectively. In addition, the lateral and propulsive force plotted over several periods showed excellent agreement between theory and experimental measurements (Figure 2-2).

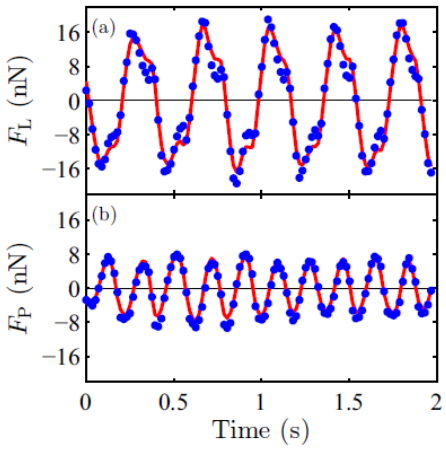

Figure 2-2 – (a) The lateral force F_L and (b) propulsive force F_P of C. *elegans* plotted as a function of time. The experimental data (blue circular markers) contain a systematic error of roughly 10% from uncertainty in the spring constant of the micropipette. The prediction from RFT (red solid line), which has been fitted to the data, has an error estimated to be 5%. Reprinted from Schulman *et al*. (2014).

The validity of RFT is also supported by experiments done using robotic swimmers. A macro-scale robotic swimmer with tail length and diameter in the order 10^{-1} m and 10^{-4} m, respectively, and speed of 21 μm/s at an actuation frequency of 35 Hz was built (Yu *et al*. 2006) to model microbes. The results show that the propulsive force matches theoretical values predicted by RFT. Another team fabricated an externally-powered propeller, with tail length and diameter in the order 10^{-6} m and 10^{-7} m, respectively, and a bending stiffness of 10^{-24} N m^2 to model cells (Pak *et al*. 2011). The theoretical predictions of speed, as a function of the external field frequency and of Sperm number Sp, fall almost within one standard deviation of the measured data.

Despite some studies showing the shortfalls of RFT (Chattopadhyay and Wu 2009, Kurtuldu *et al*. 2013, Rodenborn *et al*. 2013), this model nonetheless serves as a useful estimate for studying new scenarios, as its predictions match experimental observations at least to the order of magnitude. As Michael Cates, Lucasian Professor of Mathematics at the University of Cambridge, writes in a review (Cates 2012): "simple models are the first to be falsified. Yet a model that clearly does not fit the data, but nearly does so despite its gross simplifications, can provide crucial mechanistic insights... even if a more complicated model already exists and fits the data better."

2.2.2 Slender Body Theory

Slender Body Theory (SBT) is an improvement over RFT. While the latter ignores the effects of interactions and describes hydrodynamic force as a linear function of the local velocity, SBT provides a non-linear relation and accounts for hydrodynamic interactions across the entire body. The body is assumed to be slender, such that its cross-section is small relative to the body length, with small curvature and is in Stokes flow where inertial is negligible relative to visous forces. SBT was first introduced by examining the velocity of a long ellipsoid and a finite circular cylinder stationary under the uniform flow, and extended to general cases by Batchelor (1970) and Cox (1970). Lighthill (1976) and Higdon (1979) applied SBT to relate the velocity distribution on the flagellum to the force per unit length, by considering the contribution of Stokeslet and doublet. A Stokeslet is a concentrated point force while a doublet is a pair of concentrated point force which is equal in magnitude but opposite in direction. The theory is further developed to analyze the behavior of flagellum or filament by adding

the contributions of higher order singularities (Johnson 1980). Both Lighthill's and Johnson's SBT agree 'extremely well' with experiemental measurements of helixes of various pitch angles (Liu *et al*. 2013). For organisms with negligible rotational velocity, the flagellum can be replaced by a distribution of Stokeslets and doublets along the centerline to satisfy the no-slip boundary condition on the flagellum surface.

The velocity of a single-flagellum bacterium swimming in a straight line is compared to a mathematical model which treats the specific bacterium as a rigid helical flagellum attached to a spherical head. SBT is shown to agree with the experimental observations qualitatively, with the measured velcocity differing by ~7% for a small cell (*E. Coli*), and ~17% for a large cell (*V. alginolyticus*) (Chattopadhyay and Wu 2009). Another team compared numerical computations with experimental measurements on a nanobot driven by rotating helical flagellum and found a good match (Rodenborn *et al*. 2013). The presence of error arising from the use of SBT can generally be attributed to the fact that Stokeslets are used instead of a collection of singularities, and that imposing centerline boundary conditions correspond to better accuracy when analyzing a slender spheroid (Bouzarth and Minion 2011). SBT only allows the velocity of the swimmer to be computed. If information about the velocity, pressure and stress at any point of interest in the fluid or body is desired, it will be necessary to turn to more sophisticated models such as the Method of Regularized Stokeslet (Leiderman *et al*. 2013).

2.2.3 Rheotaxis

Rheotaxis occurs when a body experiences different local forces due to a shear flow. A review by Pedley and Kessler (1992) noted that cells swimming in flow channels have the tendency to travel upstream, due to the inclination of swimming towards the wall coupled with the torque induced by shear. Spermatozoa are one such category of cells which have long been observed to exhibit such behaviour (Bretherton 1961). There are suggestions that in the female mammalian reproductive tract, chemotaxis is significant only near the ovum and that the major factor in sperm guidance is rheotaxis (Miki and Clapham 2013). More recently, it was noted that spermatozoa do not simply swim upstream in shear flow; they tend to exhibit spiral-shaped trajectories along the boundaries of a cylindrical channel (Kantsler *et al*. 2014). In fact, a numerical study predicted that rheotaxis is possible regardless of whether there is a surface in the

vicinity, as long as the background flow does not wash the cell away (Ishimoto and Gaffney 2015).

The effects of rheotaxis for human and bull spermatozoa peaks when the shear rate reaches 3 to 3.5 s^{-1} (Winet *et al*. 1984). However, this value may vary when for spermatozoa of different species. Using the sperm of an abalone species which fertilizes externally, it has been shown that sperm velocity and fertilization success was higher at low shears of 0.1 ~ 1 s^{-1} as compared to still water, but lower when the shear is increased beyond 4 s^{-1} (Riffell and Zimmer 2007). The authors noted that the binding force between a sperm and the zona pellucida of an ovum is in the range of 10^{-10} to 10^{-9} N (Thaler and Cardullo 1996), and that a shear rate of 10 s^{-1} results in a force of 10^{-11} N, which is unlikely to cause dislocations between the gametes. Coupled with an experimental validation using a control test, they concluded that shear rates of up to 10 s^{-1} is not detrimental to cell viability, and that the lower fertilization when shear is too large is simply due to hydrodynamic factors. The effects of rheotaxis may be analysed by comparing the normalised swimming velocity with respect to the normalised velocity of shear flow (Kantsler *et al*. 2014). When subjected to shear flow with a magnitude equivalent to its free-swimming velocity, a sperm cell can achieve an upstream velocity over a third of its free-swimming velocity (Figure 2-3). The authors pointed out that viscosity of the sperm in their natural environment is approximately 3 mPa s (Owen and Katz 2005), and higher values of viscosity actually decreases the effects of rheotaxis. It was also observed that under flow reversal, the sperm realigns against the new flow direction in a matter of seconds.

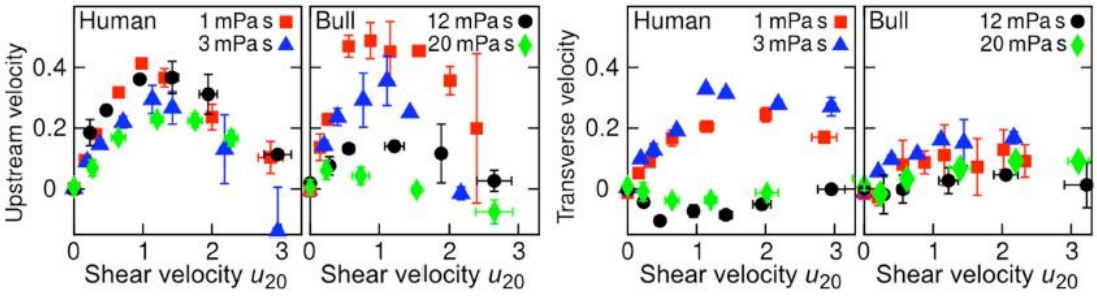

Figure 2-3 – Upstream and transverse mean velocities of human and bull spermatozoa as a function of shear flow speed u_{20} at 20 µm from the surface, for viscosities of 1 mPa s (red squares), 3 mPa s (blue triangles), 12 mPa s (black circles) and 20 mPa s (green diamonds). All velocities are normalised by the sample mean speed $v_{0\mu}$ at zero shear rate. For human sperm, in order of increasing viscosity $v_{0\mu}$ = 53.5, 46.8, 36.8, 29.7 µm/s, and for bull sperm $v_{0\mu}$ = 70.4, 45.6, 32.4, 29.6 µm/s. Reprinted from Kantsler *et al*. (2014).

It may not be immediately intuitive that a shear flow may cause some organisms to travel sideways rather than along the flow axis. However, this is indeed the case for helical swimmers such as many bacteria. Marcos *et al*. (2012) investigated the effects of rheotaxis on *B. subtilis* through experiments and found that the presence of a shear flow may induce a rheotactic velocity of nearly 10% of the mean swimming speed at a shear rate of 10 s^{-1}, in a direction perpendicular to the shear flow. They also demonstrated experimentally that bacteria rheotaxis is a passive process which results from the coupling of motility, shear, and geometry. Miki and Clapham (2013) proposed that although rheotaxis does not rely on sensory mechanisms, sperm rheotaxis is not entirely passive as it is mediated by Ca^{2+} intake via the Cation channels of sperm (*CatSper*) which induces hyper-activated motility (Qi *et al*. 2007). They demonstrated that ordinary mouse and human sperm have a high tendency to align (Figure 2-4) against a flow of ~50 µm/s, with over half of the population orienting within ±22.5° of the forward vector, but mouse sperm lacking *CatSper* are indifferent to a flow and exhibits circular trajectories. Interestingly, indifferent to the presence or absence of *CatSper*, sea urchin sperm do not demonstrate rheotaxis. The circular trajectories of a sea urchin sperm might be attributed to the fact that the ratio between the head volume and flagellar length, and therefore the torque, for a sea urchin sperm is approximately 50 times greater (Smith *et al*. 2009) than that of a human sperm.

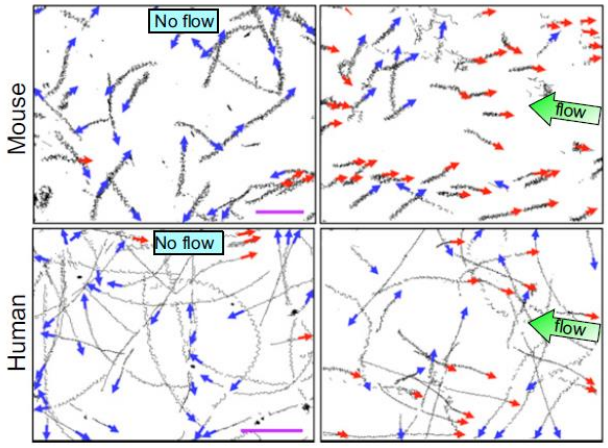

Figure 2-4 – Trajectories of mouse (top; scale bar represents 200 µm) and human (bottom; scale bar represents 100 µm) sperm without flow (left) and in flow (right), as analysed by Computer-assisted sperm analysis (CASA). Reprinted from Miki and Clapham (2013).

Even though gravitaxis, and hence gyrotaxis (Kessler 1985), is evident in motile flagellates as well as ciliates (Durham *et al*. 2009), it is negligible for spermatozoa (Winet *et al*. 1984) and hence will not be discussed here.

2.2.4 Wall effects

The presence of boundaries influences the swimming speed and trajectory of micro-swimmers. In microfluidic set-ups, the channels are usually narrow, which means that a good portion of the particles or cells studied will be in close proximity to a boundary. Research has found that a swimmer moving towards a solid boundary experiences an increased drag force and stress on its surface (Ramia *et al*. 1993), and therefore its swimming speed is reduced if the swimmer is unable to produce enough thrust for compensation. In this section, we discuss the constraints under which it is fair to neglect the wall effect on microbes.

The average velocity of a bacterium with a single helical flagellum rotating at a constant rate in the vicinity of a surface has been computed (Ramia *et al*. 1993) by the boundary element method (BEM). Having found the normalised velocity, force and torque experienced as a function of the relative separation distance, the authors concluded that hydrodynamic interactions is significant only when the separation distance is no larger than the largest physical dimension of the organism. The model was compared with experiments by Frymier *et al*. (1995), in which a three-dimensional tracking microscope to track the motion of a dilute sample of *E. coli* near a glass plate. Results show that wall effect is negligible when the bacteria is more than 10 μm from the surface, but significantly reduces the speed of bacteria within 2 μm from the planar surface. Frymier and Ford (1997) reported that the speed of the wild-type *E. coli* strain NR50, with a cell size of 1 μm, swimming perpendicular to the wall is significantly affected by the wall when it is up to 10 μm away. However, the speed of those cells swimming approximately parallel to the surface remains constant regardless of the distance.

Similar results are obtained when the monotrichous bacteria *V. alginolyticus* is observed using inverted phase-contrast microscopy (Goto *et al*. 2001; Goto *et al*. 2005). They noted that, with all else kept constant, the wall effect on cells swimming towards the boundary differs from that of cells swimming away. Observing the swimming speed and pitching rate as a function of the distance away from the wall and the orientation, it was concluded that wall effect was negligible on the bacteria at a distance of at least 12.5 times the diameter of the cell body (Figure 2-5). This is in line with the cell distribution study of *E. coli* between two glass plates, in which there is a sharp spike in

the population density within a distance of 10 to 12.5 times the cell length away from the wall but little variations at further distance (Berke *et al*. 2008).

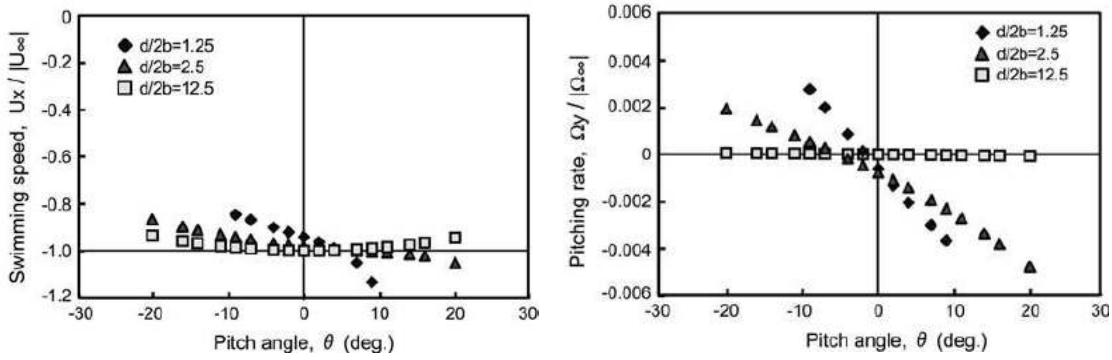

Figure 2-5 – Forward swimming speed (left) and pitching rate (right) of the bacterial model as a function of pitch angle θ and distance d from the wall normalised with the width of the bacterial cell body. When $\theta = 0$, the cell is swimming parallel to the wall. The swimming speed is normalised using the swimming speed in free space, and pitching rate is normalised with the angular velocity in free space. Reprinted from Goto *et al*. (2005).

Researchers have also looked into whether wall effects may be neglected for spermatozoa, which are much larger than the bacterial cells. Fauci and McDonald (1995) modelled two-dimensional spermatozoa with beating flagella as a distribution of the singularities to study its motion in the presence of two parallel boundaries. For the spermatozoa that was placed midway between the channel walls, the wall effect can be neglected when the ratio between the half channel width and the flagellum amplitude is around 5. The spermatozoa model has been extended to a more general case, comprising a distribution of regularized Stokeslet over an ellipsoid and along a slender filament (Gillies *et al*. 2009). The sperm motion in a slide chamber is computed, in which the walls are modelled as parallel plates and discretized by a distribution of regularized Stokeslets. The force acting on the sphere-rod body as computed by them is in good agreement with the results by Ramia *et al*. (1993), and the boundary effect becomes insignificant when half-depth of the chamber slide approaches 10 times the size of the swimmer (Figure 2-6).

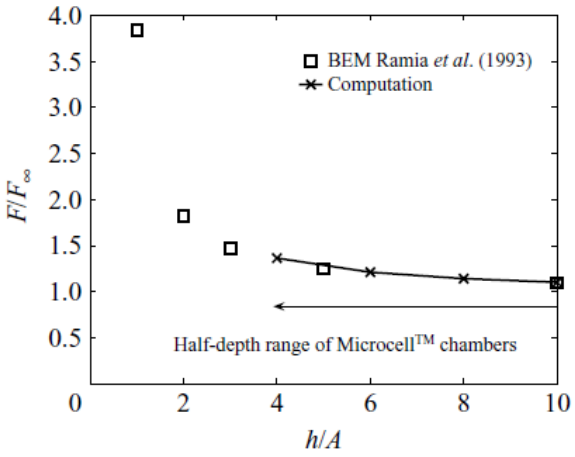

Figure 2-6 – Normalised force F/F_∞ as a function of normalised distance from the wall, for a sphere of radius A translating between parallel chamber walls where the half-depth is h. Square markers indicate the results of Ramia *et al.* (1993), while cross markers indicate the computations by Gillies *et al.* (2009) corresponding to the half-depth of the chambers used. Reprinted from Gillies *et al.* (2009).

Based on the results from studies discussed in this section, it is safe to conclude the wall effect can be neglected when the distance from the swimmer to the wall is at least an order of magnitude greater than the body length of the swimmer. If the distance from the wall is of the same order of magnitude as the body of interest, wall effects can be incorporated using Faxen's law. The drag force experienced by a sphere of radius a moving parallel to two parallel walls (Happel and Brenner 2012) as a function of the distance from the centre of the sphere to the nearer wall and the further wall. In the special case of a sphere, the drag force is

$$F = \frac{6\pi\mu aU}{1-1.004(a/l)+0.418(a/l)^3+0.21(a/l)^4+O(a/l)^5}. \tag{2.4}$$

If the sphere is moving parallel to a single plane wall (Happel and Brenner 2012) at a distance of l away, the equation becomes

$$F = \frac{6\pi\mu aU}{1-(9/16)(a/l)+(1/8)(a/l)^3-(45/256)(a/l)^4+O(a/l)^5}, \tag{2.5}$$

and for a sphere moving perpendicular to a single plane wall,

$$F = \frac{6\pi\mu aU}{1-(9/8)(a/l)+(1/2)(a/l)^3+O(a/l)^4}. \tag{2.6}$$

When the sphere is far away from boundaries such that $(a/l)\to 0$, we can see that the drag force simply becomes $F = 6\pi\mu aU$.

2.2.5 Cell-to-cell interactions

Theoretical studies on microorganisms are at times simplified by considering only a single cell in an environment many orders of magnitude greater than its length scale. While this is achievable in laboratory settings, microorganisms such as bacteria and spermatozoa are often found in dense populations under their natural environment. Hydrodynamic interactions between cell bodies are important, but only at levels of high cell concentrations (Koch and Subramanian 2011; Li and Tang 2009). As such, it is necessary to know the constraints under which such interactions are negligible, and when the behaviour of micro-swimmers will be influenced by the presence of their neighbouring counterparts.

Many researchers have studied the inter-organism hydrodynamic interaction. Synchronisation of sperm cells have been noted nearly a century ago, where Gray (1928) pointed to observations of spermatozoa tail beating synchronously when their heads are in close contact. Analytical calculations by Taylor (1951) found that significantly less energy is dissipated when the tails of neighbouring microorganisms form waves which are in phase, and that viscous stresses in the fluid creates a tendency for the waves to be in phase. Depending on whether the organism is a 'pusher' or 'puller', the cell-cell interaction alters the speed of both swimmers and reorients their swimming directions in an opposite manner (Lauga and Powers 2009). However, these hydrodynamic interactions do not significantly alter the propulsive force and torque, even at small separation distances in the order of a few body-length (Ramia *et al*. 1993). Experimental and theoretical analysis indicate that beyond a "surprisingly small length scale of a few microns", hydrodynamic interactions between microorganisms are insignificant relative to other noises present (Drescher *et al*. 2011).

Once the effective volume fraction of swimmers exceeds 10^{-2}, the behaviour of a swimmer is no longer independent, and interactions should be taken into account (Underhill *et al*. 2008). This is evident from the observation that for 10 μm beads in high concentrations of 5×10^{10} /cm^3, which corresponds to a volume fraction of about 0.03, large positional fluctuations similar to the Brownian motion of small particles can be noted and is attributed to the collective dynamics (Wu and Libchaber 2000). If the volume fraction is greater than 0.30, stark differences become obvious, as large-scale flow across the channel results in the absence of the typical high population densities

near a wall (Hernandez-Ortiz *et al*. 2005). Exceeding the certain dilution limit, a dense population of cells generates very complicated hydrodynamic behaviour (Lauga and Powers 2009). Henceforth, the hydrodynamic interactions in the limit of two identical microorganisms shall be briefly discussed.

The first 3D-model regarding the propulsion by flagellar interaction is proposed by Ramia *et al*. (1993), who applied BEM to investigate two helical swimmers parallel to each other. When swimming in phase, they found the time-averaged swimming speed, angular velocity, propulsive force and torque were almost identical to those of a solitary swimmer, as long as the separation distance was greater than the head radius. Further investigation of the swimming speed at a separation distance of half the head radius led to the conclusion that the optimal swimming speed occurs when the flagella are in anti-phase. However, the increment in swimming speed is only around 10% as compared to swimming alone. Nasseri and Phan-Thien (1997) verified the model using BEM and the reflection method. The hydrodynamic interaction for two swimmers side-by-side was concluded to be "insignificant" once the separation distance is beyond 1.5 times the total body length. When the two swimmers are in line in a highly viscous fluid medium, the leading mechanical swimmer acquires a higher velocity while the lagging one has a lower velocity due to the hydrodynamic interaction. However, this effect becomes trivial when the separation distance exceeds 6 times the total body length.

The interaction between artificial swimmers has been researched on as well. Particle-based numerical simulations have been carried out to study the hydrodynamic interaction between two artificial swimmers driven by a paramagnetic filament tail under planar and rotational magnetic field. The hydrodynamic interaction between the two swimmers, which each has a tethered sphere with a radius of slightly over a sixth of the filament length, is much less than the local force (Keaveny and Maxey 2008). When in a consecutive configuration, the speed of the swimmers is almost identical when the separation distance is 2.5 times larger than the body length. In a side by side configuration approaches, the speed of the swimmers differs by no more than 2% from that of a solitary swimmer when they are at a distance of 10 times the head radius.

2.2.6 Brownian motion

In a fluid medium, cells and particles are constantly being bombarded by the random Brownian motion of the fluid molecules. The degree of Brownian translational and rotational diffusion is respectively characterized by the diffusion coefficient D and time scale of rotational diffusion τ_{rotation} (Campbell and Ebbens 2013):

$$D = \frac{k_B T}{6\pi\eta a} = \frac{\Delta L^2}{6\Delta t}, \tag{2.7}$$

$$\tau_{rotation} = \frac{8\pi\eta a^3}{k_B T}, \tag{2.8}$$

where $k_B T$ is the thermal energy, η is the medium viscosity, a is the particle radius, and ΔL^2 is the mean-squared displacement within the time period of Δt.

If the cells or particles are sufficiently large, diffusion due to Brownian motion can be neglected. However, it is increasingly common for lap-on-a-chip devices to deal with sub-micron particles and cells (Lewpiriyawong *et al*. 2011; Lewpiriyawong and Yang 2012). In such length scale, models need to incorporate active Brownian motion in order to accurately account for their motion (Kim *et al*. 2008; Volpe *et al*. 2014), as the sub-micron bodies cannot be predicted deterministically nor simply be treated as passive particles. Applying direct numerical simulations on the generalized Taylor dispersion model, Croze *et al*. (2013) showed that the effective diffusivity of gyrotactic cells are at least an order of magnitude smaller than passive particles of similar size. In addition, swimming microorganisms modifies the flow field due to the hydrodynamic interactions and stresses they induced, and significantly so when the cell concentration is high (Bearon *et al*. 2012; Ishikawa 2009). Romanczuk *et al*. (2012) gave a comprehensive review explaining the dynamics of the active particles as well as the relevant governing equations. Separately, the similarities and differences in the dynamics of motile bacterial have been compared with the Brownian motion of micro-particles (Cates 2012).

It has been shown that 0.40 μm nanoscrews (Schamel *et al*. 2014) and micro-propellers below the length of 0.90 μm (Ghosh *et al*. 2013) are dominated by Brownian motion and directional motion is not discernible. For bacterial cells smaller than 1 μm, simulations which ignores Brownian motion leads to results that contradict microscopy observations, regardless of the parameters selected (Li *et al*. 2008). Even spheres of 1.9

µm diameter are dominated by Brownian motion. This can be seen in Figure 2-7 which portrays the trajectories of spherical Janus swimmers with heterogeneous mass distribution exhibiting synthetic negative gravitaxis (Campbell and Ebbens 2013). Directional motion becomes prominent only for the larger swimmers of 4.8 µm diameter, although some degree of randomness is still evident. The characteristic diffusion time scales as $\tau_D \propto a^3$, where τ_D is the time-scale taken for a passive micro-particle of length scale a µm to diffuse a µm via Brownian motion in water (Bechinger *et al*. 2013). As a rule of thumb, Brownian motion is negligible for particles with length scale of at least 10 µm (Garcia *et al*. 2013; Smith 2000).

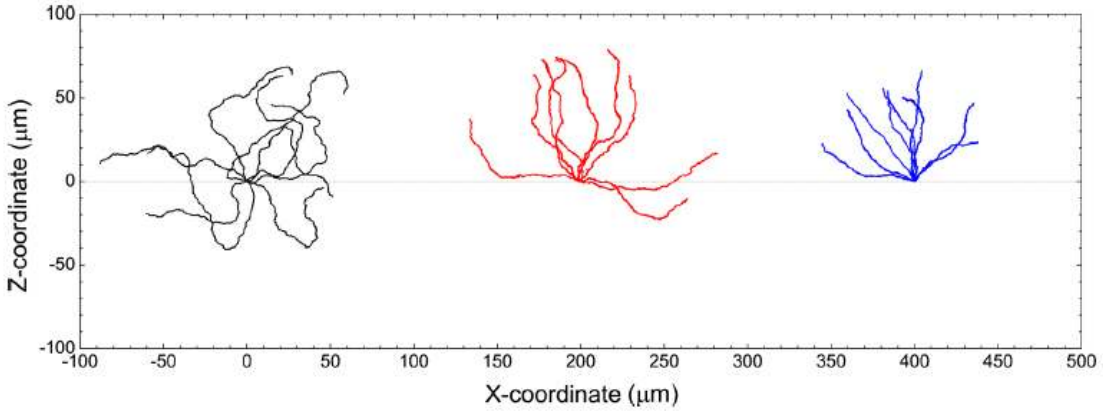

Figure 2-7 – 2D Swimming trajectories for representative Janus spheres observed in the *x*-*z* plane for spheres of radius 0.95 µm (black), 1.55 µm (red), and 2.4 µm (blue). The swimmers were suspended in a 10 wt-% solution of H_2O_2. Gravity is acting downward along the *z*-axis. Reprinted from Campbell and Ebbens (2013).

Although a sperm head has a length scale in the order of 10^0 µm, its total length is ~50 µm once the flagellum is included, and hence sperm cells are not observed to be subjected to Brownian motion (Alvarez *et al*. 2014; Smith *et al*. 2009). Interestingly, even some small bacteria, such as E. coli which has a length of ~2 µm, are reported to move in a "rather straight line" (Eisenbach 2011). Eisenbach published a list of some common bacteria species which appears to be dictated by Brownian motion as well as others which exhibit reasonable directional motion.

2.2.7 Stress-strain relation

In their natural environment, cells such as the spermatozoa carry out their activities in non-Newtonian fluid (Wolf *et al*. 1980), where stress is not linearly related to strain. Due to the time reversibility of the Stokes equation, reciprocal motion with

negligible inertia in a purely viscous fluid achieves zero net propulsion (Purcell 1977). However, this is not the case in a polymeric fluid such as the Oldroyd-B fluid. A mathematical analysis by Normand and Lauga (2008) on a two-dimensional model of a tethered flapper led to the theoretical prediction that reciprocal motion in the low Reynolds number regime does generate a net force. They extended the calculations to a more general polymeric model, FENE-P, and drew the same conclusions. Artificial swimmers have thereafter been used to demonstrate experimentally that reciprocal motion is possible in a polymeric fluid (Keim *et al*. 2012). Therefore, models ought to incorporate the non-linearity of fluid behaviour if the object of study resides in a non-Newtonian environment (Koh and Marcos 2015a). In the following paragraphs, the extent to which the kinematic behaviour of swimmers vary under different fluid medium will be explored, to determine if a common correction factor exists.

Lauga (2007) considered the Oldroyd-B model as "arguably the most famous constitutive equation", which is supported by experimental observations "reasonably well" when the Weissenberg number, $\mathrm{Wi} = \tau\dot{\gamma}$, where τ is the relaxation time of the fluid, has an order of one. The force $\mathbf{f}_{oldroyd}$ acting on a filament in an Oldroyd-B fluid is related to the force $\mathbf{f}_{viscous}$ acting on a pure Newtonian fluid by the following first-order differential equation (Fu *et al*. 2008):

$$\mathbf{f}_{oldroyd} + \tau\dot{\mathbf{f}}_{oldroyd} = \mathbf{f}_{viscous} + \left(\eta_s/\eta\right)\tau\dot{\mathbf{f}}_{viscous}, \tag{2.9}$$

which by mathematical manipulation leads to a correction factor which relates the viscous force to an Oldroyd-B force:

$$\mathbf{f}_{oldroyd} = \mathbf{f}_{viscous}\frac{1 - i\,2\pi f\tau\,\eta_s/\eta}{1 - i\,2\pi f\tau}. \tag{2.10}$$

In the Oldroyd-B model, mathematical procedures lead to the swimming velocity of an infinite sheet with travelling-wave in an Oldroyd-B fluid being related as (Lauga 2007):

$$\frac{U_{Oldroyd-B}}{U_{Newtonian}} = \frac{1 + \left(2\pi f\tau\right)^2\eta_s/\eta}{1 + \left(2\pi f\tau\right)^2}, \tag{2.11}$$

where $\eta = \eta_s + \eta_p$ is the solution viscosity, η_s and η_p are the solvent and polymer viscosity, respectively, and f is the wave frequency. (The author would like to point out

that Lauga (2007) and Fu *et al*. (2008) defined Deborah number to be $\mathrm{De} = \omega\tau$, while others such as Teran *et al*. (2010) and Spagnolie *et al*. (2013) define $\mathrm{De} = f\tau$). It was also shown that the FENE-P model, which is valid for large strain rates (Bird and Wiest 1995) unlike the Oldroyd-B model, leads to the same velocity ratio as well. Fu *et al*. (2009) applied the Oldroyd-B model to an infinite filament subjected to small deflections, and found the velocity ratio to be in agreement with Lauga (2007). In a study to verify the effect of viscoelasticity on a swimmer's velocity, the speed of *C. elegans* in Newtonian as well as viscoelastic fluid, with solvent viscosity 0.05 times of polymer viscosity, is measured experimentally (Shen and Arratia 2011). The velocity ratio at De = 1 is found to be approximately 0.65, and it reaches an asymptotic value of close to 0.4 when De is raised beyond 4. The authors reasoned that the discrepancies with equation (2.11) could be due to the finite length which was not accounted for in the theoretical model, as well as *C. elegans* being unconfined to small amplitude wiggling.

According to the preceding paragraph, an infinite sheet or filament with small amplitude deflections will necessarily achieve a lower velocity in a viscoelastic Oldroyd-B fluid. However, numerical simulations of a free finite sheet suggest otherwise. A swimmer in an Oldroyd-B fluid may be faster or slower than that in a Newtonian fluid, depending on the parameter De which is a function of the viscoelastic property of a polymeric fluid. Teran *et al*. (2010) validated their numerical simulations with Lauga (2007) under the assumptions of an infinite sheet subjected to small deflections, and found good agreement even for large deflections, but found that the results differ for a finite swimmer not confined to small deflections. When De is 1, a swimmer in an Oldroyd-B fluid attains a peak velocity and swims faster than in a Newtonian fluid (Figure 2-8), which is attributed to the higher stress concentration behind the swimmer's tail. A numerical study subsequently showed that the effect of fluid viscoelasticity on the velocity of a helical body depends on the pitch angle and filament thickness (Spagnolie *et al*. 2013). A swimmer with smaller pitch angle and thicker filament tend to achieve a lower velocity in a viscoelastic medium (Figure 2-9), while a swimmer with larger pitch angle and thinner filament may, at De ~ O(0.1), enjoy an enhanced velocity relative its counterpart in a Newtonian fluid.

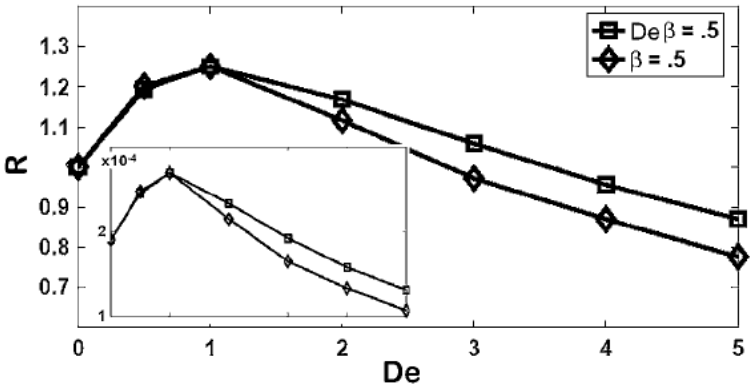

Figure 2-8 – The ratio R of average free swimmer speed to that of the Newtonian free swimmer, as a function of Deborah number De. The squares correspond to Deβ, which is the ratio of polymer to solvent viscosity, fixed at 0.5. The diamonds correspond to β, which measures the relative contribution of the polymeric stress to momentum balance, fixed at 0.5. Inset: An estimate of swimming efficiency as a function of De. Reprinted from Teran *et al.* (2010).

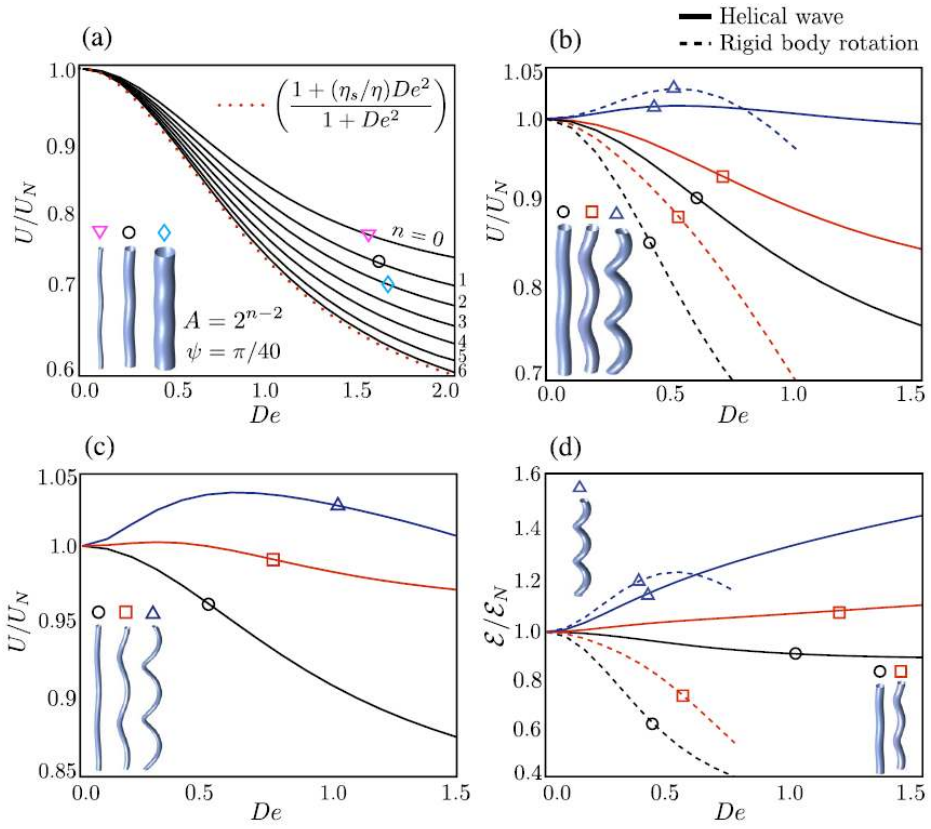

Figure 2-9 – (a) Helical-wave swimming speed U, normalised by the Newtonian swimming speed U_N, of filaments of varying thickness ($A = 2^{n-2}$ for different n), with $\psi = \pi/40$ and $\eta_s/\eta = 0.5$. (b) Normalised swimming speed with respect to Deborah number, with filament thickness fixed at $A = 0.5$. Solid lines denote helical waves, dashed lines denote rigid body rotation, for pitch angles of $\psi = \pi/40$ (black circle), $\pi/10$ (red square), and $\pi/5$ (blue triangle). (c) Normalised swimming speed with respect to Deborah number, with filament thickness fixed at $A = 0.2$, for the same pitch angles as in (b). (d) Normalised swimming efficiency with respect to Deborah number. Symbols denote the same helices as in (b). Reprinted from Spagnolie *et al.* (2013).

The viscoelasticity of a fluid can have an impact on not just the velocity of a swimmer. Expanding on the study of passive synchronisation between swimmers in a

Newtonian fluid (Elfring and Lauga 2009), Elfring *et al*. (2010) presented mathematical formulations to show that synchronisation can occur faster in an Oldroyd-B fluid, which in turn leads to improved energy efficiency and hence higher swimming velocity. The wall effects may also be altered by the viscoelasticity of the fluid. Numerical simulations showed that a 'pusher' in a viscoelastic fluid may become confined by the hydrodynamic interactions with the wall, and hence swims along the boundary in steady-state, as compared to its counterpart in a Newtonian fluid which would reorient and depart the wall (Li *et al*. 2014).

An equation relating the effect of viscoelasticity on a swimmer's velocity is appealing for analytical procedures. However, the literature in this section suggests that the equation does not accurately depict the kinetics of finite-length swimmers. Based on the studies carried out till date, a common correcting factor does not appear to exist, because the velocity ratio depends not only on the viscoelastic properties of the fluid, but also the morphology of the swimmer.

2.3 Techniques for sorting spermatozoa[2]

Having looked at how the behaviour of sperm is governed by physics, the next section of the literature review investigates how sperm may be manipulated. Common preparation methods for spermatozoa used in assisted reproduction will be introduced. The section begins with a summary on the properties of sperm, and continues with microfluidic sorting of sperm according to their motility, morphology, chromosomes and membrane integrity, as well as manipulation techniques by optics or external fields.

2.3.1 Properties of sperm and its influence on reproduction

The journey of a sperm is long and tedious, as it has to travel as much as 20 cm in the female reproduction tract (Kirkman-Brown and Smith 2011), the equivalent of a person swimming over 6 km in a realm where inertia is negligible, and once the sperm has undergone capacitation, its life span typically does not exceed 4 hours (Cohen-Dayag *et al*. 1995). Merely 0.1% of the sperm initially deposited will successfully

[2] Published in Koh JBY, Marcos (2015a) The study of spermatozoa and sorting in relation to human reproduction. *Microfluidics and Nanofluidics* 18:755-774

penetrate the cervical mucus and pass through the uterus to enter the oviducts (Fauci and Dillon 2006), and there are complicated biological reactions involved when sperm cells pass through the oocyte cumulus complex and gets near the oocyte (Zhu *et al*. 1994). Oviductal and follicular fluids induces an increase in the sperm's straight-line velocity of up to 35% and 31%, respectively (Oliveira *et al*. 1999). The hyperactivated spermatozoa also display asymmetrical flagellum wiggling pattern with large amplitude, instead of a relatively symmetrical, low amplitude wiggling pattern as displayed by non-hyperactivated spermatozoa (Suarez *et al*. 1991). In addition, chemotaxis is induced when the human sperm olfactory receptor is activated leading to an influx of calcium ions (Spehr *et al*. 2004). Without further discussion on the biological aspects of this multi-disciplinary field, this thesis will take an approach from the physical aspects.

Many researchers have looked into the properties and behaviour of spermatozoa (Brennen and Winet 1977; Dresdner and Katz 1981; Mortimer and Swan 1995). Early studies on the human spermatozoa involve studying the physical parameters. The average flagellum length and diameter is 42 μm (Cui 1997) and 0.5 μm (Dresdner and Katz 1981), respectively, while the head length ranges from 4.8 μm (Aksoy *et al*. 2012) to 5.8 μm, with a width of 3.1 μm on average (Brennen and Winet 1977). Although the head of a spermatozoon is an ellipsoid, it has been found that for a given volume of the spermatozoon head, its length-to-width ratio do not alter the straight-line velocity significantly (Gillies *et al*. 2009). Therefore, approximations can be made to consider the spermatozoon head as a perfect sphere with an equivalent volume.

It is common knowledge that the X-spermatozoa, upon fertilising the ovum, results in a female offspring, while the Y-spermatozoa results in a male. Interestingly, human spermatozoa carrying the different sex chromosomes have slightly different dimensions (Cui and Matthews 1993, Cui 1997); the average lengths of the X- and Y-spermatozoa are (42.2 ± 4.4) μm and (41.2 ± 3.5) μm, respectively. Although a recent study stated that there is negligible difference in dimension between spermatozoa carrying the different sex chromosomes (Carvalho *et al*. 2013), that study was done on bovine spermatozoa, and there have been no other studies to the best of the author's knowledge that refute the findings on human spermatozoa made by Cui (1997).

Researchers then moved on to gain a deeper understanding on the kinematics of spermatozoa, such as observing the flagellum waveform (Ishijima *et al*. 1986, Katz and

Davis 1987). The mean progressive velocity for human spermatozoa was found to vary from 17 to 42 μm s^{-1} in a sample of 100 semen (Mortimer *et al*. 1986), while the beating frequency is observed to vary from 14 Hz in semen and 17 Hz in cervical mucus (Dresdner and Katz 1981) to between 10 Hz and 24 Hz depending on the viscosity of the fluid medium (Smith *et al*. 2009). In a time scale many orders of magnitude greater than the beating period of its flagella, spermatozoa travel in a linear direction in general (David *et al*. 1981, Katz *et al*. 1978). Although a sperm's swimming speed is linearly related to its beat frequency when in semen or Tyrode's solution, but not cervical mucus, its progressive swimming speed is similar in all three fluid medium (Katz *et al*. 1978). This suggests that laboratory studies investigating the swimming speed of spermatozoa can be carried out in Tyrode's solution rather than semen or cervical mucus.

A spermatozoon is able to wiggle its flagellum due to an active force which creates relative sliding motion between groups of tubules (Summers and Gibbons 1971). This is analogous to how the interaction between myosin and actin filaments allow animals to contract their muscles and move (Krans 2010). A number of studies have incorporated an internal force in their model and linearized the problem (Camalet and Jülicher 2000; Riedel-Kruse *et al*. 2007; Fu *et al*. 2008). Gadélha *et al*. (2010) presented that under certain conditions, the internal shear force within a sperm's flagellum can result in buckling and change the waveform as well as trajectory. They hence suggested that the linearized model is inaccurate and does not capture buckling effects when the radius of curvature is under a tenth of the flagellar length or when Sp (a dimensionless parameter known as the sperm number or sperm compliance, which is inversely related to the flexural rigidity of the spermatozoon's flagellum) takes a large value. It is noteworthy that the buckling occurs when the sperm number exceeds 15, while an average human sperm has a sperm number of 7.7 (Fu *et al*. 2008) which corresponds to a flexural rigidity of approximately 16 times that which would lead to buckling.

The swimming velocity of spermatozoa, as well as the percentage of spermatozoa which have normal morphology, are found to be the key factors in determining fertility (Malo *et al*. 2005), with another important factor being the sperm concentration (Nallella *et al*. 2006). Spermatozoa with normal morphology typically swim faster and exhibit higher beat frequencies (Katz *et al*. 1982). On the other hand, those with abnormal morphology (Aziz *et al*. 2007) or low-motility (Barroso *et al*. 2006) display higher incidence of early apoptosis, which increases the likelihood of the sperm

dying before it is able to reach the oocyte. In fact, even slight morphological variations of the sperm nucleus affect the success of ICSI (Bartoov *et al*. 2002). However, an abnormal morphology does not relate to the sperm having abnormal chromosomes (Martin and Rademaker 1988), and hence a morphologically satisfactory sperm does not guarantee an offspring free from genetic disorders. There are criteria to evaluate a sperm according to its morphology (Menkveld *et al*. 1990, Bartoov *et al*. 2002) or swimming velocity (Cooper and Yeung 2006). One should remain mindful that the morphology and motility are continuous parameters, and even after a line is drawn between what is 'normal' and 'abnormal', there is still plenty of variation within each group.

Semen analysis have long been used to determine the likelihood of male-related infertility, and a range of parameters have been defined as a guide for doctors. Table 2-1 (World Health Organisation 2010) shows the lower limit of semen characteristics and sperm parameters, which is met by 95% of the sample population of men whose partners became pregnant within 12 months of discontinuing contraceptive use. The motility of spermatozoa is categorised into three groups by the World Health Organisation (2010): Progressive motility (PR) applies to spermatozoa "moving actively, either linearly or in a large circle, regardless of speed", non-progressive motility (NP) applies to spermatozoa exhibiting "all other patterns of motility with an absence of progression", and immotility (IM) applies to spermatozoa with no movement. The total motility count includes both spermatozoa with progressive as well as non-progressive motility. The previous edition of WHO manual labels "Grade A" spermatozoa as those which possess a speed of at least 25 µm/s, although no definition is made in the 2010 edition. A comparison between the semen characteristics of fertile and subfetile men was carried out by Menkveld *et al*. (2001) as shown in Table 2-2, giving an idea of the range and standard deviation of the respective parameters.

Table 2-1 – Lower reference limits (5th centiles and their 95% confidence intervals) for semen characteristics. Adopted from World Health Organisation (2010).

Parameter	Lower reference limit
Semen volume (ml)	1.5 (1.4–1.7)
Total sperm number (10^6 per ejaculate)	39 (33–46)
Sperm concentration (10^6 per ml)	15 (12–16)
Total motility (PR + NP, %)	40 (38–42)
Progressive motility (PR, %)	32 (31–34)
Vitality (live spermatozoa, %)	58 (55–63)
Sperm morphology (normal forms, %)	4 (3.0–4.0)

Table 2-2 – Descriptive statistics of the semen parameters for fertile (*n* = 107) and subfertile (*n* = 103) groups. P < 0.0001 for differences between means of all semen parameters presented in the table. AI = acrosome index; P10 = 10th percentile; SC = strict criteria; TZI = teratozoospermia index. Adopted from Menkveld *et al*. (2001).

Parameter	Fertile				Subfertile			
	Mean ± SD[a]	Range	Median	P10	Mean ± SD[a]	Range	Median	P10
Morphology (WHO) (% normal)	40.1 ± 14.1	9–69	38	24	21.7 ± 10.9	0–47	20	8.5
Morphology (SC) (% normal)	6.5 ± 3.9	1–19	5	2	3.0 ± 2.6	0–12	2	1
TZI	1.51 ± 0.2	1.17–2.07	1.54	1.33	1.81 ± 0.3	1.26–2.64	1.81	1.74
AI (% normal)	11.2 ± 5.9	1–33	10	5	5.6 ± 3.7	1–20	5	1
Concentration ($\times 10^6$/ml)	81.07 ± 49.7	1.30–230.0	75.0	20.0	18.97 ± 26.5	0.30–130.0	8.00	1.71
Motility (% motile)	53.1 ± 15.9	20–90	57.5	30.0	31.9 ± 19.2	2–80	30	10
Motile quality (0–6)	4.4 ± 0.6	2.5–6.0	4.5	3.5	3.5 ± 0.8	2.0–5.0	3.5	2.4

[a]Fertile versus subfertile populations. $P < 0.0001$ for differences between means of all semen parameters presented in the table.
AI = acrosome index; P10 = 10th percentile; SC = strict criteria; TZI = teratozoospermia index.

2.3.2 Sperm preparation to obtain pure sample for fertilisation

Details on sperm preparation methods have been given by Mortimer (2000), while Henkel and Schill (2003) have summarized the advantages and disadvantages of common sperm preparation procedures such as the swim-up, migration-sedimentation, density gradient centrifugation and glass wool filtration methods.

In the normal swim-up procedure, semen sample is diluted and centrifuged, and the resulting pellet is re-suspended and centrifuged again. The appropriate medium is then added and the sample incubated before the supernatant, which contains the swim-up spermatozoa, is collected (Lopes *et al*. 1998). Concerns over the forces experienced by the spermatozoa during centrifugation prompted some to avoid the centrifugation process, and hence a direct swim-up procedure is introduced. Younglai *et al*. (2001) carried out a trial to compare human spermatozoa obtained from the two types of swim-up procedures, and found that DNA damage was under 5% for both, but sperm concentration decreased from 59 to 35 and 6.5 million/ml for normal and direct swim-up method, respectively. Meanwhile, normal morphology improved from 69%, and motility improved from 61%, to over 90% for both normal and direct swim-up. The swim-up technique results in a sperm sample with superior DNA integrity relative to an unprocessed sample (Marchesi *et al*. 2010), but one drawback is that spermatozoa at the bottom are trapped regardless of their motility (Henkel *et al*. 1994). Some studies found that the sperm prepared this way and used in assisted reproduction led to a higher proportion of male births (Check and Katsoff 1993, Khatamee *et al*. 1999, Manzur *et al*. 2004). However, Yan *et al*. (2006) concluded that the ratio between the X- and Y-spermatozoa remains statistically indifferent even after 150 minutes of swim-up.

The migration-sedimentation method is another way in which sperm can be prepared. Motile sperm 'jump' across the boundary and subsequently settle in the central tube due to gravity, where they are collected by aspiration. The average motility of the human sperm prepared from this method improved from 51% to 93%, while abnormal morphology decreased from 36% to 21%, and the sample are free from cellular debris (Tea *et al*. 1984). The prepared sperm was used for IVF and each patient have at least one oocyte fertilised, even for husbands with asthenozoospermia (low sperm motility). Risopatron *et al*. (1996) tested the migration-sediment method using bovine sperm and found that spermatozoa motility was 85% while fertilisation rate was 93%, although this is at the expense of a low 17% yield.

Another sperm preparation method is the density gradient centrifugation. Unlike the migration-sedimentation or swim-up procedure, which is meant for sorting motile spermatozoa, this method can be applied to any particle in general. Hinton and Dobrota (1978) explained the working principles of density gradient centrifugation, such as how a density gradient influences the particles' speed and supports the sedimenting zones. After centrifugation, motile and morphologically normal sperm will settle in the lower region of the gradient, while dead or abnormal spermatozoa settle in the middle, and debris settle at the upper layer of the gradient (Bolton and Braude 1984). By collecting the lowermost 1 ml, Bolton and Braude (1984) recovered 16% of the total spermatozoa and found that percentage motility increased from 63% to 93%.

A basic and intuitive method of sorting will be to use a filter, with gaps large enough to allow, or small enough to prevent, particles of a target size from passing. Glass wool filtration is an example of how this can be applied to sperm preparation, in which columns of glass wool separates human spermatozoa based on its head size and motility (Henkel *et al*. 1994). Henkel *et al*. (1994) also reported that the quality of the sperm chromatin condensation is correlated to its head size, and 61% of the spermatozoa prepared from this technique has good chromatin condensation as compared to 41% of those prepared from standard swim-up. In addition, spermatozoa motility improved to 87%, with over a 1.5 times yield of total spermatozoa as compared to the swim-up technique done in comparison. Van der Ven *et al*. (1988) showed that viability of the spermatozoa remains good, with 78% of the 64 samples collected from glass wool filtration fertilising at least one human egg in IVF.

2.3.3 Sorting by sperm's motility

By making use of the fact that motile sperm orientate and swim against the flow, Seo *et al*. (2007) used a Polydimethylsiloxane (PDMS) microchannel to separate non-motile sperm and debris and collect motile sperm at the outlet, with flow being driven by hydrostatic pressure of up to 10 mm difference in the height of liquid columns. PDMS is often used in soft lithography as it can be easily fabricated, largely suitable for use in biological experiments, and allows the synthesis of cell micro-environment at the cellular resolution (El-Ali *et al*. 2006). Seo *et al*. (2007) also proposed modifying the device to include a function of separating the sperm head and flagellum for ICSI procedures.

A "microscale integrated sperm sorter" as depicted in Figure 2-10 can be used to sort out and collect motile spermatozoa, because the non-motile spermatozoa remain within their initial streamlines during the 20 seconds in the microchannel while motile ones are able to deviate from the stream and into a different outlet (Cho *et al*. 2003). The fluid reservoirs are arranged to balance gravity and surface tension, allowing a steady flow rate. A purity of nearly 100% motile spermatozoa could be obtained regardless of the initial motile sperm purity, and the proportion with desirable morphology improved from 10% to 22%. Another study reported a 98% purity of motile spermatozoa using this concept of sorting, but admitted the drawback being that only 10-20 µl of semen can be processed in half hour (Schuster *et al*. 2003). Wu *et al*. (2006) proposed a modification to the sperm-sorting microchannels by using graft-co-polymerization to make the channel surface moderately hydrophilic and non-fouling, thus minimizing adsorption of cellular debris or flow resistance.

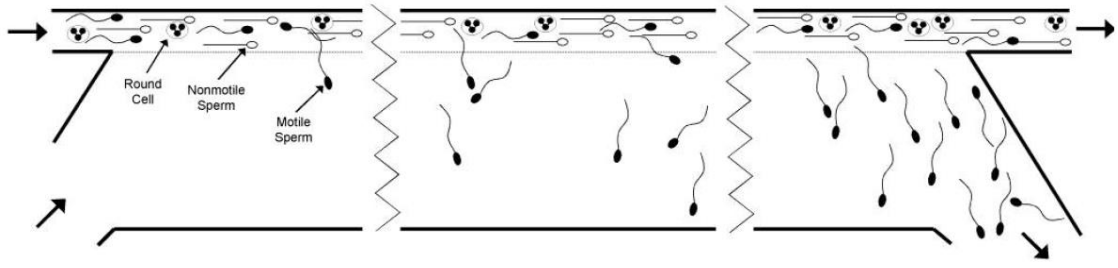

Figure 2-10 – Schematic of the microscale integrated sperm sorter. Sperm sample enters from the left, and motile sperm deviate from their initial streamline while nonmotile sperm and cellular debris remain along the straight path. Motile sperm are collected at the bottom right of the channel. Reprinted from Cho *et al*. (2003).

Chen *et al*. (2011) proposed an interesting set-up as shown in Figure 2-11 to access the concentration and motility of sperms, by using a detector to count the number of sperms which successfully swim against a flow field within a specified time. If the concentration and/or the motility is low, the corresponding number of counts will be low as well. Although this device is proposed for use as an assessment of sperm quality, it can potentially be modified for separating spermatozoa by their motility as well.

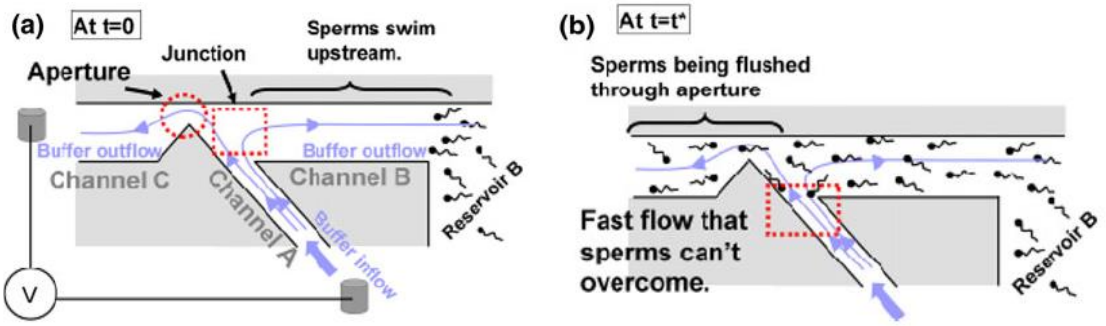

Figure 2-11 – (a) Schematic of the microdevice for evaluating sperm quality. Flow enters via channel A and exits via channels B and C. (b) Only motile sperm are able to overcome the flow in channel B and go past the aperture to be counted. Reprinted from Chen *et al*. (2011).

2.3.4 Sorting by hydrodynamic effects

This sorting technique is another example of how knowledge is built upon knowledge. It was observed many decades ago that motile sperm accumulate near the wall surface (Rothschild 1963), and hence Sakar (1984) made use of a pipette to create a cylindrical flow column in which non-motile sperm and debris are flushed away, enriching the motility level of the remaining sperm.

Subsequently, it was explained that microorganisms such as sperms and bacterial tend to swim near walls due to hydrodynamic interactions (Berke *et al*. 2008, Elgeti *et al*. 2010). Experimental observations showed that sperms swim not just near walls, but rather almost against channel walls and corners (Denissenko *et al*. 2012). The influence of an external flow on micro-swimmers near walls have also been considered recently (Chilukuri *et al*. 2014). Another experimental study found that sperm cells are trapped near the apex of a V-shape wall, but are not trapped when the V-tip is made rounded (Guidobaldi *et al*. 2014). Therefore, it is possible to use this method to increase the sperm concentration for the purpose of IUI, without subjecting the sperm to any unnaturally high forces or shear stresses.

2.3.5 Sorting by sperm's chromosomes

Spermatozoa can be sorted not only according to their motility and morphology, but also according to the chromosomes they contain. This allows gender selection by tapping on the differences between the X- and Y-chromosome-bearing sperm, because sperm can be selected from a skewed population, giving a higher probability of the offspring having the desired gender. According to the Human Fertilisation Embryology authority, UK (2003), sex selection is regulated for couples who wish to "avoid having a child with a serious inherited disorder", such as Duchenne's Muscular Dystrophy which affects males but not females. There are papers discussing the ethical (Robertson 2001) and social (Chan *et al*. 2002, Hesketh and Zhu 2006, Zhu *et al*. 2009) issues involving gender selection. In this thesis, the author explores the possibility of gender selection solely from a technical perspective.

Ericsson *et al*. (1973) first proposed the method of separating the faster Y-sperm from the slower X-sperm by passing them through liquid albumin until a sample with higher concentration of Y-sperm is obtained. The sample has to first be centrifuged, and the pellet re-suspended in Tyrode's solution and laid over an albumin column with various concentrations. The albumin medium, in which motile spermatozoa had swam into, is centrifuged and the pellet re-suspended and laid over albumin again. Using a three-step isolation procedure, a population of 85% Y-sperm have been obtained, with a motility of 98%. Beernink *et al*. (1993) reported that passing sperm through liquid albumin, and insemination on human patients using the sorted sperm resulted in over 1,000 births. There are four protocols, each with unique procedures and different albumin gradients. One protocol led to a 16% conception rate with 76% male births, while another protocol gave a 22% conception rate with 69% females births. The authors admitted that the mechanism leading to a skewed gender ratio is "unknown" and "unclear', but suggested different swimming speed and response to clomiphene citrate as contributing factors.

A clinic in Hong Kong applied Ericsson's method of sperm separation and concluded that "sex selection for boys is effective", as substantiated by 15 out of the 18 couples giving birth to boys as desired (Rose and Wong 1998). However, Rose and Wong (1998) were unable to obtain the enriched population of Y-sperm as described by Ericsson *et al*. (1973). They suggested that the theory "may be wrong even though the practice of gender selection is effective", and proposed that the reason for a skewed

probability towards males is because the albumin inactivates X-spermatozoa to a greater extent than Y-spermatozoa. Flaherty *et al*. (1997) found that the X:Y ratio as determined by fluorescence in-situ hybridization remains very close to 1.0. and concluded that any skewed sex ratio at birth is not the result of a higher percentage of Y-spermatozoa. In the rest of this section, we turn our attention to flow cytometry, which is a proven gender selection technique applied to animals (Garner 2001).

Flow cytometry is defined as the measurement of physical or chemical characteristic of cells or particles as they pass through a flow cytometer in a fluid stream. For example, laser beam can be used to differentiate stained sperms by virtue of differences in their nucleus. A cell sorter is a flow cytometry which uses mechanical or electrical means to divert and collect cells with a certain range of user-defined characteristics. Details on how flow cytometry work and various flow sorting techniques are presented by Shapiro (2005), and the development of flow cytometry technology for sperm sorting in terms of rate and efficiency have been described by Sharpe and Evans (2009). Fluorescence activated cell sorting involves marking target cells with fluorescence, detecting the marked cells, and collecting the cells through some microfluidic means. (Krüger *et al*. 2002; Wang *et al*. 2005).

This method has proven to be successful in obtaining spermatozoa for the desired gender with a purity of over 80% (Johnson *et al*. 1987). The cell viability was verified by live births of rabbits, but due to the staining of the nuclei, there was increase embryo motility presumably attributed to the stained DNA (Johnson *et al*. 1989). However, Munné (1994) advised caution over the flow cytometry process, citing that exposing the spermatozoa to ultraviolet light may cause mutation such as chromosome structural abnormalities (Matsuda and Tobari 1988). He added that the DNA binding stain, Hoechst 33342, have been reported by Durand and Olive (1982) to cause mutagenesis. Another drawback is that sorting by high-speed flow cytometry subjects the spermatozoa to a pressure of up to 50 psi, which damages the spermatozoa and leads to a decrease in its motility (Suh *et al*. 2005). Sorting by gender has also been tested on bovine sperm, where the cell DNA was stained and the allele amplified using polymerase chain reaction before sorting by flow cytometry (Welch *et al*. 1995). A greater than 90% purity for both the X- and Y-sperm populations have been verified by molecular genetic analysis on hundreds of sperm or flow cytometric measurement on thousands of sperm.

Technology today has progressed to the stage where gender selection has already become a reality for people. The world's first clinical pregnancy from sorted sperm was reported (Levinson *et al*. 1995) some two decades ago, and 22 out of 25 embryos were analysed to be female. The concept of sorting sperm based on DNA is as follows: Sperm is stained with Hoechst 33342, and during the flow cytometry process, X-sperm (which has more DNA contents than the Y-sperm) shines more brightly when passed through the laser. This procedure is patented as MicroSort®, and have been reported in 1998 that sorted sample X-spermatozoa had a purity of approximately 85%, with pregnancies from IUI, IVF, or ICSI giving 88% female foetus as desired (Fugger *et al*. 1998). The track record continues growing, achieving 88% purity for XSort® and 73% purity for YSort® out of more than 5000 sorts. Amongst the over 900 human babies borned, XSort® resulted in 92% females while YSort® resulted in 82% males, with major congenital malformations were comparable to pregnancies from unsorted sperm (Karabinus 2009). The author would like to reiterate that gender selection is not advocated in this thesis; rather, potential applications of sperm sorting are investigated purely in the interest of broadening academic knowledge.

2.3.6 Manipulation by optics

Electromagnetic wave can be utilised for manipulating particles, and there is a brief review on optical manipulation, which talks about how optical tweezers use a strongly focused light beam to exert a force for various applications (Grier 2003). Optoelectronic tweezers have allowed parallel micro-manipulation of human cells (Chiou *et al*. 2005), while individual spermatozoon can be micro-manipulated in three dimensions through the use of a laser trap (Colon *et al*. 1992). Apart from micro-manipulation, optical forces can also be used to actively direct cell path along a channel. Wang *et al*. (2005) described using a laser for the detection and measurement of fluorescence, and a focused beam deflects target cell to a collection channel while other cells flow to the waste channel as shown in Figure 2-12, such that the collected cells remain viable and unstressed. There is also the development of the optoelectronic tweezer (Hsu *et al*. 2010), which makes use of optically-induced DEP for increased parallel manipulation with the flexibility of optical tweezers, allowing 15,000 individual traps spanning 1 mm^2.

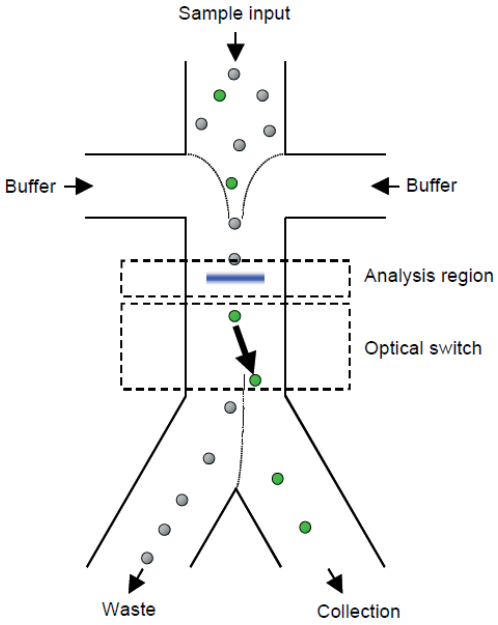

Figure 2-12 – Schematic of microfluidic sorting junction and the optical switch. Cells are aligned to the channel centre by flow focusing. Based on the analysis, the laser directs target cells to the collection output while other cells flow to the waste output. Reprinted from Wang *et al*. (2005).

Sperm motility is approximately linearly related (Nascimento *et al*. 2006) to the required laser power for trapping it. Based on this fact, Shao *et al*. (2007) reported using a three-dimensional ring-shaped laser trap with adjustable power to confine human sperm with motility below a certain threshold within the trap while allowing sperm with higher motility to escape. A sample of highly motile sperm is desirable for increasing success rate in IUI, if it can be verified that the cells are not impaired after sorting. Annular laser trapping is subsequently improved for high-throughput analysis and sorting of human and gorilla sperm (Shi *et al*. 2009). Optical trapping can also be used as a non-invasive technique for cell analysis. Subramani *et al*. (2014) studied the rotational dynamics of optically trapped human sperm, and found that the rotational speed of sperm from infertile men is significantly lower than the control group.

2.3.7 Sorting by magnetophoresis

Magnetic-activated cell sorting (MACS) is another approach which can be used on cells. Sperm can be separated according to their membrane integrity using paramagnetic microbeads conjugated with a protein which bind to apoptotic spermatozoa or those with damaged membrane, but not to healthy spermatozoa (Paasch *et al*. 2003). The undesired cells marked with magnetic colloids can be separated using a magnetic field of 0.5 to 1.5 tesla, resulting in a higher percentage of motile and viable

sperm (Said *et al*. 2005). The removal of apoptotic spermatozoa via MACS also leads to a higher proportion of normal morphology sperm and improved cryosurvival rates (Said *et al*. 2008), with higher oocyte penetration capacity documented.

Apart from manipulating damaged sperm cells, healthy spermatozoa can also be loaded with superparamagnetic nanoparticles and directed with magnetic field, by virtue of the principle of targeted drug delivery (Schulze *et al*. 2005). PVA–Fe_3O_4 nanoparticles can significantly increase the sperm's relative magnetic susceptibility and hence its response to the applied field, without impeding the sperm's motility or compromising its fertilisation capability (Ben-David Makhluf *et al*. 2006). In fact, a healthy baby was born from ICSI using sperm subjected to magnetic field (Rawe *et al*. 2010). Even so, comprehensive studies on a large number of babies will be required to understand the potential risks involved.

In its natural form, sperm cells can also be manipulated by diamagnetic force. Unlabelled living cells are generally diamagnetic, and hence exhibit diamagnetophoresis, also known as negative magnetophoresis, where they experience a repulsive force in the presence of a magnetic field (Hejazian *et al*. 2015). While it is beneficial to have a sorting procedure where the sperm cells do not have to be modified in any way, diamagnetic forces are much weaker than magnetic forces (Hejazian *et al*. 2015) and a stronger magnetic field will be required for sorting.

In the presence of a magnetic field B, a particle of volume ~~V~~ experiences a magnetic force as follows (Peyman *et al*. 2009):

$$\mathbf{F}_B = \frac{(\chi_p - \chi_m)}{\mu_0} \text{~~V~~} (\mathbf{B} \cdot \nabla)\mathbf{B}, \tag{2.12}$$

where χ_p and χ_m are the particle and medium magnetic susceptibility, respectively, and μ_0 is the vacuum magnetic permeability. Reference is available for the magnetic susceptibility of some biological materials (Senftle and Hambright 1969). A magnetic particle suspended in diamagnetic medium leads to a positive $(\chi_p - \chi_m)$, and hence experiences a magnetic force $\mathbf{F}_B$ directed towards the region of higher magnetic field density. On the other hand, a diamagnetic particle in paramagnetic medium (Peyman *et al*. 2009) experiences a magnetic force $\mathbf{F}_B$ directed away from the region of higher magnetic field density due to a negative $(\chi_p - \chi_m)$.

2.3.8 Sorting by dielectrophoresis

Micro-particles can be sorted by dielectrophoresis, in which a particle in a non-uniform electric field becomes polarised but experiences different magnitude of forces on either end due to the different electric field strength. This non-uniform electric field can be generated by a variety of electrode set-ups (Khoshmanesha *et al*. 2011). It has a proven track record of sorting a wide variety of particles with high efficiency, giving numerous industrial and clinical applications (Lewpiriyawong and Yang 2014). Dielectrophoresis (DEP) has been used to separate bacteria and yeast cells (Moncada-Hernández and Lapizco-Encinas 2010), viable and non-viable human cells (Jen and Chen 2011), different submicron viruses (Morgan *et al*. 1999), as well as human leukaemia cells (Huang *et al*. 1997), breast cancer cells (Becker *et al*. 1995), or malaria-infected cells (Gascoyne *et al*. 2002) from normal blood cells.

The principles of dielectrophoresis and its relevant equations are well-established in various reviews (Gascoyne and Vykoukal 2002, Pethig 2010). When a particle, regardless of its charge, is placed in a non-uniform field, it experiences a net electric force. This dielectrophoresis force has the following expression using a dipole approximation where higher-order poles are neglected (Pethig 2010):

$$\mathbf{F}_{DEP} = \Gamma \varepsilon_{medium} \mathrm{Re}(f_{CM}) \nabla \mathbf{E}^2, \tag{2.13}$$

where Γ is the shape factor, ε_{medium} is the medium permittivity, $\mathrm{Re}(f_{CM})$ is the real part of the Clausius-Mossotti factor (Lewpiriyawong and Yang 2012), which accounts for the effective polarizability of the body, and ∇E^2 is the gradient of the mean square of the electric field. The shape factor for a cylindrical rod of length L and radius p is $\Gamma = \left(\pi p^2 L\right)/6$, while that for a sphere of radius a is $\Gamma = 2\pi a^3$. $\mathrm{Re}(f_{CM})$ is the real part of the Clausius-Mossotti factor which takes a value between +1 and -0.5 (Voldman 2006). It depends on the complex permittivity of the particle and its surrounding fluid, which in turn is dependent on their electrical conductivity, dielectric constant, and frequency of the electric field. A typical mammalian cell experiences negative DEP at low frequencies, but when low medium conductivity with sufficiently high frequency, the cell experiences positive DEP as it becomes more polarizable relative to the fluid.

The ratio between the contribution from the dipolar and quadrupolar terms can be estimated by scaling analysis (Jones and Washizu 1996, Jones 2003), but is

dependent on the electrode geometry as well as particle size. Jones (2003) commented that for most micro-sized particles, "quadrupolar corrections are negligible", but the higher order terms "may become dominant" at the scale of 100 nm where electrical charge distribution becomes discernible. This is in line with the observation that electrostatic interactions become significant once the distance is as low as 10 ~ 100 nm (Klein *et al*. 2003). On the other hand, the approximation also becomes less accurate as particles increase in size (Jones 1985).

Apart from particle size, the validity of the dipole approximation also depends on the relative electrode spacing and spatial distribution of the particles. Schnelle *et al*. (1999) calculated that for particles with a diameter under a tenth of the electrode spacing, the error is less than 1%, and the error increases to 5% when the particle is a quarter of the electrode spacing. Once the particle diameter reaches half the electrode spacing, dipole approximation becomes inaccurate as the quadrupole and octupole contributes 22% and 3%, respectively, to the total force. An analytical investigation on the interaction between two particles found that the dipole approximation is inaccurate when they are closer than a tenth of their diameter, but is otherwise accurate (Washizu and Jones 1996). Analytical solutions modelling 1 to 5 μm particles between an infinite bottom electrode and semi-infinite top electrode showed that the "first-order DEP force alone is sufficient" to determine the total DEP force, as higher-order terms are at least one order of magnitude smaller and have "negligible contributions" (Kua *et al*. 2008).

Based on the above-mentioned findings, it is evident that the dipole approximation can accurately determine the DEP force acting on particles in the scale of 1~10 μm, which are located away from the centre of the field and spaced no closer than a tenth of their dimension, with the electrode separation being at least an order of magnitude larger than the particles.

Despite having been established for decades and showing success in a multitude of sorting applications, dielectrophoresis has not been widely studied on sperm cells. The first publication of such research was by Rosales-Cruzaley *et al*. (2013), in which insulator-based dielectrophoresis was used to separate mature spermatozoa from non-mature spermatogenic cells due to different dielectrophoretic effect. The viability of the sperm cells remained above 80% after being subjected to DC potential of 1,000 V for 30 seconds, with a maximum electric field in excess of 2.6×10^5 V/m. Subsequently,

theoretical studies explored the feasibility of sorting spermatozoa by dielectrophoresis by modelling a passive sperm in Newtonian fluid (Koh and Marcos 2014) as well as an active sperm in an Oldroyd-B fluid (Koh and Marcos 2015b). Due to the novelty of sperm sorting using an electric field for ART, there is a lack of published materials to substantiate the safety or risks of this method. The cell viability is a necessary, but not a sufficient, metric for assessing the suitability of sorting sperm by dielectrophoresis. The fertilisation capability of spermatozoa subjected to strong electric fields, as well as the health of the offspring if conception is successful, remains an unknown to be researched.

2.4 Moving forward

Current assisted reproduction procedures have an unimpressive success rate, and it is known that selecting motile spermatozoa of normal morphology will increase the chances of success. IUI, being the least invasive procedure, is a good first approach to assisted reproduction chosen by many. Since the natural selection process is not bypassed and fertilisation still occurs the natural way, couples have little reason to worry about potential health complications associated with IVF or ICSI. The sperm sample used in IUI is first prepared to obtain an enriched population. However, due to the large number of sperm used in IUI, there is no individual selection of ideal healthy cells. The author proposes combining the preparation with a subsequent sorting by an external electric or magnetic field to obtain a population skewed towards a range of desired morphology. This will be studied from a theoretical approach to establish a relation between the sperm velocity and parameters which can be tuned to manipulate the sperm. The physics associated with microscale locomotion and existing sperm sorting techniques reviewed in this chapter are summarised in Table 2-3. According to the literature review carried out, there is no published work till date on the use of dielectrophoresis or magnetophoresis for sorting sperm by morphology to improve assisted reproduction. Meanwhile, theoretical computations carried out on sperm studies are typically focused on the precise mathematics of sperm not subjected to any electromagnetic fields. Hence, experimentalist do not have access to a direct quantitative prediction of the extent of sperm response and its associated sorting outcomes.

Table 2-3 – Summary of theoretical aspects of microscale locomotion and sperm sorting techniques discussed in Chapter 2.

Theoretical aspects of microscale locomotion	Resistive Force Theory	Neglect body-to-body interactions. Relate the local force as a linear function of relative velocity. Predicted velocity vary from measurements by tens of percentage points.
	Slender Body Theory	Takes into account body-to-body interactions. Gives accurate theoretical results which differ from measurements by as little as a few percentage points.
	Stress-strain relation of fluid	Influences cell kinematics substantially. General correction factor not known to exist. Sperm motion in Newtonian and viscoelastic fluid considered in thesis.
	Rheotaxis	Flow field of environment influence directionality of sperm. Shear rate up to 10 s^{-1} not detrimental to viability. Insignificant influence on waveform or velocity when shear rate is under a tenth of flagellum beating frequency.
	Wall effects	Significantly reduces swimmer's velocity at a distance of less than five times the cell length. May be neglected when distance from wall is over one order of magnitude greater than cell length.
	Cell-to-cell interactions	Beyond a few microns, interactions are insignificant relative to other noises. Negligible effect when separation distance is an order of magnitude greater than the cell length scale.
	Brownian motion	Significant for particles which scale under 1 µm, but may be neglected when body is over 10 µm. Insignificant effect on sperm motion.
Typical sperm preparation procedures for ART	Swim-up	Pellet of sperm sample suspended and incubated, supernatant containing cells which swam up is collected.
	Migration-sedimentation	Motile sperm able to cross elevated boundary and settle in a tube by gravity.
	Density gradient centrifugation	After centrifugation, motile and normal sperm reside in lower portion of the gradient.
	Glass wool filtration	Separate sperm according to their head size and motility. Improve sperm chromatin condensation.
Other sperm sorting techniques	By motility	Motile sperm able to swim upstream against flow, or across streamlines, and collected in different outlet.
	By hydrodynamic effects	Sperm swim near walls due to hydrodynamic effects. Microchannel may be designed for sperm to accumulate.
	By optics	Laser trap allows three-dimensional manipulation of individual sperm, power can be adjusted to confine sperm with low motility.
	By dielectrophoresis	Has been used to separate mature spermatozoa from non-mature spermatogenic cells. Theoretical framework to sort sperm by morphology will be studied in thesis.
	By magnetophoresis	Has been used to remove apoptotic sperm. Fertilisation capability maintained. Theoretical framework to sort sperm by morphology will be studied in thesis.

In this thesis, Resistive Force Theory and Slender Body Theory will be used to compute the swimming velocity of a sperm. The effect of dielectrophoresis and magnetophoresis on the sperm kinematics will be considered. Statistical analysis will be performed to predict the feasibility of sorting sperm using an external field, such that distribution and uncertainties are accounted for. Finally, an ensemble of supervised learning algorithms will be used to make predictions on the sorting outcome, to assess whether machine learning can be used in this context to give comparable results with substantially lower computational costs.

Chapter 3
Sperm in Newtonian Fluid with Sinusoidal Flagellum[3]

In this chapter, a simple analytical model will be used to predict how the velocity of a sperm with a sinusoidal flagellum waveform is influenced by a non-uniform electric field (Koh and Marcos 2014). An approximate analytical solution will be obtained for the velocity as a function of the sperm dimensions and electric field properties.

3.1 The model

As a preliminary study, the spermatozoon is modelled as a perfect sphere of radius *a*, depicting its head, attached to a thin filament of length Λ with uniform thickness, depicting its flagellum. Although the head of a sperm is an ellipsoid, it has been shown that variations in the length-to-width ratio of a sperm head does not alter its linear velocity significantly for the same head volume (Gillies *et al*. 2009). Since the spermatozoa of many organisms take on a sinusoidal wave form (Brennen and Winet 1977, Fulford *et al*. 1998), the motion of the flagellum in this model is assigned to take the shape of a single complete sine wave:

$$y = b\sin\left(\frac{2\pi(x-a)}{\lambda} - \omega_{wave}t\right), \tag{3.1}$$

where *b* is the amplitude, λ is the wavelength, and ω_{wave} is the beating frequency of the flagellum. The waveform of the flagellum is prescribed to follow a small amplitude deflection (Katz *et al*. 1982) of one less order of magnitude relative to the flagellum length, so as to allow an analytical expression for the velocity of the spermatozoa to be derived. The axis of origin is set at the centre of the spermatozoon head (Figure 3-1). The spermatozoon is assumed to move only in the *x*-*y* plane and has three degrees of freedom. The ratio between the wavelength and arclength of the flagellum is introduced as a dimensionless constant

$$\alpha = \frac{\lambda}{\Lambda} = \frac{(x-a)}{s}. \tag{3.2}$$

[3] Published in Koh JBY, Marcos (2014) Effect of dielectrophoresis on spermatozoa. *Microfluidics and Nanofluidics* 17:613-622

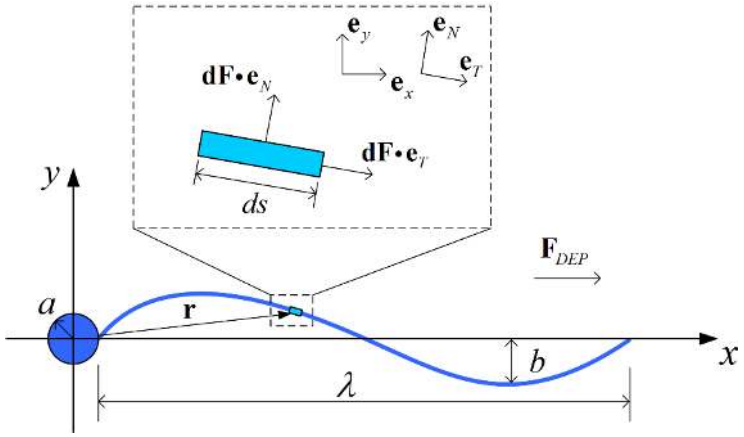

Figure 3-1 – Schematic of a spermatozoon with the origin located at the centre of its head. Inset: Normal and tangential hydrodynamic forces acting on an elemental segment of length *ds* of the flagellum. Modified from Koh and Marcos (2014)

The sperm has a translational velocity of u_x and u_y in the x-direction and y-direction, respectively, and an angular velocity $\dot{\phi}$, such that the velocity of a point on the flagellum due to the sperm swimming is

$$\mathbf{v}_{swim} = u_x \mathbf{e}_x + u_y \mathbf{e}_y + \dot{\phi}\mathbf{e}_z \times \mathbf{r}\,, \tag{3.3}$$

where the position vector $\mathbf{r}$ can be expressed as

$$\mathbf{r} = (a + \alpha s)\mathbf{e}_x + b\sin\left(2\pi s/\Lambda - \omega_{wave} t\right)\mathbf{e}_y\,. \tag{3.4}$$

The wiggling velocity of each elemental segment of the flagellum is the time rate of change of the respective position vector

$$\mathbf{v}_{wiggling} = \frac{d\mathbf{r}}{dt}\,. \tag{3.5}$$

The relative velocity of fluid with respect to each elemental segment is determined as follows:

$$\mathbf{v}_{rel} = -\mathbf{v}_{swim} - \mathbf{v}_{wiggling}\,. \tag{3.6}$$

According to the resistive force theory (Childress 1981; Gray and Hancock 1955), the force acting on a flagellum is directly proportional to the relative fluid velocity. The normal and tangential component of the force, F_N and F_T, acting on a slender filament of length z is

$$dF_{T(viscous)} = \left(\mathbf{v}_{rel} \bullet \mathbf{e}_T\right) K_T \, ds \,, \tag{3.7}$$

$$dF_{N(viscous)} = \left(\mathbf{v}_{rel} \bullet \mathbf{e}_N\right) K_N \, ds \,. \tag{3.8}$$

with K_N and K_T being the normal and tangential resistance coefficients as defined in equations (2.2) and (2.3) of the previous chapter. The normal component of the relative velocity can be computed from the tangential component

$$\left(\mathbf{v}_{rel} \bullet \mathbf{e}_N\right) \mathbf{e}_N = \mathbf{v}_{rel} - \left(\mathbf{v}_{rel} \bullet \mathbf{e}_T\right) \mathbf{e}_T \,, \tag{3.9}$$

where the unit tangential vector is

$$\mathbf{e}_T = \frac{d\mathbf{r}}{ds} \Bigg/ \left| \frac{d\mathbf{r}}{ds} \right| . \tag{3.10}$$

Dimensionless analysis shall be performed, using Λ as the characteristic length and $1/\omega_{wave}$ as the characteristic time, $\Lambda\omega_{wave}$ as the characteristic velocity, $K_N \Lambda^2 \omega_{wave}$ as the characteristic force, and $K_N \Lambda^3 \omega_{wave}$ as the characteristic moment:

$$\tilde{x} = \frac{x}{\Lambda}, \quad \tilde{y} = \frac{y}{\Lambda}, \quad \tilde{r} = \frac{r}{\Lambda}, \quad \tilde{s} = \frac{s}{\Lambda}, \quad \tilde{a} = \frac{a}{\Lambda}, \quad \tilde{b} = \frac{b}{\Lambda}, \quad \tilde{p} = \frac{p}{\Lambda}, \tag{3.11}$$

$$\tilde{t} = t\omega_{wave}, \quad \tilde{\dot{\phi}} = \frac{\dot{\phi}}{\omega_{wave}}, \quad \tilde{\mathbf{v}} = \frac{\mathbf{v}}{\Lambda\omega_{wave}}, \tag{3.12}$$

$$\tilde{\mathbf{F}} = \frac{\mathbf{F}}{K_N \Lambda^2 \omega_{wave}}, \quad \tilde{\mathbf{M}} = \frac{\mathbf{M}}{K_N \Lambda^3 \omega_{wave}}. \tag{3.13}$$

The force due to the relative motion between each elemental segment of the flagellum (referred to as tail for ease of expression) and the fluid is

$$d\mathbf{F}_{tailmotion} = \left[K_T \left(\mathbf{v}_{rel} \bullet \mathbf{e}_T\right) \mathbf{e}_T + K_N \left(\mathbf{v}_{rel} - \left(\mathbf{v}_{rel} \bullet \mathbf{e}_T\right) \mathbf{e}_T\right)\right] ds \,, \tag{3.14}$$

which in non-dimensionalised form is

$$d\tilde{\mathbf{F}}_{tailmotion} = \left[\left(\tilde{\mathbf{v}}_{rel} \bullet \mathbf{e}_T\right) \left(\frac{K_T}{K_N} - 1 \right) \mathbf{e}_T + \tilde{\mathbf{v}}_{rel} \right] d\tilde{s} \,. \tag{3.15}$$

In the following section, DEP force due to the presence of a non-uniform electric field will be added to the model.

3.2 Adding dielectrophoresis force

The DEP force is this model is postulated to act solely in the *x*-direction and that varies linearly with *x* and *y*. The constants ε_{medium} and $\mathrm{Re}(f_{CM})$ are merged into the coefficient of ∇E^2, such that

$$\varepsilon_{medium}\,\mathrm{Re}(f_{CM})\nabla E^2 = D_0 + D_1 x + D_2 y\,. \tag{3.16}$$

The use of a dipole approximation to represent the DEP force is justified in Section 2.3.8. This is consistent with how the hydrodynamics analysis is treated using RFT, in which body-to-body interactions are neglected as they are typically insignificant for small cell bodies (Johnson and Brokaw 1979). Since DEP force, which also depends on the particle's volume, is non-dimensionalised with respect to $K_N \Lambda^2 \omega_{wave}$, equation (3.16) should be non-dimensionalised with respect to $K_N \omega_{wave} / \Lambda$:

$$\frac{\varepsilon_{medium}\,\mathrm{Re}(f_{CM})\nabla E^2}{K_N \omega_{wave}/\Lambda} = \frac{D_0 + D_1 x + D_2 y}{K_N \omega_{wave}/\Lambda} = \tilde{D}_0 + \tilde{D}_1 \tilde{x} + \tilde{D}_2 \tilde{y}\,, \tag{3.17}$$

such that

$$\tilde{D}_0 = \frac{D_0 \Lambda}{K_N \omega_{wave}}\,, \quad \tilde{D}_1 = \frac{D_1 \Lambda^2}{K_N \omega_{wave}}\,, \quad \tilde{D}_2 = \frac{D_2 \Lambda^2}{K_N \omega_{wave}}\,. \tag{3.18}$$

The real part of the Clausius-Mossotti factor has a maximum magnitude of 1, while ε_{medium} typically has an order of 10^{-9} F/m. The AC frequency as well as relative complex permittivities between the body and suspending fluid will affect the Clausius-Mossotti factor, but these will not be independently considered given that they are already absorbed within D_0, D_1 and D_1. Variations which lead to a smaller $\mathrm{Re}(f_{CM})$ can be balanced out by using a larger field gradient. Using the relation given in equation (2.13), the DEP force acting on an elemental segment of the flagellum, and the DEP force on the head, can be expressed in terms of non-dimensionalised constants $\tilde{D}_0$, $\tilde{D}_1$ and $\tilde{D}_2$, as follows:

$$d\tilde{\mathbf{F}}_{tailDEP} = \left(\pi \tilde{p}^2/6\right)\left[\tilde{D}_0 + \tilde{D}_1 \alpha \tilde{s} + \tilde{D}_2 \tilde{b}\sin(2\pi\tilde{s} - \tilde{t})\right]\mathbf{e}_x\, d\tilde{s}\,, \tag{3.19}$$

$$\tilde{\mathbf{F}}_{headDEP} = 2\pi \tilde{a}^3 \tilde{D}_0\, \mathbf{e}_x\,. \tag{3.20}$$

The spermatozoa's velocity is not influenced by $\tilde{D}_2$ in this model, as will be shown later in this chapter. The total force acting on the flagellum is the sum of the force due to relative fluid motion and the force due to dielectrophoresis, integrated over the length of the flagellum. The moment, which is the cross product of the position vector and force, can also be expressed as a function of the spermatozoon's linear and angular velocity:

$$\tilde{\mathbf{F}}_{tail} = \int \left(d\tilde{\mathbf{F}}_{tailmotion} + d\tilde{\mathbf{F}}_{tailDEP} \right), \tag{3.21}$$

$$\tilde{\mathbf{M}}_{tail} = \int \left(\tilde{\mathbf{r}} \times d\tilde{\mathbf{F}}_{tail} \right). \tag{3.22}$$

3.3 Solving for linear and angular velocity

The drag force and the moment experienced by a sphere of radius a due to motion in a viscous fluid (Happel and Brenner 2012) are

$$\mathbf{F}_{headmotion} = -6\pi\mu a \left(u_x \mathbf{e}_x + u_y \mathbf{e}_y \right), \tag{3.23}$$

$$\mathbf{M}_{headmotion} = -8\pi\mu a^3 \dot{\phi} \mathbf{e}_z . \tag{3.24}$$

After non-dimensionalisation, the above two equations become

$$\tilde{\mathbf{F}}_{headmotion} = -1.5\tilde{a} \left(\ln\left(0.18\alpha/\tilde{p}\right) + 0.5 \right) \left(\tilde{u}_x \mathbf{e}_x + \tilde{u}_y \mathbf{e}_y \right), \tag{3.25}$$

$$\tilde{\mathbf{M}}_{headmotion} = -2\tilde{a}^3 \left(\ln\left(0.18\alpha/\tilde{p}\right) + 0.5 \right) \tilde{\dot{\phi}} \mathbf{e}_z . \tag{3.26}$$

The force acting on the spermatozoa head has two components; one due to drag experienced when the spermatozoa is in motion, and the other due to the DEP force. The moment experienced by the spermatozoon head is simply the moment due to motion, since there is no moment resulting from the DEP force acting on the head. Therefore, total force and total moment experienced by the whole spermatozoon is

$$\tilde{\mathbf{F}} = \tilde{\mathbf{F}}_{tail} + \left(\tilde{\mathbf{F}}_{headmotion} + \tilde{\mathbf{F}}_{headDEP} \right), \tag{3.27}$$

$$\tilde{\mathbf{M}} = \tilde{\mathbf{M}}_{tail} + \tilde{\mathbf{M}}_{headmotion} . \tag{3.28}$$

The spermatozoon in this model moves only in the *x*-*y* plane and therefore, $\tilde{\mathbf{F}} = \left\{\tilde{F}_x,\ \tilde{F}_y,\ 0\right\}$ and $\tilde{\mathbf{M}} = \left\{0,\ 0,\ \tilde{M}_z\right\}$. $\tilde{F}_x$, $\tilde{F}_y$ and $\tilde{M}_z$ can be expressed in matrix form as functions of $\tilde{u}_x$, $\tilde{u}_y$ and $\dot{\tilde{\phi}}$:

$$\begin{bmatrix} \tilde{F}_x \\ \tilde{F}_y \\ \tilde{M}_z \end{bmatrix} = \begin{bmatrix} \zeta_{11} & \zeta_{12} & \zeta_{13} \\ \zeta_{21} & \zeta_{22} & \zeta_{23} \\ \zeta_{31} & \zeta_{32} & \zeta_{33} \end{bmatrix} \begin{bmatrix} \tilde{u}_x \\ \tilde{u}_y \\ \dot{\tilde{\phi}} \end{bmatrix} + \begin{bmatrix} \xi_1 \\ \xi_2 \\ \xi_3 \end{bmatrix}. \tag{3.29}$$

where ζ_{11} to ζ_{33} and ξ_1 to ξ_3 are functions of constants $\tilde{D}_0$, $\tilde{D}_1$ and $\tilde{D}_2$. In low Reynolds number regime, inertia forces are negligible as compared to viscous forces, the total forces and moments equate to zero. Thus, $\tilde{u}_x$, $\tilde{u}_y$ and $\dot{\tilde{\phi}}$ can be obtained as functions of $\tilde{D}_0$, $\tilde{D}_1$ and $\tilde{D}_2$ as well as time $\tilde{t}$:

$$\begin{bmatrix} \tilde{u}_x \\ \tilde{u}_y \\ \dot{\tilde{\phi}} \end{bmatrix} = -\begin{bmatrix} \zeta_{11} & \zeta_{12} & \zeta_{13} \\ \zeta_{21} & \zeta_{22} & \zeta_{23} \\ \zeta_{31} & \zeta_{32} & \zeta_{33} \end{bmatrix}^{-1} \begin{bmatrix} \xi_1 \\ \xi_2 \\ \xi_3 \end{bmatrix}. \tag{3.30}$$

Taking the integral over a time period, the dimensionless time-averaged linear and angular velocities can be found as

$$\begin{bmatrix} <\tilde{u}_x> \\ <\tilde{u}_y> \\ <\dot{\tilde{\phi}}> \end{bmatrix} = \frac{1}{2\pi} \int_0^{2\pi} \begin{bmatrix} \tilde{u}_x \\ \tilde{u}_y \\ \dot{\tilde{\phi}} \end{bmatrix} d\tilde{t}\ . \tag{3.31}$$

The waveform of the flagellum is defined to follow a small amplitude deflection such that $\tilde{b}$ is small, allowing the denominator in equation (3.10) to be simplified by approximating $\cos^2\left(2\pi s - \omega_{wave} t\right) \approx 0.5$. The small amplitude model also enables the relation between *x* and the curvilinear coordinate *s* along the flagellum to be approximated as a constant α rather than a function of space and time.

The human sperm is very directional (Gillies *et al*. 2009) and its $<\tilde{u}_y>$ and $<\dot{\tilde{\phi}}>$ are almost zero. To study the effect of DEP force on $<\tilde{u}_y>$ and $<\dot{\tilde{\phi}}>$, the flagellum is set to be stationary, and the force $<\tilde{F}_y>$ and moment $<\tilde{M}_z>$ due solely to DEP force is considered. $<\tilde{F}_y>$ is found to be zero for a sinusoidal flagellum, while

$<\tilde{M}_z>$ is proportional to $\tilde{b}^2\tilde{p}^2$, which is negligible. Therefore, it is justified to assume that the DEP force will only have an effect on $<\tilde{u}_x>$ while $<\tilde{u}_y>$ and $<\dot{\tilde{\phi}}>$ will remain approximately zero. As such, $\tilde{F}_x$ is taken to be a function of only $\tilde{u}_x$, and equation (3.29) becomes

$$\tilde{F}_x = 2\pi\tilde{b}^2\alpha\left(\frac{K_T}{K_N}-1\right)\int_0^1 \frac{\cos^2\left(2\pi\tilde{s}-\tilde{t}\right)}{\alpha^2+4\pi^2\tilde{b}^2\cos^2\left(2\pi\tilde{s}-\tilde{t}\right)}d\tilde{s} + \left(2\pi\tilde{a}^3+\frac{\pi\tilde{p}^2}{6}\right)\tilde{D}_0+\frac{\pi\tilde{p}^2\alpha}{12}\tilde{D}_1 - \tilde{u}_x\left[1.5\tilde{a}\left(\ln\left(\frac{0.18\alpha}{\tilde{p}}\right)+0.5\right)+\int_0^1 \frac{\alpha^2\left(K_T/K_N\right)+4\pi^2\tilde{b}^2\cos^2\left(2\pi\tilde{s}-\tilde{t}\right)}{\alpha^2+4\pi^2\tilde{b}^2\cos^2\left(2\pi\tilde{s}-\tilde{t}\right)}d\tilde{s}\right]. \tag{3.32}$$

Equating $\tilde{F}_x$ to be zero, the time-dependent velocity $\tilde{u}_x$ can be obtained:

$$\tilde{u}_x = \frac{2\pi\tilde{b}^2\alpha\left(\frac{K_T}{K_N}-1\right)\int_0^1 \frac{\cos^2\left(2\pi\tilde{s}-\tilde{t}\right)}{\alpha^2+4\pi^2\tilde{b}^2\cos^2\left(2\pi\tilde{s}-\tilde{t}\right)}d\tilde{s} + \left(2\pi\tilde{a}^3+\frac{\pi\tilde{p}^2}{6}\right)\tilde{D}_0+\frac{\pi\tilde{p}^2\alpha}{12}\tilde{D}_1}{\left[1.5\tilde{a}\left(\ln\left(\frac{0.18\alpha}{\tilde{p}}\right)+0.5\right)+\int_0^1 \frac{\alpha^2\left(K_T/K_N\right)+4\pi^2\tilde{b}^2\cos^2\left(2\pi\tilde{s}-\tilde{t}\right)}{\alpha^2+4\pi^2\tilde{b}^2\cos^2\left(2\pi\tilde{s}-\tilde{t}\right)}d\tilde{s}\right]}. \tag{3.33}$$

Taking an integration over the dimensionless time period of the flagellum beat cycle gives the time-averaged velocity $<\tilde{u}_x>$. Finally, the time-averaged velocity can be converted back into dimensional form

$$\langle u_x\rangle = \frac{\Lambda\omega_{wave}}{2\pi}\int_0^{2\pi}\langle\tilde{u}_x\rangle\,d\tilde{t}\ . \tag{3.34}$$

The resulting velocity becomes a linear function of $\tilde{D}_0$ and $\tilde{D}_1$, which are non-dimensionalised parameters dependent not only on the gradient of the electric field squared, but also on other variables used in the non-dimensionalisation. For the avoidance of doubt, the variables D_0 and D_1 in the analytical solution of Koh and Marcos (2014) are actually non-dimensionalised parameters, as represented by $\tilde{D}_0$ and $\tilde{D}_1$ in this thesis. The extent to which the time-averaged velocity $<\tilde{u}_x>$ is altered by each unit change in $\tilde{D}_0$ and $\tilde{D}_1$ can be determined by taking the partial derivative of equation (3.33). The effect of DEP may thus be expressed as a function of D_0 and D_1 using equation (3.18), such that

$$\frac{\partial \langle u_x \rangle}{\partial D_0} = \frac{\partial \langle u_x \rangle}{\partial \tilde{D}_0} \Lambda / K_N \omega_{wave} , \tag{3.35}$$

$$\frac{\partial \langle u_x \rangle}{\partial D_1} = \frac{\partial \langle u_x \rangle}{\partial \tilde{D}_1} \Lambda^2 / K_N \omega_{wave} . \tag{3.36}$$

The first term in equation (3.33) arises from flagellum propulsion while the second and third terms represent the contibution of DEP force towards velocity. Since force is linearly related to velocity, the magnitude of DEP relative to viscous force can be estimated from the ratio of the resultant velocity relative to free-swimming velocity.

3.4 Difference in velocity of X- and Y-spermatozoa

The sperm velocity can be significantly altered by subjecting it to DEP force. Furthermore, DEP may be used to sort spermatozoa containing different sex-chromosomes, by virtue of inherent difference in their physical dimensions (Cui 1997) as shown in Table 3-1. The human sperm head has a 'flattened shape' with a height of 1.1 μm (Smith *et al*. 2009), with no reported statistical distribution to the best of the author's knowledge. Modelling the head as a sphere, the equivalent head radius for the X- and Y-spermatozoa is (1.33 ± 0.08) μm and (1.32 ± 0.07) μm, respectively. The flagellum beating frequency for a human sperm varies depending on the medium, with typical values ranging from 14 to 17 Hz in Tyrode's solution containing serum (Dresdner and Katz 1981), and 23 to 26 Hz in human cervical mucus at body temperature (Katz *et al*. 1982). The flagellum beating frequency and amplitude of human sperm is experimentally measured to relatively consistent in cervical mucus, with a standard deviation in frequency of 1 Hz (Katz *et al*. 1982).

Table 3-1 – Parameters of measurement for X- and Y-spermatozoa (mean ± SD) from Cui (1997).

	X	Y
Head length (μm)	5.38 ± 0.43	5.23 ± 0.40
Head width (μm)	3.53 ± 0.33	3.53 ± 0.30
Neck and tail length (μm)	42.22 ± 4.37	41.18 ± 3.47
Head perimeter (μm)	15.26 ± 1.17	14.73 ± 1.07
Head area (μm^2)	14.74 ± 2.09	13.93 ± 1.79

Using a flagellum beating frequency ω_{wave} of 23 Hz, the X-spermatozoon is expected to have an average linear velocity (Koh and Marcos 2014) of

$$\langle u_x \rangle_{(\mathrm{X})} = \left[-59.6 + 0.0559\tilde{D}_1 + 1.43\tilde{D}_0 \right] \mu\mathrm{m\,s}^{-1}. \tag{3.37}$$

The linear velocity of a 'small' and 'large' X-spermatozoon, corresponding to dimensions of one standard deviation below and above the mean, respectively, is

$$\langle u_x \rangle_{(\mathrm{X\_small})} = \left[-52.9 + 0.0495\tilde{D}_1 + 1.45\tilde{D}_0 \right] \mu\mathrm{m\,s}^{-1}, \tag{3.38}$$

$$\langle u_x \rangle_{(\mathrm{X\_large})} = \left[-66.3 + 0.0621\tilde{D}_1 + 1.42\tilde{D}_0 \right] \mu\mathrm{m\,s}^{-1}. \tag{3.39}$$

For a Y-spermatozoon, the expected average linear velocity is

$$\langle u_x \rangle_{(\mathrm{Y})} = \left[-57.6 + 0.0570\tilde{D}_1 + 1.46\tilde{D}_0 \right] \mu\mathrm{m\,s}^{-1}. \tag{3.40}$$

Meanwhile, the linear velocity of a 'small' and 'large' Y-spermatozoon, corresponding to dimensions of one standard deviation below and above the mean, respectively, is

$$\langle u_x \rangle_{(\mathrm{Y\_small})} = \left[-52.4 + 0.0518\tilde{D}_1 + 1.46\tilde{D}_0 \right] \mu\mathrm{m\,s}^{-1}, \tag{3.41}$$

$$\langle u_x \rangle_{(\mathrm{Y\_large})} = \left[-62.9 + 0.0622\tilde{D}_1 + 1.44\tilde{D}_0 \right] \mu\mathrm{m\,s}^{-1}. \tag{3.42}$$

In the absence of DEP force, the velocity of spermatozoa within one standard deviation from the mean is computed to range between 51 and 65 μm/s. This is in agreement with experimentally measured straight line velocity of the human spermatozoa, which is reported to have values ranging from 40 μm/s in Hanks' solution (Ishijima *et al*. 1986) to 74 ± 18 μm/s in BWW (Biggers-Whitten-Whittingham) medium (Mortimer *et al*. 1998).

When subjected to a non-uniform electric field, the effect of DEP is greater on the larger spermatozoa, which does not come as a surprise. Since the head of a sperm has a volume one order of magnitude greater than its flagellum, the DEP force acting on the head contributes more significantly to its velocity as compared to that on the flagellum. Although a larger sperm experiences more drag force, the effect of dielectrophoresis is more than enough to compensate for the drag. DEP force scales proportionately to the volume of the head, and hence to its radius raised to the third

power. On the other hand, drag force in low Reynolds number is linearly related to the length scale. Therefore, DEP enhances the velocity of a larger sperm to a greater extent.

Figure 3-2 and Figure 3-3 show the linear velocities of sperm, within one standard deviation from the mean, as a function of $\tilde{D}_0$ and $\tilde{D}_1$, respectively. The solid red and dotted blue lines represent the X- and Y-sperm, respectively. For each combination of $\tilde{D}_0$ and $\tilde{D}_1$, 68% of the sperm population have velocities between the upper and lower lines demarcating the values at one standard deviation from the mean.

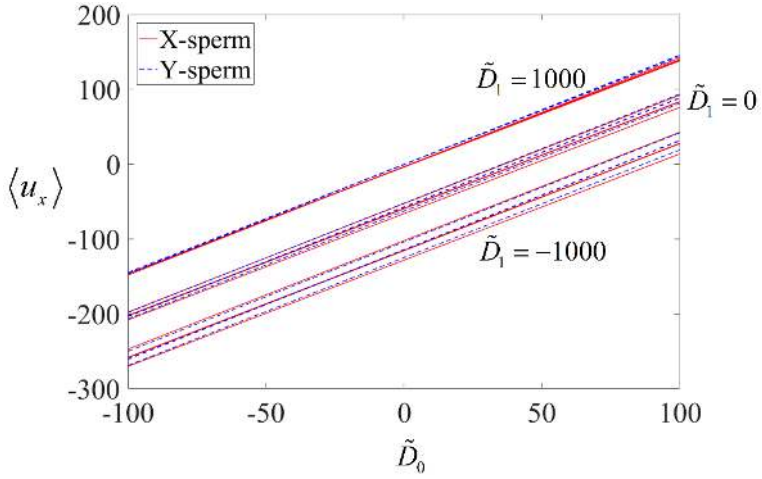

Figure 3-2 – Time-averaged velocity $<u_x>$ in µm/s against $\tilde{D}_0$, for $\tilde{D}_1$ = 1000, $\tilde{D}_1$ = 0, and $\tilde{D}_1$ = -1000, for spermatozoa of above and below one standard deviation of the average morphology. Solid red and dotted blue lines represent X- and Y- spermatozoon, respectively. The bold lines denote the velocity corresponding to the average spermatozoa dimension, while the fine lines denote the velocity corresponding to one standard deviation.

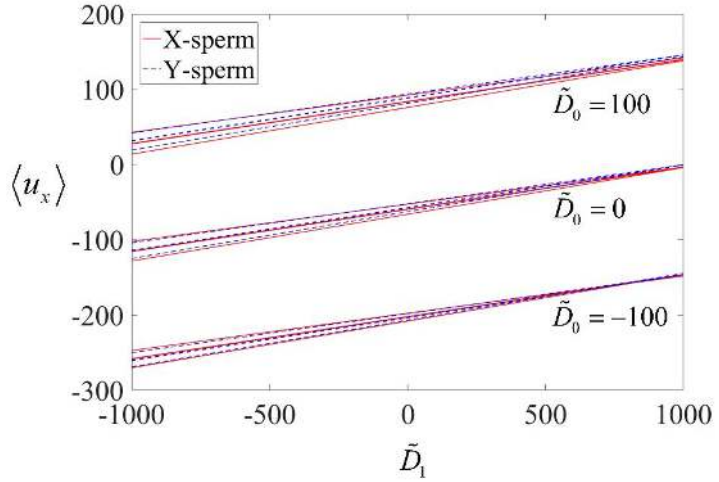

Figure 3-3 – Time-averaged velocity $<u_x>$ in µm/s against $\tilde{D}_1$, for $\tilde{D}_0$ = 100, $\tilde{D}_0$ = 0, and $\tilde{D}_0$ = -100, for spermatozoa of above and below one standard deviation of the average morphology. Solid red and dotted blue lines represent X- and Y- spermatozoon, respectively. The bold lines denote the velocity corresponding to the average spermatozoa dimension, while the fine lines denote the velocity corresponding to one standard deviation.

DEP force alters the velocity of the X- and Y-spermatozoa to different extent. Therefore, by applying a non-uniform electric field to a sperm population, the probability distribution of X- and Y-spermatozoa will vary spatially, leading to skewed populations. Despite the controversies of gender selection (Hesketh and Zhu 2006), selecting the sex of one's offspring may be authorized (Dahl 2004) for avoiding gender-linked genetic diseases such as Duchenne muscular dystrophy (Hussey *et al*. 1999).

3.5 Feasibility of sorting

Under some conditions such as $\tilde{D}_0 = 100$ with $\tilde{D}_1 = 0$, there exists velocities of the X-sperm outside a one-standard-deviation range of the Y-sperm, where the chances of a Y-sperm being present is less than 16%. On the other hand, the velocities of the Y-sperm within one standard-deviation from its mean overlap with those of its X-chromosome-bearing counterparts. Using a simple approximation, it is estimated that there exists a possibility of obtaining sperm sorted by their chromosomes, with a 84% success rate in choosing a female, and a success rate of between 50% and 84% in choosing a male.

The desired values of $\tilde{D}_0$ and $\tilde{D}_1$ can be obtained by varying the separation distance between the electrodes. Suppose $\nabla(E^2)$, after non-dimensionalisation, is to be proportional to $\tilde{D}_0 + \tilde{D}_1\tilde{x}$. If the square of the electric field is designed to vary only in the x-direction, the gradient is $\partial(E^2)/\partial x = M_0 + M_1 x$, where M_0 and M_1 are parameters to be adjusted. In this way, the electric field can be expressed as

$$E = \sqrt{M_0 x + 0.5 M_1 x^2} = V \Bigg/ \left(\frac{1}{\sqrt{\frac{M_0}{V^2} x + \frac{0.5 M_1}{V^2} x^2}} \right), \tag{3.43}$$

where V is the voltage across the electrodes. The electrode separation will follow the equation:

$$d_{sep} = \frac{1}{\sqrt{\frac{M_0}{V^2} x + \frac{0.5 M_1}{V^2} x^2}}. \tag{3.44}$$

Since $\varepsilon_{medium}\,\mathrm{Re}(f_{cm})\nabla E^2$ is non-dimensionalised with $K_N\omega/\Lambda$,

$$\frac{\varepsilon_{medium}\,\mathrm{Re}(f_{cm})\nabla E^2}{K_N\omega/\Lambda} = \frac{\varepsilon_{medium}\,\mathrm{Re}(f_{cm})\left[M_0+M_1x\right]}{K_N\omega/\Lambda} = \tilde{D}_0+\tilde{D}_1\tilde{x}\,. \tag{3.45}$$

It can be observed from Figure 3-2 that setting $\tilde{D}_0=100$ and $\tilde{D}_1=-1$ will allow the X-spermatozoa to have a velocity beyond one standard deviation from the Y-spermatozoa. The choice of $\tilde{D}_1$ is made in the interest of reducing the maximum electric field. This corresponds to $M_0\simeq 10^{15}$ and $M_1\simeq -10^{17}$. For V = 300 V, the spacing will be:

$$d_{sep}=\frac{1}{\sqrt{10^{10}x-10^{12}x^2}}\,. \tag{3.46}$$

A pari of electrodes can be designed such that

$$y_{top}=\frac{1}{2\sqrt{10^{10}x-10^{12}x^2}},\quad y_{bottom}=-\frac{1}{2\sqrt{10^{10}x-10^{12}x^2}}\,. \tag{3.47}$$

An electric field of 2100 V/mm at 2 MHz is needed for cells to lyse (Lee and Tai 1999), while the electric field according to the above setup is at most 1500 V/mm where the electrodes are 0.2 mm apart. Since microelectrodes can be made as small as having a gap of 40 μm (Khoshmanesha *et al*. 2009), it is technically feasible to carry out the sorting as discussed.

3.6 Chapter Summary

In this chapter, RFT is applied to solve for the swimming velocity of a single sperm subjected to a linearly-varying DEP force. Modelling the flagellum beating pattern as a sinusoidal waveform with a small displacement, it is concluded that the swimming sperm is highly directional. The velocity along the *x*-axis is expressed analytically as a function of the sperm parameters as well as $\tilde{D}_0$ and $\tilde{D}_1$ which depends on the gradient of the electric field squared. As DEP influences the velocity of each sperm to a different extent depending on its morphology, the velocity distribution of the X- and Y-spermatozoa differs. This opens the possibility using a non-uniform electric field to obtain a skewed population of spermatozoa containing the desired type of chromosomes for artificial fertilisation.

Chapter 4
Sperm in Viscoelastic Fluid with Active Flagellum[4]

Having obtained interesting preliminary results in the previous chapter, a more detailed analysis will now be done. In this chapter, the sperm is considered to have an active flagellum with internal sliding force, and the beating pattern will be determined by considering the force balance on each infinitesimal segment of the flagellum. The straight-line velocity in the inertia frame will be compared with the time-averaged velocity, to assess whether it is justified to approximate the former using the latter. Given that many biological fluids are non-Newtonian, the effect of dielectrophoresis on the flagellum shape and velocity of spermatozoa in a Newtonian fluid medium is compared with that in a viscoelastic fluid medium (Koh and Marcos 2015b).

4.1 Flagellum shape

Many phenomena, ranging from physical processes (Hirsch *et al*. 2012) to events in financial markets (El Karoui *et al*. 1997), can be modelled by differential equations. In this chapter, the beating pattern of a microswimmer is likewise formulated to obey a partial differential equation (PDE) as a function of both space and time. A partial differential equation can be reduced to an ordinary differential equation (ODE) by symmetry reduction (Bluman and Kumei 2013) such as separation of variables.

The spermatozoon is modelled, similar to that in Chapter 3, as a perfect sphere of radius a, attached to a thin filament of length Λ with uniform radius p (Figure 4-1). For an infinitesimal segment of the flagellum of length ds as depicted in the inset, the position vector is $\mathbf{r}$. Acting on each segment are the shear force Q, tension T, bending moment M_{bend}, internal sliding force $f_m \cdot ds$, hydrodynamic force $dF_{N(Oldroyd)}$ in the normal direction and $dF_{T(Oldroyd)}$ in the tangential direction, as well as DEP force $d\mathbf{F}_{DEP}$. The flagellum is modelled to have microtubules exerting a sliding force on one another (Fu *et al*. 2008), such that the equivalent moment acting on each infinitesimal segment

[4] Published in Koh JBY, Marcos (2015b). Dielectrophoresis of spermatozoa in viscoelastic medium. *Electrophoresis* 36:1514-1521

is due to a force per unit length f_m acting on the top in the positive tangential direction $\mathbf{e}_T$ as well as on the bottom in the negative tangential direction. The spermatozoon is defined to move only in the *x*-*y* plane and has three degrees of freedom.

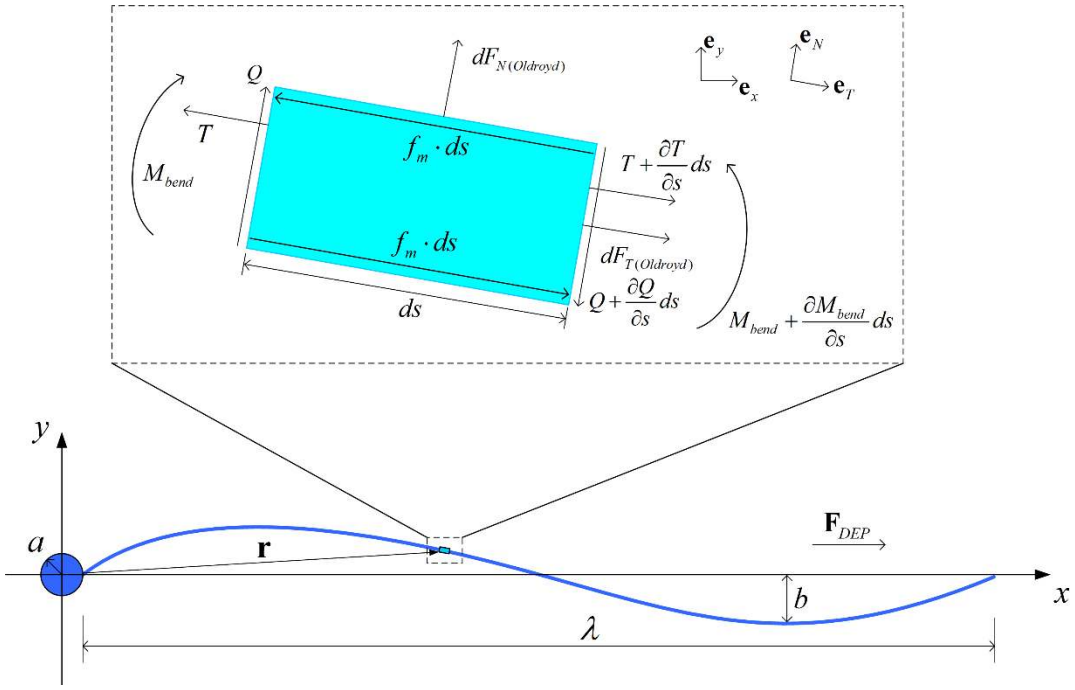

Figure 4-1 – Schematic of a spermatozoon with the origin located at the centre of its head. Inset: Normal and tangential hydrodynamic forces, internal shear and axial forces, and bending moment acting on an elemental segment of length ds of the flagellum. Modified from Koh and Marcos (2015)

In this chapter, the flagellum wave pattern will be determined by solving *y* as a function of *s*. The position vector of an infinitesimal segment along the flagellum is

$$\mathbf{r} = x\,\mathbf{e}_x + y\,\mathbf{e}_y\,. \tag{4.1}$$

where *x* is related to the curvilinear position *s* by the dimensionless constant α as defined in Chapter 3. Resistive force theory shall again be applied here. The force on an elemental segment of the flagellum, without dielectrophoresis or internal sliding force of the active flagellum, is

$$d\mathbf{F}_{viscous} = \left[K_T\left(\mathbf{v}_{rel}\bullet\mathbf{e}_T\right)\mathbf{e}_T + K_N\left(\mathbf{v}_{rel} - \left(\mathbf{v}_{rel}\bullet\mathbf{e}_T\right)\mathbf{e}_T\right)\right]ds\,, \tag{4.2}$$

as defined in equation (3.14), where the relative fluid velocity follows the definition in equation (3.6):

$$\mathbf{v}_{rel} = -\left(u_x\,\mathbf{e}_x + u_y\,\mathbf{e}_y + \dot{\phi}\mathbf{e}_z \times \mathbf{r}\right) - \frac{d\mathbf{r}}{dt}\,. \tag{4.3}$$

The unit tangential vector is expressed as:

$$\mathbf{e}_T = \frac{\dfrac{d\mathbf{r}}{ds}}{\left|\dfrac{d\mathbf{r}}{ds}\right|} = \frac{\dfrac{\partial x}{\partial s}\mathbf{e}_x + \dfrac{\partial y}{\partial s}\mathbf{e}_y}{\sqrt{\left(\dfrac{\partial x}{\partial s}\right)^2 + \left(\dfrac{\partial y}{\partial s}\right)^2}}. \tag{4.4}$$

Cervical mucus has viscosities in the range of a few thousand cP (Ishijima *et al*. 1986) and differs in its viscoelastic properties according to a woman's fertility cycle. The variations in a fluid's stress-strain relation can be substantial; for example, sperm cells are unable to traverse the cervical mucus during non-ovulatory period due to heightened viscoelasticity (Lai *et al*. 2009). The Oldroyd-B model is one of the constitutive relation used to study the behaviour of swimmers in a viscoelastic fluid medium, because it describes the elastic and memory effects displayed by "most polymer and biological liquids" (Zhao and Yang 2009). Here, the spermatozoon is modelled to be in an Oldroyd-B viscoelastic fluid, which displays a fading memory model (Fu *et al*. 2008):

$$\mathbf{f}_{oldroyd} + \tau \dot{\mathbf{f}}_{oldroyd} = \mathbf{f}_{viscous} + \left(\eta_s/\eta\right)\tau \dot{\mathbf{f}}_{viscous}. \tag{4.5}$$

where τ is the fluid relaxation time, η_s/η is the ratio of solvent viscosity to total viscosity, while $\mathbf{f}_{viscous}$ and $\mathbf{f}_{oldroyd}$ are the hydrodynamic forces in a Newtonian fluid and Oldroyd-B fluid, respectively.

The hydrodynamic forces are assumed to follow the time dependency of flagella beating:

$$\mathbf{f}_{viscous} = \overline{\mathbf{f}}_{viscous}\, e^{-i\omega t}, \tag{4.6}$$

$$\mathbf{f}_{oldroyd} = \overline{\mathbf{f}}_{oldroyd}\, e^{-i\omega t}. \tag{4.7}$$

with $\overline{\mathbf{f}}_{viscous}$ and $\overline{\mathbf{f}}_{oldroyd}$ being the respective hydrodynamic forces as a function of space only, ω being the angular frequency at which the flagellum wiggles, and t as time. As such, the Oldroyd force can be expressed as a function of viscous force and Deborah number (Fu *et al*. 2008):

$$\overline{\mathbf{f}}_{\text{oldroyd}} = \overline{\mathbf{f}}_{\text{viscous}}\left(\frac{1 - i\,\text{De}_2}{1 - i\,\text{De}}\right), \tag{4.8}$$

where the Deborah number $\mathrm{De} = \tau\omega$ represents 2π times the ratio between the relaxation time and the flagella beating period, and $\mathrm{De}_2 = \mathrm{De}(\eta_s/\eta)$ is the product of the Deborah number and viscosity ratio. A Deborah number of zero indicates that the fluid medium is Newtonian, while a non-zero De indicates otherwise. Since the flagellum is assumed to wiggle in the *y*-direction only, *x* is time-independent and only a function of space. The flagellum is approximated to have small beating amplitude and a small deflection gradient, such that

$$\frac{\partial x}{\partial s} \simeq 1, \ \frac{\partial y}{\partial s} \simeq 0. \tag{4.9}$$

Apart from the viscoelastic force, another external force acting on the spermatozoon is the DEP force due to a non-uniform electric field. The DEP force acting on an elemental segment of the flagellum, and on the head, is prescribed to act solely in the *x*-direction:

$$d\mathbf{F}_{tailDEP} = \frac{1}{6}\pi p^2 \left[\boldsymbol{\varepsilon}_{medium} \mathrm{Re}(f_{CM}) \nabla E^2 \right] ds \, \mathbf{e}_x, \tag{4.10}$$

$$\mathbf{F}_{headDEP} = 2\pi a^3 \left[\varepsilon_{medium} \mathrm{Re}(f_{CM}) \nabla E^2 \right] \mathbf{e}_x. \tag{4.11}$$

where ε_{medium} is the medium permittivity, $\mathrm{Re}(f_{CM})$ is the real part of the Clausius-Mossotti factor, and *E* is the electric field. The DEP force is defined to be a linear function of *x*, so that the equation of motion obtained will be linear and can be solved conveniently. The constants ε_{medium} and $\mathrm{Re}(f_{CM})$ are merged into the coefficient of ∇E^2 such that $\varepsilon_{medium} \mathrm{Re}(f_{CM}) \nabla E^2$ can be written as $D_0 + D_1 x$. Since the DEP force acts only in the *x*-direction, the DEP force on each infinitesimal segment of the flagellum is

$$d\mathbf{F}_{tailDEP} = \frac{1}{6}\pi p^2 \left[D_0 + D_1 (a + \alpha s) \right] ds \, \mathbf{e}_x. \tag{4.12}$$

As the Reynolds number is negligible for the swimming of spermatozoa, the net force and moment equate to zero. The net force acting in the normal direction is

$$\left(Q + \frac{\partial Q}{\partial s} ds \right) - Q + dF_{N(Oldroyd)} + d\mathbf{F}_{DEP(flagellum)} \cdot \mathbf{e}_N = 0. \tag{4.13}$$

By approximation of small beating amplitude and a small deflection gradient, the above equation becomes

$$\frac{\partial Q}{\partial s}ds+\left\{-\frac{\partial y}{\partial t}K_N\left(\frac{1-i\,\mathrm{De}_2}{1-i\,\mathrm{De}}\right)ds\right\}-\left\{\frac{1}{6}\pi p^2\left[D_0+D_1(a+\alpha s)\right]ds\right\}\frac{\partial y}{\partial s}=0\,. \quad (4.14)$$

Considering the net moment on an elemental segment about its centre, to the first order of *ds*,

$$\frac{\partial^2 M_{bend}}{\partial s^2}+\frac{\partial Q}{\partial s}-2p\frac{\partial f_m}{\partial s}=0\,. \quad (4.15)$$

The bending moment can be expressed by (Landau and Lifshitz 1970)

$$M_{bend}=EI\frac{\partial^2 y}{\partial s^2}. \quad (4.16)$$

where E is the Young's modulus and I is the cross-sectional moment of inertia. The same dimensionless parameters as defined in Chapter 3 shall be used, with Λ being the characteristic length and $1/\omega$ as the characteristic time, $\Lambda\omega$ as the characteristic velocity, $K_N\Lambda^2\omega$ as the characteristic force, and $K_N\Lambda^3\omega$ as the characteristic moment.

The equation of motion governing the shape of an active flagellum in an Oldroyd-B fluid, as given in equation (4.14), can be non-dimensionalised as

$$\frac{\partial^4\tilde{y}}{\partial\tilde{s}^4}+\mathrm{Sp}^4\left(\frac{1-i\,\mathrm{De}_2}{1-i\,\mathrm{De}}\right)\frac{\partial\tilde{y}}{\partial\tilde{t}}+\frac{1}{6}\pi\tilde{p}^2\,\mathrm{Sp}^4\left[\tilde{D}_0+\tilde{D}_1(\tilde{a}+\alpha\tilde{s})\right]\frac{\partial\tilde{y}}{\partial\tilde{s}}-\frac{\partial\tilde{f}_m}{\partial\tilde{s}}=0\,, \quad (4.17)$$

where $\tilde{f}_m$ is the non-dimensional form of f_m

$$\tilde{f}_m=\frac{f_m}{EI/\left(2p\Lambda^2\right)}, \quad (4.18)$$

and non-dimensional constants $\tilde{D}_0$ and $\tilde{D}_1$ are related to dimensional constants D_0 and D_1 as defined in equation (3.18), and the Sperm number is inversely related to the flexural rigidity of the flagellum

$$\mathrm{Sp}=\left(\frac{K_N\Lambda^4\omega}{EI}\right)^{1/4}. \quad (4.19)$$

To solve the equation of motion, four boundary conditions will be required. At free end, corresponding to $\tilde{s}=1$, there is no net moment or shear force. Therefore,

$$\left.\frac{\partial^2 \tilde{y}}{\partial \tilde{s}^2}\right|_{\tilde{s}=1} = 0, \tag{4.20}$$

$$\left.\frac{\partial^3 \tilde{y}}{\partial \tilde{s}^3}\right|_{\tilde{s}=1} - \tilde{f}_m = 0. \tag{4.21}$$

Since the flagellum is hinged at the head and total moment is zero at equilibrium:

$$\tilde{y}\big|_{\tilde{s}=0} = 0, \tag{4.22}$$

$$-\left.\frac{\partial^2 \tilde{y}}{\partial \tilde{s}^2}\right|_{\tilde{s}=0} - \int_0^1 \tilde{f}_m \, d\tilde{s} - \frac{1}{6}\pi \tilde{p}^2 \,\mathrm{Sp}^4 \int_0^1 \tilde{y}\left[\tilde{D}_0 + \tilde{D}_1(\tilde{a}+\alpha\tilde{s})\right] d\tilde{s} = 0. \tag{4.23}$$

The deflection $\tilde{y}$ and internal sliding force $\tilde{f}_m$ can be separated into a space-dependent function and time-dependent exponential function:

$$\tilde{y}\left(\tilde{s},\tilde{t}\right) = \tilde{h}(\tilde{s})\, e^{-i\tilde{t}}, \tag{4.24}$$

$$\tilde{f}_m\left(\tilde{s},\tilde{t}\right) = \overline{f}_m\, e^{i\tilde{k}\tilde{s}}\, e^{-i\tilde{t}}. \tag{4.25}$$

where $\tilde{h}$ is the non-dimensional position along the *y*-axis as a function of $\tilde{s}$ only, $\tilde{k}$ is the non-dimensional constant in which the spatial distribution of internal force is related to, and $\overline{f}_m$ is a non-dimensional constant independent of space and time. The rational for using separation of variables with a complex exponential governing the time-dependence is discussed in Appendix B. The equation of motion can hence be reduced into an ordinary differential equation as follows:

$$\tilde{h}'''' - i\,\mathrm{Sp}^4\left(\frac{1-i\,\mathrm{De}_2}{1-i\,\mathrm{De}}\right)\tilde{h} + \frac{1}{6}\pi\tilde{p}^2\,\mathrm{Sp}^4\left[\tilde{D}_0 + \tilde{D}_1(\tilde{a}+\alpha\tilde{s})\right]\tilde{h}' - \frac{\partial}{\partial\tilde{s}}\overline{f}_m\, e^{i\tilde{k}\tilde{s}} = 0. \tag{4.26}$$

Assume that a particular solution to the non-homogeneous differential equation is

$$\tilde{h}_p\left(\tilde{s}\right) = C_p\, e^{i\tilde{k}\tilde{s}}, \tag{4.27}$$

where C_p is a constant which can be determined by substituting equation (4.27) into (4.26). The particular solution can hence be written as

$$\tilde{h}_p\left(\tilde{s}\right)=\frac{i\tilde{k}\,\overline{\tilde{f}}_m\,e^{i\tilde{k}\tilde{s}}}{\tilde{k}^4-i\,\mathrm{Sp}^4\left(\dfrac{1-i\,\mathrm{De}_2}{1-i\,\mathrm{De}}\right)+i\tilde{k}\,\mathrm{Sp}^4\left[\dfrac{\pi}{6}\tilde{p}^2\left(\tilde{D}_0+\tilde{D}_1(\tilde{a}+\alpha\tilde{s})\right)\right]}. \tag{4.28}$$

The homogeneous solution to a fourth order equation has four roots, which can be obtained by substituting $\tilde{h}=e^{r\tilde{s}}$ into the homogeneous part of equation (4.26) and solving the fourth order polynomial:

$$r^4+\frac{1}{6}\pi\tilde{p}^2\,\mathrm{Sp}^4\left[\tilde{D}_0+\tilde{D}_1(\tilde{a}+\alpha\tilde{s})\right]r-i\,\mathrm{Sp}^4\left(\frac{1-i\,\mathrm{De}_2}{1-i\,\mathrm{De}}\right)=0\,, \tag{4.29}$$

where the four roots, which shall be denoted r_1 to r_4, to the above equation gives the homogeneous time-independent solution:

$$\tilde{h}_h\left(\tilde{s}\right)=C_1e^{r_1\tilde{s}}+C_2e^{r_2\tilde{s}}+C_3e^{r_3\tilde{s}}+C_4e^{r_4\tilde{s}}\,. \tag{4.30}$$

The coefficients C_1 to C_4 can be determined using the four boundary conditions in equations (4.20) to (4.23), where the time-dependence can be separated using equation (4.24). Thereafter, the flagellum deflection can be obtained by adding the homogeneous and particular solution of the space-dependent ordinary differential equation, and substituting into equation (4.24) to give the full time-dependent solution

$$\tilde{y}\left(\tilde{s},\tilde{t}\right)=\mathrm{Re}\left\{\left[\begin{array}{c}C_1e^{\tilde{r}_1\tilde{s}}+C_2e^{\tilde{r}_2\tilde{s}}+C_3e^{\tilde{r}_3\tilde{s}}+C_4e^{\tilde{r}_4\tilde{s}}+\ldots\\ \dfrac{i\tilde{k}\,\overline{\tilde{f}}_m\,e^{i\tilde{k}\tilde{s}}}{\tilde{k}^4-i\,\mathrm{Sp}^4\left(\dfrac{1-i\,\mathrm{De}_2}{1-i\,\mathrm{De}}\right)+i\tilde{k}\,\mathrm{Sp}^4\left[\dfrac{\pi}{6}\tilde{p}^2\left(\tilde{D}_0+\tilde{D}_1\tilde{x}\right)\right]}\end{array}\right]e^{-i\tilde{t}}\right\}. \tag{4.31}$$

In the absence of DEP, the plots in Figure 4-2 are identical to those presented by Fu *et al*. (2008), therefore validating the accuracy of the mathematical procedures as well as numerical code used. A value of $\tilde{k}=0$ corresponds to the internal force being uniformly distributed and varying only with time, while higher values of $\tilde{k}$ correspond to the internal force having a larger spatial variation. A modification of the code to the 'hinged with prescribed angle' boundary condition also gives consistent results with the beating patterns and velocities presented by Marcos *et al*. (2014) for the scenario of zero shear flow.

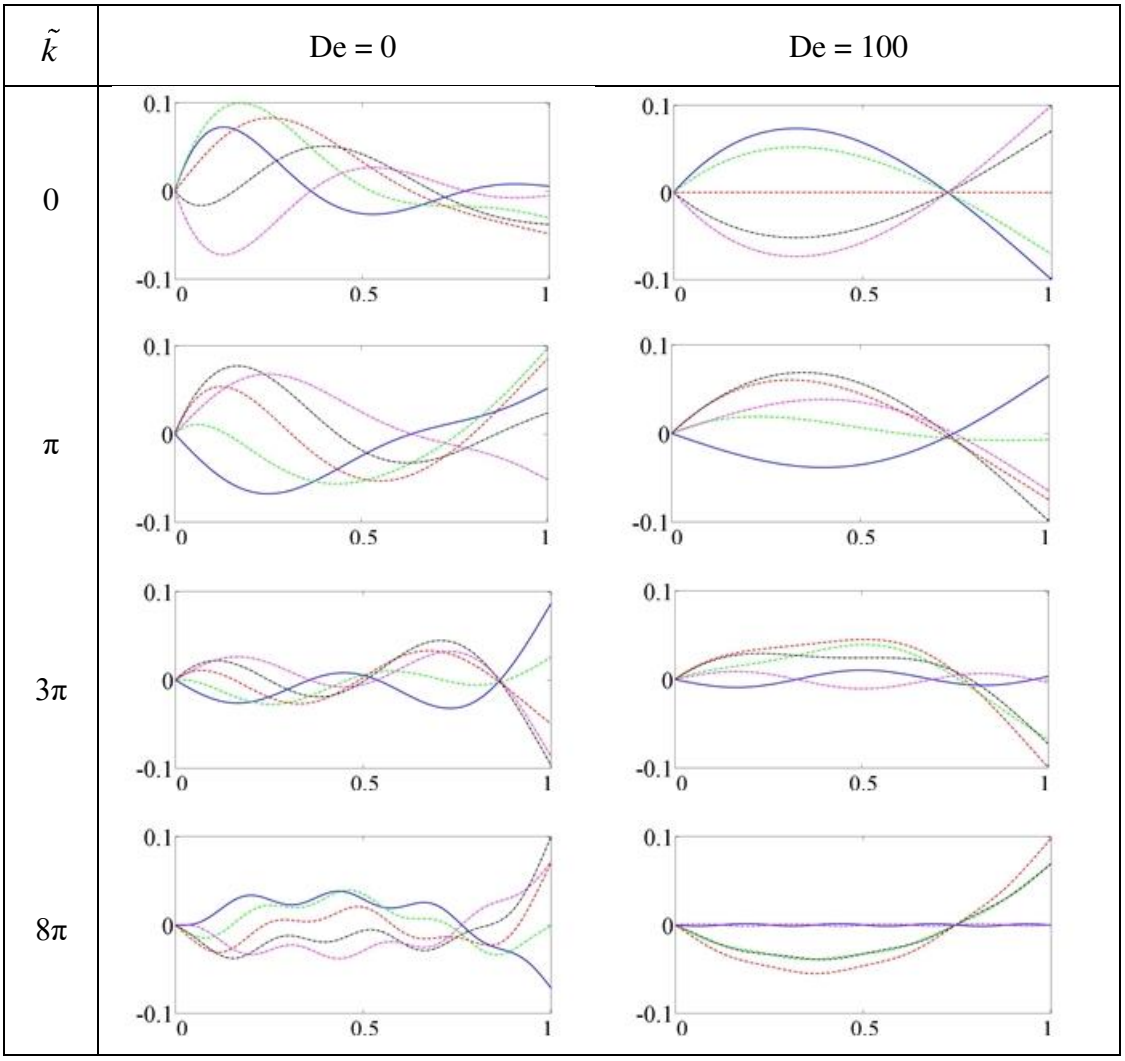

Figure 4-2 – Flagellum shape for Sp = 7, corresponding to different internal force and De. The solid blue line corresponds to a dimensionless time of $\tilde{t} = 0$ while the dashed green, dashed red, dash-dotted black and dash-dotted pink lines corresponds to $\tilde{t} = \pi/4$, $\tilde{t} = \pi/2$, $\tilde{t} = 3\pi/4$ and $\tilde{t} = \pi$, respectively.

The influence of a non-uniform internal force for different Sp is considered in Figure 4-3. The *x*-axis and *y*-axis corresponds to $\tilde{x}$ and $\tilde{y}$, respectively, not labeled in the plots due to space constraints. Following equation (4.19), a sperm with Sp = 7 has flexural rigidity which is four times that of a sperm with Sp = 10, and a quarter that of a sperm with Sp = 5. $\overline{f}_m$, which governs the internal sliding force, has been adjusted such that each flagellum has a beat amplitude of 10%. The higher the Sperm number, the greater the internal force needed to create the same beat amplitude of 10%. It can be observed that for the case of the non-uniformly distributed internal force, the end of the flagellum has a larger deflection in general. With the flagellum shape having been obtained, the derivatives of *x* and *y* are known, and the velocity of the spermatozoa in the body-fixed frame can henceforth be computed.

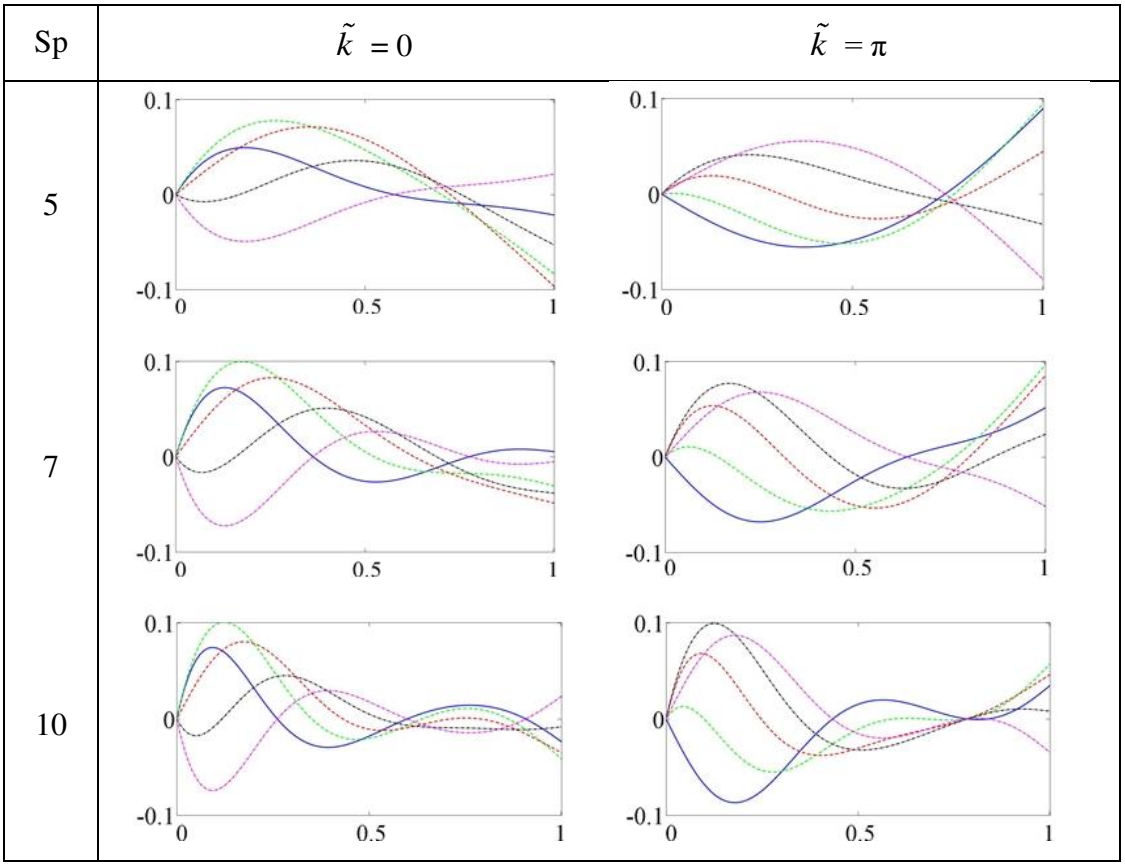

Figure 4-3 – Flagellum shape for De = 0, corresponding to different Sp and *k*. The solid blue line corresponds to a dimensionless time of $\tilde{t} = 0$ while the dashed green, dashed red, dash-dotted black and dash-dotted pink lines corresponds to $\tilde{t} = \pi/4$, $\tilde{t} = \pi/2$, $\tilde{t} = 3\pi/4$ and $\tilde{t} = \pi$, respectively.

4.2 Velocity and trajectory

Having obtained the flagellum shape, the non-dimensional linear and angular velocity can be computed by solving the relation presented in equation (3.30), reprinted here for the reader's convenience:

$$\begin{bmatrix} \tilde{u}_x \\ \tilde{u}_y \\ \tilde{\dot{\phi}} \end{bmatrix} = -\begin{bmatrix} \zeta_{11} & \zeta_{12} & \zeta_{13} \\ \zeta_{21} & \zeta_{22} & \zeta_{23} \\ \zeta_{31} & \zeta_{32} & \zeta_{33} \end{bmatrix}^{-1} \begin{bmatrix} \xi_1 \\ \xi_2 \\ \xi_3 \end{bmatrix}, \tag{4.32}$$

where

$$\zeta_{11} = \left(\frac{1-i\,\mathrm{De}_2}{1-i\,\mathrm{De}}\right)\int\left[\frac{-\frac{K_T}{K_N}\left(\frac{\partial\tilde{x}}{\partial\tilde{s}}\right)^2-\left(\frac{\partial\tilde{y}}{\partial\tilde{s}}\right)^2}{\left(\frac{\partial\tilde{x}}{\partial\tilde{s}}\right)^2+\left(\frac{\partial\tilde{y}}{\partial\tilde{s}}\right)^2}\right]d\tilde{s}\;-\left(\frac{1-i\,\mathrm{De}_2}{1-i\,\mathrm{De}}\right)\frac{3}{2}\tilde{a}\left[\ln\left(\frac{0.18\lambda}{\tilde{p}}\right)+0.5\right] \tag{4.33}$$

$$\zeta_{12}=\left(\frac{1-i\,\mathrm{De}_2}{1-i\,\mathrm{De}}\right)\int\left[\frac{\left(1-\frac{K_T}{K_N}\right)\frac{\partial\tilde{x}}{\partial\tilde{s}}\frac{\partial\tilde{y}}{\partial\tilde{s}}}{\left(\frac{\partial\tilde{x}}{\partial\tilde{s}}\right)^2+\left(\frac{\partial\tilde{y}}{\partial\tilde{s}}\right)^2}\right]d\tilde{s} \tag{4.34}$$

$$\zeta_{13}=\left(\frac{1-i\,\mathrm{De}_2}{1-i\,\mathrm{De}}\right)\int\left[\frac{\left(\frac{K_T}{K_N}\left(\frac{\partial\tilde{x}}{\partial\tilde{s}}\right)^2+\left(\frac{\partial\tilde{y}}{\partial\tilde{s}}\right)^2\right)\tilde{y}+\left(1-\frac{K_T}{K_N}\right)\tilde{x}\frac{\partial\tilde{x}}{\partial\tilde{s}}\frac{\partial\tilde{y}}{\partial\tilde{s}}}{\left(\frac{\partial\tilde{x}}{\partial\tilde{s}}\right)^2+\left(\frac{\partial\tilde{y}}{\partial\tilde{s}}\right)^2}\right]d\tilde{s} \tag{4.35}$$

$$\zeta_{21}=\left(\frac{1-i\,\mathrm{De}_2}{1-i\,\mathrm{De}}\right)\int\left[\frac{\left(1-\frac{K_T}{K_N}\right)\frac{\partial\tilde{x}}{\partial\tilde{s}}\frac{\partial\tilde{y}}{\partial\tilde{s}}}{\left(\frac{\partial\tilde{x}}{\partial\tilde{s}}\right)^2+\left(\frac{\partial\tilde{y}}{\partial\tilde{s}}\right)^2}\right]d\tilde{s} \tag{4.36}$$

$$\zeta_{22}=\left(\frac{1-i\,\mathrm{De}_2}{1-i\,\mathrm{De}}\right)\int\left[\frac{-\left(\frac{\partial\tilde{x}}{\partial\tilde{s}}\right)^2-\frac{K_T}{K_N}\left(\frac{\partial\tilde{y}}{\partial\tilde{s}}\right)^2}{\left(\frac{\partial\tilde{x}}{\partial\tilde{s}}\right)^2+\left(\frac{\partial\tilde{y}}{\partial\tilde{s}}\right)^2}\right]d\tilde{s}-\left(\frac{1-i\,\mathrm{De}_2}{1-i\,\mathrm{De}}\right)\frac{3}{2}\tilde{a}\left[\ln\left(\frac{0.18\lambda}{\tilde{p}}\right)+0.5\right] \tag{4.37}$$

$$\zeta_{23}=\left(\frac{1-i\,\mathrm{De}_2}{1-i\,\mathrm{De}}\right)\int\left[\frac{\left(\frac{K_T}{K_N}-1\right)\tilde{y}\frac{\partial\tilde{x}}{\partial\tilde{s}}\frac{\partial\tilde{y}}{\partial\tilde{s}}-\left(\left(\frac{\partial\tilde{x}}{\partial\tilde{s}}\right)^2+\frac{K_T}{K_N}\left(\frac{\partial\tilde{y}}{\partial\tilde{s}}\right)^2\right)\tilde{x}}{\left(\frac{\partial\tilde{x}}{\partial\tilde{s}}\right)^2+\left(\frac{\partial\tilde{y}}{\partial\tilde{s}}\right)^2}\right]d\tilde{s} \tag{4.38}$$

$$\zeta_{31}=\left(\frac{1-i\,\mathrm{De}_2}{1-i\,\mathrm{De}}\right)\int\left[\frac{\left(\frac{K_T}{K_N}\left(\frac{\partial\tilde{x}}{\partial\tilde{s}}\right)^2+\left(\frac{\partial\tilde{y}}{\partial\tilde{s}}\right)^2\right)\tilde{y}+\left(1-\frac{K_T}{K_N}\right)\tilde{x}\frac{\partial\tilde{x}}{\partial\tilde{s}}\frac{\partial\tilde{y}}{\partial\tilde{s}}}{\left(\frac{\partial\tilde{x}}{\partial\tilde{s}}\right)^2+\left(\frac{\partial\tilde{y}}{\partial\tilde{s}}\right)^2}\right]d\tilde{s} \tag{4.39}$$

$$\zeta_{32}=\left(\frac{1-i\,\mathrm{De}_2}{1-i\,\mathrm{De}}\right)\int\left[\frac{\left(\frac{K_T}{K_N}-1\right)\tilde{y}\frac{\partial\tilde{x}}{\partial\tilde{s}}\frac{\partial\tilde{y}}{\partial\tilde{s}}-\left(\left(\frac{\partial\tilde{x}}{\partial\tilde{s}}\right)^2+\frac{K_T}{K_N}\left(\frac{\partial\tilde{y}}{\partial\tilde{s}}\right)^2\right)\tilde{x}}{\left(\frac{\partial\tilde{x}}{\partial\tilde{s}}\right)^2+\left(\frac{\partial\tilde{y}}{\partial\tilde{s}}\right)^2}\right]d\tilde{s} \tag{4.40}$$

$$\zeta_{33}=\left(\frac{1-i\,\mathrm{De}_2}{1-i\,\mathrm{De}}\right)\int\left[\frac{2\left(\frac{K_T}{K_N}-1\right)\tilde{x}\tilde{y}\frac{\partial\tilde{x}}{\partial\tilde{s}}\frac{\partial\tilde{y}}{\partial\tilde{s}}}{\left(\frac{\partial\tilde{x}}{\partial\tilde{s}}\right)^2+\left(\frac{\partial\tilde{y}}{\partial\tilde{s}}\right)^2}\right]d\tilde{s}-\left(\frac{1-i\,\mathrm{De}_2}{1-i\,\mathrm{De}}\right)2\tilde{a}\left[\ln\left(\frac{0.18\lambda}{\tilde{p}}\right)+0.5\right]$$
$$+\left(\frac{1-i\,\mathrm{De}_2}{1-i\,\mathrm{De}}\right)\int\left[\frac{-\left(\frac{\partial\tilde{x}}{\partial\tilde{s}}\right)^2\left(\tilde{x}^2+\frac{K_T}{K_N}\tilde{y}^2\right)-\left(\frac{\partial\tilde{y}}{\partial\tilde{s}}\right)^2\left(\frac{K_T}{K_N}\tilde{x}^2+\tilde{y}^2\right)}{\left(\frac{\partial\tilde{x}}{\partial\tilde{s}}\right)^2+\left(\frac{\partial\tilde{y}}{\partial\tilde{s}}\right)^2}\right]d\tilde{s} \tag{4.41}$$

$$\xi_1=\left(\frac{1-i\,\mathrm{De}_2}{1-i\,\mathrm{De}}\right)\int\left[\frac{\left(1-\frac{K_T}{K_N}\right)\frac{\partial\tilde{x}}{\partial\tilde{s}}\frac{\partial\tilde{y}}{\partial\tilde{s}}\frac{\partial\tilde{y}}{\partial\tilde{t}}}{\left(\frac{\partial\tilde{x}}{\partial\tilde{s}}\right)^2+\left(\frac{\partial\tilde{y}}{\partial\tilde{s}}\right)^2}+\frac{\pi}{6}\tilde{p}^2\left(\tilde{D}_0+\tilde{D}_1\tilde{x}\right)\right]d\tilde{s}+2\pi\tilde{a}^3\left(\tilde{D}_0+\tilde{D}_1x\right) \tag{4.42}$$

$$\xi_2=\left(\frac{1-i\,\mathrm{De}_2}{1-i\,\mathrm{De}}\right)\int\left[\frac{-\left(\left(\frac{\partial\tilde{x}}{\partial\tilde{s}}\right)^2+\frac{K_T}{K_N}\left(\frac{\partial\tilde{y}}{\partial\tilde{s}}\right)^2\right)\frac{\partial\tilde{y}}{\partial\tilde{t}}}{\left(\frac{\partial\tilde{x}}{\partial\tilde{s}}\right)^2+\left(\frac{\partial\tilde{y}}{\partial\tilde{s}}\right)^2}\right]d\tilde{s} \tag{4.43}$$

$$\xi_3=\left(\frac{1-i\,\mathrm{De}_2}{1-i\,\mathrm{De}}\right)\int\left[\frac{\left(\frac{K_T}{K_N}-1\right)\tilde{y}\frac{\partial\tilde{x}}{\partial\tilde{s}}\frac{\partial\tilde{y}}{\partial\tilde{s}}\frac{\partial\tilde{y}}{\partial\tilde{t}}-\left(\left(\frac{\partial\tilde{x}}{\partial\tilde{s}}\right)^2+\frac{K_T}{K_N}\left(\frac{\partial\tilde{y}}{\partial\tilde{s}}\right)^2\right)\tilde{x}\frac{\partial\tilde{y}}{\partial\tilde{t}}}{\left(\frac{\partial\tilde{x}}{\partial\tilde{s}}\right)^2+\left(\frac{\partial\tilde{y}}{\partial\tilde{s}}\right)^2}\right]d\tilde{s} \tag{4.44}$$
$$-\int\left[\frac{\pi}{6}\tilde{p}^2\left(\tilde{D}_0+\tilde{D}_1\tilde{x}\right)\tilde{y}\right]d\tilde{s}$$

As numerical procedures will be used, a compromise has to be made between computational time and precision. A convergence test is carried out to determine the optimal $d\tilde{s}$ and $d\tilde{t}$ for the tolerable level of discretization error, which is chosen to be less than 0.5%. Table 4-1 shows the magnitude of the *x*-velocity in body lengths per second, for various combinations of $d\tilde{s}$ and $d\tilde{t}$, corresponding to the case of Sp = 7 in Newtonian fluid with uniform spatial distribution of the internal sliding force. The dimensionless arclength will hence be divided into 100 infinitesimal segments of length $d\tilde{s}$, and the period of each beat cycle divided into 256 temporal-steps of duration $d\tilde{t}$.

Table 4-1 - Convergence test using swimming velocity in body lengths per second, corresponding to various combinations space- and time-discretization.

$d\tilde{t}$ \ $d\tilde{s}$	$\frac{1}{20}$	$\frac{1}{50}$	$\frac{1}{100}$	$\frac{1}{200}$	$\frac{1}{500}$	$\frac{1}{1000}$
$2\pi/32$	0.5024	0.5005	0.5002	0.5002	0.5002	0.5002
$2\pi/64$	0.4970	0.4951	0.4948	0.4948	0.4948	0.4948
$2\pi/128$	0.4943	0.4924	0.4921	0.4921	0.4920	0.4920
$2\pi/256$	0.4939	0.4910	0.4907	0.4907	0.4907	0.4907
$2\pi/512$	0.4923	0.4903	0.4901	0.4900	0.4900	0.4900
$2\pi/1024$	0.4919	0.4900	0.4897	0.4896	0.4896	0.4896
$2\pi/2048$	0.4917	0.4898	0.4895	0.4895	0.4895	0.4895

The actual velocity in the inertial frame is not identical to the time-averaged value over a cycle, because the heading of the spermatozoon is constantly changing. Therefore, the study shall be extended to consider the orientation of the spermatozoon at each time-step, and the body-fixed velocity is translated motion in the inertial frame. As shown in Figure 4-4, the position vector from the origin of the inertial frame to an element point can be expressed as a sum of two vectors,

$$\mathbf{R} = \mathbf{o} + \mathbf{r} . \tag{4.45}$$

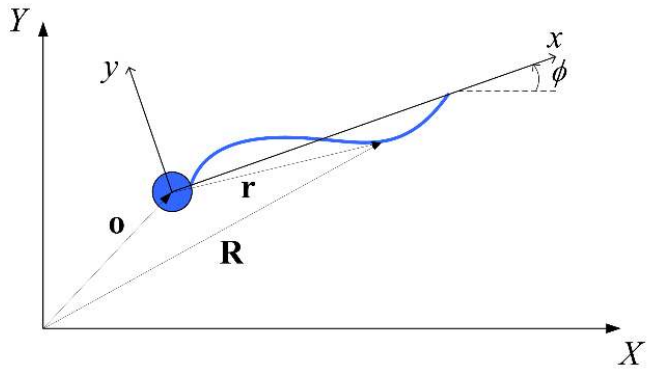

Figure 4-4 – Sperm with body-fixed frame centred at o in the inertial frame. The position vector r represents a vector in the body-fixed frame, while R represents a vector in the inertial frame.

The co-ordinates in the inertial frame can be transformed to co-ordinates in the body-fixed frame and vice versa by the following relation:

$$\begin{pmatrix} X \\ Y \end{pmatrix} = \begin{pmatrix} o_X \\ o_Y \end{pmatrix} + \begin{pmatrix} \cos\phi & -\sin\phi \\ \sin\phi & \cos\phi \end{pmatrix} \begin{pmatrix} x \\ y \end{pmatrix} \tag{4.46}$$

$$\begin{pmatrix} x \\ y \end{pmatrix} = \begin{pmatrix} \cos\phi & \sin\phi \\ -\sin\phi & \cos\phi \end{pmatrix} \begin{pmatrix} X \\ Y \end{pmatrix} - \begin{pmatrix} o_X \\ o_Y \end{pmatrix} \tag{4.47}$$

where o_X and o_Y denote the origin of the body-fixed frame, and ϕ is the angular orientation of the body-fixed-frame with respect to the inertial frame, The velocity in the inertial frame can be computed by considering the instantaneous velocity in the body-fixed frame, and then transforming the coordinates into inertial frame, followed by updating the new position and orientation for each time step *dt*.

Figure 4-5 shows the trajectory of the spermatozoon in its first two seconds of motion, corresponding to over 40 beat cycles. The Newtonian medium is represented by De = 0 while the viscoelastic medium is represented by De = 5, which corresponds to cervical mucus having a relaxation time of 0.033 s (Smith *et al*. 2009).

Figure 4-6 shows the spermatozoon trajectory for De = 0, compared against different values of Sperm number Sp and spatial variation $\tilde{k}$ of the internal force. The vertical axis corresponds to $\tilde{Y}$, and the horizontal axis corresponds to $\tilde{X}$, not labelled in the interest of space. The path taken by the spermatozoon is marked by a red line, and the flagellum has a waveform corresponding to $\tilde{y}(\tilde{s},\tilde{t}) = \tilde{h}(\tilde{s})$ since $e^{-i\tilde{t}} = 0$ when $\tilde{t}$ takes the value of 0 or multiples of 2π.

By observing how the flagellum wiggle for each case, a trend can be noticed between the beat patterns and the corresponding linear velocity. The more the flagellum is wiggled like a transverse wave, the higher the linear velocity in the *X*-direction. On the other hand, the more the flagellum moves like a stationary wave, the lower the linear velocity. This can be substantiated qualitatively, because a transverse wave 'pushes' against the fluid to propel the spermatozoon forward, whereas a stationary wave is incapable of pushing the spermatozoa in the transverse direction.

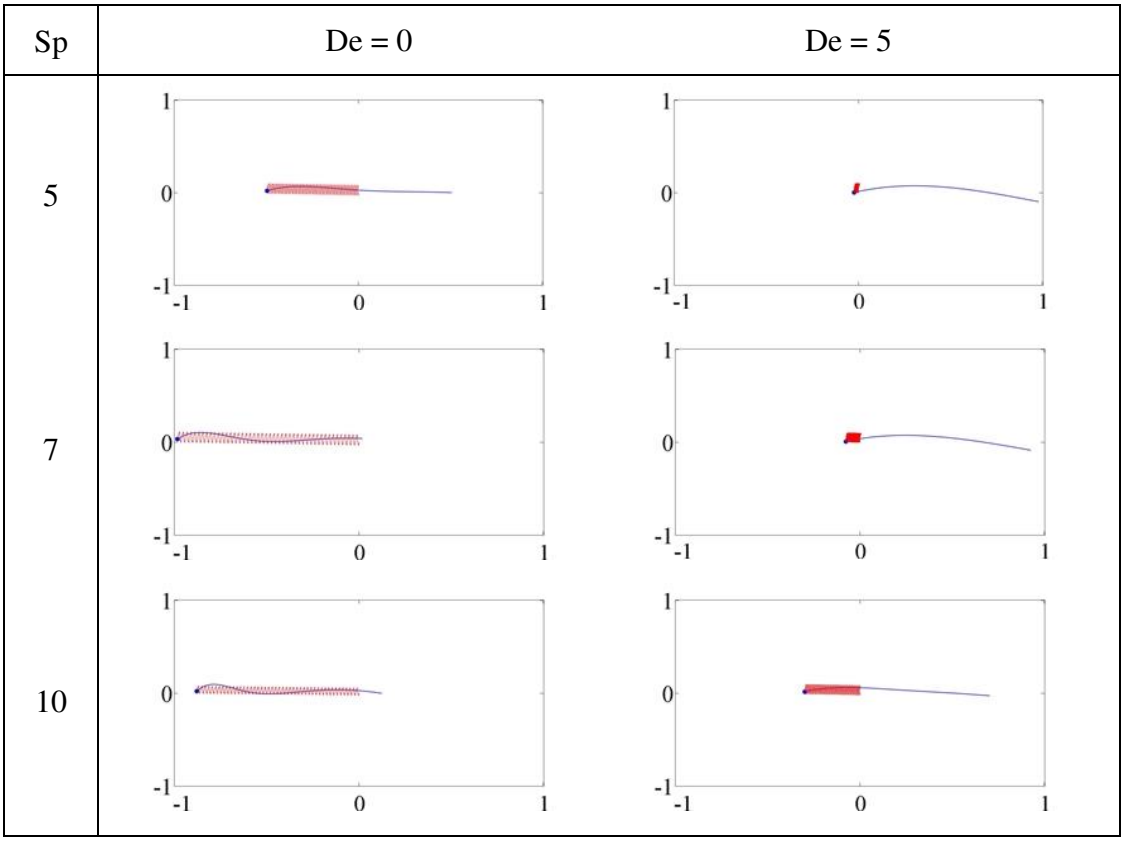

Figure 4-5 – Trajectory of spermatozoon for $\widetilde{k}$ = 0, corresponding to Sp and De. The path history is marked by the red line. The vertical axis corresponds to $\widetilde{Y}$, and the horizontal axis corresponds to $\widetilde{X}$.

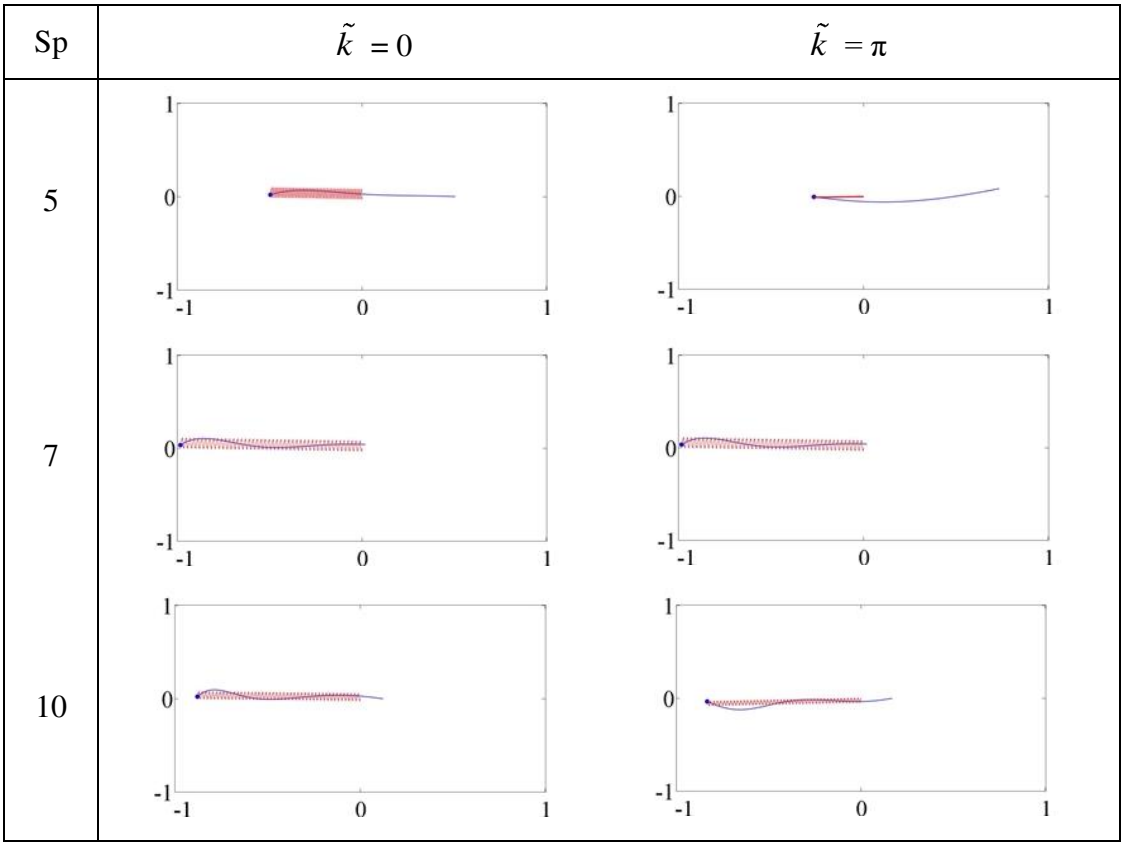

Figure 4-6 – Trajectory of spermatozoon for De = 0, corresponding to Sp and $\widetilde{k}$. The path history is marked by the red line. The vertical axis corresponds to $\widetilde{Y}$, and the horizontal axis corresponds to $\widetilde{X}$.

The results obtained shows that a sperm is able to achieve greater net motion a Newtonian fluid, and when the internal force has little variations with respect to space. The variable Sp affects the wiggling pattern, while the variable De affects the wiggling pattern as well as the hydrodynamic force, and their relation to the velocity cannot be expressed analytically. If the flagellum is too rigid, as in the case for Sp = 5, the spermatozoon will be 'flapping' its flagellum up and down in a nearly reciprocating motion, resulting in a very low net velocity. It can also be seen the sperm is highly directional in a time period greater than the flagella beat cycle, despite instantaneous fluctuations in the angular direction, which is in agreement with experimental observations (David *et al*. 1981, Katz *et al*. 1978). This substantiates the earlier analytical study in Chapter 3, where the time-averaged angular velocity as well as velocity in the *y*-direction is deemed negligible.

The straight-line velocities of the sperm computed in the inertial frame are actually similar to the time-averaged velocity in the body-fixed frame. This is because despite the continuous fluctuations in the instantaneous linear and angular velocity, the heading angle of the sperm remains close to zero. Henceforth, the straight-line velocity will be approximated using the time-averaged body-fixed velocity in the *x*-direction.

4.3 Shape of flagellum in presence of DEP

Due to the finite rigidity of the sperm flagellum, its shape will inevitably be modified in the presence of DEP force. The DEP force is a distributed force but is approximated to act on the centre of each infinitesimal segment. Having established the governing equation in (4.17), the waveform can be obtained by solving for the solution.

Figure 4-7 shows the flagellum pattern, for Sp = 7 and $\tilde{k} = \pi$, under different $\tilde{D}_0$, $\tilde{D}_1$ and De. The spatial distribution of internal sliding force, $\tilde{k}$, is taken to be because the flagellum wiggling pattern corresponding to this value appears realistic (Ishijima *et al*. 1986). In the interest of space, the *y*-axis corresponding to $\tilde{y}$ and the *x*-axis corresponding $\tilde{x}$ to are not labelled in the plots. The flagellum shape is shown to be uninfluenced by $\tilde{D}_0$, which is the constant component of the DEP force. This is to be expected, because each infinitesimal segment of the flagellum experiences the same force.

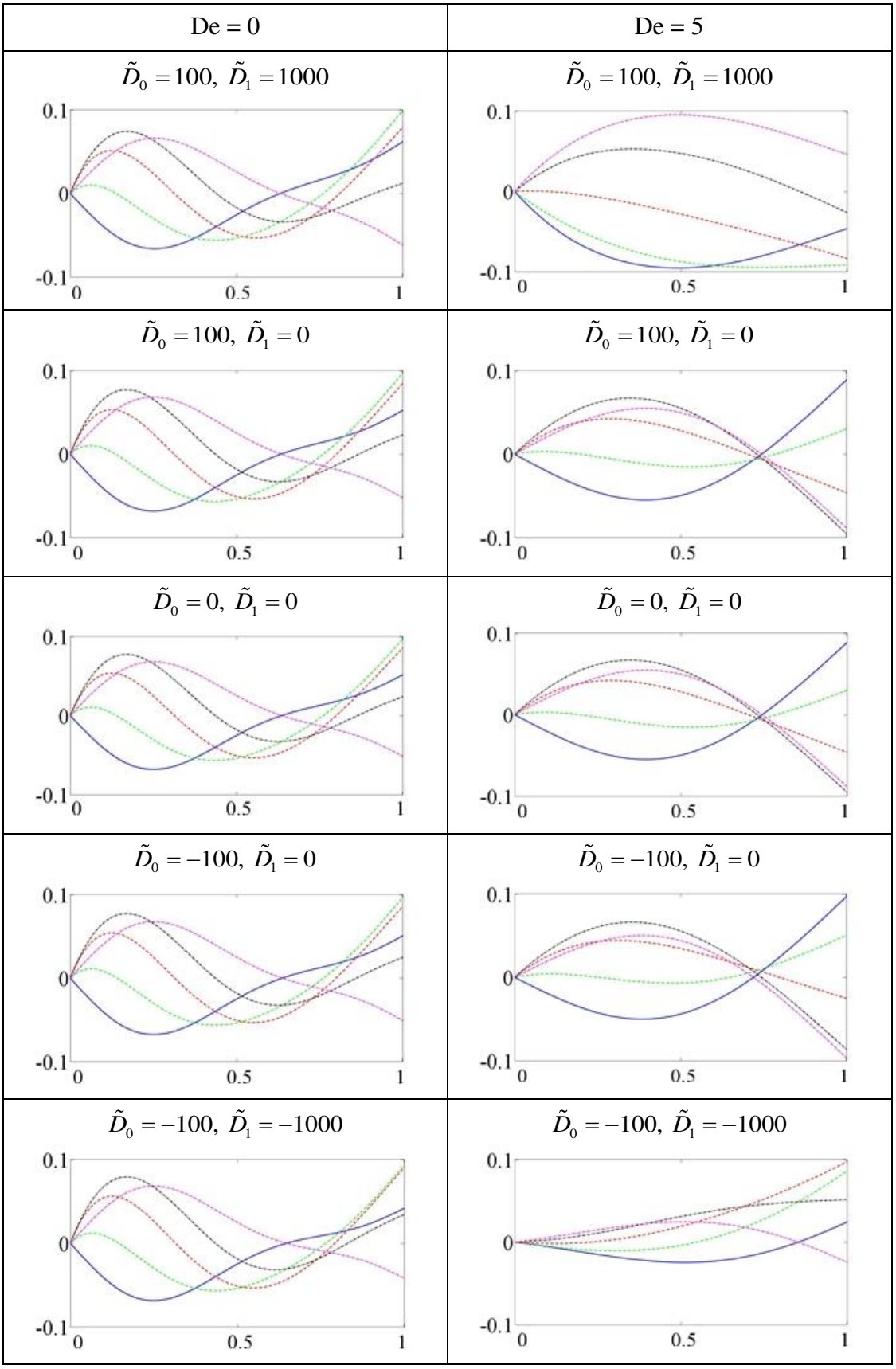

Figure 4-7 – Shape of flagellum under different DEP force, for Sp = 7 and $\tilde{k} = \pi$. The solid blue line corresponds to a dimensionless time of $\tilde{t} = 0$ while the dashed green, dashed red, dash-dotted black and dash-dotted pink lines corresponds to $\tilde{t} = \pi/4$, $\tilde{t} = \pi/2$, $\tilde{t} = 3\pi/4$ and $\tilde{t} = \pi$, respectively. The *x*-axis and *y*-axis represent the positions *x* and *y*, non-dimensionalised with respect to the flagellum wavelength.

The flagellum beating pattern in Oldroyd-B medium appears to be sensitive to DEP force, while it remains similar in a Newtonian fluid medium. This suggests that a non-uniform electric field could potentially influence the behaviour of spermatozoa in a viscoelastic fluid to a greater extent than in a Newtonian fluid, and hence it is meaningful to explore the sorting of spermatozoa in the viscoelastic fluid.

4.4 Velocity in presence of DEP

The theoretical analysis as presented in Chapter 3 have shown that the velocity of spermatozoa in a Newtonian fluid can be altered significantly by DEP, and that the extent of influence varies between the X- and Y-spermatozoa, hence allowing sorting. The study shall now be extended to explore the effect of DEP on spermatozoa with active flagellar, in Newtonian as well as viscoelastic fluid medium.

Figure 4-8 shows how the time-averaged linear velocity $< u_x >$ relates to $\tilde{D}_0$ and $\tilde{D}_1$ in a Newtonian fluid as well as viscoelastic fluid, for a range of X- and Y-spermatozoa within one standard deviation from the mean. It should be noted that different internal forces are required as adjustments have been made to keep the beating amplitude at 10%. As discussed earlier, the spermatozoa trajectory is highly directional and only the time-averaged linear velocity in the *x*-direction $< u_x >$ will be considered.

In the absence of DEP force, the velocity is significantly dependent on the flagellum wiggling pattern. However, in the presence of DEP force, the velocity is influenced primarily by the gradient of the electric field, and the flagellum pattern affects the drag force but has only a small effect on the velocity. On average, $\partial \langle u_x \rangle / \partial \tilde{D}_0 = 1.84\,\mu\text{m s}^{-1}$ and $\partial \langle u_x \rangle / \partial \tilde{D}_1 = 0.0790\,\mu\text{m s}^{-1}$ for an X-spermatozoa while $\partial \langle u_x \rangle / \partial \tilde{D}_0 = 1.88\,\mu\text{m s}^{-1}$ and for $\partial \langle u_x \rangle / \partial \tilde{D}_1 = 0.0808\,\mu\text{m s}^{-1}$ for a Y-spermatozoa in a Newtonian fluid. The results suggest that the Y-spermatozoa is more sensitive to DEP as compared to the X-spermatozoa. There exist values of $\tilde{D}_0$ and $\tilde{D}_1$ which correspond to some velocity where the X-spermatozoa is more than one standard deviation away from the Y-spermatozoa. As discussed in Chapter 3.5, this suggests the possibility of using dielectrophoresis to attain a skewed population of spermatozoa containing the desired type of sex chromosomes.

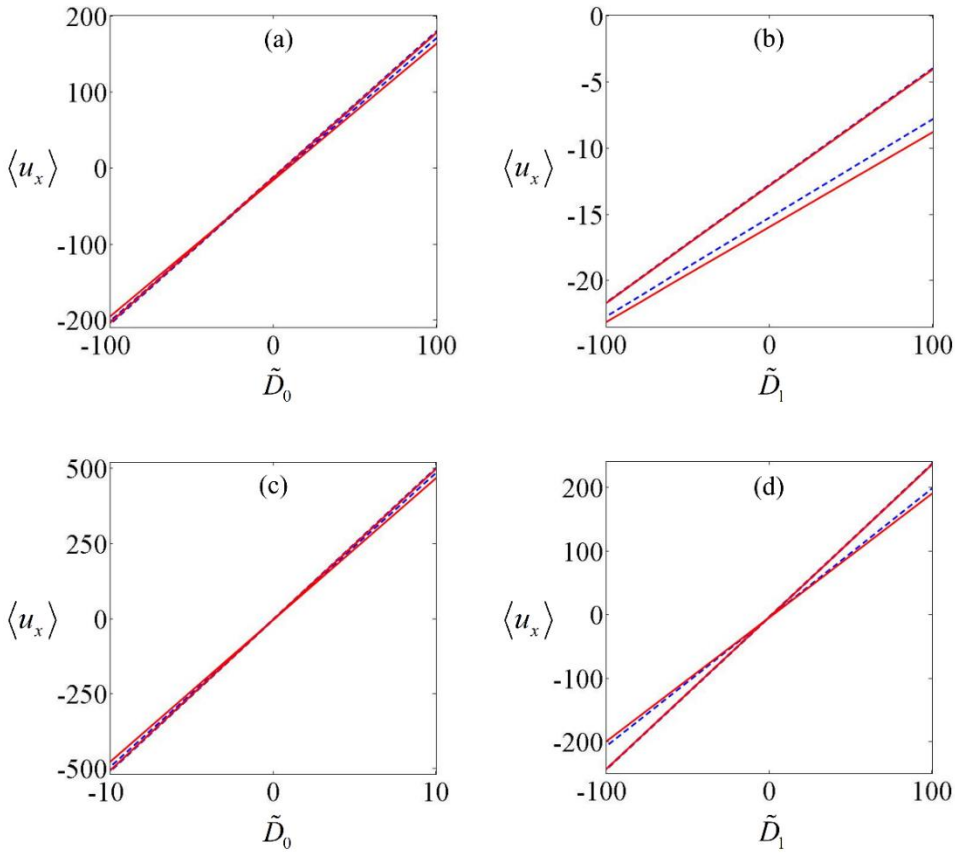

Figure 4-8 – Velocity of spermatozoa (in µm s^{-1}) one standard deviation away from the mean value, where the solid red lines and dotted blue lines denotes the X- and Y-spermatozoa, respectively. The plots on the top corresponds to a Newtonian fluid of De = 0, for (a) $\tilde{D}_1 = 0$ and (b) $\tilde{D}_0 = 0$, while the plots on bottom corresponds to a viscoelastic fluid of De = 5, for (c) $\tilde{D}_1 = 0$ and (d) $\tilde{D}_0 = 0$.

In Chapter 3 where the flagellum was assumed to follow a moving sinusoidal wave in a Newtonian fluid, $\partial \langle u_x \rangle / \partial \tilde{D}_0 = 1.43\,\mu\text{m s}^{-1}$ and $\partial \langle u_x \rangle / \partial \tilde{D}_1 = 0.0559\,\mu\text{m s}^{-1}$ for the average X-sperm, and $\partial \langle u_x \rangle / \partial \tilde{D}_0 = 1.46\,\mu\text{m s}^{-1}$ and $\partial \langle u_x \rangle / \partial \tilde{D}_1 = 0.0570\,\mu\text{m s}^{-1}$ for the average Y-sperm (Koh and Marcos 2014). Therefore, it can be seen that the effect of dielectrophoresis on the velocity of spermatozoa in a Newtonian fluid are qualitatively consistent in these two studies. In Chapter 4, the effect of dielectrophoresis is slightly enhanced compared to results obtained in Chapter 3, likely because the beating pattern of the flagellum is a 'pulsating' moving wave rather than a moving sinusoidal wave, and hence less dragged is experienced.

In an Oldroyd-B fluid, $\partial \langle u_x \rangle / \partial \tilde{D}_0 = 48.5\,\mu\text{m s}^{-1}$ and $\partial \langle u_x \rangle / \partial \tilde{D}_1 = 2.15\,\mu\text{m s}^{-1}$ for an X-sperm while $\partial \langle u_x \rangle / \partial \tilde{D}_0 = 49.6\,\mu\text{m s}^{-1}$ and $\partial \langle u_x \rangle / \partial \tilde{D}_1 = 2.20\,\mu\text{m s}^{-1}$ for a Y-sperm with mean parameters. Since each unit change in $\tilde{D}_0$ and $\tilde{D}_1$ results in a

substantially larger change in swimming velocity of the spermatozoon, the difference in velocity distribution is also amplified, suggesting that sorting in a viscoelastic fluid could be more effective than in a Newtonian fluid. From a mathematical perspective, the hydrodynamic force in an Oldroyd-B fluid influences the force balance and hence alters the partial differential equation governing the flagellum waveform, resulting in a different velocity. From a physical perspective, this may be attributed (Koh and Marcos 2015b) to the 'memory effect' of the Oldroyd-B fluid. In the reference frame of a spermatozoon swimming from right to left, the fluid particles are moving from left to right. Since each infinitesimal segment of the fluid attempts to undo the deformation, the fluid will have the tendency to revert back to the position where they started, and in this process carrying the spermatozoon along, thereby increasing its velocity along its heading direction.

4.5 Chapter Summary

In this chapter, the flagellum was modelled with an internal sliding force, and the beating pattern was determined by solving the 4th order differential equation derived from force and moment balance. The velocity in the body-fixed frame and inertia frame is then computed, and it is shown that the straight-line velocity resembles the time-averaged velocity in the x-direction of the body-frame. The effect of dielectrophoresis on a sperm in a Newtonian fluid is compared with that in a viscoelastic Oldroyd-B medium. DEP alters the sperm velocity substantially more in an Oldroyd-B medium, allowing the X- and Y-sperm to be sorted under a weaker electric field gradient. The results obtained for the Newtonian case are in agreement with the moving sinusoidal waveform model of the preceding chapter.

Chapter 5
Slender Body Theory for Sperm Locomotion

Progressing from Resistive Force Theory, this chapter utilises Slender Body Theory which incorporates hydrodynamic interactions and has superior accuracy (Huber *et al*. 2011, Koh *et al*. 2016) over the former. First, the mathematical framework associated with SBT will be presented. The differences between RFT and SBT will be explored by considering a simple horizontal filament, followed by a segmented flagellum to provide a fair basis for comparison. SBT will then be applied to model a sperm swimming with a prescribed beating pattern. The hydrodynamic force distribution on the flagellum will be shown to remain similar regardless of whether RFT or SBT is used. Numerical methods will be used to compute the flagellum waveform resulting from the associated force. This chapter is concluded by the rational for using a prescribed flagellum waveform in the subsequent analysis on the feasibility of sorting to be carried out within the scope of this thesis.

5.1 Mathematical model

In Slender Body Theory (Higdon 1979), the flagellum is represented by a series of Stokeslets and dipoles. By the no-slip boundary condition, fluid particles adjacent to the flagellum surface of a swimmer attains the same velocity as the flagellum. This fluid velocity can also be attained if the flagellum had been replaced with a series of concentrated force along the flagellum centreline. SBT actually relates the force acting on the fluid to the velocity of the fluid, but the same force-velocity relation can be applied to study the force acting on the flagellum. Consider a rod translating towards the left, which could be achieved using an external field given that inertia is negligible in a low Reynolds number environment. This translating rod exerts a leftward force on the fluid. By Newton's third law, the fluid exerts a rightward force of equal magnitude on the rod, which can be interpreted as the drag force. Moreover, in the reference frame of the rod, the fluid appears to have a velocity towards the right. Therefore, the same coefficients in SBT can be applied to relate the force acting on the body to the relative fluid velocity.

The flagellum is assumed to have a small curvature and is divided into N segments of length $2q$ each, where $p \ll q < \Lambda$. Each segment has a local coordinate system $\left(X^L, Y^L\right)$ whose origin is at the centre of the section of length $2q$, with the X^L axis tangential to the flagellum centreline. Within each interval from $(-q,0)$ to $(+q,0)$ the force per unit length $\mathbf{f}^L$ is assumed to be constant. The location of the origin of each segment has a curvilinear coordinate s_n measured from the point of contact between the spherical head and the flagellum, such that a point in the local frame is

$$x_j^L = \theta_{jk}(s_n)\left[x_k - X_k(s_n)\right], \tag{5.1}$$

where the transformation matrix that maps general coordinates into local coordinates is

$$\boldsymbol{\Theta} = \begin{bmatrix} \cos\theta & \sin\theta \\ -\sin\theta & \cos\theta \end{bmatrix}. \tag{5.2}$$

such that θ is the angle of the local X^L axis of the segment with respect to the general x-axis of the body-fixed frame (Figure 5-1).

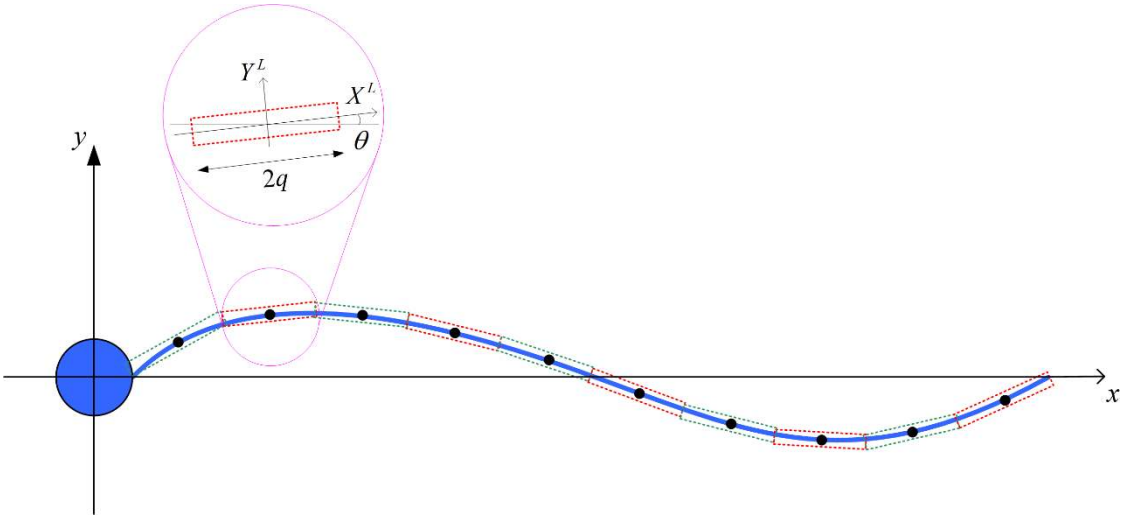

Figure 5-1 – Flagellum comprising N discrete straight segments, each represented by a dotted rectangle. Inset: The local coordinate system X^L and Y^L of a segment at an angle θ with respect to the general x-axis of the body-fixed frame.

The induced velocity at point $\mathbf{x}$ due to the collective Stokeslets and dipoles in the interval is given by Higdon (1979):

$$u_j^L\left(\mathbf{x}^L\right) = f_k^L\left[K_{jk}^L\left(\mathbf{x}^L - \mathbf{X}^L\right)\right]\Big|_{\mathbf{X}^L=(-q,0)}^{\mathbf{X}^L=(q,0)}, \tag{5.3}$$

where

$$K_{11}^{L}=\frac{1}{8\pi\mu}\left\{2\ln\left[r-\left(x-X\right)\right]+\frac{x-X}{r}\right\}, \tag{5.4}$$

$$K_{12}^{L}=\frac{1}{8\pi\mu}\left\{\frac{y-Y}{r}-\frac{p^{2}}{2}\frac{y-Y}{r^{3}}\right\}, \tag{5.5}$$

$$K_{21}^{L}=\frac{1}{8\pi\mu}\left\{\frac{y-Y}{r}\right\}, \tag{5.6}$$

$$K_{22}^{L}=\frac{1}{8\pi\mu}\left\{\ln\left[r-\left(x-X\right)\right]-\frac{x-X}{r}-\frac{p^{2}}{2\left(y-Y\right)^{2}}\left[\frac{\left(x-X\right)^{3}}{r^{3}}-\frac{2\left(x-X\right)}{r}\right]\right\}, \tag{5.7}$$

with all variables in local coordinates. It is necessary to make a conversion from the local coordinate system for each segment, where the force-velocity relation is governed by equation (5.3), to the general coordinates in the body frame. The velocity induced at point **x** due to the singularities in the n^{th} segment is

$$u_{j}\left(\mathbf{x}\right)=K_{jk}\left(\mathbf{x},\mathbf{X}(s_{n})\right)f_{k}(s_{n}), \tag{5.8}$$

where

$$K_{jk}\left(\mathbf{x},\mathbf{X}(s_{n})\right)=\Theta_{ij}(s_{n})\Theta_{lk}(s_{n})\left[K_{il}^{L}\left(\mathbf{x}^{L}-\mathbf{X}^{L}\right)\right]\Big|_{\mathbf{X}^{L}=(-q,0)}^{\mathbf{X}^{L}=(q,0)}. \tag{5.9}$$

Before proceeding further, readers should be cautious to note that K_{jk}^{L} represents a definite integral in the body-fixed frame. In vector form, equation (5.9) is

$$\left[\mathbf{K}\right]=\left[\mathbf{\Theta}\right]^{T}\left[\mathbf{K}^{L}\right]\Big|_{(-q,0)}^{(q,0)}\left[\mathbf{\Theta}\right]. \tag{5.10}$$

When the point of interest corresponds to the same segment as the location of the Stokeslets and dipole, equations (5.4) and (5.7) will result in taking the logarithm of zero, given that $r = (x - X)$ at the limits of integration. To circumvent this, equation (5.3) can replaced by the following with an accuracy to the order p^{2}/q^{2} (Higdon 1979):

$$\boldsymbol{u}^{L}=\begin{bmatrix}f_{x}^{L}\left(\ln\left(2q/p\right)-0.5\right)/2\pi\mu\\ f_{y}^{L}\left(\ln\left(2q/p\right)+0.5\right)/4\pi\mu\end{bmatrix}. \tag{5.11}$$

Using the above equation for an expression in terms of K_{jk}^{L}, the following relation is used in place of equations (5.4) to (5.7), in order to determine the contribution from singularities at the same segment as the point of interest.

$$\begin{bmatrix} K_{11}^{L} & K_{12}^{L} \\ K_{21}^{L} & K_{22}^{L} \end{bmatrix}\Bigg|_{\mathbf{X}^{L}=(-q,0)}^{\mathbf{X}^{L}=(q,0)} = \begin{bmatrix} \left(\ln\left(2q/p\right)-0.5\right)/2\pi\mu & 0 \\ 0 & \left(\ln\left(2q/p\right)+0.5\right)/4\pi\mu \end{bmatrix}. \quad (5.12)$$

The induced velocity at each segment is a result of hydrodynamic interactions from all *N* segments of the flagellum, which expressed in indicial notation is

$$u_j\left(\mathbf{x}\right) = \sum_{n=1}^{N}\left\{K_{jk}\left(\mathbf{x},\mathbf{X}(s_n)\right) f_k\left(s_n\right)\right\}. \quad (5.13)$$

Hydrodynamic interactions between the flagellum and cell body have an insignificant influence (Guasto *et al*. 2012, Chattopadhyay and Wu 2009) and hence will be ignored in this model. In vector form, the above equation allows the induced velocity at segment *n* to be computed as follows:

$$\begin{bmatrix} u_x^{(n)} \\ u_y^{(n)} \end{bmatrix} = \begin{bmatrix} K_{11}^{(n,1)} & K_{12}^{(n,1)} \\ K_{21}^{(n,1)} & K_{22}^{(n,1)} \end{bmatrix}\begin{bmatrix} f_x^{(1)} \\ f_y^{(1)} \end{bmatrix} + \begin{bmatrix} K_{11}^{(n,2)} & K_{12}^{(n,2)} \\ K_{21}^{(n,2)} & K_{22}^{(n,2)} \end{bmatrix}\begin{bmatrix} f_x^{(2)} \\ f_y^{(2)} \end{bmatrix} + \cdots + \begin{bmatrix} K_{11}^{(n,N)} & K_{12}^{(n,N)} \\ K_{21}^{(n,N)} & K_{22}^{(n,N)} \end{bmatrix}\begin{bmatrix} f_x^{(N)} \\ f_y^{(N)} \end{bmatrix}. \quad (5.14)$$

where the superscript in $K_{ij}^{(n,m)}$ indicates the contribution by the Stokeslets and dipoles at segment *m* toward the induced velocity at segment *n*. The induced velocity due to all Stokeslets and dipoles across the entire flagellum is therefore

$$\begin{bmatrix} u_x^{(1)} \\ u_y^{(1)} \\ u_x^{(2)} \\ u_y^{(2)} \\ \vdots \\ \vdots \\ u_x^{(N)} \\ u_y^{(N)} \end{bmatrix} = \begin{bmatrix} \begin{bmatrix} K_{11}^{(1,1)} & K_{12}^{(1,1)} \\ K_{21}^{(1,1)} & K_{22}^{(1,1)} \end{bmatrix} & \begin{bmatrix} K_{11}^{(1,2)} & K_{12}^{(1,2)} \\ K_{21}^{(1,2)} & K_{22}^{(1,2)} \end{bmatrix} & \cdots & \cdots & \begin{bmatrix} K_{11}^{(1,N)} & K_{12}^{(1,N)} \\ K_{21}^{(1,N)} & K_{22}^{(1,N)} \end{bmatrix} \\ \begin{bmatrix} K_{11}^{(2,1)} & K_{12}^{(2,1)} \\ K_{21}^{(2,1)} & K_{22}^{(2,1)} \end{bmatrix} & \begin{bmatrix} K_{11}^{(2,2)} & K_{12}^{(2,2)} \\ K_{21}^{(2,2)} & K_{22}^{(2,2)} \end{bmatrix} & & & \\ \vdots & & \ddots & & \\ \vdots & & & \ddots & \\ \begin{bmatrix} K_{11}^{(N,1)} & K_{12}^{(N,1)} \\ K_{21}^{(N,1)} & K_{22}^{(N,1)} \end{bmatrix} & & & & \begin{bmatrix} K_{11}^{(N,N)} & K_{12}^{(N,N)} \\ K_{21}^{(N,N)} & K_{22}^{(N,N)} \end{bmatrix} \end{bmatrix} \begin{bmatrix} f_x^{(1)} \\ f_y^{(1)} \\ f_x^{(2)} \\ f_y^{(2)} \\ \vdots \\ \vdots \\ f_x^{(N)} \\ f_y^{(N)} \end{bmatrix}. \quad (5.15)$$

By simple algebraic manipulation, the force per unit length acting on each segment of the flagellum is

$$\begin{bmatrix} f_x^{(1)} \\ f_y^{(1)} \\ f_x^{(2)} \\ f_y^{(2)} \\ \vdots \\ \vdots \\ f_x^{(N)} \\ f_y^{(N)} \end{bmatrix} = \begin{bmatrix} \begin{bmatrix} K_{11}^{(1,1)} & K_{12}^{(1,1)} \\ K_{21}^{(1,1)} & K_{22}^{(1,1)} \end{bmatrix} & \begin{bmatrix} K_{11}^{(1,2)} & K_{12}^{(1,2)} \\ K_{21}^{(1,2)} & K_{22}^{(1,2)} \end{bmatrix} & \cdots & \cdots & \begin{bmatrix} K_{11}^{(1,N)} & K_{12}^{(1,N)} \\ K_{21}^{(1,N)} & K_{22}^{(1,N)} \end{bmatrix} \\ \begin{bmatrix} K_{11}^{(2,1)} & K_{12}^{(2,1)} \\ K_{21}^{(2,1)} & K_{22}^{(2,1)} \end{bmatrix} & \begin{bmatrix} K_{11}^{(2,2)} & K_{12}^{(2,2)} \\ K_{21}^{(2,2)} & K_{22}^{(2,2)} \end{bmatrix} & & & \\ \vdots & & \ddots & & \\ \vdots & & & \ddots & \\ \begin{bmatrix} K_{11}^{(N,1)} & K_{12}^{(N,1)} \\ K_{21}^{(N,1)} & K_{22}^{(N,1)} \end{bmatrix} & & & & \begin{bmatrix} K_{11}^{(N,N)} & K_{12}^{(N,N)} \\ K_{21}^{(N,N)} & K_{22}^{(N,N)} \end{bmatrix} \end{bmatrix}^{-1} \begin{bmatrix} u_x^{(1)} \\ u_y^{(1)} \\ u_x^{(2)} \\ u_y^{(2)} \\ \vdots \\ \vdots \\ u_x^{(N)} \\ u_y^{(N)} \end{bmatrix}. \tag{5.16}$$

where $u_x^{(n)}$ and $u_y^{(n)}$ are the relative fluid velocity with respect to the flagellum segment *n*. This velocity is dependent on the swimming velocity $\mathbf{v}_{swim} = u_x \mathbf{e}_x + u_y \mathbf{e}_y$ of the sperm, its angular velocity $\dot{\phi}\mathbf{e}_z$ as well as the wiggling of the flagellum:

$$\begin{bmatrix} u_x^{(n)} \\ u_y^{(n)} \end{bmatrix} = -\left(u_x \mathbf{e}_x + u_y \mathbf{e}_y + \dot{\phi}\mathbf{e}_z \times \mathbf{r}^{(n)} \right) - \frac{d\mathbf{r}^{(n)}}{dt}. \tag{5.17}$$

Thereafter, the total force and moment acting on the sperm can be computed by adding the drag force experienced by the head to the sum of forces acting on all the segment of length Λ/N each:

$$F_x = \sum_{n=1}^{N} \left(f_x^{(n)} \frac{\Lambda}{N} \right) + F_x^{head}, \tag{5.18}$$

$$F_y = \sum_{n=1}^{N} \left(f_y^{(n)} \frac{\Lambda}{N} \right) + F_y^{head}, \tag{5.19}$$

$$M_z = \int_0^1 \mathbf{r} \times \mathbf{dF} + M_z^{head} = \sum_{n=1}^{N} \left[\left(x^{(n)} f_y^{(n)} - y^{(n)} f_x^{(n)} \right) \frac{\Lambda}{N} \right] + M_z^{head}. \tag{5.20}$$

where $x^{(n)}$ and $y^{(n)}$ are the coordinates of the midpoint of segment *n* in the body-fixed frame. The force per unit length and the moment can be non-dimensionalised as follows

$$\tilde{\mathbf{f}} = \frac{\mathbf{f}}{(8\pi\mu)\Lambda\omega_{wave}}, \quad \tilde{\mathbf{M}} = \frac{\mathbf{M}}{(8\pi\mu)\Lambda^3\omega_{wave}}, \tag{5.21}$$

while the coefficients relating force to velocity can be non-dimensionalised by

$$\tilde{\mathbf{K}} = (8\pi\mu)\mathbf{K}. \tag{5.22}$$

Given that the total force and moment are linear functions of the sperm's linear and angular velocity,

$$\begin{bmatrix} \tilde{F}_x \\ \tilde{F}_y \\ \tilde{M}_z \end{bmatrix} = \begin{bmatrix} \zeta_{11} & \zeta_{12} & \zeta_{13} \\ \zeta_{21} & \zeta_{22} & \zeta_{23} \\ \zeta_{31} & \zeta_{32} & \zeta_{33} \end{bmatrix} \begin{bmatrix} \tilde{u}_x \\ \tilde{u}_y \\ \tilde{\dot{\phi}} \end{bmatrix} + \begin{bmatrix} \xi_1 \\ \xi_2 \\ \xi_3 \end{bmatrix}. \tag{5.23}$$

Since inertial is negligible relative to viscous forces, the total force and moment acting on the sperm is negligible. Therefore, the instantaneous linear and angular velocity can be calculated using

$$\begin{bmatrix} \tilde{u}_x \\ \tilde{u}_y \\ \tilde{\dot{\phi}} \end{bmatrix} = \begin{bmatrix} \zeta_{11} & \zeta_{12} & \zeta_{13} \\ \zeta_{21} & \zeta_{22} & \zeta_{23} \\ \zeta_{31} & \zeta_{32} & \zeta_{33} \end{bmatrix}^{-1} \begin{bmatrix} -\xi_1 \\ -\xi_2 \\ -\xi_3 \end{bmatrix}. \tag{5.24}$$

5.2 Difference between RFT and SBT

In the preceding section, the procedures for applying SBT had been presented. Before using SBT to compute the hydrodynamic force in the model, the differences in results predicted by SBT and RFT shall be explored in a rudimentary model – a horizontal rod.

Both RFT and SBT stem from the use of Stokeslets and dipoles to model the induced velocity of a swimmer, and require the body to be slender. However, there are subtle differences within the derivation process, thereby resulting in two different models. To begin with the similarity, consider the flagellum of a swimming cell. By the no-slip boundary condition, the fluid particles immediately adjacent to the flagellum must necessarily have the same velocity as that of the local flagellum surface. The velocity of these fluid particles, which are induced by the moving flagellum, can also be achieved had the flagellum been replaced by a series of Stokeslets along its centreline. In turn, the body of a swimmer experiences a viscous force related to the relative fluid velocity, which can be computed using SBT as discussed in the previous section.

In SBT, the force per unit length acting on the flagellum is uniform across each discretized segment and follows a step function which is piecewise constant but changes abruptly across each segment, although hydrodynamic interactions from all segments of the flagellum are taken into account. On the other hand, RFT ignores interactions and gives a localised force-velocity relation. As seen in equation (A.37) and (A.43) of Appendix A, RFT computes the velocity at a point on the flagellum surface using only Stokeslets within a distance of $\pm q$ away, where q is small relative to the flagellum length and taken to be 0.09Λ (Lighthill 1976), while Stokeslets further away beyond the distance of q are ignored and assumed to have zero contribution.

Straightforward algebra allows for the force per unit length at a point on the flagellum surface to be related to the local velocity. Instead of taking this value to be constant within $\pm q$, the force at any other point is computed by the same virtue, thus giving a localised force-velocity relation in RFT. A subtle difference to be mindful of is that in SBT, the length of each of the N segments over which the force per unit length is modelled to be constant is $2q$, where $q = \Lambda/2N$ instead of 0.09Λ. Another difference between SBT and RFT is the scope of the model. As seen in equation (5.3), the fluid velocity at an arbitrary point away from the flagellum can be computed by SBT, allowing us to determine the flow field, while the use of RFT limits us to study only the points on the flagellum surface.

Consider a rigid horizontal rod 50 μm in length, subjected to a relative velocity at an angle β with respect to its longitudinal axis (Figure 5-2). Given that the rod has no rotational motion, the relative fluid velocity at all points on the rod is identical. The coefficient relating the force, in the x- and y-direction, to the viscosity and magnitude of the relative fluid velocity is computed as presented in the following two tables below. Given that the unit tangential and normal vectors are aligned with the x- and y-axis respectively, the coefficients correspond to K_T/μ and K_N/μ.

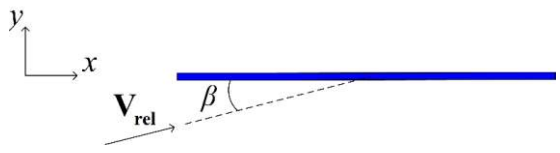

Figure 5-2 – Passive horizontal cylindrical rod subjected to a relative fluid velocity of magnitude V_{rel} at an angle β with respect to the x-axis.

In RFT, these coefficients are solely dependent on the ratio between the length and radius of the body. Since the coefficients are uniform across the entire rod, the force per unit length are constant as well. In SBT, the force per unit length is influenced by interactions and hence varies across different segments of the rod. However, by taking the sum of forces acting on the body as a whole, an equivalent coefficient can be computed from the SBT model. It cannot be used in a similar fashion to K_T and K_N in RFT, where the local force can be found once the relative local velocity at that point is known. However, this equivalent coefficient can be used to give a simple linear relation between the overall force acting on the entire rod and the relative fluid velocity, which is constant at all points on the horizontal rod. The coefficients presented in Table 5-1 and Table 5-2, which gives the relation in the *x*- and *y*-direction respectively, provides a convenient basis for comparison between RFT and SBT.

Table 5-1 – Force per unit length in the *x*-direction, normalised with viscosity μ and relative fluid velocity at angles of between 0 and 0.25π rad, computed using RFT or SBT of varying number of discretized segments.

$\frac{f_x}{\mu V_{rel}}$	$\beta = 0$	$\beta = \frac{10\pi}{180}$	$\beta = \frac{20\pi}{180}$	$\beta = \frac{30\pi}{180}$	$\beta = \frac{45\pi}{180}$
RFT	1.753	1.727	1.648	1.519	1.240
SBT (N = 1)	1.310	1.290	1.231	1.134	0.926
SBT (N = 3)	1.367	1.346	1.285	1.184	0.967
SBT (N = 5)	1.384	1.363	1.300	1.198	0.978
SBT (N = 7)	1.392	1.371	1.308	1.206	0.985
SBT (N = 10)	1.401	1.379	1.316	1.213	0.990
SBT (N = 15)	1.409	1.388	1.324	1.220	0.997
SBT (N = 20)	1.416	1.395	1.331	1.226	1.001
SBT (N = 30)	1.429	1.407	1.343	1.238	1.011

The computed values of $f_x/(\mu V_{rel})$ and $f_y/(\mu V_{rel})$ gives a prediction on the force acting on the rod per unit relative fluid velocity. It is not surprising that as the angle β increases, the tangential force acting on the rod decreases while the normal force increases, following the change in the tangential and normal relative fluid velocity. When $\beta = \pi/4$, the tangential and normal relative velocity are equal in magnitude, while f_y is greater than f_x due to drag anisotropy. Therefore, there is a clear agreement in the trend predicted by RFT and SBT.

Table 5-2 – Force per unit length in the *y*-direction, normalised with viscosity μ and relative fluid velocity at angles of between 0 and 0.25π rad, computed using RFT or SBT of varying number of discretized segments.

$\frac{f_y}{\mu V_{rel}}$	$\beta = 0$	$\beta = \frac{10\pi}{180}$	$\beta = \frac{20\pi}{180}$	$\beta = \frac{30\pi}{180}$	$\beta = \frac{45\pi}{180}$
RFT	0	0.534	1.053	1.539	2.176
SBT ($N = 1$)	0	0.376	0.741	1.084	1.533
SBT ($N = 3$)	0	0.390	0.768	1.122	1.587
SBT ($N = 5$)	0	0.393	0.775	1.133	1.602
SBT ($N = 7$)	0	0.395	0.778	1.138	1.609
SBT ($N = 10$)	0	0.396	0.781	1.141	1.614
SBT ($N = 15$)	0	0.397	0.783	1.144	1.618
SBT ($N = 20$)	0	0.398	0.783	1.145	1.619
SBT ($N = 30$)	0	0.397	0.782	1.143	1.617

It can be seen that regardless of the number of segments which the flagellum is discretized into, the SBT model predicts that for a given fluid viscosity and relative velocity, the tangential as well as normal force is over 20% smaller than that predicted by RFT. Such a difference is glaring and deserves further attention. However, before making any hasty conclusions, it will be beneficial to recall that the net hydrodynamic force acting on a free swimmer is zero in low Reynolds number. Qualitatively, a larger force per unit length per unit velocity will result in not just greater drag but also greater propulsion. In order to understand the extent to which the swimming velocity computed by RFT and SBT differs, there are two issues that should be looked into. The first is to understand the source of deviation between SBT and RFT mathematically, so as to supplement the qualitative discussions made at the beginning of this section regarding the difference in assumptions of the two models. The second is to determine the relation between the predicted velocities and the resistive coefficients.

To start off, it is interesting to note that even in the limit of $N = 1$, in which there are no interactions taken into account for both models, the deviation in results does not diminish. Despite the qualitative similarities in this scenario, SBT and RFT do not use the same relation for q, and consequently this affects the length $2q$ of the interval over which the strength of each Stokeslets are assumed to be uniform. When considering the entire flagellum as a single segment in SBT, such that $N = 1$, q takes the value 0.5Λ, whereas in RFT, q takes a constant value of 0.09Λ.

It might then appear that when N is adjusted until q is approximately 0.09Λ, the coefficients relating force and velocity would be similar. However, this will not happen, because when N is greater than one, interactions in the SBT model would make the force-velocity relation different from RFT. Even if the effects of interactions were to be ignored, the diagonal entries of the resistance matrix will be consistent between RFT and SBT if and only if $f_{x,RFT} = f_{x,SBT}^{(n,n)}$ and $f_{y,RFT} = f_{y,SBT}^{(n,n)}$. To satisfy the equation along the x-direction, the denominator of K_T in equation (2.3) has to be equal to the denominator of K_{11}^L in equation (5.12) and are to be equivalent, that is

$$\ln\left[\frac{2(0.09\Lambda)}{p}\right] = \ln\left[\frac{2(\Lambda/2N)}{p}\right] - 0.5, \tag{5.25}$$

To satisfy the equation along the y-direction, the denominator of K_N in equation (2.2) has to be equal to the denominator of K_{22}^L in equation (5.12), that is

$$\ln\left[\frac{2(0.09\Lambda)}{p}\right] = \ln\left[\frac{2(\Lambda/2N)}{p}\right], \tag{5.26}$$

N takes the value of 3.37 in equation (5.25), but has to take the value 5.56 to satisfy equation (5.26). This indicates that there is no solution to satisfy $\mathbf{f}_{RFT} = \mathbf{f}_{SBT}$, regardless of whether interactions are considered. In the x-direction, the difference between the local resistance coefficient in the two theories is

$$\varepsilon = \frac{f_{x,RFT} - f_{x,SBT}^{(n,n)}}{f_{x,SBT}^{(n,n)}} = \left[\frac{\ln(2q_{SB}/p) - 0.5}{\ln(2q_{RF}/p)} - 1\right]. \tag{5.27}$$

The ratio between the two forces, and consequently the error, depends on the flagellum radius as well as the choice of number of discrete segments used in the SBT model.

$$\frac{f_{x,RFT}}{f_{x,SBT}^{(n,n)}} = \frac{\ln(1/\tilde{p}) - \ln N - 0.5}{\ln(1/\tilde{p}) + \ln(0.18)}. \tag{5.28}$$

If the above ratio is to converge regardless of the choice of N, both the following equations has to be satisfied:

$$\ln(1/\tilde{p}) \gg \ln N + 0.5, \tag{5.29}$$

$$\ln(1/\tilde{p}) \gg \ln(0.18). \tag{5.30}$$

To satisfy equations (5.29) and (5.30) by at least an order of magnitude, with N being in the order of 10, $\tilde{p}$ needs to be as small as 10^{-10}. For a typical sperm flagellum of length 50 μm, it would imply that the flagellum radius has to be smaller than 1 Å, which is unphysical and hence equation (5.28) can never approach unity. Therefore, the choice of N has two implications; it influences the number of discrete segments and hence the extent of interactions in SBT, as well as the local resistance coefficient even before interactions are taken into account.

Recall that the objective of this section is to explore the source of deviation between SBT and RFT, as well as the degree of agreement between the swimming velocities predicted by the two models. Now, it would be beneficial to take a step back and recall that the non-dimensionalised swimming velocity is a function of the ratio K_N/K_T rather than the absolute value of either coefficients. Moreover, the characteristic velocity is the product of the flagellum length and beat frequency. The next logical step will hence be to look into how K_N/K_T differs for RFT and SBT with different choice of the number of discrete segments N (Table 5-3).

Table 5-3 – Resistive coefficients K_N and K_T and their ratios, where the superscript RFT and SBT denote values computed using RFT and SBT models, respectively, for different number of discrete segments N.

N	K_N^{SBT}	K_T^{SBT}	$\left(\frac{K_N^{SBT}}{K_T^{SBT}}\right)$	$\frac{K_N^{RFT}-K_N^{SBT}}{K_N^{SBT}}$	$\frac{K_T^{RFT}-K_T^{SBT}}{K_T^{SBT}}$	$\left(\frac{K_N^{RFT}}{K_T^{RFT}}\right)\Big/\left(\frac{K_N^{SBT}}{K_T^{SBT}}\right)$
1	2.167μ	1.310μ	1.65	42%	34%	1.06
3	2.245μ	1.367μ	1.64	37%	28%	1.07
5	2.265μ	1.384μ	1.64	36%	27%	1.08
7	2.275μ	1.392μ	1.63	35%	26%	1.08
10	2.283μ	1.401μ	1.63	35%	25%	1.08
15	2.288μ	1.409μ	1.62	34%	24%	1.08
20	2.289μ	1.416μ	1.62	34%	24%	1.09
30	2.286μ	1.429μ	1.60	35%	23%	1.10

The rightmost column of the preceeding table shows that the ratio between the normal and tangential resistive coefficient are similar for both models. This suggests that the predicted velocity will be in reasonably good agreement. Before moving on to validate the swimming velocity of a model sperm with a sinusoidal beating waveform,

one more fundamental knowledge remains to be verified with the simple passive horizontal rod.

In the case of modelling a typical human sperm, where the flagellum length is approximately 200 times larger than the flagellum radius, the constraint of $p \ll q$ for the SBT assumptions to be satisfied restricts our choice in the number of segments *N* for which the flagellum can be discretized into. This is the reason for the upper limit of *N* being 30 in the table above; any larger value of *N* would severely violate the SBT model. However, it would be interesting to observe how the model would behave if the flagellum can legitimately be discretized into extremely small segments, for the purpose of understanding the dependent factors in SBT. As such, straight slender rods of various thickness will be considered here, regardless of whether such dimensions correspond to any organism which exists in reality. In this spirit, a flagellum 50 μm in length with a range of radius, subjected to a relative fluid velocity directed along its longitudinal axis such that $\beta = 0$, is studied. At the same time, the number of segments which the flagellum is discretized into will be adjusted, such that the length $2q$ of each segment remains as a fixed multiple of the flagellum radius. The corresponding K_N / K_T ratio for the two theories are compared and presented in Table 5-4.

The table shows that as the flagellum becomes more slender, with decreasing flagellum radius *p* while length is kept constant, both the K_N / K_T ratio from RFT as well as SBT gradually approach the theoretical limit of two. Moreover, there exists a clear trend that the coefficient relating the force and velocity converges as the flagellum radius decreases, suggesting that the effect of hydrodynamic interactions diminishes, leading to better agreement between RFT and SBT. The approximate analytical relation in equation (3.33) gives a straightforward and convenient way to predict how the ratio between the resistive coefficients influences the swimming velocity. The first term in the equation shows that with all else being equal, the velocity is directly proportional to $\left(K_T / K_N\right) - 1$. Since that the sperm is heading in the negative direction (Figure 3-1), a larger value for K_N / K_T results in a more negative factor and hence faster speed. Given that the ratio is consistently greater in RFT, than the ratio of equivalent coefficients in SBT, this suggests that RFT will tend to overestimate the swimming speed. This is supported by the conclusion made by Higdon (1979).

Table 5-4 – Force per unit length f_x, resistive coefficients K_N and K_T and their ratios, for different number of discrete segments N and radius p of a rod 50 μm in length.

N	10	20	50	100	250	1000
p / μm	0.25	0.125	0.05	0.025	0.01	0.0025
$\frac{f_x^{RFT}}{\mu V_{rel}}$	1.753	1.470	1.210	1.068	0.924	0.767
$\frac{f_x^{SBT}}{\mu V_{rel}}$	1.401	1.219	1.037	0.930	0.819	0.693
$\frac{f_x^{RFT} - f_x^{SBT}}{f_x^{SBT}}$	25%	21%	17%	15%	13%	11%
$\left(\frac{K_N^{RFT}}{K_T^{RFT}}\right)$	1.76	1.79	1.82	1.84	1.86	1.88
$\left(\frac{K_N^{SBT}}{K_T^{SBT}}\right)$	1.63	1.67	1.71	1.74	1.77	1.80
$\left(\frac{K_N^{RFT}}{K_T^{RFT}}\right) \Big/ \left(\frac{K_N^{SBT}}{K_T^{SBT}}\right)$	1.08	1.07	1.06	1.06	1.05	1.04

From Table 5-4, it can also be observed that the ratio K_N / K_T of resistive coefficients from RFT and SBT approaches each other as the flagellum radius p becomes smaller. In order to check that the convergence is a result of decreasing flagellum radius rather than an increase in the number of segments considered in the SBT model, the flagellum radius shall be kept constant while the number of discretization N varies. The flagellum radius shall be set as an extremely small value of 0.0025 μm, so as to satisfy the condition for $p \ll q$ when N gets large. The corresponding results, where the slenderness of the flagellum is kept constant unlike the preceding table where the flagellum thickness changes across each column, is presented in Table 5-5.

Table 5-5 – Force per unit length f_x, resistive coefficients K_N and K_T and their ratios, for different number of discrete segments N of a rod 50 µm in length and 0.0025 µm in radius.

N	10	20	50	100	250	1000
p (µm)	0.0025					
$\frac{f_x^{RFT}}{\mu V_{rel}}$	0.7673					
$\frac{f_x^{SBT}}{\mu V_{rel}}$	0.6891	0.6907	0.6919	0.6923	0.6927	0.6933
$\frac{f_x^{RFT} - f_x^{SBT}}{f_x^{SBT}}$	11.3%	11.1%	10.9%	10.8%	10.8%	10.7%
$\left(\frac{K_N^{RFT}}{K_T^{RFT}}\right)$	1.885					
$\left(\frac{K_N^{SBT}}{K_T^{SBT}}\right)$	1.802	1.802	1.801	1.801	1.801	1.799
$\left(\frac{K_N^{RFT}}{K_T^{RFT}}\right)\Big/\left(\frac{K_N^{SBT}}{K_T^{SBT}}\right)$	1.046	1.046	1.047	1.047	1.047	1.048

The table shows that the ratio between K_N^{RFT}/K_T^{RFT} and K_N^{SBT}/K_T^{SBT} is nearly identical for N in the range of 10 to 1000 segments, and gives three learning points. First, the converging results between RFT and SBT in the previous table can be attributed to the decreasing flagellum radius rather than the increase in the number of segments. Second, discretizing the flagellum of a human sperm into 10 segments when using the SBT model is sufficient for the scope of this thesis. As can be inferred from equation (5.15), the computational time is quadratic with respect to the number of segments N. In the context of this project, using a value of 10 gives results which have reasonably converged, while keeping computational costs low at the same time. Third, the force-velocity coefficient in RFT and SBT will inevitable differ slightly, even in extreme hypothetical scenarios where the flagellum radius is 20,000 times smaller than its length. This deviation cannot be avoided by adjusting the number of discretization in the SBT model, as it is due to the inherent difference in the assumptions leading to the two models as discussed at the beginning of this section.

Before proceeding further in applying SBT to solve for the flagellum shape, a verification will be carried out to pick out potential errors which may be introduced in

the process of formulating the equations or writing the program code. A necessary, though not a sufficient, condition for any hydrodynamic model to be valid is the accurate prediction of a swimmer's behaviour in the simplest case scenario – which is motion with a single degree of freedom. The famous 'Scallop Theorem' by Purcell (1977) is an interesting example of how anything that has only one degree of freedom will exhibit time-reversibility, resulting in reciprocal motion.

To model such a swimmer, a hypothetical sperm with a flagellum of infinite flexural rigidity will be considered here, as illustrated in Figure 5-3 which shows the position of the flagellum corresponding to different phases of its beating cycle. The rigid flagellum will essentially behave as a rod hinged at the spherical head, with the maximum deflection set to be 10% of the flagellum length. The instantaneous linear and angular velocities, according to RFT and SBT respectively, is plotted in Figure 5-4.

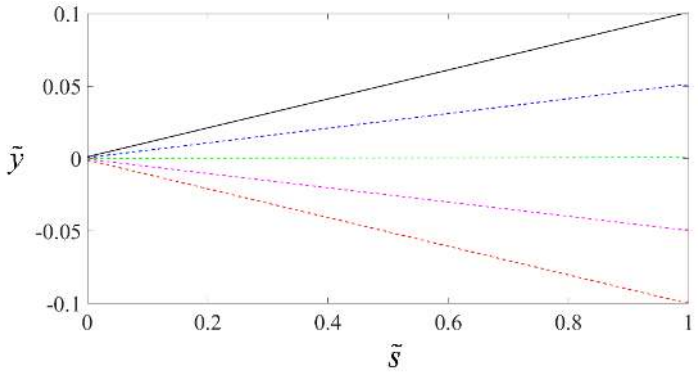

Figure 5-3 – Flagellum shape when flexural rigidity is infinite. The solid black line corresponds to a non-dimensional time of $\tilde{t}$ = 0, while the dashed blue, green, magenta, and red lines correspond to $\tilde{t} = \pi/4$, $\tilde{t} = \pi/2$, $\tilde{t} = 3\pi/4$ and $\tilde{t} = \pi$, respectively.

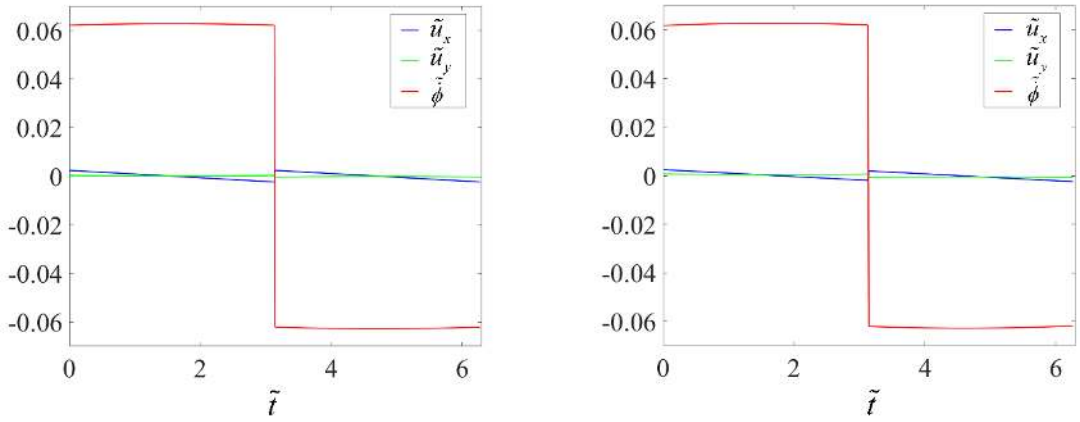

Figure 5-4 – Instantaneous non-dimensionalised linear and angular velocities for a sperm with a flagellum of infinite flexural rigidity, over a non-dimensionalised time from 0 to 2π, where hydrodynamic force is computed using (Left) RFT and (Right) SBT. The solid blue, green, and red line corresponds to $\tilde{u}_x$, $\tilde{u}_y$ and $\tilde{\phi}$, respectively.

The results obtained by RFT and SBT strongly agree with one another, for all instance over the entire beat cycle. The non-dimensionalised time averaged velocity of the swimmer exhibiting such a reciprocal motion is 10^{-5} in the *x*-direction, while the linear velocity in the *y*-direction and the angular velocity over a beat cycle are many orders of magnitude smaller than 10^{-5}. In dimensional term, the hypothetical sperm with infinite rigidity achieves a net translation in the order of 10^{-3} times its body length per second in the *x*-direction. This time-averaged velocity is practically negligible but not perfectly zero because SBT approximates the force per unit length across each segment to be constant. The same approximation is also applied to the RFT model to allow for a fair comparison. Each segment translates with no rotational motion from one time-step to another, such that the force and velocity acting on each segment are uniform, resulting in a motion which is nearly, but not absolutely, time-reversible. Nonetheless, it is justified to conclude that the numerical models utilised in this thesis obeys the 'Scallop Theorem'. Moving forward, a more realistic sperm model shall be analysed using both RFT and SBT.

5.3 Discretized flagellum under SBT model

In this section, a sperm, comprising a spherical head and a flagellum formed by *N* discrete horizontal segments of equal length (Figure 5-5), will be analysed. The mid-point of each segment, as marked by the black dots, will follow the path of a moving sinusoidal wave, with the local X^L axis of each segment parallel to the tangent of the centre-line represented by the imaginary sinusoidal curve.

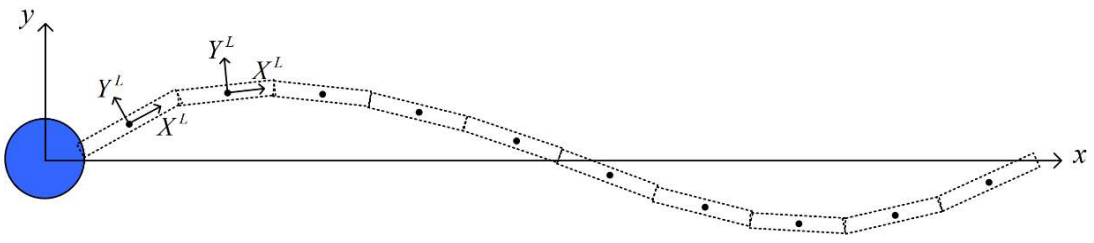

Figure 5-5 – Schematic of a sperm comprising a spherical head and *N* discrete straight segments of equal length.

Figure 5-6 shows the position of the sperm flagellum corresponding to different phases of its beating cycle, plotted with respect to its curvilinear coordinate *s*. Given the local axis of each segment is defined to be tangential to the centre-line in accordance

with SBT (Higdon 1979), the ends of each discrete segment will not have the exact same position as the adjacent segments, resulting in slight discontinuities which are no more than 0.01 times the wavelength. There is little cause for concern over such discontinuities inherent in SBT, given that it has been proven to give highly accurate predictions (Autrusson *et al*. 2011; Jabbarzadeh *et al*. 2014; Rodenborn *et al*. 2013). The extent of discontinuities can be reduced by discretizing the flagellum into more segments. However, the constraints of $p \ll q$ such that each segment is slender, or equivalently $N \ll \frac{1}{2}\Lambda/p$, limits the choice of N. Here, the sperm flagellum is discretized into $N = 15$ segments, so that the length of each segment is over 10 times the flagellum radius, and less than a tenth of the flagellum length.

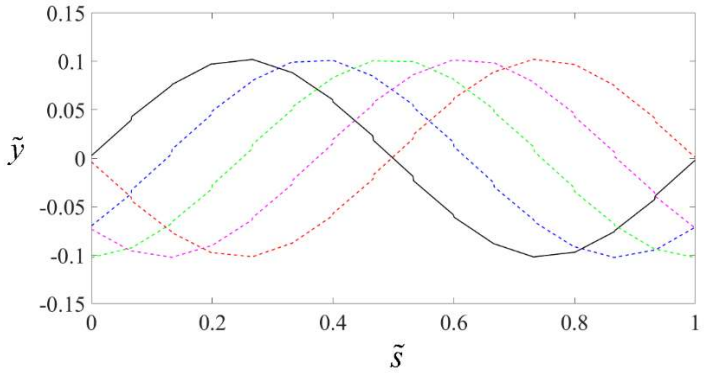

Figure 5-6 – Flagellum discretized into 15 straight segments., where the mid-point of each segment follows a moving sinusoidal wave, with the local axis of each segment parallel to the tangent of the imaginary sinusoidal curve. The solid black line corresponds to a dimensionless time of $\tilde{t} = 0$, while the dash-dotted blue, green, magenta, and red line corresponds to $\tilde{t} = \pi/4$, $\tilde{t} = \pi/2$, $\tilde{t} = 3\pi/4$ and $\tilde{t} = \pi$, respectively.

To compute the hydrodynamic force on the flagellum, consider an infinitesimal element of a segment n of the flagellum. During a small time-step from t to $(t + dt)$, each segment is modelled to move laterally in the y-direction. The relative fluid velocity acting at a point on segment n is

$$\begin{aligned}\mathbf{v}_{rel}^{(n)} &= -\mathbf{v}_{swim}^{(n)} - \mathbf{v}_{wiggling}^{(n)} \\ &= \left(u_x \mathbf{e}_x + u_y \mathbf{e}_y + \dot{\phi}\,\mathbf{e}_z \times \mathbf{r}^{(n)}\right) - \frac{d\mathbf{r}^{(n)}}{dt} \\ &= \begin{bmatrix} -u_x + \dot{\phi}\, y^{(n)} \\ -u_y - \dot{\phi}\, x^{(n)} - dy^{(n)}/dt \end{bmatrix},\end{aligned} \tag{5.31}$$

where the unit tangent and normal vector for each segment is

$$\mathbf{e}_T^{(n)} = \cos\theta^{(n)}\mathbf{e}_x + \sin\theta^{(n)}\mathbf{e}_y, \tag{5.32}$$

$$\mathbf{e}_N^{(n)} = -\sin\theta^{(n)}\mathbf{e}_x + \cos\theta^{(n)}\mathbf{e}_y. \tag{5.33}$$

The tangential and normal component of the relative fluid velocity at each segment is

$$\left(\mathbf{v}_{rel}^{(n)} \bullet \mathbf{e}_T^{(n)}\right)\mathbf{e}_T^{(n)} = \left(\begin{bmatrix} -u_x + \dot{\phi}y^{(n)} \\ -u_y - \dot{\phi}x^{(n)} - dy^{(n)}/dt \end{bmatrix} \bullet \begin{bmatrix} \cos\theta^{(n)} \\ \sin\theta^{(n)} \end{bmatrix}\right)\begin{bmatrix} \cos\theta^{(n)} \\ \sin\theta^{(n)} \end{bmatrix}, \tag{5.34}$$

$$\left(\mathbf{v}_{rel}^{(n)} \bullet \mathbf{e}_N^{(n)}\right)\mathbf{e}_N^{(n)} = \left(\begin{bmatrix} -u_x + \dot{\phi}y^{(n)} \\ -u_y - \dot{\phi}x^{(n)} - dy^{(n)}/dt \end{bmatrix} \bullet \begin{bmatrix} -\sin\theta^{(n)} \\ \cos\theta^{(n)} \end{bmatrix}\right)\begin{bmatrix} -\sin\theta^{(n)} \\ \cos\theta^{(n)} \end{bmatrix}. \tag{5.35}$$

The relative velocity within each segment is taken to be uniform within the interval, following the value determined from the centre point of the segment. Given that each segment is translating linearly in the body-fixed frame, *dy*/*dt* remains unchanged across the interval. Although the local velocity away from the centre of each segment will vary due to the rotational motion of the body-frame, the variations are linear, such that differences in the left and right of each segment cancels out and results in the same force computed over the interval. Using resistive force theory, the force and moment acting on the infinitesimal element of length *ds* is

$$\mathbf{dF}_{RFT}^{(n)} = \left[K_T\left(\mathbf{v}_{rel} \bullet \mathbf{e}_T\right)\mathbf{e}_T + K_N\left(\mathbf{v}_{rel} - \left(\mathbf{v}_{rel} \bullet \mathbf{e}_T\right)\mathbf{e}_T\right)\right]ds, \tag{5.36}$$

$$\mathbf{dM}_{RFT}^{(n)} = \mathbf{r}^{(n)} \times \mathbf{dF}_{RFT}^{(n)}. \tag{5.37}$$

Summing the force and moment over the entire sperm,

$$\mathbf{F}_{RFT} = \mathbf{F}^{flagellum} + \mathbf{F}^{head} = \sum_{n=1}^{N}\left(\int_{(n-1)\Lambda/N}^{n\Lambda/N} \mathbf{dF}_{RFT}^{(n)}\right) + 6\pi\mu a\mathbf{u}, \tag{5.38}$$

$$\mathbf{M}_{RFT} = \mathbf{M}^{flagellum} + \mathbf{M}^{head} = \sum_{n=1}^{N}\left(\int_{(n-1)\Lambda/N}^{n\Lambda/N} \mathbf{r}^{(n)} \times \mathbf{dF}_{RFT}^{(n)}\right) + 8\pi\mu a^3\dot{\phi}. \tag{5.39}$$

In SBT, the force-velocity relation is determined not only by the local conditions, but also influenced by interactions from the Stokeslets and dipoles across the entire flagellum. As discussed earlier, the force per unit length acting on each segment of the flagellum is given by equation (5.16). These are summed over the entire sperm to give

$$\mathbf{F}_{SBT} = \mathbf{F}^{flagellum} + \mathbf{F}^{head} = \sum_{n=1}^{N}\left(\mathbf{f}^{(n)}\,\Lambda/N\right) + 6\pi\mu a\mathbf{u}, \tag{5.40}$$

$$\mathbf{M}_{SBT} = \mathbf{M}^{flagellum} + \mathbf{M}^{head} = \sum_{n=1}^{N}\left(\left(x^{(n)} f_y^{(n)} - y^{(n)} f_x^{(n)}\right)\frac{\Lambda}{N}\right) + 8\pi\mu a^3\dot{\phi}\,. \tag{5.41}$$

The force and moment are linear functions of u_x, u_y and $\dot{\phi}$, and can be expressed as

$$F_x = \frac{\partial F_x}{\partial u_x}u_x + \frac{\partial F_x}{\partial u_y}u_y + \frac{\partial F_x}{\partial \dot{\phi}}\dot{\phi} + \xi_1\,, \tag{5.42}$$

$$F_y = \frac{\partial F_y}{\partial u_x}u_x + \frac{\partial F_y}{\partial u_y}u_y + \frac{\partial F_y}{\partial \dot{\phi}}\dot{\phi} + \xi_2\,, \tag{5.43}$$

$$M_z = \frac{\partial M_z}{\partial u_x}u_x + \frac{\partial M_z}{\partial u_y}u_y + \frac{\partial M_z}{\partial \dot{\phi}}\dot{\phi} + \xi_3\,. \tag{5.44}$$

When RFT is used to predict the velocity, the force per unit length acting on each segment will be determined solely by the local resistive coefficient and the local relative velocity, which is equivalent to setting all off-diagonal terms in the resistance matrix in equation (5.16) to zero. The coefficients ζ_{11} to ζ_{33} and ξ_1 to ξ_3 are:

$$\zeta_{11} = \frac{\partial F_x}{\partial u_x} = 6\pi\mu a + \sum_{n=1}^{N}\left(K_T\left[-\cos^2\theta^{(n)}\right] + K_N\left[-\sin^2\theta^{(n)}\right]\right)\frac{\Lambda}{N} \tag{5.45}$$

$$\zeta_{12} = \frac{\partial F_x}{\partial u_y} = \sum_{n=1}^{N}\left(K_T\left[-\sin\theta^{(n)}\cos\theta^{(n)}\right] + K_N\left[\sin\theta^{(n)}\cos\theta^{(n)}\right]\right)\frac{\Lambda}{N} \tag{5.46}$$

$$\zeta_{13} = \frac{\partial F_x}{\partial \dot{\phi}} = \sum_{n=1}^{N}\left(\begin{matrix}K_T\left[-\sin\theta^{(n)}\cos\theta^{(n)}x^{(n)} + \cos^2\theta^{(n)}y^{(n)}\right]\\ +K_N\left[\sin\theta^{(n)}\cos\theta^{(n)}x^{(n)} + \sin^2\theta^{(n)}y^{(n)}\right]\end{matrix}\right)\frac{\Lambda}{N} \tag{5.47}$$

$$\zeta_{21} = \frac{\partial F_y}{\partial u_x} = \sum_{n=1}^{N}\left(K_T\left[-\sin\theta^{(n)}\cos\theta^{(n)}\right] + K_N\left[\sin\theta^{(n)}\cos\theta^{(n)}\right]\right)\frac{\Lambda}{N} \tag{5.48}$$

$$\zeta_{22} = \frac{\partial F_y}{\partial u_y} = 6\pi\mu a + \sum_{n=1}^{N}\left(K_T\left[-\sin^2\theta^{(n)}\right] + K_N\left[-\cos^2\theta^{(n)}\right]\right)\frac{\Lambda}{N} \tag{5.49}$$

$$\zeta_{23} = \frac{\partial F_y}{\partial \dot{\phi}} = \sum_{n=1}^{N}\left(\begin{matrix}K_T\left[-\sin^2\theta^{(n)}x^{(n)} + \sin\theta^{(n)}\cos\theta^{(n)}y^{(n)}\right]\\ +K_N\left[-\cos^2\theta^{(n)}x^{(n)} - \sin\theta^{(n)}\cos\theta^{(n)}y^{(n)}\right]\end{matrix}\right)\frac{\Lambda}{N} \tag{5.50}$$

$$\zeta_{31} = \frac{\partial M_z}{\partial u_x} = \sum_{n=1}^{N}\left(\begin{matrix}x^{(n)}\left(K_N - K_T\right)\sin\theta^{(n)}\cos\theta^{(n)}\\ +y^{(n)}\left(K_T\cos^2\theta^{(n)} + K_N\sin^2\theta^{(n)}\right)\end{matrix}\right)\frac{\Lambda}{N} \tag{5.51}$$

$$\zeta_{32} = \frac{\partial M_z}{\partial u_y} = \sum_{n=1}^{N} \begin{pmatrix} -x^{(n)} \left(K_T \sin^2 \theta^{(n)} + K_N \cos^2 \theta^{(n)} \right) \\ +y^{(n)} \left(K_T - K_N \right) \sin \theta^{(n)} \cos \theta^{(n)} \end{pmatrix} \frac{\Lambda}{N} \tag{5.52}$$

$$\zeta_{33} = \frac{\partial M_z}{\partial \dot{\phi}} = \sum_{n=1}^{N} \begin{pmatrix} -\left(K_T \sin^2 \theta^{(n)} + K_N \cos^2 \theta^{(n)} \right) \left(x^{(n)} \right)^2 \\ -\left(K_T \cos^2 \theta^{(n)} + K_N \sin^2 \theta^{(n)} \right) \left(y^{(n)} \right)^2 \\ +2 \left(K_T - K_N \right) \sin \theta^{(n)} \cos \theta^{(n)} x^{(n)} y^{(n)} \end{pmatrix} \frac{\Lambda}{N} \tag{5.53}$$

$$\xi_1 = \sum_{n=1}^{N} \left(\left(K_N - K_T \right) \sin \theta^{(n)} \cos \theta^{(n)} \frac{\partial y^{(n)}}{\partial t} \right) \frac{\Lambda}{N} \tag{5.54}$$

$$\xi_2 = \sum_{n=1}^{N} \left(-\left(K_T + K_N \right) \sin \theta^{(n)} \cos \theta^{(n)} \frac{\partial y^{(n)}}{\partial t} \right) \frac{\Lambda}{N} \tag{5.55}$$

$$\xi_3 = 8\pi\mu a^3 + \sum_{n=1}^{N} \left[-x^{(n)} \left(K_T + K_N \right) - y^{(n)} \left(K_N - K_T \right) \right] \sin \theta^{(n)} \cos \theta^{(n)} \frac{\partial y^{(n)}}{\partial t} \frac{\Lambda}{N} \tag{5.56}$$

On the other hand, if SBT is used to predict the swimming velocity, the coefficients are:

$$\zeta_{11} = \sum_{n=1}^{N} \frac{\partial f_x^{(n)}}{\partial u_x} \frac{\Lambda}{N}, \quad \zeta_{12} = \sum_{n=1}^{N} \frac{\partial f_x^{(n)}}{\partial u_y} \frac{\Lambda}{N}, \quad \zeta_{13} = \sum_{n=1}^{N} \frac{\partial f_x^{(n)}}{\partial \dot{\phi}} \frac{\Lambda}{N} \tag{5.57}$$

$$\zeta_{21} = \sum_{n=1}^{N} \frac{\partial f_y^{(n)}}{\partial u_x} \frac{\Lambda}{N}, \quad \zeta_{22} = \sum_{n=1}^{N} \frac{\partial f_y^{(n)}}{\partial u_y} \frac{\Lambda}{N}, \quad \zeta_{23} = \sum_{n=1}^{N} \frac{\partial f_y^{(n)}}{\partial \dot{\phi}} \frac{\Lambda}{N} \tag{5.58}$$

$$\zeta_{31} = \sum_{n=1}^{N} \left(x^{(n)} \frac{\partial f_y^{(n)}}{\partial u_x} - y^{(n)} \frac{\partial f_x^{(n)}}{\partial u_x} \right) \left(\frac{\Lambda}{N} \right) \tag{5.59}$$

$$\zeta_{32} = \sum_{n=1}^{N} \left(x^{(n)} \frac{\partial f_y^{(n)}}{\partial u_y} - y^{(n)} \frac{\partial f_x^{(n)}}{\partial u_y} \right) \left(\frac{\Lambda}{N} \right) \tag{5.60}$$

$$\zeta_{33} = \sum_{n=1}^{N} \left(x^{(n)} \frac{\partial f_y^{(n)}}{\partial \dot{\phi}} - y^{(n)} \frac{\partial f_x^{(n)}}{\partial \dot{\phi}} \right) \left(\frac{\Lambda}{N} \right) \tag{5.61}$$

$$\xi_1 = \sum_{n=1}^{N} \left(f_x^{(n)} \frac{\Lambda}{N} \right) - \zeta_{11} u_x - \zeta_{12} u_y - \zeta_{13} \dot{\phi} \tag{5.62}$$

$$\xi_2 = \sum_{n=1}^{N} \left(f_y^{(n)} \frac{\Lambda}{N} \right) - \zeta_{21} u_x - \zeta_{22} u_y - \zeta_{23} \dot{\phi} \tag{5.63}$$

$$\xi_3 = \sum_{n=1}^{N}\left(x^{(n)} f_y^{(n)} - y^{(n)} f_x^{(n)}\right)\left(\frac{\Lambda}{N}\right) - \zeta_{31} u_x - \zeta_{32} u_y - \zeta_{33}\dot{\phi} \tag{5.64}$$

The resulting non-dimensionalised instantaneous velocity in the *x*-direction, as computed by RFT as well as SBT, is presented in Figure 5-7. Converted back to dimensional form, the time-averaged swimming velocity of a sperm with typical physical parameters as listed in Table 3-1 is -58 μm/s according to RFT, and -46 μm/s according to SBT. This is consistent with Higdon's findings (1979) that Lighthill's (1976) RFT overestimates the swimming speed. The predictions made by both theories are also well within the range observed experimentally (Ishijima *et al*. 1986; Mortimer *et al*. 1998). Moving forward, the model shall be refined by solving for the flagellum beating pattern rather than using a prescribed sinusoidal waveform.

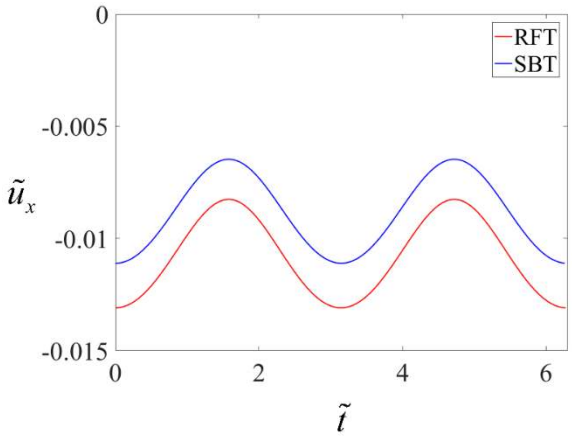

Figure 5-7 – Instantaneous velocity in the x-direction of the body-fixed frame, computed using RFT (solid red line) and SBT (solid blue line) from a non-dimensionalised time of 0 to 2π.

5.4 Numerical solution for flagellum waveform

In Chapter 4, the PDE which governs the flagellum waveform is reduced to a linear ODE as shown in equation (4.26), where an analytical solution is subsequently derived. For the avoidance of doubt, readers are reminded that $\tilde{y}(\tilde{s},\tilde{t}) = \tilde{h}(\tilde{s})\, e^{-i\tilde{t}}$, where the justification of such as time dependence is discussed in Appendix B1. The contribution from the hydrodynamic force acting on the flagellum towards the governing PDE is, according to RFT, directly proportional to the local relative fluid velocity. When reduced to the ODE, the hydrodynamic force under the small amplitude approximation can be expressed analytically as a linear function of the dependant

variable *y*. However, if the hydrodynamic force is determined by SBT to account for non-linear contributions resulting from body-to-body interactions, the force distribution does not allow the flagellum waveform to be described by a straightforward analytical equation. Hence, a numerical approach will be used. The governing equation can be converted into a finite difference equation (Ames 2014), in which the solution depends on the initial or boundary conditions. When discretized, the derivatives in these conditions are replaced by a linear combination of discrete values in the neighbourhood of the point of interest. A family of numerical methods (Butcher 2016) exist to solve such equations. These numerical methods are well documented in the literature, but for completeness, the fundamental idea of some techniques is discussed in Appendix B2 to give an appreciation of the approach taken to solve differential equations numerically.

Using MATLAB's built-in solver for a boundary value problem (BVP), a numerical solution satisfying all boundary conditions as well as the governing equation in accordance with the SBT model cannot be obtained. To maintain focus on the main objectives of this thesis, the challenges encountered as well as the corresponding actions taken are discussed in Appendix B3. As it is beyond the scope of this thesis to code a more robust algorithm, an alternative approach shall be taken. Moving forward, the BVP shall be framed as an initial value problem (IVP) to assess whether a plausible flagellum waveform may be obtained using the SBT model. The procedures for solving the IVP have been documented in the appendix as well.

Using the force distribution obtained from RFT, the numerical solution obtained using a 4^{th} order Runge-Kutta method is practically identical to the analytical solution obtained from the small amplitude approximation. It is necessary to note that the differential equation is complex, and even though the flagellum shape is determined only by the real part of the solution, the imaginary components of the intial conditions must be taken into account. Having validated this approach of solving for the flagellum shape, the force distribution based on SBT will be applied. As there is no known analytical approach corresponding to the SBT model, the numerical results will be compared with the RFT flagellum pattern as a reference.

Before moving further, it is prudent to be clear about the underlying difference which would eventually lead to a different force distribution between the RFT model and the SBT model. Other than the difference in mathematical procedures used to

compute the hydrodynamic forces, which arises from the effects of body-to-body interactions, the flagellum beating pattern associated with SBT is also different. As discussed in Chapter 5, the flagellum will be modelled as a number of discrete straight segments, and the force acting on each segment is uniform within that segment. Since the number of discretization is confined to the requirement that each segment is slender, a convergence towards a smooth continuous flagellum is not possible. On the other hand, the flagellum under the RFT model is discretized into a large number of infinitesimal elements, thus allowing a convergence test to be done.

The RFT model with small amplitude approximation has led to a plausible flagellum waveform, while no solution is found when the SBT model is approached as a BVP. In order to gain insight on what was the final nail in the coffin, modifications will be made one at a time and the corresponding results will be analysed. The motion of the flagellum will be guided by the analytical solution as given in equation (4.31), making the appropriate adjustments where necessary for a flagellum comprising discrete straight segments. This reference is required because the flagellum beating pattern is needed to compute the force distribution, while the force distribution is in turn needed to compute the beating pattern. Given that the analytical solution of y is complex, the relative fluid velocity and hydrodynamic force will also be complex quantities.

The first modification will be the removal of the following approximation relating the normal force per unit length to the time-derivative of y:

$$f_n^{RFT} = K_N\left(\mathbf{v}_{rel}\bullet\mathbf{e}_N\right) \approx K_N\left(\mathbf{v}_{rel}\bullet\mathbf{e}_y\right) = K_N\frac{\partial y}{\partial t}. \tag{5.65}$$

In a Newtonian fluid where the Deborah number is zero, the above approximation leads to the normal force per unit length on the flagellum being represented by $i\mathrm{Sp}^4\tilde{h}$ in equation (4.26), reprinted here for the reader's convenience:

$$\tilde{h}'''' - i\mathrm{Sp}^4\tilde{h} + \frac{1}{6}\pi\tilde{p}^2\mathrm{Sp}^4\left[\tilde{D}_0 + \tilde{D}_1(\tilde{a}+\alpha\tilde{s})\right]\tilde{h}' - \frac{\partial}{\partial\tilde{s}}\bar{f}_m e^{i\tilde{k}\tilde{s}} = 0. \tag{5.66}$$

A more accurate representation of the normal force per unit length should have been $f_n^{RFT} = K_N\left(\mathbf{v}_{rel}\bullet\mathbf{e}_N\right)$, such that $i\mathrm{Sp}^4\tilde{h}$ gets replaced with $\mathrm{Sp}^4 f_n^{RFT}$. To further improve the generality of the governing equation, it should be expressed without restricting the use of RFT to compute the hydrodynamic force on the flagellum.

$$\tilde{h}'''' - \mathrm{Sp}^4 f_n + \frac{1}{6}\pi\tilde{p}^2\,\mathrm{Sp}^4\left[\tilde{D}_0 + \tilde{D}_1(\tilde{a}+\alpha\tilde{s})\right]\tilde{h}' - \frac{\partial}{\partial\tilde{s}}\bar{f}_m\, e^{i\tilde{k}\tilde{s}} = 0\,. \qquad (5.67)$$

Figure 5-8 shows that $i\mathrm{Sp}^4\tilde{h}$, $\mathrm{Sp}^4 f_n^{RFT}$ and $\mathrm{Sp}^4 f_y^{RFT}$ are very similar to one another.

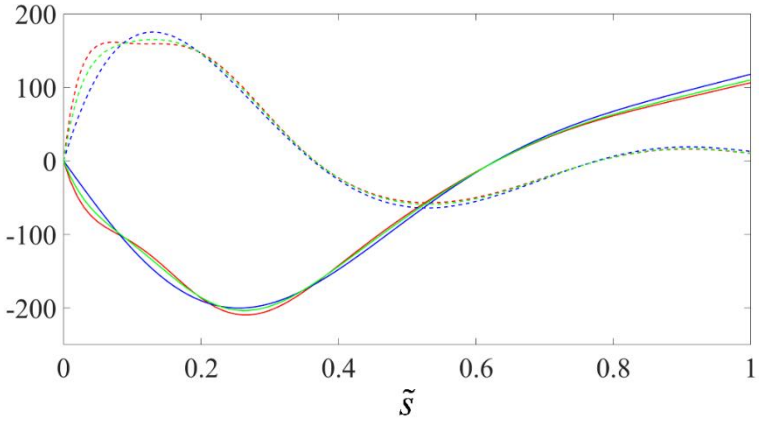

Figure 5-8 – Non-dimensionalised force per unit length, multiplied by the relevant coefficients in the differential equations, along the curvilinear coordinate $\tilde{s}$. The blue, green, and red lines represent $i\mathrm{Sp}^4\tilde{h}$, f_y^{RFT} and f_n^{RFT}, respectively. The real and imaginary parts are represented independently by the solid and dashed lines, respectively.

Despite the seemingly insignificant difference between $\mathrm{Sp}^4 f_n^{RFT}$ and its approximated form, $i\mathrm{Sp}^4\tilde{h}$, the numerical solution of the non-approximated model diverges slightly from the analytical solution of the approximated model near the end of the flagellum. This is shown in Figure 5-9, where the green line (obtained when the hydrodynamic force contribution is represented by $\mathrm{Sp}^4 f_n^{RFT}$) deviates from the black line (the analytical solution when the hydrodynamic force contribution is represented $i\mathrm{Sp}^4\tilde{h}$). However, by making small adjustments of no more than 0.8% in the initial conditions, the numerical solution becomes in agreement with the analytical solution, and satisfies the boundary conditions as defined in equations (4.20) to (4.23). As discussed earlier, the initial conditions y' and y''' have to be guessed to give zero net force and moment at the free end of the flagellum where $\tilde{s}=1$.

It is useful to keep in mind that the analytical solution referred to is equation (4.31). This is the exact solution to the ordinary differential equation (4.26), multiplied by a time dependence according to the relation in equation (4.24), and perfectly satisfies all four boundary conditions. However, equation (4.26) itself is obtained from the assumptions of small amplitude and RFT, and therefore does not capture the full essence of the physics of the swimming sperm.

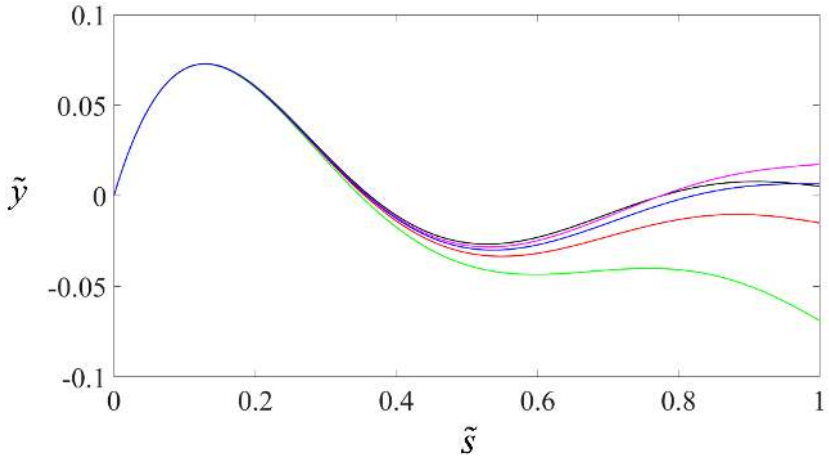

Figure 5-9 – Numerical solution of flagellum waveform, obtained using the analytically-obtained exact initial conditions (green line), and modifying the initial conditions of $\tilde{y}'''$ by a factor 1.005 (red line), 1.007 (blue line) and 1.008 (magenta line), plotted against analytical solution (black line) in equation (4.31).

Moving forward towards the SBT model, the flagellum shall now be modelled as a number of discrete straight segments as discussed in Chapter 5, rather than a continuous smooth filament. However, the hydrodynamic force per unit length will still be computed using RFT, which is dependent only on the local fluid velocity multiplied by the resistive coefficient. This would be the only difference between this 'intermediate model' and the actual SBT model, giving a fair basis of comparison as any difference in the results can be attributed directly to the way the hydrodynamic force was computed.

The left column of Figure 5-10 shows the distribution of the non-dimensionalised force per unit length, multiplied by the relevant coefficients, for a segmented flagellum varying from $N = 10$ to $N = 20$ discrete segments. This is compared against the force distribution for a continuous smooth flagellum and an analytical approximation used in equation (4.26), with all else being equal on the same plot. The solid lines represent the real component of the force, while the dotted lines represent the imaginary component which arises because the waveform solution y and its derivatives are complex. Apart from being used to predict the flagellum waveform, knowledge of the force distribution allows us to compute the swimming velocity based on the total force acting on the entire sperm. The right column of Figure 5-10 shows the numerical solution for the corresponding step-wise RFT force distribution, plotted against the segmented flagellum derived from the analytical solution in Chapter 4. Discretization beyond 20 segments is not considered as it clearly violates the framework of SBT which requires the flagellum radius to be much smaller than the segment length.

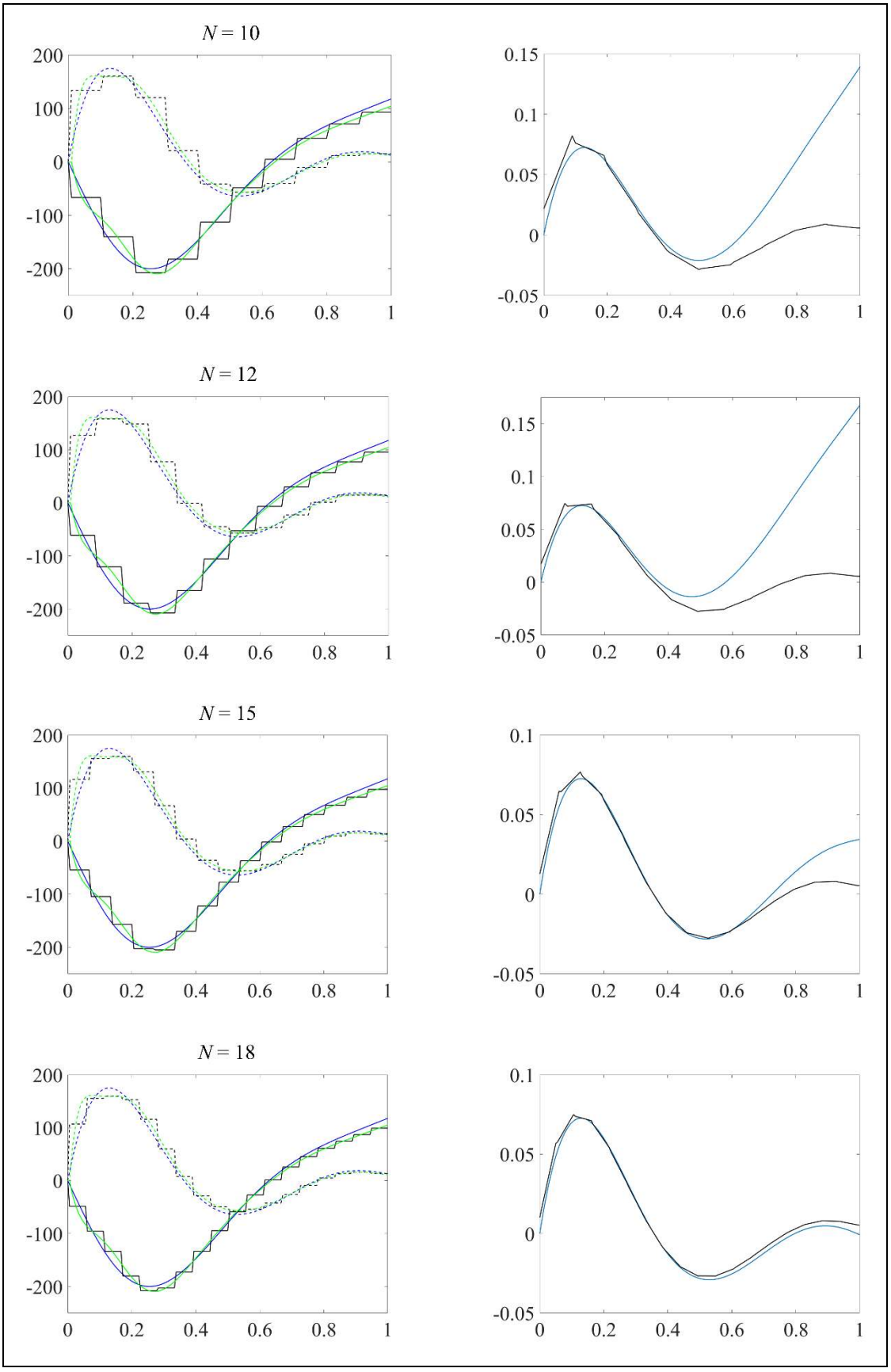
N = 10
N = 12
N = 15
N = 18

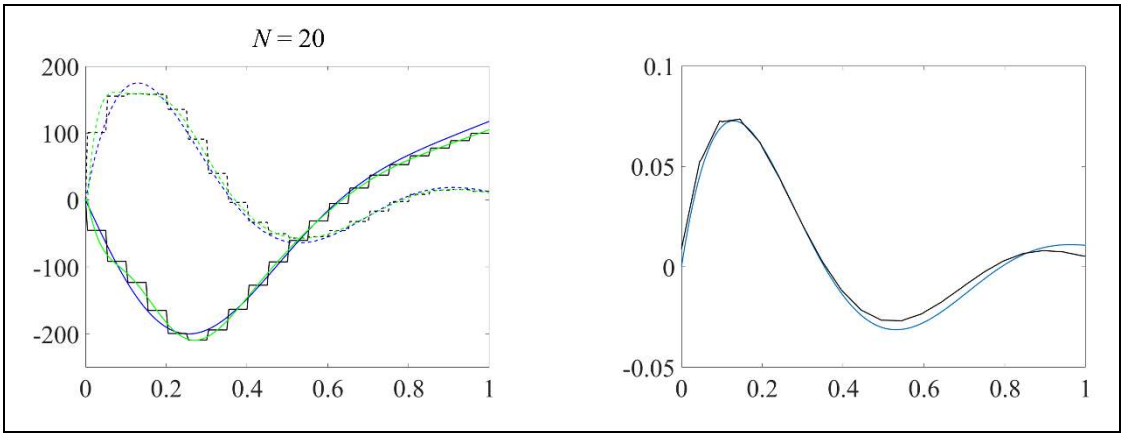

Figure 5-10 – (Left) Non-dimensionalised force per unit length, multiplied by the relevant coefficients in the differential equations, along the curvilinear coordinate $\tilde{s}$ of the flagellum. The blue line represents $i\mathrm{Sp}^4 h$, while the green and black lines represent f_n^{RFT} for a continuous and discretized flagellum, respectively, varying from N = 10 to N = 20 discrete segments. The real and imaginary parts are represented independently by the solid and dashed lines, respectively. (Right) Numerical solution (blue line), representing the flagellum waveform, plotted against the segmented flagellum obtained from the analytical solution (black line).

When the flagellum is discretized into 18 to 20 segments, the force distribution on the flagellum leads to a numerical solution which is in good agreement with the analytical solution. With the confidence that modelling the flagellum as a finite number of straight discrete segments in accordance with the SBT framework does not significantly alter the force distribution or flagellum waveform given by RFT, the force distribution for the actual SBT model will be investigated in the following section.

5.5 Causality dilemma in solving flagellum waveform

The complex f_n^{RFT} is calculated directly using the complex values of y. On the other hand, the imaginary part of f_n^{SBT} is computed by multiplying i to the result obtained from the value of the imaginary part of y, and adding the real part of f_n^{SBT} computed from the real part of y. That is, $f_n^{SBT}(a+bi) = f_n^{SBT}(a) + f_n^{SBT}(b)\,i$.

Figure 5-11 shows that within the reasonable range of number of discretization, f_n^{SBT} is consistently less negative, or more positive, as compared to f_n^{RFT} throughout the entire flagellum. Therefore, the numerical solution diverges upwards in the positive y-direction. Similar to the case in the normal direction, the force acting on the flagellum in the x- and y-direction are also of smaller when computed using SBT instead of RFT. As such, the swimming velocity computed by SBT would be lower, as confirmed by Higdon (1979) that Lighthill's resistive coefficients overestimates the swimming speed.

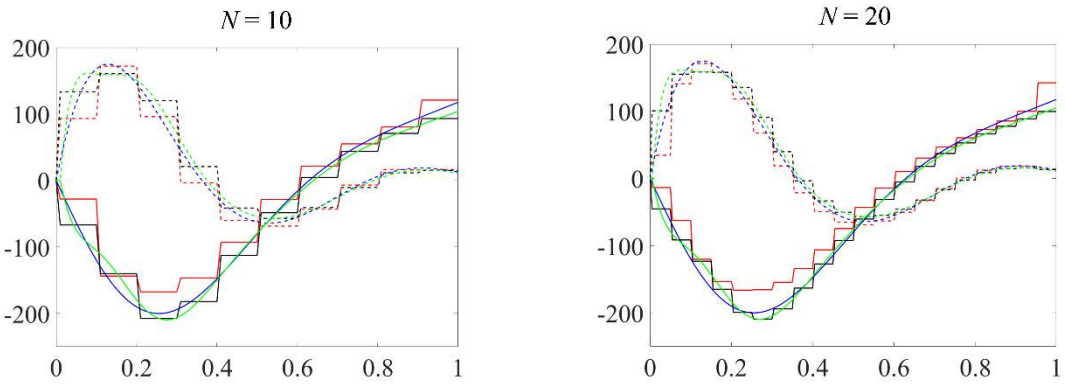

Figure 5-11 – Non-dimensionalised force per unit length, multiplied by the relevant coefficients in the differential equations, along the curvilinear coordinate $\tilde{s}$ of the flagellum. The blue line represents $i\,\mathrm{Sp}^4 h$, the green line represents f_n^{RFT} for a continuous flagellum, while the black and red lines represent f_n^{RFT} and f_n^{SBT}, respectively, for a discretized flagellum varying from $N = 10$ to $N = 20$ discrete segments.

Given that the result is sensitive to both the real and imaginary parts of the complex initial conditions, of which $y'|_{\tilde{s}=0}$ and $y'''|_{\tilde{s}=0}$ have to be guessed, the integration often diverges before the end of the interval, resulting in unphysical amplitudes greater than the flagellum arclength itself. Small adjustments in the initial conditions results in different flagellum pattern, making the solution highly dependent on the initial guess. Figure 5-12 shows the numerical solutions obtained from a flagellum with SBT force distribution, with the guessed initial conditions being multiplied by adjustment factors of various combinations such that the resulting waveform has an amplitude of approximately 0.10.

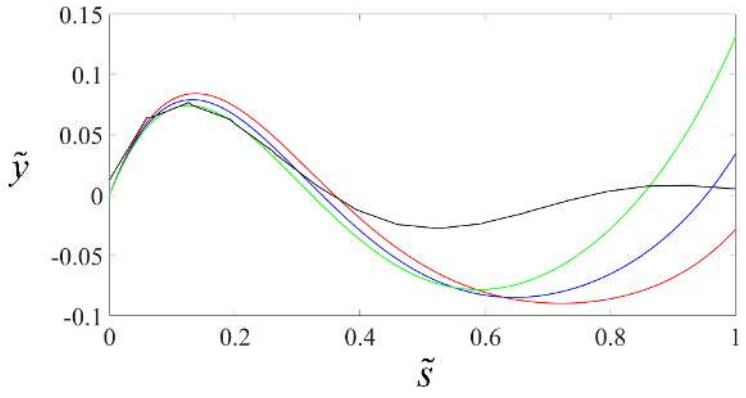

Figure 5-12 – Numerical solutions corresponding to initial conditions $[y\ y'\ y''\ y''']\big|_{\tilde{s}=0}^{\text{guess}} = [y\ 1.08{*}y'\ y''\ 0.895y''']\big|_{\tilde{s}=0}^{\text{FDA}}$ (green), $[y\ y'\ y''\ y''']\big|_{\tilde{s}=0}^{\text{guess}} = [y\ 1.05{*}y'\ y''\ 0.90y''']\big|_{\tilde{s}=0}^{\text{FDA}}$ (blue), and $[y\ y'\ y''\ y''']\big|_{\tilde{s}=0}^{\text{guess}} = [y\ 1.02{*}y'\ y''\ 0.91y''']\big|_{\tilde{s}=0}^{\text{FDA}}$ (red line), plotted against the analytical solution discretized into 15 straight segments (black line).

Although quite different from the analytical solution to the approximate RFT model, the alternative waveforms as shown above appears plausible. However, a necessary, though not sufficient, condition for the flagellum waveform to be accepted is for all four boundary conditions to be satisfied. The boundary conditions of zero net moment or shear force at the free end and zero displacement or moment at $\tilde{s}=0$, as presented in equations (4.20) to (4.23), is expressed here using the finite difference approximation (Fornberg 1988).

$$\tilde{y}\big|_{\tilde{s}=0}=0 \tag{5.68}$$

$$\frac{\frac{15}{4}y\big|_{\tilde{s}=0}-\frac{77}{6}y\big|_{\tilde{s}=\Delta s}+\frac{107}{6}y\big|_{\tilde{s}=2\Delta s}-\frac{13}{1}y\big|_{\tilde{s}=3\Delta s}+\frac{61}{12}y\big|_{\tilde{s}=4\Delta s}-\frac{5}{6}y\big|_{\tilde{s}=5\Delta s}}{\left(\Delta s\right)^2}+\tilde{f}_m=0 \tag{5.69}$$

$$\frac{\frac{15}{4}y\big|_{\tilde{s}=1}-\frac{77}{6}y\big|_{\tilde{s}=1-\Delta s}+\frac{107}{6}y\big|_{\tilde{s}=1-2\Delta s}-\frac{13}{1}y\big|_{\tilde{s}=1-3\Delta s}+\frac{61}{12}y\big|_{\tilde{s}=1-4\Delta s}-\frac{5}{6}y\big|_{\tilde{s}=1-5\Delta s}}{\left(\Delta s\right)^2}=0 \tag{5.70}$$

$$\frac{\frac{49}{8}y\big|_{\tilde{s}=1}-\frac{29}{1}y\big|_{\tilde{s}=1-\Delta s}+\frac{461}{8}y\big|_{\tilde{s}=1-2\Delta s}-\frac{62}{1}y\big|_{\tilde{s}=1-3\Delta s}+\frac{307}{8}y\big|_{\tilde{s}=1-4\Delta s}-\frac{13}{1}y\big|_{\tilde{s}=1-5\Delta s}+\frac{15}{8}y\big|_{\tilde{s}=1-6\Delta s}}{\left(\Delta s\right)^3}-\tilde{f}_m=0 \tag{5.71}$$

The error in the boundary conditions of the analytical solution are in the order of 10^{-5} or less. However, the error corresponding to the visually-plausible numerical solutions of the SBT model are of order 10^0 to 10^1. Given that $y'\big|_{\tilde{s}=0}$ and $y'''\big|_{\tilde{s}=0}$ have to be guessed when solving the IVP, there are four components in the initial conditions which influence the flagellum waveform, namely, the real and imaginary parts of those two derivatives. What we have is essentially an optimisation problem, as the objective is to find a set of initial conditions which minimizes the error in the four boundary conditions. The local minimum can be found via the steepest descent which is an iterative optimization algorithm that is applicable to both linear as well as many non-linear problems (Fletcher 2013, Kelley 1999). However, the force and moment at the ends of the flagellum are obtained from a finite difference approximation of the numerical solution to the governing differential equation, of which an input is the hydrodynamic force acting on the flagellum that is itself non-linear in the SBT model. There is no straightforward way to express the gradient of the function to be minimized in terms of the initial conditions, and attempts to write an algorithm for this problem will be beyond the scope of this project. In addition to satisfying the boundary

conditions, there is an added requirement of the solution needing to have a physically realistic waveform with an amplitude in the order of 10^{-1} times the flagellum length.

Another approach taken to solve for the waveform by trial coupled with interpolation have also proved futile. Changing only a single component of the initial conditions each time while holding all else constant, it is found that even small systematic variations to the initial conditions, which lead to only a slight observable difference in the flagellum waveform, resulted in erratic changes in $y'''|_{\tilde{s}=1}$ where the local minimum error in the boundary conditions are of magnitude 1.

With the SBT force being a function of the governing equation, no solution is found to perfectly satisfy all boundary conditions simultaneously. This might be attributable to the fact that we are seeking a solution to only the first round of an iteration, given that the hydrodynamic force is computed on the basis of an assumed flagellum waveform, namely, that which follows the analytical solution in the RFT model. A causality dilemma, more commonly known in layman terms as the 'chicken and egg problem', is encountered because $\mathbf{F}^{SBT}$ is required to compute $y(s,t)$ but is itself a function of $y(s,t)$ and $\dot{y}(s,t)$ at the same time.

There are two cycles in this inherent causality dilemma (Figure 5-13). The framework of SBT requires the relative position of each segment of the filament to be known before the hydrodynamic force can be computed. Furthermore, the relative fluid velocity, and hence the time-rate of change of each segment of the flagellum, is required in order to compute the new hydrodynamic force for the numerically-determined flagellum shape. This would involve solving for the shape at the next time step, and taking a finite difference approximation between the flagellum position at time t and ($t + dt$). However, the shape at ($t + dt$) is itself an estimated solution just like the waveform at time t, and the hydrodynamic force acting on the flagellum at this instance is unknown. To obtain an accurate force distribution in the differential equation, the time-derivative at each point of the flagellum is required, which in turn requires knowledge of the flagellum shape at ($t + 2dt$), as illustrated in Figure 5-14. Repeating this process over the entire flagellum wiggling period completes the first round of iteration, after which the hydrodynamic force corresponding to the numerically-solved shape at time t can be determined. As this force distribution will not be identical to the approximated

force distribution derived from the analytical solution, it in turn leads to a new numerically-determined flagellum shape, and hence a new force distribution.

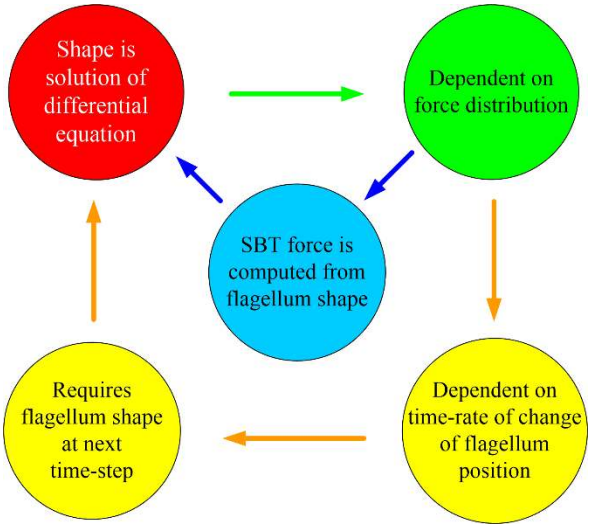

Figure 5-13 – Causality dilemma encountered in solving for the flagellum shape using Slender Body Theory.

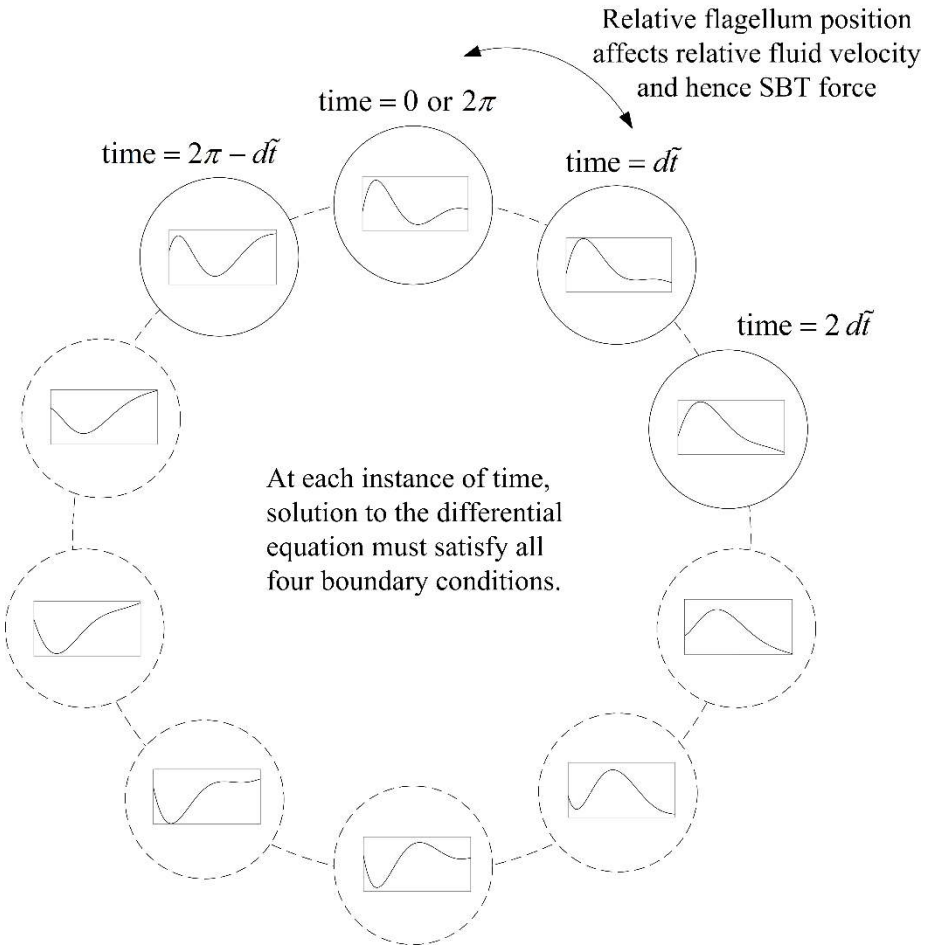

Figure 5-14 – Illustration of how the flagellum waveform at different phases of a beating period are related.

The demanding requirements associated with using SBT to solve for the shape of a sperm flagellum might explain why, to the best of the author's knowledge, there have yet to be publications on this research gap. Before investing resources to solving this unknown, we should recall that the governing equation established to describe the flagellum waveform is itself an approximation, whereby the wiggling motion is modelled to be driven by microtubles with an internal sliding force of a prescribed direction and distribution (Figure 4-1).

Revisting the objectives of this thesis, the purpose of determining the flagellum waveform is to compute the swimming velocity of sperm cells subjected to DEP force, to find out if the variation in morphology translatates to a substantially different velocity distribution that allows for sorting. Using the RFT model, it has been found (Koh and Marcos 2015b) that moderate magnitudes of DEP force can alter the kinematics of a sperm cell by a few times its free-swimming velocity, without any significant influence on its flagellum waveform. While the waveform does affect the free-swimming velocity as well as drag, the force from an external field, which is a function of the cell morphology, dominates. The objective of this thesis is not to compute the swimming velocity of a sperm precisely, but to incorporate variations between individual sperm cells and investigate their relative velocities in an overall distribution. Therefore, a prescribed sinusoidal waveform will be utilised in the subsequent simulations for statistical analysis on the feasibility of sorting by morphology.

5.6 Chapter Summary

The mathematical procedures for applying SBT to compute the force and hence swimming velocity of a sperm is presented. The qualitative and quantitative differences between RFT and SBT are then discussed. Modelling the sperm flagellum as discrete straight segments with a constant force within each segment, the resulting instantaneous velocity computed from RFT and SBT show a similar trend albeit with a one-fifth difference in magnitude. The complexity associated with solving for the waveform was illustrated. Keeping to the scope of this thesis, the conclusion reached was that prescribing a sinusoidal waveform is appropriate for predicting the velocity distributions in the following chapter.

Chapter 6
Statistical Analysis[5] and Machine Learning[6]

Considering ethical concerns involved in carrying out experiments with human sperm, it is beneficial for researchers to first carry out theoretical studies to assess the feasibility of sorting using various techniques under different experimental set-ups. Mathematical models of increasing complexity and accuracy have been developed to understand the kinematics of micro-swimmers such as sperm cells (Gaffney *et al*. 2011). These theoretical computations are often taken from the deterministic approach. However, as sperm cells differ in their morphology, more insights can be gained by studying their behaviour from a statistical approach. In spite of technological advances, precise theoretical models are still computationally expensive, and running numerical simulations for a large number of samples to obtain statistically reliable results may be time-consuming.

In this chapter, statistical analysis will be carried out to study the sorting of spermatozoa via magnetophoresis. Thereafter, the feasibility of using machine learning to save computational or laboratory costs will be investigated (Koh *et al*. 2018). The findings can be generalised to other theoretical simulations utilising a different mathematical model, as well as to experimentalists obtaining actual data.

6.1 The model

As discussed in Chapter 2, sperm cells may be doped with paramagnetic nanoparticles or manipulated in its natural form by diamagnetic force in the presence of a magnetic field. Given that sperm cells subjected to magnetic fields have been reported to maintain its fertilisation potential (Rawe *et al*. 2010) and even lead to a healthy baby borned from ICSI (Ben-David Makhluf *et al*. 2006), the feasibility of sorting will now be explored with a magnetic rather than electric field. SBT, which has been experimentally verified to produce accurate computation results (Autrusson *et al*. 2011),

[5] Published in Koh JBY, Marcos (2017) Sorting spermatozoa by morphology using magnetophoresis. *Microfluidics and Nanofluidics* 21:75

[6] Published in Koh JBY, Shen X, Marcos (2018) Supervised learning to predict sperm sorting by magnetophoresis. *Magnetochemistry* 4:31

will be utilised according to the framework presented in Chapter 5.1.

Since the motion of a human sperm is highly directional (Gillies *et al*. 2009), we consider the sperm to be in a two-dimensional plane for computational efficiency. The flagellum is modelled to follow a sinusoidal waveform (Fulford *et al*. 1998), modified with an exponential factor to ensure that the prescribed flagellum is attached to the sperm head with no deflection at the fixed end:

$$y(x,t) = b\sin\left(2\pi x/\Lambda - \omega_{wave}t\right)\left(1-\exp\left(-\frac{x/\Lambda}{k_E}\right)^2\right) \tag{6.1}$$

where the variables and subsequent non-dimensionalisation follow the same definitions presented in Chapter 3. k_E controls the tapering (David *et al*. 1981) of the flagellum and is chosen to be 1/4 which gives a fair depiction of the actual sperm beating pattern (Ishijima *et al*. 1986). At each time frame, the axial length x_f is computed to satisfy $\int_0^{x_f}\sqrt{1+\left(\partial y/\partial x\right)^2}\,dx = \Lambda$. In accordance with the SBT framework, the flagellum is discretized into 15 discrete segments (Figure 6-1), each of length $2q$ where $p << q << \Lambda$, with a constant force per unit length $\mathbf{f}$ on each segment. Each segment has a local coordinate system $\left(X^L, Y^L\right)$ where its origin at the centre, with the X^L axis tangential to the flagellum centreline and at an angle θ with respect to the x-axis of the body-frame.

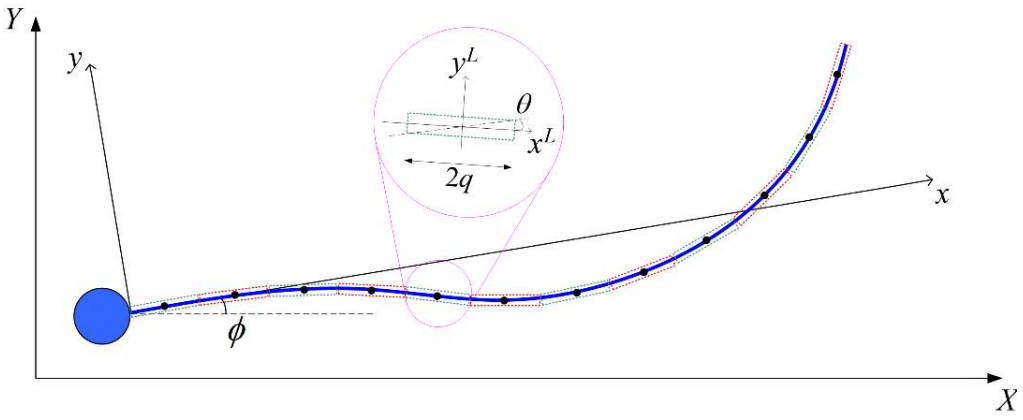

Figure 6-1 – Flagellum comprising *N* discrete straight segments, each represented by a dotted rectangle. Inset: The local coordinate system x^L and y^L of a segment at an angle θ with respect to the general *x*-axis of the body-fixed frame *x*-*y*.

A diluted sperm sample shall be considered, such that the effects of cell-to-cell interactions are negligible (Drescher *et al*. 2011; Keaveny and Maxey 2008). For a

sufficiently large channel, the swimming velocity is also largely uninfluenced by wall effects (Koh *et al*. 2016) for most locations and will be ignored here, as the focus is on statistical analysis and machine learning.

Since the magnetic field can be designed to give a magnetic force perpendicular (Moore *et al*. 2001) or parallel (Watarai and Namba 2002) to the flow direction, the magnetic field will be modelled as $\mathbf{B} = (C_1 + C_2 x)\mathbf{i}$, resulting in $(\mathbf{B}\cdot\nabla)\mathbf{B}$ being approximately constant when C_2 is small (Koh and Marcos 2017). Consequently, the magnetic force

$$\mathbf{F}_B = \frac{(\chi_p - \chi_m)}{\mu_0}(\mathbf{B}\cdot\nabla)\mathbf{B}\forall \tag{6.2}$$

is simplified to

$$\mathbf{F}_B = C_0 \forall \mathbf{i}\,, \tag{6.3}$$

where C_0 is a function of the magnetic field as well as relative magnetic susceptibility. A positive C_0 indicates either positive magnetophoresis with an increasing magnetic field density along the positive $\mathbf{i}$ direction, or negative magnetophoresis with a decreasing magnetic field density. The converse is true for a negative C_0.

The magnetic force acting on the sperm head and each segment of the flagellum is $\mathbf{F}_{B,head} = (4/3)\pi a^3 C_0 \mathbf{i}$ and $\mathbf{F}_{B,segment} = \pi p^2 (\Lambda/N) C_0 \mathbf{i}$. The total hydrodynamic and magnetic force and moment is then summed over the entire sperm, expressed as a function of its linear and angular velocity as presented in Chapter 5.3. Given that the net force and moment acting over the entire sperm is zero under low Reynolds number, the time-dependent velocity can be obtained by matrix arithmetic. The trajectory of the swimming sperm can subsequently be obtained by transforming between the body-frame and inertia frame, as described in Chapter 4.2.

The sperm magnetic susceptibility is absorbed into the variable C_0 instead of being considered independently. The combined effect of the magnetic field and its gradient, as well as the relative magnetic susceptibility can be adjusted collectively to obtain the desired force per unit volume. In addition, the magnetic properties of the sperm head and flagellum are assumed to be similar. As discussed in Chapter 1, the objective of this thesis is not to provide a precise calculation of velocity under an

external electric or magnetic field, but rather to assess the feasibility of sorting to improve the proportion of morphologicaly normal sperm cells. The actual velocity might differ slightly from the theoretical model, but it is postulated that any difference applies to all sperms, normal or abnormal, such that the relative velocity distribution of the population remains similar. While the sperm cells may be in a different region of the microchannel, those which are computed to swim faster will still be ahead of others, while the slower ones will still lag behind. The premise of sorting in this thesis is that spermatozoa respond differently in accordance to their physical morphology, and that any approximations made or effects not accounted for by the theoretical model will influence all cells to the same extent and hence cancel out. Similarly, any synchronisation between sperm, or modifications to the external field due to the presence of neighbouring cells, are treated in the same light. Given that the application is for sorting in a controlled laboratory environment, biological sperm response such as hyperactivation are taken to be irrelevant.

The introduction of an external force results in a stabilising effect (Koh *et al.* 2018), such that the x-axis of the body-frame tends to be aligned with the magnetic force. This is because there are two dominant forces on the sperm; the external magnetic force acting on the head and the drag force acting in the opposite direction on the flagellum. Consider a sperm swimming towards the negative x-direction under an external force acting in the same direction. If it is perturbed clockwise, there will be a net anti-clockwise restoring moment, and vice-versa if perturbed in another direction. Even if the sperm is initially heading in the opposite direction, a C_0 value of 0.1 mN/mm^3 will cause the sperm to be aligned with the direction of the applied force within 20 seconds and continue swimming in that direction thereafter (Figure 6-2). As such, the initial orientation is not assumed to be random; instead, all sperm cells are defined to be heading in the same direction as the magnetic force. Since the cells are swimming in the negative x-direction by definition of the flagellum waveform, only negative values of C_0 are considered. This is because a positive C_0 will cause the sperm to turn around to the positive x-direction, leading to a similar scenario as considered here.

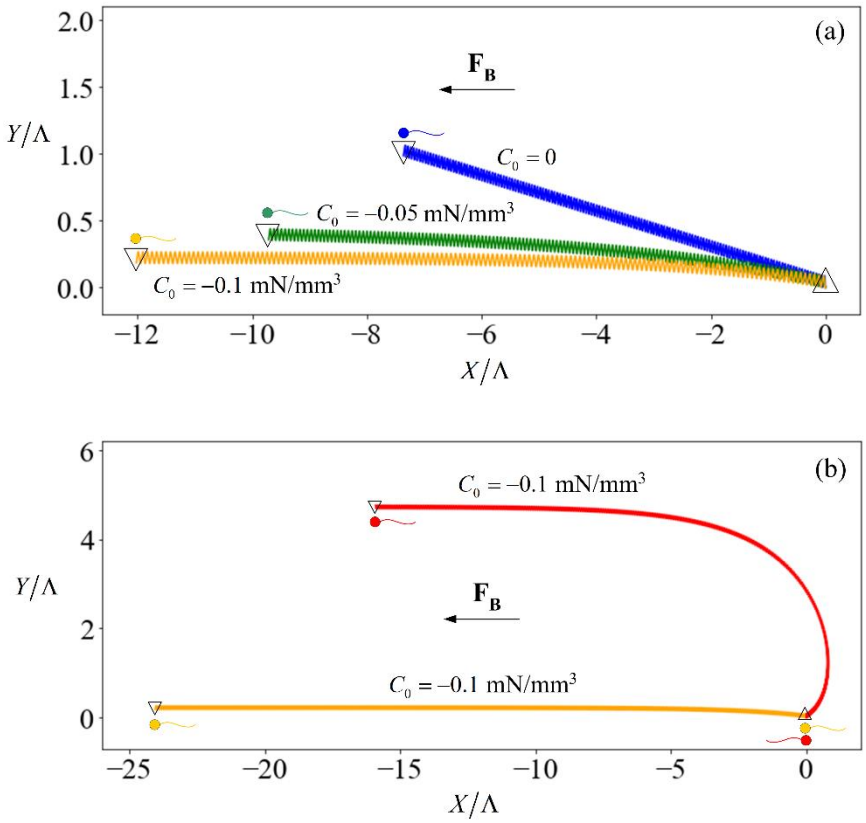

Figure 6-2 – (a) Trajectory of spermatozoa, initially heading in the negative *x*-direction, subjected to C_0 = - 0.1 mN/mm^3 (orange line), - 0.05 mN/mm^3 (green line), and 0 (blue line) over 10 seconds. (b) Trajectory of spermatozoa, initially heading in the negative (orange) or positive (red line) *x*-direction, subjected to C_0 = - 0.1 mN/mm^3 for 20 seconds. In both plots, the upward-pointing triangles denote the starting position of the sperm while the inverted triangles denote the ending position. The horizontal and vertical axes are the *X*- and *Y*-position of the inertial frame, normalised with respect to the flagellum arclength.

6.2 Sperm morphology and sorting assessment

Assessment of sperm which satisfies the strict (Tygerberg) condition gives a good indication of the expected fertilisation rates (Menkveld and Kruger 1995). Quantitatively, the sperm should have a head length of 3 to 5 µm and width of 2 to 3 µm, as well as a head width to length ratio of between three-fifths and two-thirds, with a tail measuring about 45 µm in length (Menkveld *et al*. 1990). As the biological aspects of spermatozoa are not considered here, a cell which fulfils these physical dimensions will be deemed as conditionally satisfactory and termed as 'normal', while a cell which fails at least one condition will be classified as 'abnormal'.

The physical parameters and flagellar beat frequency vary in a normal distribution. A human sperm head has a length of 4.81 ± 0.43 µm and width of 3.32 ± 0.38 µm (Katz *et al*. 1986), and a flagellum length of 42 ± 4 µm (Cui 1997). Using

MATLAB® 2016b and setting the seed number as i for the i^{th} sperm, a pseudo-random value is generated for each parameter, independently of one another. The beat frequency and amplitude are then generated using the relevant mean and standard deviation based on the category (Table 6-1) which the sperm belongs to (Katz *et al.* 1982). The proportion of cells classified as 'normal' by this approach is around 11%. This is reasonable, given that the proportion of normal cells is reported to be 6.5 ± 3.9% (Menkveld *et al.* 2001).

Table 6-1 – Categories of sperm according to their head morphology, and the corresponding flagellum beat frequency and amplitude given with their respective standard deviations. Data from Katz *et al.* (1982).

Types of head	Normal	Amorphous	Elongated tapering	Piriform tapering	Megalo-cephalic
length / µm	3 – 5	3 – 5	> 5	3 – 5	> 5
width / µm	2 – 3	> 3	< 3	< 2	> 3
f / Hz	15.2 ± 0.7	13.3 ± 1.0	13.0 ± 0.9	12.2 ± 1.3	11.2 ± 1.4
b / µm	4.76 ± 0.27	4.73 ± 0.43	4.98 ± 0.33	5.36 ± 0.45	4.96 ± 0.70

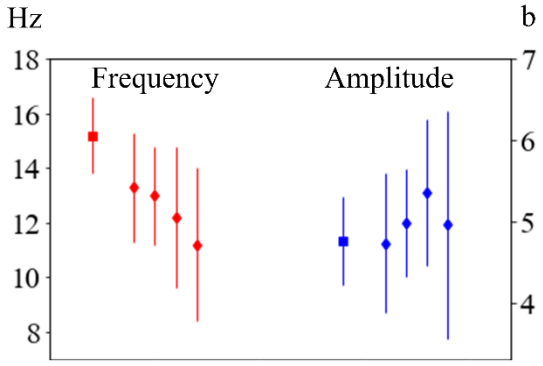

Figure 6-3 – Frequency in Hz (plotted red, with respect to left vertical axis) and amplitude in µm (plotted blue, with respect to right vertical axis) of the different categories of sperm. Mean values are represented with a square marker (for normal sperm) or diamond marker (for amorphous, elongated tapering, piriform tapering and megalocephalic sperm), with error bars extending to two standard deviations.

Due to differences in the sperm parameters, the velocity distribution differs between normal and abnormal sperm. One possibility of sorting the cells is to introduce an opposing flow equal in magnitude to the chosen cut-off velocity. In low shear rates where the non-dimensionalised shear $Z = \dot{\gamma}/(2\pi f)$ is in the order of 0.1, the effect of shear has insignificant influence on the flagellum waveform or sperm velocity (Marcos

et al. 2014). Considering the channel dimensions to be much greater than the sperm characteristic length, the flow far from the walls acts as a bulk advection (Koh and Marcos 2017). Cells with velocities less negative than the cut-off will acquire a net positive velocity due to advection in the positive x-direction and be eventually flushed out of the right end of the channel (Figure 6-4). Meanwhile, those which overcome the advection will have a net negative velocity and head towards the left end of the channel. The proportion of normal cells can be increased by modifying the cut-off velocity, but will have to come at the expense of discarding some normal cells as well.

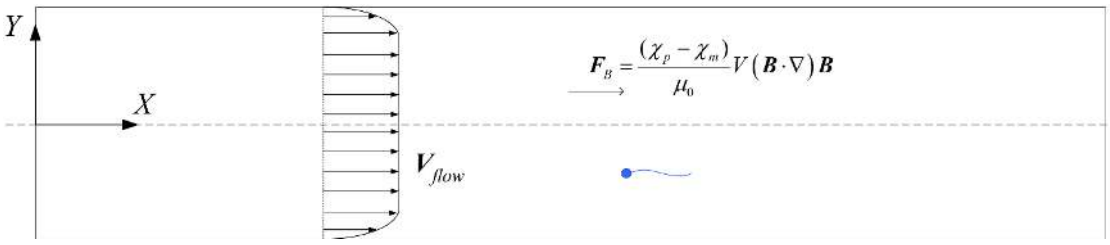

Figure 6-4 – Sperm in 2D channel heading in the negative *X*-direction, subjected to magnetic force and a flow in the positive *X*-direction.

For sorting to be effective, the percentage of conditionally satisfactory spermatozoa in the sorted sample should be meaningfully higher, so as to improve the odds of a morphologically normal sperm fertilising the oocyte. At the same time, the absolute number of satisfactory spermatozoa should remain high after sorting. Therefore, the effectiveness of sorting will be accessed according to the purity χ and yield η as defined here:

$$\chi = \frac{\text{number of conditionally satisfactory sperm collected}}{\text{total number of sperm collected}}, \tag{6.4}$$

$$\eta = \frac{\text{number of conditionally satisfactory sperm collected}}{\text{initial number of conditionally satisfactory sperm}}. \tag{6.5}$$

To illustrate how χ and η changes, consider a initial sample comprising 100 sperm cells, of which 11 are conditionally satisfactory. Suppose we collect 50 of those from sorting, of which 10 sperm cells satisfy the criteria for being conditionally satisfactory. The sorted sample will thus have an improved χ_{CS} of 20%, while η_{CS} will be 91% since 10 out of the 11 desired cells are collected.

6.3 Statistical analysis

Before proceeding, it is necessary to determine the quantity of data required to obtain convergence in the results, so that a benchmark is available for subsequent comparisons. The cumulative mean flagellum length, head length, and computed velocity are presented in Figure 6-5, normalised with their respective mean values obtained from 100,000 samples. For the avoidance of doubt, this sample size is chosen *a posteriori*, after convergence is obtained. The normalised value ψ is

$$\psi = \frac{\left(\sum_{i=1}^{n} \varphi_i\right) \Big/ n}{\left(\sum_{i=1}^{n_{final}} \varphi_i\right) \Big/ n_{final}}, \tag{6.6}$$

where n is the sample size considered, n_{final} is 10^5, and φ is the sperm parameter of interest. The proportion of morphologically normal cells, which is the purity before sorting, is presented in its absolute percentage points as a function of the sample size.

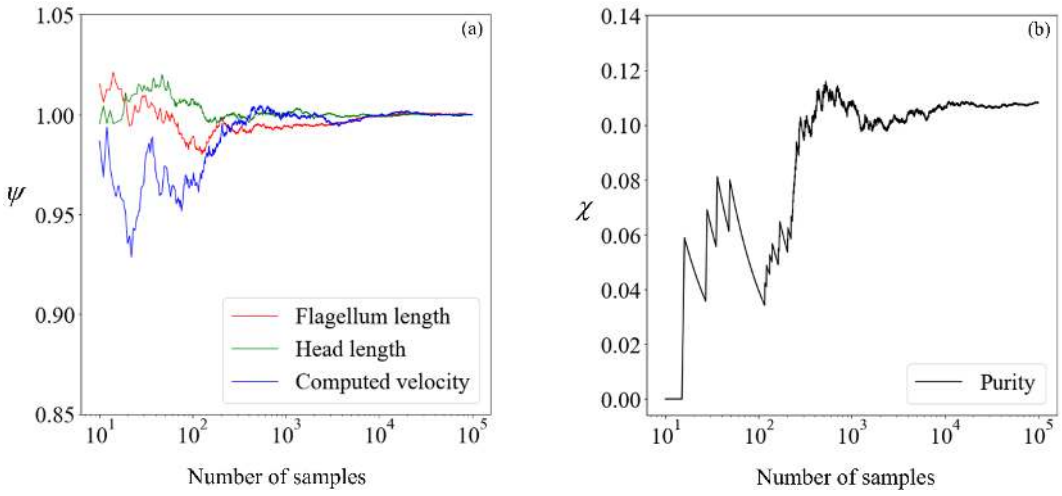

Figure 6-5 – (a) Cumulative mean flagellum length (red line), head length (green line), and computed velocity (blue line) normalised with respect to mean values obtained from 100,000 samples. (b) Proportion of morphologically normal cells in percentage points. The *x*-axis, in logarithmic scale, of each plot denotes the number of samples used in the computation.

Given that there are little fluctuations in all parameters when the sample size is increased from 10^4 to 10^5, results computed using 100,000 samples will be deemed to have converged. The achievable purity corresponding to a target yield of 50% to 90% is

computed for 21 different values of C_0 ranging from 0 to -1 mN/mm^3 in intervals of 0.05 mN/mm^3. Each marker in Figure 6-6 denotes the resulting purity obtained by running the full computation on 100,000 samples and ranking all cells by their velocity. Based on the target yield, a cut-off velocity necessary to keep the required number of normal sperm cells is determined, and all cells having at least this minimum velocity are deemed to be collected. A best-fit polynomial is then added to the plot.

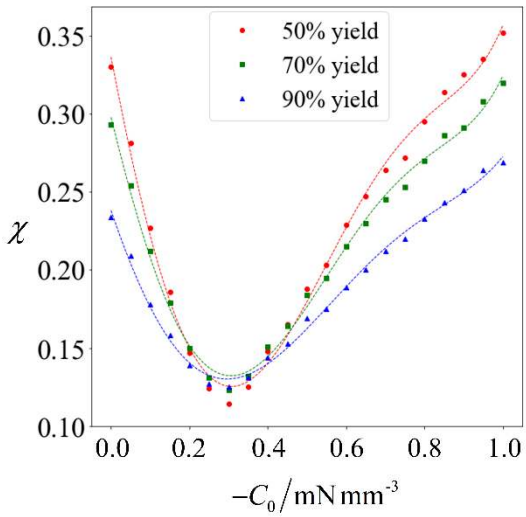

Figure 6-6 – Purity as a function of C_0. The red circles, green squares and blue triangles denote the computed purity corresponding to a yield of 50%, 70% and 90%, respectively. The dotted lines in matching color are the best-fit polynomials.

It can be observed that when the magnitude of C_0 increases, the achievable purity initially decreases. This is because the normal cells generally have a higher speed than abnormal ones. Since the abnormal sperm are generally larger than the normal ones, they are more strongly influenced when subjected to the external force. As C_0 is in the swimming direction of the sperm cells, it increases the speed of the abnormal cells to a greater extent than their normal counterparts, hence causing the abnormal cells to catch-up. Under weak magnetophoresis, the relative shift in velocity distribution causes the two categories to become less distinct, because the abnormal sperm will be moving amongst the normal ones. However, increasing the strength of magnetophoresis further will increase the extent of the relative shift and eventually amplify the differences. When the magnitude of C_0 increases beyond 0.9 mN/mm^3, sorting can further improve the proportion of normal cells.

To assess the feasibility of sorting sperm with a magnetic force in the order of 1 mN/mm^3, consider $C_0 = \left(\chi_p - \chi_m\right) C_1 C_2 \big/ \mu_0$ as derived from equations (6.2) and (6.3). Given that the magnetic susceptibility of sperm cells is similar to that of water (Senftle and Hambright 1969), $\left(\chi_p - \chi_m\right) \big/ \mu_0$ is in the order of 10^{-1} for sperm in non-magnetic medium, for which a very large magnetic field gradient is required to achieve $\left|C_0\right| = 1$ mN/mm^3. Hence, it may be more appropriate to dope the sperm with paramagnetic particles or use a magnetic fluid medium. For small values of χ_p and χ_m where demagnetization effects (Aharoni 2000) can be neglected, the doping has to be limited such that $\chi_p - \chi_m$ is of order 10^{-1} or smaller. For $\left|C_0\right| = 1$ mN/mm^3, the minimum value of $C_1 C_2$ has to be 10, which can be attained using $B_X = 5 + 2X$ so that $\mathrm{O}(C_2 X) \ll \mathrm{O}(C_1)$ in the scale of a microchannel. This corresponds to a magnetic field of 5 T, which is technically achievable (Singleton *et al*. 2004) but its effects on the viability of sperm cells has not been reported to the best of the author's knowledge and remains to be verified. To use a weaker magnetic field with a ceiling of 1.5 T (Said *et al*. 2005), which human sperm cells have been reported to remain viable in, the value of $\chi_p - \chi_m$ has to be of order unity. In this case, demagnetization effects will have to be considered and accounted for, which is beyond the scope of this thesis. The focus of this chapter is on the analysis procedure utilising supervised learning. The use of magnetism for biological applications is an exciting field which warrants many follow-up experimental work as well as detailed theoretical analysis, and hopefully this chapter can provide insights and serve as a framework for future studies.

6.4 Supervised learning to predict sperm sorting

In spite of technological advances, precise theoretical models are still computationally expensive, and running numerical simulations for a large number of samples to obtain statistically reliable results may be time-consuming. The use of machine learning (Michalski *et al*. 2013) has been proven to provide accurate predictions and is gaining popularity, but its use in microfluidics research is still not widespread despite the great potential. Moving forward, the feasibility of running the

simulation on a smaller number of samples and making use of supervised learning to predict the expected purity will be looked into.

Using supervised learning algorithms from Python's sklearn package (Pedregosa *et al*. 2011), we build four models using the input variables of the training set. Namely, the models used are k-nearest neighbour regression (Burba *et al*. 2009), ridge regression (Khalaf and Shukur 2005), random forest regression (Liaw and Wiener 2002), and artificial neural network (Krogh 2008). In k-nearest neighbor regression, the predictor and target variables of all known samples are stored. For each new data to be predicted, only the k samples having the least 'distance' will be considered, with the simple or weighted-average value taken. Ridge regression is linear regression with L2 regularization, where a penalty term is added to the sum of square errors to be minimized, thus avoiding overly-large coefficients in the linear model. In a random forest model, a large number of decision trees is built, each using a subset of predictor variables so as to avoid overfitting. For each decision tree, the population is split based on one variable at a time, where the chosen variable as well as threshold determining the split minimizes the sum of square errors (in the case of regression). In artificial neural networks, the first layer or nodes receives input from the predictor variables, adds a bias to the weighted sum and passes it through a non-linear function, and feeds the output to the subsequent layer of nodes. This continues until an output is obtained from the final single node after the hidden layer. The weights and bias are 'learnt' by minimizing the cost function via optimization. Each model has its own hyperparameters to be tuned, and there are also other well-established supervised learning algorithms, but the four mentioned above will suffice for the scope of this thesis.

It takes 3.0 seconds on a Windows® 64bit PC (CPU E5–1650 v4, 64Gb RAM) to prescribe the flagellum shape, perform the steps listed in equations (5.1) to (5.24) for each instance in time and repeat over a complete beating cycle. This adds up to over three days per 100,000 computations. On the other hand, the above-mentioned algorithms can 'learn' from a known training set of 10,000 samples and make predictions on the remaining samples in less than five minutes. The suitability of using supervised learning to predict sperm velocity will be put to test here.

First, supervised learning will be implemented using each of the above-mentioned four algorithms to train a model using a prescribed number of sample data.

The sperm velocity is predicted using only the following six variables as inputs; the flagellum length, the head length and width, the beating frequency and amplitude, and the applied field strength. Each sperm will be classified as collected or excluded depending on its velocity relative to the overall distribution. The purity predicted by each algorithm trained on a tenth of the total samples is compared (Figure 6-7) with the purity obtained by computing the velocities of all 100,000 samples for each case, where statistics obtained from a sample size of 100,000 are deemed to have converged (Figure 6-5). A slight offset in the horizontal position is deliberately added for better visualisation of overlapping points.

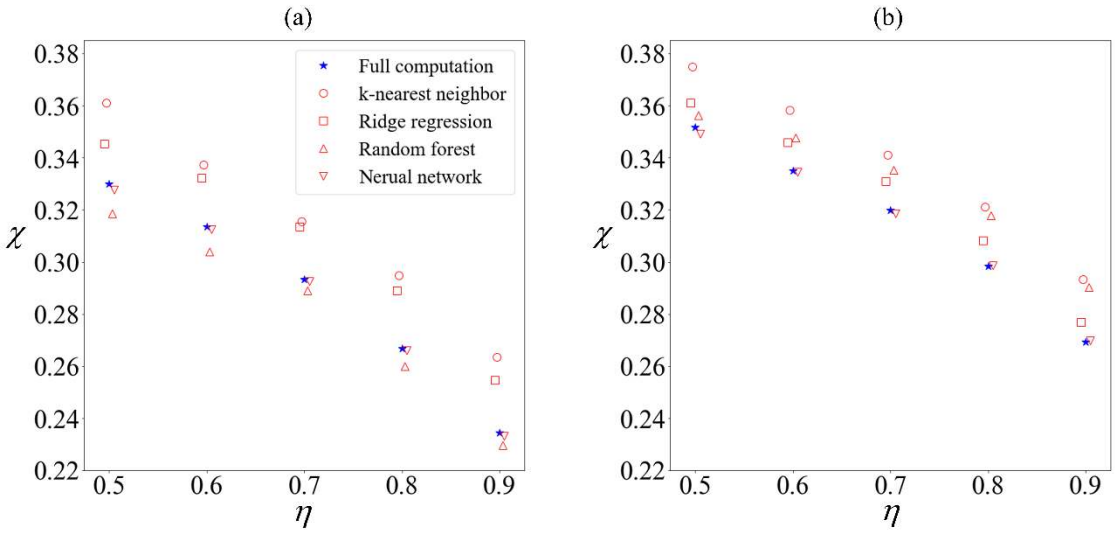

Figure 6-7 – (a) Sperm subjected to no external field, versus (b) sperm subjected to C_0 of -1 mN/mm^3. Purity χ computed using 100,000 samples (blue star) for different yield η, compared with purity obtained from supervised learning algorithms trained on 10,000 samples to predict remaining 90,000 samples (hollow red markers) using k-nearest neighbor (circle), ridge regression (square), random forest (triangle) and artificial neural network (inverted triangle).

There are minor variations in the predictions of each algorithm, regardless of whether an external field was applied. However, given that none of them are outliers, the four algorithms will remain in the ensemble. Without the benefit of hindsight, it can not be known which algorithm gives a closer prediction to the 'true' result. This is consistent with the fact that ensembles often out-perform (Dietterich 2000) their individual components, because there is no single best learning algorithm (Kotsiantis *et al*. 2007). Moving forward, the mean prediction obtained from k-nearest neighbour, ridge regression, random forest regression, and artificial neural network will be used.

The velocity of 10^5 sperm cells under no external field and subjected to C_0 = -1 mN/mm^3 are first obtained by randomly generating parameters of each individual cell and computing its velocity. 10% of the data are placed in the training set, while the other 90% are placed in the test set. Data in the test set is unseen in the training process, so as to give a fair validation of the model and avoid overfitting (Krogh and Vedelsby 1995). The velocity distributions of samples in the test set are presented (Figure 6-8a and Figure 6-9a) as histograms of normal cells super-imposed with that of abnormal cells. The machine learning model is then trained to learn a relationship between input parameters and the computed velocity in the training set. Thereafter, the velocity distribution of the unseen 90,000 cells is predicted as shown in Figure 6-8b and Figure 6-9b.

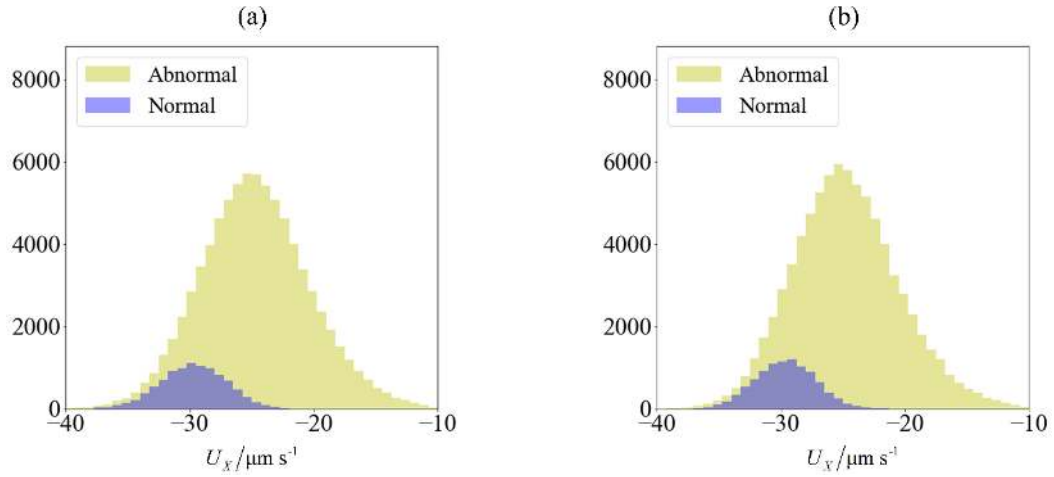

Figure 6-8 – Velocity of spermatozoa in the test set of 90,000 samples (a) computed using SBT computation and (b) obtained from predictions made using an ensemble of supervised learning trained on 10,000 samples. The blue and green region represents the number of morphologically normal and abnormal cells, respectively. The sperm cells are not subjected to any applied field (C_0 = 0).

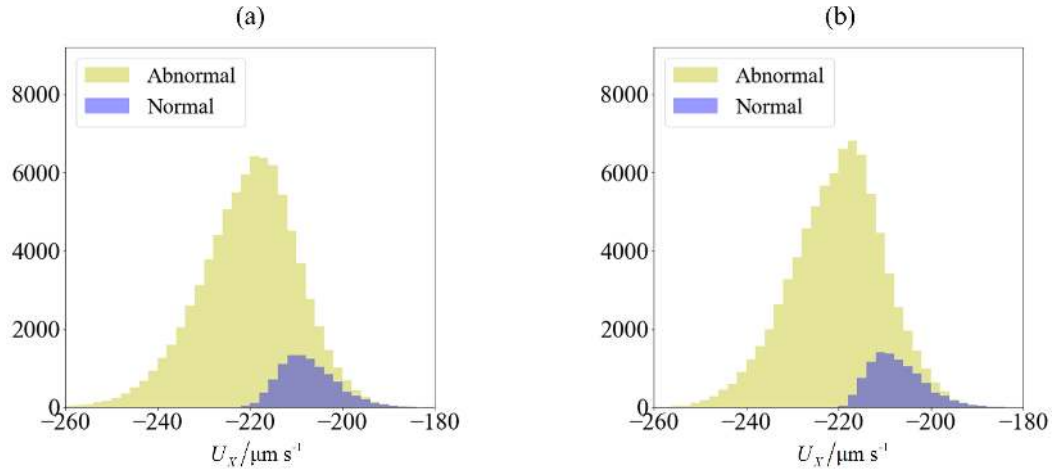

Figure 6-9 – Velocity of spermatozoa in the test set of 90,000 samples (a) computed using SBT computation and (b) obtained from predictions made using an ensemble of supervised learning trained on 10,000 samples. The blue and green region represents the number of morphologically normal and abnormal cells, respectively. The sperm cells are subjected to C_0 = -1 mN/mm^3.

In both scenarios, where C_0 is zero or -1 mN/mm^3, the normal cells have a narrower range of velocity than the abnormal cells. This illustrates the possibility of sorting, as discussed in Chapter 6.2, to obtain a subpopulation with an increased proportion of normal cells.

Despite the computed and predicted velocity distributions being qualitatively similar, the predicted velocities have a lower variance, with outliers predicted to have less extreme values than what is computed. This is not surprising, due to the nature of regression trees in the random forest as well as the k-nearest neighbor regressor in which substantial variations are averaged out with other samples of similar characteristics having less extreme velocities. Since the normal and abnormal cells are predicted to have velocities that are less spreaded, the distinction between normal and abnormal sperm cells become more pronounced, leading to an optimistic estimate of the achievable purity. This effect is more substantial (Figure 6-10 and Figure 6-11) when a small training set comprising 0.1% of the total sample size is chosen. Nonetheless, the qualitative conclusions from both the computed and predicted velocity distributions remain the same, that the normal sperm cells can be segregated. The quantitative differences will be explored in what follows.

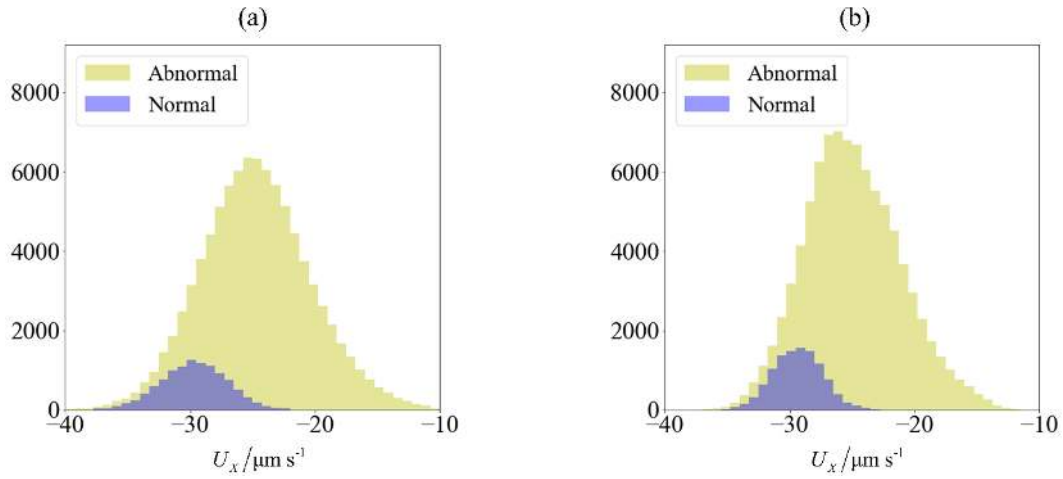

Figure 6-10 – Velocity of spermatozoa in the test set of 99,900 samples (a) computed using SBT computation and (b) obtained from predictions made using an ensemble of supervised learning trained on 100 samples. The blue and green region represents the number of morphologically normal and abnormal cells, respectively. The sperm cells are not subjected to any applied field ($C_0 = 0$).

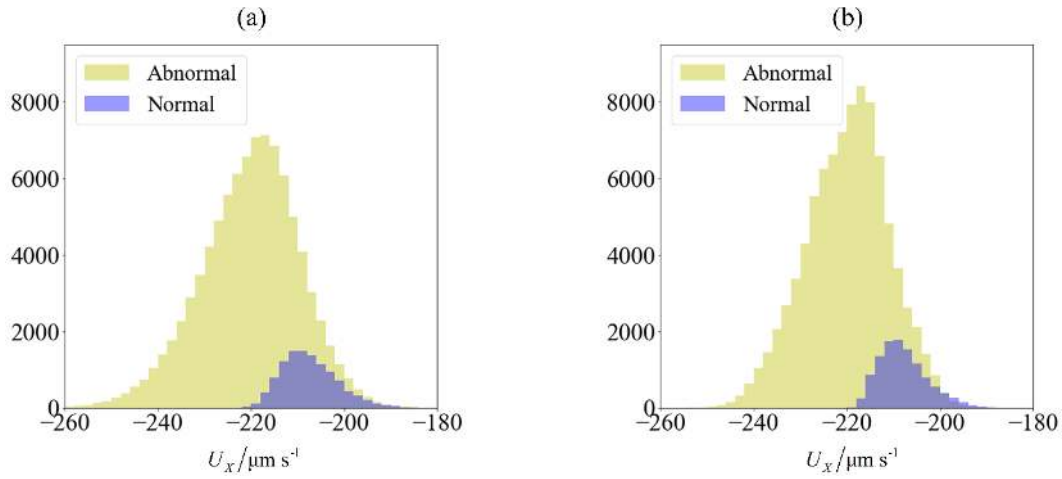

Figure 6-11 – Velocity of spermatozoa in the test set of 99,900 samples (a) computed using SBT computation and (b) obtained from predictions made using an ensemble of supervised learning trained on 100 samples. The blue and green region represents the number of morphologically normal and abnormal cells, respectively. The sperm cells are subjected to C_0 = -1 mN/mm^3.

Non-deterministic processes such as sperm sorting can be studied from different approaches, as illustrated in Figure 6-12. We can either perform a large number of computations or experiments to obtain reliable results that converge, perform a small number of computations at the possible expense of unreliable results, or perform a small number of computations followed by the application of machine learning.

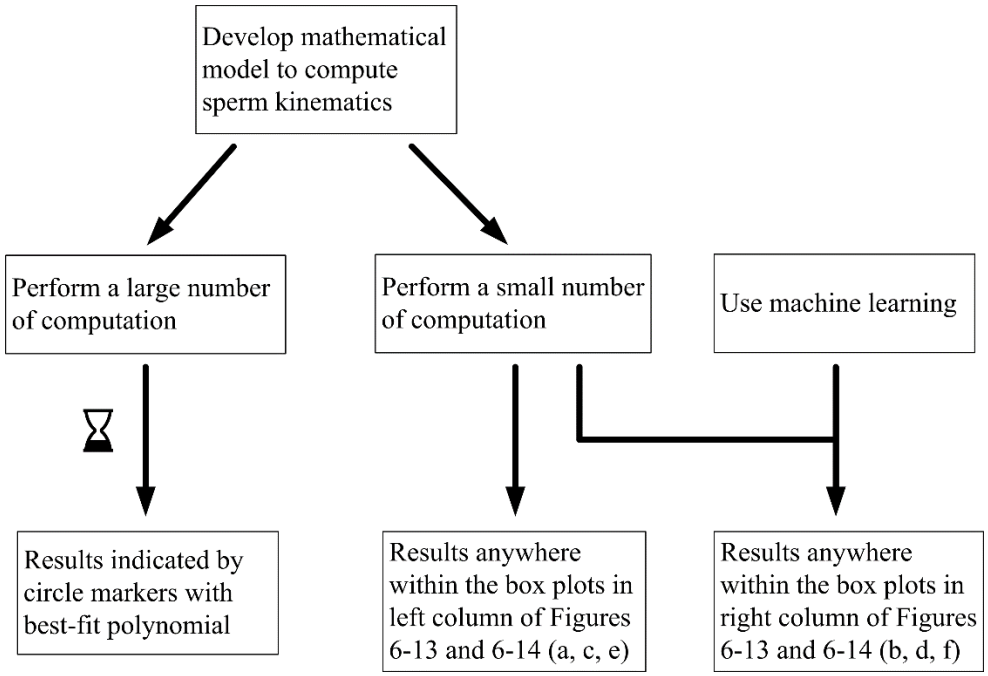

Figure 6-12 – Flowchart illustrating possible approaches to investigate the non-deterministic process of sperm sorting.

The computed and predicted purity for a target yield of 50% will be compared, presented in box-plots, super-imposed over the best-fit polynomial for results computed using 10^5 samples for C_0 = -1 mN/mm^3 (Figure 6-13) and C_0 = 0 (Figure 6-14). As a sample size of 10^5 has shown convergence in the sperm parameters and purity (Figure 6-5), the results as indicated by the circle markers will be used as a benchmark. Subsets of size 100, 1,000 and 10,000 are considered, by resampling with replacement (Wu 1986) from the population of 100,000. Larger sample sizes are deemed redundant for consideration. Given that the variance in purity is inversely proportional to the sample size, we set the number of repetitions to be 10^5 divided by the size of each training set. Using the first row of Figure 6-13 as an illustration, a set of 100 samples is drawn to train the machine learning models. The purity using these data are computed using the SBT model. This process is repeated 10,000 times to obtain the boxplots in Figure 6-13a. Predictions are then made on the remaining 90,000 unseen samples, with a new machine learning model retrained for each repetition, and the results are presented in Figure 6-13b.

Instead of running the full computation for 10^5 samples, one can draw the same conclusion on how sorting purity depends on yield as well as C_0 by using the results predicted from one-tenth of the sample and using machine learning to make predictions on the rest. This is more reliable than solely making a conclusion from the same subset without machine learning, as evident from the shorter whiskers of each plot in the right column of Figure 6-13 and Figure 6-14 as compared to their counterparts on the left column. By computing the purity from the velocity histogram obtained from a subset of 1,000 computed velocities followed by predictions on the remaining 99,000 sperm, the uncertainty in results is substantially lower than if the purity had been computed without the additional predictions. However, the improved precision obtained by machine learning comes at a cost of some reduction in accuracy, as the purity are consistently over-predicted. This can be mitigated by adding a correction factor obtained from observations, or by introducing Gaussian noise to the predicted velocity to spread out the distribution. Depending on the objectives of their study, researchers can substantially reduce computational costs by using an ensemble of supervised machine learning model trained on a subset of the data. This allows more cases to be considered for a given amount of resources, as indicated by the path following the green arrows in Figure 6-15.

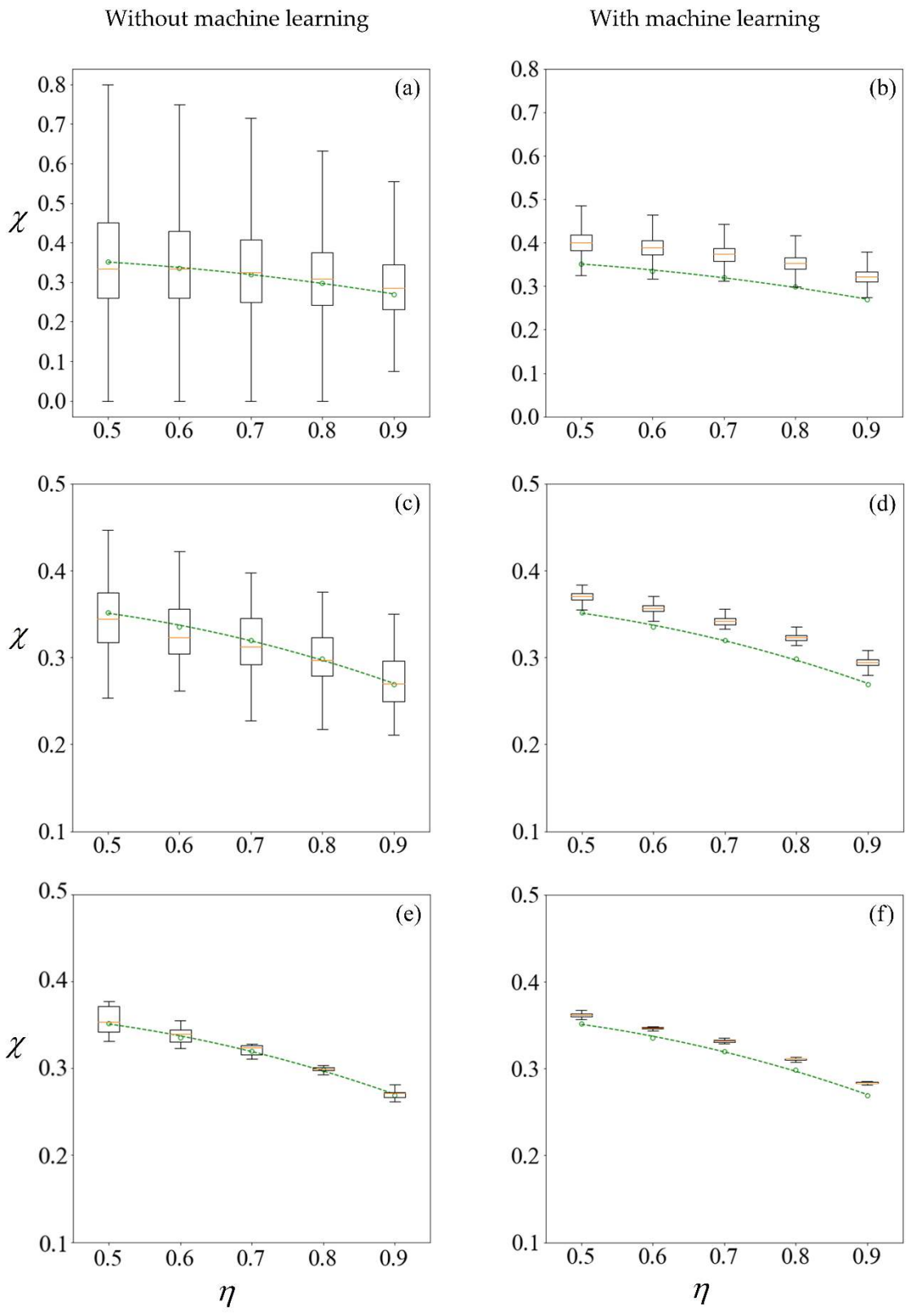

Figure 6-13 – Boxplots representing results computed (left column) and predicted (right column) from training sets of size 100, 1,000, and 10,000 samples in the first row (a, b), second row (c, d) and third row (e, f), respectively. The circle markers are results computed from 10^5 samples, while the dashed-line is the best fit polynomial. The sperm cells are subjected to C_0 = -1 mN/mm^3. The machine learning model makes predictions on the remaining of the 100,000 samples less those used for training.

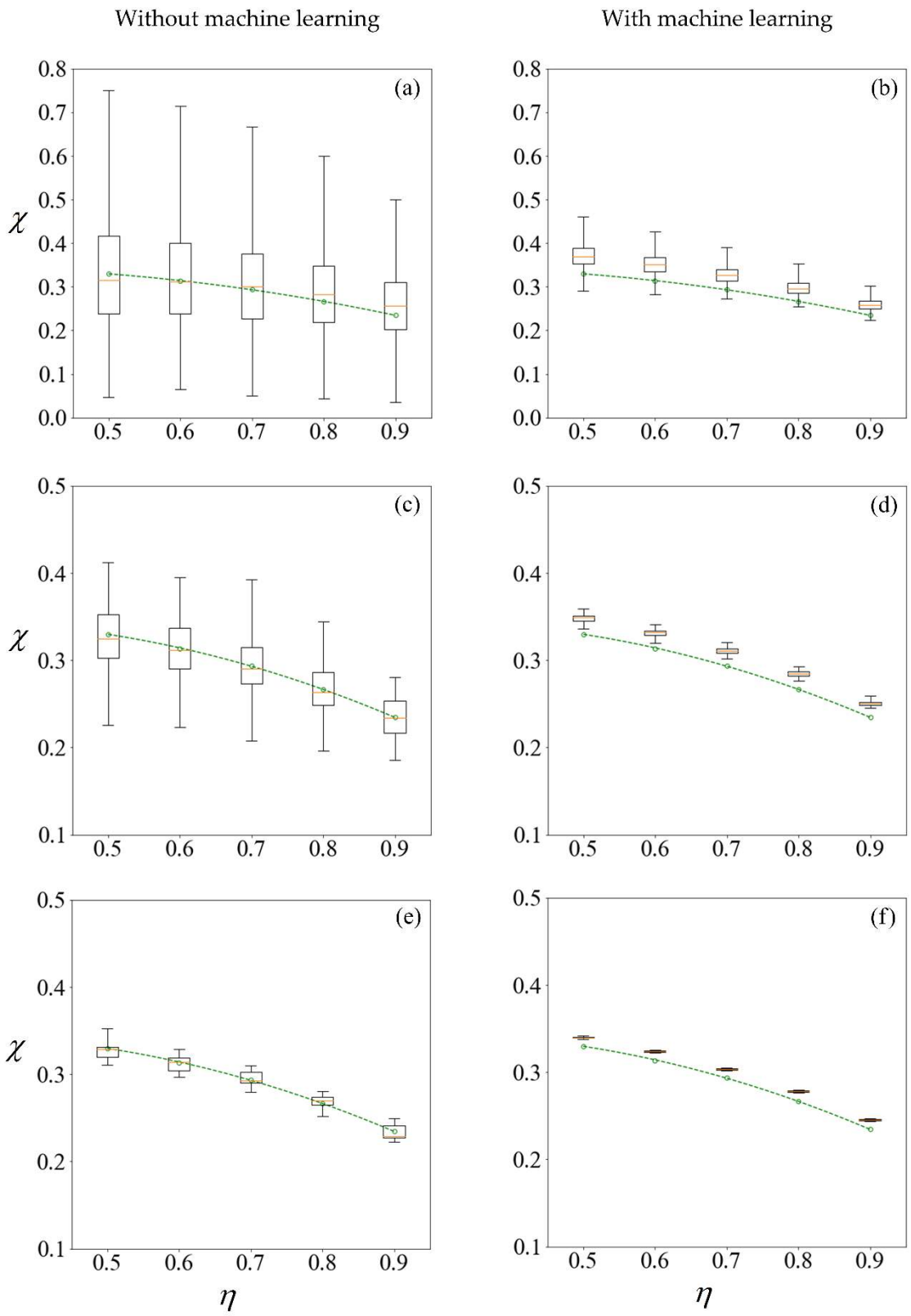

Figure 6-14 – Boxplots representing results computed (left column) and predicted (right column) from training sets of size 100, 1,000, and 10,000 samples in the first row (a, b), second row (c, d) and third row (e, f), respectively. The circle markers are results computed from 10^5 samples, while the dashed-line is the best fit polynomial. The sperm cells are not subjected to any applied field. The machine learning model makes predictions on the remaining of the 100,000 samples less those used for training.

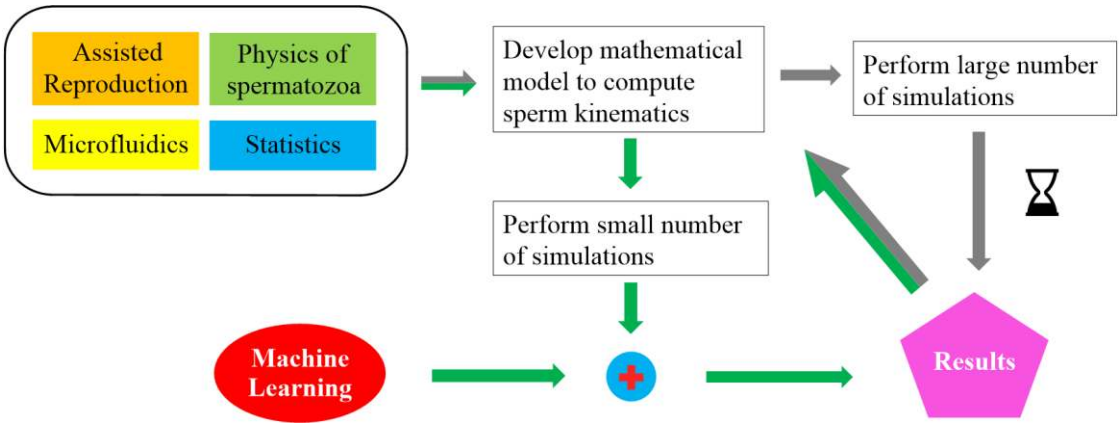

Figure 6-15 – Flowchart illustrating approach taken for performing statistical analysis in Chapter 6. The green and grey arrows indicate the path taken with and without utilising machine learnining, respectively.

6.5 Chapter Summary

In this chapter, the use of magnetic activated cell sorting to increase the proportion of normal cells for use in IUI is investigated theoretically. The sperm velocity is computed with SBT. Since magnetophoresis influence each cell to a different extent, the prospect of sorting is assessed based on the relative velocity distributions of normal and abnormal cells. An ensemble of supervised learning algorithms is successfully deployed to establish a relation between the given sperm characteristics and its resulting velocity. The predictions from machine learning allows the achievable purity to be estimated, providing similar results with substantially lower computational costs.

Chapter 7
Conclusions

7.1 Summary of research done

In this thesis, the principles and associated benefits as well as limitations of common assisted reproduction techniques are summarised. Sperm motility and morphology is understood to be a significant indicator influencing the outcome of reproduction, be it *in vivo* or *in vitro*. Hence, attention is turned to understanding the kinematics of a sperm cell and its properties. A literature review is done to gain awareness of the microfluidic sorting techniques which have successfully manipulated microscale particles or cells. The author sees untapped potential in the study of sorting human sperm, and seeks to fill the research gap by providing a theoretical framework for modelling sperm subjected to an external field, taking statistical variations into account.

As a preliminary study, the sperm is modelled as a sphere attached to a slender filament with a prescribed sinusoidal waveform. Using Resistive Force Theory, the hydrodynamic force acting on the flagellum is represented as a linear function of the relative fluid velocity due to the translational and rotational motion of the sperm together with the wiggling of its flagellum. Using a dipole approximation where higher-order poles are neglected, the DEP force due to a non-uniform electric field is added to the model. The total force and moment acting on the entire sperm is summed and expressed as a function of the linear and angular velocity. With the assumption of small amplitude, the x-velocity in the body-frame is solved, leading to an analytical solution being a function of the sperm morphological parameters and two DEP parameters which encompasses the medium permitivitty, Clausius-Mossotti factor and gradient of the electric field squared. It is reasoned qualitatively, and shown in a subsequent chapter, that the time-avearaged y-velocity as well as angular velocity are negligible here. Substituing the parameters of an X- and Y-sperm above and below one standard deviation of their respective mean, it is found that DEP can be used to alter their velocities to different extent, allowing a skewed population of spermatozoa containing the desired type of chromosomes to be selected.

An active flagellum driven by internal sliding force is then modelled, and the flagellum shape is determined by solving a partial differential equation. Having considered motion in a Newtonian fluid earlier, the kinematic behaviour of the sperm subjected to DEP force is now investigated in a viscoelastic fluid medium of different Deborah number. Variations in the internal sliding force within the flagellum are also considered. The flagellum waveform, in the absence of an external field, is validated against published work in the literature. After solving for the body-fixed velocity, the sperm trajectory is plotted in the inertial frame and is shown to exhibit high directionality. As the flagellum has a more streamlined beating pattern in this model as compared to a sinusoidal waveform, each unit of DEP force resulted in a slightly larger change in sperm velocity. More notably, the effect of DEP is enhanced in a viscoelastic fluid. The velocity difference between the X- and Y-sperm also indicate the possibility of sorting, in both Newtonian or viscoelastic fluid, to skew the odds of having a female or male offspring.

Slender Body Theory, which takes into account body-to-body interactions and provides better accuracy than Resistive Force Theory, is subsequently used to compute the hydrodynamic force. The qualitative and quantitative difference between the two theories are compared, and the velocity of a microswimmer with a discretized flagellum comprising 15 straight segments is computed. The instantaneous velocity obtained from RFT and SBT follows a similar trend, although RFT consistently over-estimates the speed in the order of 10% to 20%. The force distribution along a flagellum is shown to be similar, albeit consistently more positive, when SBT is used in place of RFT. However, due to the numerical complexity involved in seeking a solution, the waveform corresponding to SBT is not obtained. Instead, a prescribed sinusoidal waveform multiplied by an exponential factor will be used in the subsequent statical analysis in the interest of computational costs.

Finally, the sorting of sperm is studied using the overall velocity distribution of a large population in which statistical convergence is displayed. Using an external magnetic field, the achievable purity and yield are computed. The purity is the proportion of conditionally satisfactory sperm cells which at least partially fulfils the criteria of being strictly normal, given that biological aspects are not considered in this thesis. The application of a magnetic field allows the purity to be over twice that of an unsorted population, and points to the prospect of being utilised in IUI for better odds

of success. Additionally, the trajectory of a swimming sperm shows that its heading is strongly aligned to the direction of the external force. An ensemble of supervised learning algorithms is deployed to predict the velocity of each sperm according to its parameters, significantly reducing computational costs. By training the ensemble on a tenth of the total samples, the histogram of predicted velocity shows little distinction from the histogram of computed velocity. Their corresponding purity are also similar, varying by no more than a handful of percentage points. The machine learning is repeated multiple times, and the conclusions are consistent.

7.2 A closer look

7.2.1 Original contributions

This thesis is built upon the meticulous research work of many others, and have resulted in a number of original contributions by the author. In chapter 3, an analytical equation was established for the sperm velocity as a function of its morphology as well as properties which encompass the effective polarizability and external electric field strength and gradient. From equation (3.33), $\partial\langle u_x\rangle/\partial\tilde{D}_0$ and $\partial\langle u_x\rangle/\partial\tilde{D}_1$ allows experimentalist to estimate the requirements to alter the sperm velocity to the extent desired. Once the experiment set-up is determined, the DEP force which each sperm is subjected to and the effect of dielectrophoresis can be computed according to the individual morphology of each sperm. Moreover, the maximum electric field can be determined following the framework in Section 3.5.

In chapter 4, the PDE describing the waveform of an active flagellum is modified, beginning from force and moment balance, to account for an external DEP force. The author demonstrated that DEP induces little change in the waveform of a sperm in a Newtonian fluid, but led to a noticeable alteration of the flagellum waveform in a viscoelastic Oldroyd-B fluid. It was also found that the velocity change due to an external field is enhanced in an Oldroyd-B medium, as substantiated by quantitative computation as well as qualitative discussion, indicating that sorting may be more effective here.

In chapter 5, the procedure adopted to solve for the flagellum waveform using SBT instead of RFT is presented. The results are non-conclusive due to the causality

dilemma arising from how force is computed by SBT. Nonetheless, the attempt is an original work which has not been published to the best of the author's knowledge, and serves as a reference and starting point for future researchers who wish to probe deeper.

In chapter 6, the author made the proposal of using data science in the research of sperm sorting for assisted reproduction. By repeating the velocity calculation for sperm of different morphology, the proportion of morphologically normal cells attainable as a function of acceptable yield and magnetic force is presented. In addition, supervised learning is introduced as a tool for reducing numerical computational time. The boxplots in Section 6.4 illustrate that machine learning can be used to predict the purity achievable from sperm sorting with decent accuracy and confidence.

7.2.2 Validations of results

Given that the theoretical results presented in this thesis are largely original work, there is no basis to validate everything as a whole with the available published literature. While it will be ideal to have experiments support the theoretical results in Chapters 3 to 6, this is beyond of scope of the author's doctoral thesis. Nonetheless, validations have been done on various base cases to ensure that progress is made in the correct track. The relevant citations have been provided in the earlier chapters when each point was first discussed, but will be summarised here for a comprehensive support of the thesis.

With regard to the reliability of theoretical calculations made by RFT and SBT, the free-swimming speed of a sperm with average parameters is found to be 58 μm/s and 46 μm/s, respectively. These values are within the range of experimental measurements (Mortimer *et al*. 1998), and also in agreement with one another given that RFT tend to give a larger speed than SBT. In addition, kinematic reversibility is observed for a rod with a single degree of freedom. The flagellum waveform computed from RFT is also validated against the theoretical work by Fu *et al*. (2008) for the different Sperm number, internal force distribution as well as Deborah number. These plots are qualitatively similar to experimental observations by Ishijima *et al*. (1986).

The feasibility of sperm sorting by an external field for ART has been considered from both the technical as well as biological aspects. From a solely technical perspective, there is evidence to suggest that current technology allows us to generate

the required electric or magnetic field for sorting and to fabricate the microfluidic device. Chapter 3 proposes sorting via DEP where $\varepsilon_{medium}\,\mathrm{Re}(f_{cm})\nabla E^2$ is 100 times the value of $K_N\omega/\Lambda$. A possible set-up corresponds to a potential of 300 V with a minimum electrode separation of 200 μm and a maximum electric field of 1500 V/mm. Meanwhile, chapter 6 proposes that sorting via magnetophoresis with a force density of 1 mN/mm^3 for C_0 can increase the proportion of morphologically normal cells substantially. By doping the sperm with paramagnetic particles such that the relative magnetic susceptibility is in the order of unity, the required magnetic field can be under 1 T. From a biological perspective, human sperm cells have been reported to remain viable in electric field of up to 260 V/mm arising from 1,000 V (Rosales-Cruzaley *et al*. 2013) and in magnetic field of 1.5 T (Said *et al*. 2015). In addition, sperm can be loaded with paramagnetic particles (Schulze *et al*. 2005), and its fertilisation capability is maintained (Ben-David Makhluf *et al*. 2006). The use of MACS followed by ICSI has also led to the birth of a healthy human baby (Rawe *et al*. 2010). Nonetheless, one should be aware that the baby was not conceived from sperm doped with paramagnetic particles. The viability of human sperm subjected to larger electric fields remain to be assessed in the laboratory, and the subsequent step would be to assess the fertilisation potential of the sorted sperm using a sperm penetration assay (Oehninger *et al*. 2014).

7.2.3 DEP or magnetophoresis

The manipulation of spermatozoa in this thesis is considered using an external electric or magnetic field. There are two benefits to sorting sperm by magnetophoresis instead of dielectrophoresis. First, there is experimental evidence that spermatozoa exposed to magnetic field maintains its fertilisation capability and led to the birth of a healthy human, while no publications on sorting human sperm by electric field for assisted reproduction are found. Second, the possibility of doping spermatozoa with paramagnetic nanoparticles to increase their magnetic susceptibility enables a weaker magnetic field to be used for sorting.

Nonetheless, sorting sperm by dielectrophoresis has its advantages over magnetophoresis. DEP force scales according to shape factor Γ, while magnetic force scales proportionately to volume. The ratio between the DEP force acting on the head and flagellum of a sperm is around 10 times greater than the ratio due to a magnetic

force. Since most conditions for a morphologically normal sperm depend on the head parameters, sorting by DEP can be more effective than magnetophoresis. This is because for the same total external force, the effect due to differences in head morphology will be magnified when DEP is used, enabling the proportion of morphologically normal cells to be further increased.

7.3 Closing remarks

The author has thus demonstrated a systematic framework in which the feasibility of sperm sorting is analysed with progessive complexity. The research path begins with seeking a simplified analytical relation of the body-fixed velocity for a sperm prescribed with a sinusoidal waveform in Newtonian fluid. This is extended to solving for the trajectory of a sperm with an active flexible flagellum governed by a partial differential equation, in a viscoelastic fluid. Thereafter, SBT is used in place of RFT to account for interactions. Statistical variations are duly considered to evaluate the sorting, and machine learning is implemented to assess the feasibility of replacing SBT computations with predictions.

In view of the promising theoretical results, it will be exciting to build upon this work in future studies. The theoretical model can be strengthened by considering cell-to-cell interactions, so that sorting need not be confined to dilute samples, and studied in three-dimensional space. The hydrodynamic force can also be represented using the method of regularized Stokeslets, which works well even for a non-slender flagellum, if higher accuracy in the velocity distribution is wanted.

Even with the most ideal theoretical results, experiments are certainly needed to validate the mathematical predictions. After acquiring the practical expertise to obtain a sorted sample comprising a higher proportion of normal sperm, it is preferable to establish an accurate relation between the distribution of parameters of sperm cells collected and the combination of external field and microfluidic set-up used. This will allow the target output or design of the device to be adjusted according to the demands. If experimental observations do not match theory computations, an empirically obtained correction factor might be useful. Attention also has to be given to the biological aspects of the sperm cells, such as modelling the effects of hyperactivation and capacitation, and diagnosing the sperm viability after sorting. Apart from verifying whether fertilisation

occurs normally, the health of the feutus as well as its subsequent development until adulthood is also important. These may first be tested on animals such as chimpanzees and bonobos which has close resemblance to humans in terms of both DNA and gestation period.

The use of Artificial Intelligence has vast potential, and the supervised learning adopted here merely scratches the surface of this field. The benefits it brings is not only in computational cost savings, for there are cases where it is not feasible to carry out experiments or the full computation on a large scale. For a start, the supervised learning model can be improved in numerous ways. Apart from amending the predictor variables, a refined hyperparameter tuning can improve the machine learning performance, provided the data in the training set is appropriate. Other algorithms may also be included in the ensemble, with the weights from each constituent optimized to suit the problem at hand. Convolutional neural networks may even be utilised for image analysis as a follow-up to experimental observations.

Given the interdisciplinary nature of this research, as well as the decades of experimental observations which would be associated with clinical trials, substantial progress will require a concerted team effort. While the vast amount of manpower and time called for may seem daunting, we should keep in mind that assisted reproduction currently leads to the birth of over one in every hundred infants in developed countries, despite its rather low success rate. Improving the odds will lead to substantial cost savings as well as non-monetary benefits which cannot be labelled with a price tag.

List of Papers Published

1. **Koh JBY**, Marcos (2014) Effect of dielectrophoresis on spermatozoa. *Microfluidics and Nanofluidics* 17:613-622

2. **Koh JBY**, Marcos (2015a) The study of spermatozoa and sorting in relation to human reproduction. *Microfluidics and Nanofluidics* 18:755-774

3. **Koh JBY**, Marcos (2015b) Dielectrophoresis of spermatozoa in viscoelastic medium. *Electrophoresis* 36:1514-1521

4. **Koh JBY**, Shen X, Marcos (2016) Theoretical modeling in microscale locomotion. *Microfluidics and Nanofluidics* 20:1-27

5. **Koh JBY**, Marcos (2017) Sorting spermatozoa by morphology using magnetophoresis. *Microfluidics and Nanofluidics* 21:75

6. **Koh JBY**, Shen X, Marcos (2018) Supervised learning to predict sperm sorting by magnetophoresis. *Magnetochemistry* 4:31

Conference Presentations

1. **Koh** JBY, Marcos (December 2013). Effect of Dielectrophoresis on Spermatozoa. ASME 4th International Conference on Micro/Nanoscale Heat and Mass Transfer at Hong Kong, China

2. **Koh** JBY, Marcos (November 2016). Sorting of Sperm by Morphology. 69th Annual Meeting of the APS Division of Fluid Dynamics at Portland, Oregon, United States

3. **Koh** JBY, Marcos (November 2017). Statistical analysis of sperm sorting. 70th Annual Meeting of the APS Division of Fluid Dynamics at Denver, Colorado, United States

References

Agarwal A, Manglona A, Loughlin KR (1992) Improvement in semen quality and sperm fertilizing ability after filtration through the L4 membrane: comparison of results with swim up technique. *J Urology* 147:1539-1541

Agarwal A, Said TM (2003) Role of sperm chromatin abnormalities and DNA damage in male infertility. *Hum Reprod Update* 9:331-345

Aharoni A (2000) *Introduction to the Theory of Ferromagnetism* (Vol. 109). Clarendon Press

Aksoy E, Aktan TM, Duman S, Cuce G (2012) Assessment of spermatozoa morphology under light microscopy with different histologic stains and comparison of morphometric measurements. *Int J Morphol* 30:1544-1550

Alvarez L, Friedrich BM, Gompper G, Kaupp UB (2014) The computational sperm cell. *Trends Cell Biol* 24:198-207

Ames WF (2014) Numerical methods for partial differential equations, 3rd edition. *Academic press*

Andersen AMN, Wohlfahrt J, Christens P, Olsen J, Melbye M (2000) Maternal age and fetal loss: population based register linkage study. *BMJ* 320:1708-1712

Anthony S, Buitendijk SE, Dorrepaal CA, Lindner K, Braat DDM, den Ouden AL (2002) Congenital malformations in 4224 children conceived after IVF. *Hum Reprod* 17:2089-2095

Antinori M, Licata E, Dani G, Cerusico F, Versaci C, d'Angelo D, Antinori S (2008) Intracytoplasmic morphologically selected sperm injection: a prospective randomized trial. *Reprod Biomed Online* 16:835-841

Autrusson N, Guglielmini L, Lecuyer S, Rusconi R, Stone HA (2011) The shape of an elastic filament in a two-dimensional corner flow. *Phys Fluids* 23:063602

Aziz N, Said T, Paasch U, Agarwal A (2007) The relationship between human sperm apoptosis, morphology and the sperm deformity index. *Hum Reprod* 22:1413-1419

Balaban B, Yakin K, Alatas C, Oktem O, Isiklar A, Urman B (2011) Clinical outcome of intracytoplasmic injection of spermatozoa morphologically selected under high magnification: a prospective randomized study. *Reprod Biomed Online* 22:472-476

Barroso G, Taylor S, Morshedi M, Manzur F, Gaviño F, Oehninger S (2006) Mitochondrial membrane potential integrity and plasma membrane translocation of phosphatidylserine as early apoptotic markers: a comparison of two different sperm subpopulations. *Fertil Steril* 85:149-154

Bartoov B, Berkovitz A, Eltes F (2001) Selection of spermatozoa with normal nuclei to improve the pregnancy rate with intracytoplasmic sperm injection. *New Engl J Med* 345:1067-1068

Bartoov B, Berkovitz A, Eltes F, Kogosowski A, Menezo Y, Barak Y (2002) Real-time fine morphology of motile human sperm cells is associated with IVF-ICSI outcome. *J Androl* 23:1-8

Bartoov B, Berkovitz A, Eltes F, Kogosovski A, Yagoda A, Artzi S, Gross M, Lederman H, Barak Y (2003) Pregnancy rates are higher with intracytoplasmic morphologically selected sperm injection than with conventional intracytoplasmic injection. *Fertil Steril* 80:1413-1419

Batchelor G (1970) Slender-body theory for particles of arbitrary cross-section in Stokes flow. *J Fluid Mech* 44:419-440

Bayly P, Lewis B, Ranz E, Okamoto R, Pless R, Dutcher S (2011) Propulsive forces on the flagellum during locomotion of Chlamydomonas reinhardtii. *Biophys J* 100:2716-2725

Bearon R, Bees M, Croze O (2012) Biased swimming cells do not disperse in pipes as tracers: a population model based on microscale behaviour. *Phys Fluids* 24:121902

Bechinger C, Sciortino F, Ziherl P (2013) Physics of Complex Colloids (Vol 184). *IOS Press*

Becker FF, Wang XB, Huang Y, Pethig R, Vykoukal J, Gascoyne PR (1995) Seperation of human breast cancer cells from blood by differential dielectric affinity. *Proc Natl Acad Sci USA* 92:860-864

Beernink FJ, Dmowski WP, Ericsson RJ (1993) Sex preselection through albumin separation of sperm. *Fertil Steril* 59:382-386

Ben-David Makhluf S, Qasem R, Rubinstein S, Gedanken A, Breitbart H (2006) Loading magnetic nanoparticles into sperm cells does not affect their functionality. *Langmuir* 22:9480-9482

Berke AP, Turner L, Berg HC, Lauga E (2008) Hydrodynamic attraction of swimming microorganisms by surfaces. *Phys Rev Lett* 101:038102

Bird RB, Wiest JM (1995) Constitutive equations for polymeric liquids. *Annu Rev Fluid Mech* 27:169-193

Bluman G, Kumei S (2013) Symmetries and differential equations (Vol. 154). *Springer Science & Business Media*

Bolton VN, Braude PR (1984) Preparation of human spermatozoa for in vitro fertilization by isopycnic centrifugation on self-generating density gradients. *Syst Biol Reprod Mec* 13:167-176

Bouzarth EL, Minion ML (2011) Modeling slender bodies with the method of regularized Stokeslets. *J Comput Phys* 230:3929-3947

Box GE (1976) Science and statistics. *J Am Stat Assoc* 71:791-799

Box GE (1979) Robustness in the strategy of scientific model building. *Robustness in statistics* 1:201-236

Brennen C, Winet H (1977) Fluid mechanics of propulsion by cilia and flagella. *Annu Rev Fluid Mech* 9:339-398

Bretherton F (1961) Rheotaxis of spermatozoa. *P Roy Soc Lond B Bio* 153:490-502

Bródy F, Vámos T (1995) The neumann compendium (Vol. 1). *World Scientific*

Burba F, Ferraty F, Vieu P (2009) k-Nearest Neighbour method in functional nonparametric regression. *J Nonparametr Stat* 21:453-469

Butcher JC (1987) The numerical analysis of ordinary differential equations. Runge-Kutta methods and general linear methods. *John Wiley & Sons*

Butcher JC (2016) Numerical methods for ordinary differential equations, 3rd edition. *John Wiley & Sons*

Camalet S, Jülicher F (2000) Generic aspects of axonemal beating. *New J Phys* 2:24

Campana A, Sakkas D, Stalberg A, Bianchi PG, Comte I, Pache T, Walker D (1996) Intrauterine insemination: evaluation of the results according to the woman's age, sperm quality, total sperm count per insemination and life table analysis. *Hum Reprod* 11:732-736

Campbell AI, Ebbens SJ (2013) Gravitaxis in spherical Janus swimming devices. *Langmuir* 29:14066-14073

Carvalho JO, Silva LP, Sartori R, Dode MAN (2013) Nanoscale differences in the shape and size of X and Y chromosome-bearing bovine sperm heads assessed by atomic force microscopy. *Plos One* 8:59387

Cates M (2012) Diffusive transport without detailed balance in motile bacteria: does microbiology need statistical physics? *Rep Prog Phys* 75:042601

Chattopadhyay S, Wu XL (2009) The effect of long-range hydrodynamic interaction on the swimming of a single bacterium. *Biophys J* 96:2023-2028

Check JH, Katsoff D (1993) A prospective study to evaluate the efficacy of modified swim-up preparation for male sex selection. *Hum Reprod* 8:211-214

Chen YA, Huang ZW, Tsai FS, Chen CY, Lin CM, Wo AM (2011) Analysis of sperm concentration and motility in a microfluidic device. *Microfluid Nanofluid* 10:59-67

Chilukuri S, Collins CH, Underhill PT (2014) Impact of external flow on the dynamics of swimming microorganisms near surfaces. *J Phys Condens Mat* 26:115101

Chiou PY, Ohta AT, Wu MC (2005) Massively parallel manipulation of single cells and microparticles using optical images. *Nature* 436:370-372

Cho BS, Schuster TG, Zhu X, Chang D, Smith GD, Takayama S (2003) Passively driven integrated microfluidic system for separation of motile sperm. *Anal Chem* 75:1671-1675

Cohen-Dayag A, Tur-Kaspa I, Dor J, Mashiach S, Eisenbach M (1995) Sperm capacitation in humans is transient and correlates with chemotactic responsiveness to follicular factors. *Proc Natl Acad Sci USA* 92:11039-11043

Colon JM, Sarosi P, McGovern PG, Askin A, Dziedzic JM, Skurnick J, Weiss G, Bonder EM (1992) Controlled micromanipulation of human sperm in three dimensions with an infrared laser optical trap: effect on sperm velocity. *Fertil Steril* 57:695-698

Cooper TG, Yeung CH (2006) Computer-aided evaluation of assessment of "grade A" spermatozoa by experienced technicians. *Fertil Steril* 85:220-224

Cox R (1970) The motion of long slender bodies in a viscous fluid part. *J Fluid Mech* 44:791-810

Croze OA, Sardina G, Ahmed M, Bees MA, Brandt L (2013) Dispersion of swimming algae in laminar and turbulent channel flows: consequences for photobioreactors. *J Roy Soc Interface* 10:20121041

Cui KH (1997) Size differences between human X and Y spermatozoa and prefertilization diagnosis. *Mol Hum Reprod* 3:61-67

Cui KH, Matthews CD (1993) X larger than Y. *Nature* 366:117-118

Dahl E (2004) The presumption in favour of liberty: a comment on the HFEA's public consultation on sex selection. *Reprod BioMed Online* 8:266-267

David G, Serres C, Jouannet P (1981) Kinematics of human spermatozoa. *Gamete Res* 4:83-95

De Vos A, Van De Velde H, Joris H, Verheyen G, Devroey P, Van Steirteghem A (2003) Influence of individual sperm morphology on fertilization, embryo morphology, and pregnancy outcome of intracytoplasmic sperm injection. *Fertil Steril* 79:42-48

Denissenko P, Kantsler V, Smith DJ, Kirkman-Brown J (2012) Human spermatozoa migration in microchannels reveals boundary-following navigation. *Proc Natl Acad Sci USA* 109:8007-8010

Diebel J (2006) Representing attitude: Euler angles, unit quaternions, and rotation vectors. *Matrix* 58:1-35

Dietterich TG (2000) Ensemble methods in machine learning. In International workshop on multiple classifier systems. *Springer, Berlin, Heidelberg*

Dormand JR, Prince PJ (1980) A family of embedded Runge-Kutta formulae. *J Comput Appl Math* 6:19-26

Drescher K, Dunkel J, Cisneros LH, Ganguly S, Goldstein RE (2011) Fluid dynamics and noise in bacterial cell–cell and cell–surface scattering. *Proc Natl Acad Sci USA* 108:10940-10945

Dresdner RD, Katz DF (1981) Relationships of mammalian sperm motility and morphology to hydrodynamic aspects of cell function. *Biol Reprod* 25:920-930

Drobnis EZ, Zhong CQ, Overstreet JW (1991) Separation of cryopreserved human semen using Sephadex columns, washing, or Percoll gradients. *J Androl* 12:201-208

Durand RE, Olive PL (1982) Cytotoxicity, Mutagenicity and DNA damage by Hoechst 33342. *J Histochem Cytochem* 30:111-116

Durham WM, Kessler JO, Stocker R (2009) Disruption of vertical motility by shear triggers formation of thin phytoplankton layers. *Science* 323:1067-1070

Edelmann RJ, Connolly KJ (1986) Psychological aspects of infertility. *Brit J Med Psychol* 59:209–219

Edwards RG (2000) Human embryos in vitro: pioneer illustrations of oocyte maturation, fertilization, cleavage and blastulation. *Hum Reprod* 15:1-9

Edwards RG (2001) The bumpy road to human in vitro fertilization. *Nat Med* 7:1091-1094

Eisenbach M (2011) Bacterial chemotaxis. In: *eLS. John Wiley & Son, Ltd: Chichester*

El Karoui N, Peng S, Quenez MC (1997) Backward stochastic differential equations in finance. *Math Financ* 7:1-71

El-Ali J, Sorger PK, Jensen KF (2006) Cells on chips. *Nature* 442:403-411

Elfring GJ, Lauga E (2009) Hydrodynamic phase locking of swimming microorganisms. *Phys Rev Lett* 103:088101

Elfring GJ, Pak OS, Lauga E (2010) Two-dimensional flagellar synchronization in viscoelastic fluids. *J Fluid Mech* 646:505-515

Elgeti J, Kaupp UB, Gompper G (2010) Hydrodynamics of sperm cells near surfaces. *Biophys J* 99:1018-1026

Elgeti J, Winkler RG, Gompper G (2015) Physics of microswimmers - single particle motion and collective behavior: a review. *Rep Prog Phys* 78:056601

Ericsson RJ, Langevin CN, Nishino M (1973) Isolation of fractions rich in human Y sperm. *Nature* 246: 421-424

Fauci LJ, Dillon R (2006) Biofluidmechanics of reproduction. *Annu Rev Fluid Mech* 38:371-394

Fauci LJ, McDonald A (1995) Sperm motility in the presence of boundaries. *B Math Biol* 57:679-699

Fisch H, Lipshultz LI (1992) Diagnosing male factors of infertility. *Arch Pathol Lab Med* 116:398-405

Flaherty SP, Michalowska J, Swann NJ, Dmowski WP, Matthews CD, Aitken RJ (1997) Albumin gradients do not enrich Y-bearing human spermatozoa. *Hum Reprod* 12:938-942

Fletcher R (2013) Practical methods of optimization. *John Wiley & Sons*

Fornberg B (1988) Generation of finite difference formulas on arbitrarily spaced grids. *Math Comput* 51:699-706

Friedrich BM, Riedel-Kruse IH, Howard J, Jülicher F (2010) High-precision tracking of sperm swimming fine structure provides strong test of resistive force theory. *J Exp Biol* 213:1226-1234

Frymier PD, Ford RM (1997) Analysis of bacterial swimming speed approaching a solid–liquid interface. *AIChE J* 43:1341-1347

Frymier PD, Ford RM, Berg HC, Cummings PT (1995) Three-dimensional tracking of motile bacteria near a solid planar surface. *Proc Natl Acad Sci USA* 92:6195-6199

Fu HC, Wolgemuth CW, Powers TR (2008) Beating patterns of filaments in viscoelastic fluids. *Phys Rev E* 78:041913

Fu HC, Wolgemuth CW, Powers TR (2009) Swimming speeds of filaments in nonlinearly viscoelastic fluids. *Phys Fluids* 21:033102

Fugger EF, Black SH, Keyvanfar K, Schulman JD (1998) Births of normal daughters after MicroSort sperm separation and intrauterine insemination, in-vitro fertilization, or intracytoplasmic sperm injection. *Hum Reprod* 13:2367-2370

Fulford GR, Katz DF, Powell RL (1998) Swimming of spermatozoa in a linear viscoelastic fluid. *Biorheology* 35:295-309

Gadélha H, Gaffney EA, Smith DJ, Kirkman-Brown JC (2010) Non-linear instability in flagellar dynamics: A novel modulation mechanism in sperm migration? *J Roy Soc Interface* 7:1689-1697

Gaffney EA, Gadêlha H, Smith DJ, Blake JR, Kirkman-Brown JC (2011) Mammalian sperm motility: observation and theory. *Annu Rev Fluid Mech* 43:501-528

Garcia X, Rafaï S, Peyla P (2013) Light control of the flow of phototactic microswimmer suspensions. *Phys Rev Lett* 110:138106

Garner DL (2001) Sex-sorting mammalian sperm: Concept to application in animals. *J Androl* 22:519-526

Gascoyne P, Mahidol C, Ruchirawat M, Satayavivad J, Watcharasit P, Becker FF (2002) Microsample preparation by dielectrophoresis: isolation of malaria. *Lab Chip* 2:70-75

Gascoyne P, Vykoukal J (2002) Particle separation by dielectrophoresis. *Electrophoresis* 23:1973-1983

Ghosh A, Paria D, Rangarajan G, Ghosh A (2013) Velocity fluctuations in helical propulsion: how small can a propeller be. *J Phys Chem Lett* 5:62-68

Gillies EA, Cannon RM, Green RB, Pacey AA (2009) Hydrodynamic propulsion of human sperm. *J Fluid Mech* 625:445-474

Goto T, Masuda S, Terada K, Takano Y (2001) Comparison between observation and boundary element analysis of bacterium swimming motion. *JSME Int J C - Mech Sy* 44:958-963

Goto T, Nakata K, Baba K, Nishimura M, Magariyama Y (2005) A fluid-dynamic interpretation of the asymmetric motion of singly flagellated bacteria swimming close to a boundary. *Biophys J* 89:3771-3779

Gray J (1928) Ciliary movements. *Cambridge University Press*

Gray J, Hancock G (1955) The propulsion of sea-urchin spermatozoa. *J Exp Biol* 32:802-814

Grier DG (2003) A revolution in optical manipulation. *Nature* 424:810-816

Grow DR, Oehninger S, Seltman HJ, Toner JP, Swanson RJ, Kruger TF, Muasher SJ (1994) Sperm morphology as diagnosed by strict criteria: probing the impact of teratozoospermia on fertilization rate and pregnancy outcome in a large in vitro fertilization population. *Fertil Steril* 62:559-567

Guasto JS, Rusconi R, Stocker R (2012) Fluid mechanics of planktonic microorganisms. *Annu Rev Fluid Mech* 44:373-400

Guidobaldi A, Jeyaram Y, Berdakin I, Moshchalkov VV, Condat CA, Marconi VI, Giojalas L, Silhanek AV (2014) Geometrical guidance and trapping transition of human sperm cells. *Physical Review E* 89:032720

Hancock G (1953) The self-propulsion of microscopic organisms through liquids. *Proc Roy Soc Lond A* 217:96-121

Hansen M, Bower C, Milne E, de Klerk N, Kurinczuk JJ (2005) Assisted reproductive technologies and the risk of birth defects—a systematic review. *Hum Reprod* 20:328-338

Happel J, Brenner H (2012) Low Reynolds number hydrodynamics: with special applications to particulate media (Vol. 1). Springer Science & Business Media

Hejazian M, Li W, Nguyen NT (2015) Lab on a chip for continuous-flow magnetic cell separation. *Lab Chip* 15:959–970

Henkel RR, Franken DR, Lombard CJ, Schill WB (1994) Selective capacity of glass-wool filtration for the separation of human spermatozoa with condensed chromatin: a possible therapeutic modality for male-factor cases. *J Assist Reprod Gen* 11:395-400

Henkel RR, Schill WB (2003) Sperm preparation for ART. *Reprod Biol Endocrin* 1:108

Hernandez-Ortiz JP, Stoltz CG, Graham MD (2005) Transport and collective dynamics in suspensions of confined swimming particles. *Phys Rev Lett* 95:204501

Hesketh T, Zhu WX (2006) Abnormal sex ratios in human populations: causes and consequences. *Proc Natl Acad Sci USA* 103:13271-13275

Higdon JJL (1979) A hydrodynamic analysis of flagellar propulsion. *J Fluid Mech* 90:685-711

Hinton RJ, Dobrota M (1978) Density gradient centrifugation. In: Laboratory techniques in biochemistry and molecular biology (Vol. 6). *Elsevier/North-Holland Biomedical Press*

Hirsch MW, Smale S, Devaney RL (2012) Differential equations, dynamical systems, and an introduction to chaos, 3rd edition. *Academic press*

Hruska KS, Furth PA, Seifer DB, Sharara FI, Flaws JA (2000) Environmental factors in infertility. *Clin Obstet Gynecol* 43:821-829

Hsu HY, Ohta AT, Chiou PY, Jamshidi A, Neale SL, Wu MC (2010) Phototransistor-based optoelectronic tweezers for dynamic cell manipulation in cell culture media. *Lab Chip* 10:165-172

Huang Y, Wang XB, Becker FF, and Gascoyne PR (1997) Introducing dielectrophoresis as a new force field for field-flow fractionation. *Biophysical Journal* 73:1118-1129

Huber G, Koehler SA, Yang J (2011) Micro-swimmers with hydrodynamic interactions. *Math Comput Model* 53:1518-1526

Human Fertilisation Embryology Authority, United Kingdom. http://www.hfea.gov.uk/ Accessed 04 June 2018

Hunt JE, Wallach EE (1974) Uterine factors in infertility – An overview. *Clin Obstet Gynecol* 17:44-64

Hussey ND, Donggui H, Froiland DA, Hussey DJ, Haan EA, Matthews CD, Craig JE (1999) Analysis of five Duchenne muscular dystrophy exons and gender determination using conventional duplex polymerase chain reaction on single cells. *Mol Hum Reprod* 5:1089-1094

Hydon PE (2000) Symmetry methods for differential equations, *Cambridge University Press*

Iserles A (2009) A first course in the numerical analysis of differential equations. *Cambridge university press*

Ishijima S, Oshio S, Mohri H (1986) Flagellar movement of human spermatozoa. Ga*mete Res* 13:185-197

Ishikawa T (2009) Suspension biomechanics of swimming microbes. *J Roy Soc Interface* rsif20090223
Ishimoto K, Gaffney EA (2015) Fluid flow and sperm guidance: a simulation study of hydrodynamic sperm rheotaxis. *J Roy Soc Interface* 12:20150172
Jabbarzadeh M, Hyon Y, Fu HC (2014) Swimming fluctuations of micro-organisms due to heterogeneous microstructure. *Phys Rev E* 90:043021
Jen CP, Chen WF (2011) An insulator-based dielectrophoretic microdevice for the simultaneous filtration and focusing of biological cells. *Biomicrofluidics* 5:044105
Johnson LA, Flook JP, Hawk HW (1989) Sex preselection in rabbits: Live births from X and Y sperm separated by DNA and cell sorting. *Biol Reprod* 41:199-203
Johnson LA, Flook JP, Look MV, Pinkel D (1987) Flow sorting of X and Y chromosome-bearing spermatozoa into two populations. *Gamete Res* 16:l-9
Johnson RE (1980) An improved slender-body theory for Stokes flow. *J Fluid Mech* 99:411-431
Johnson RE, Brokaw CJ (1979) Flagellar hydrodynamics. A comparison between resistive-force theory and slender-body theory. *Biophys J* 25:113-127
Jones TB (2003) Basic theory of dielectrophoresis and electrorotation. *IEEE Eng Med Biol Mag* 22:33-42
Jones TB (1985) Multipole corrections to dielectrophoretic force. *IEEE Trans Ind Appl* 4:930-934
Jones TB, Washizu M (1996) Multipolar dielectrophoretic and electrorotation theory. *J Electrostat* 37:121-34
Jørgensen N, Joensen UN, Jensen TK, Jensen MB, Almstrup K, Olesen IA, Juul A, Andersson AM, Carlsen E, Petersen JH, Toppari J, Skakkebaek NE (2012) Human semen quality in the new millennium: a prospective cross-sectional population-based study of 4867 men. *BMJ Open* 2:e000990
Kantsler V, Dunkel J, Blayney M, Goldstein RE (2014) Rheotaxis facilitates upstream navigation of mammalian sperm cells. *ELife* 3:e02403
Karabinus DS (2009) Flow cytometric sorting of human sperm: MicroSort® clinical trial update. *Theriogenology* 71:74-79
Katalinic A, Rösch C, Ludwig M (2004) Pregnancy course and outcome after intracytoplasmic sperm injection: a controlled, prospective cohort study. *Fertil Steril* 81:1604-1616
Katz DF, Davis RO (1987) Automatic analysis of human sperm motion. *J Androl* 8:170-181
Katz DF, Brofeldt BT, Overstreet JW, Hanson FW (1982) Alteration of cervical mucus by vanguard human spermatozoa. *J Reprod Fertil* 65:171-175
Katz DF, Diel L, Overstreet JW (1982) Differences in the movement of morphologically normal and abnormal human seminal spermatozoa. *Biol Reprod* 26:566-570
Katz DF, Mills RN, Pritchett TR (1978) The movement of human spermatozoa in cervical mucus. *J Reprod Fertil* 53:259-265
Katz DF, Overstreet JW, Samuels SJ, Niswander PW, Bloom TD, Lewis EL (1986) Morphometric analysis of spermatozoa in the assessment of human male fertility. *J Androl* 7:203-210
Keaveny EE, Maxey MR (2008) Interactions between comoving magnetic microswimmers *Phys Rev E* 77:041910
Keim NC, Garcia M, Arratia PE (2012) Fluid elasticity can enable propulsion at low Reynolds number. *Phys Fluids* 24:081703

Kelley CT (1999) Iterative methods for optimization. *Society for Industrial and Applied Mathematics*

Kessler JO (1985) Hydrodynamic focusing of motile algal cells. *Nature* 313:218-220

Khalaf G, Shukur G (2005) Choosing ridge parameter for regression problems. *Commun Stat* 34:1177-1182

Khatamee MA, Horn SR, Weseley A, Farooq T, Jaffe SB, Jewelewicz R (1999) A controlled study for gender selection using swim-up separation. *Gynecol Obstet Inves* 48:7-13

Khoshmanesha K, Chen Z, Tovar-Lopez F J, Nahavandi S, Baratchi S, Kalantar-zadeh K, Mitchell A (2009) Dielectrophoretic manipulation and separation of microparticles using curved microelectrodes. *Electrophoresis* 30:3707-3717

Khoshmanesha K, Nahavandia S, Baratchib S, Mitchellc A, Kalantar-zadeh K (2011) Dielectrophoretic platforms for bio-microfluidic systems. *Biosens Bioelectron* 26: 1800-1814

Kidd SA, Eskenazi B, Wyrobek AJ (2001) Effects of male age on semen quality and fertility: a review of the literature. *Fertil Steril* 75:237-248

Kierzenka J, Shampine LF (2001) A BVP solver based on residual control and the Maltab PSE. *ACM Math Software* 27:299-316

Kim M-C, Wang Z, Lam RH, Thorsen T (2008) Building a better cell trap: Applying Lagrangian modeling to the design of microfluidic devices for cell biology. *J Appl Phys* 103:044701

Kirkman-Brown JC, Smith DJ (2011) Sperm motility: is viscosity fundamental to progress? *Mol Hum Reprod* 17:539-544

Klein JD, Clapp AR, Dickinson RB (2003) Direct measurement of interaction forces between a single bacterium and a flat plate. *J Colloid Interf Sci* 261:379-85.

Koch DL, Subramanian G (2011) Collective hydrodynamics of swimming microorganisms: Living fluids. *Annu Rev Fluid Mech* 43:637-659

Koh JBY, Marcos (2017) Sorting spermatozoa by morphology using magnetophoresis. *Microfluid Nanofluid* 21:75

Koh JBY, Shen X, Marcos (2016) Theoretical modeling in microscale locomotion. *Microfluid Nanofluid* 20:1-27

Koh JBY, Marcos (2015a) The study of spermatozoa and sorting in relation to human reproduction. *Microfluid Nanofluid* 18:755-774

Koh JBY, Marcos (2015b) Dielectrophoresis of spermatozoa in viscoelastic medium *Electrophoresis* 36:1514-1521

Koh JBY, Marcos (2014) Effect of dielectrophoresis on spermatozoa. *Microfluid Nanofluid* 17:613-622

Komiya A, Watanabe A, Kato T, Kawauchi Y, Fuse H (2014) Observation of spermatozoa by a high-magnification microscope. *Reprod Med Biol* 13:21-28

Kotsiantis SB, Zaharakis I, Pintelas P (2007) Supervised machine learning: A review of classification techniques. *Emerging artificial intelligence applications in computer engineering* 160:3-24

Krans JL (2010) The sliding filament theory of muscle contraction. *Nature Education* 3:66

Krogh A (2008) What are artificial neural networks?. *Nat Biotechnol* 26:195

Krogh A, Vedelsby J (1995). Neural network ensembles, cross validation, and active learning. In *Advances in neural information processing systems* pp. 231-238

Krüger J, Singh K, O'Neill A, Jackson C, Morrison A, O'Brien P (2002) Development of a microfluidic device for fluorescence activated cell sorting. *J Micromech Microeng* 12:486-494

Kua CH, Lam YC, Yang C, Youcef-Toumi K, Rodriguez I (2008) Modeling of dielectrophoretic force for moving dielectrophoresis electrodes. *J Electrostat* 66:514-525.

Kurtuldu H, Tam D, Hosoi A, Johnson KA, Gollub J (2013) Flagellar waveform dynamics of freely swimming algal cells. *Phys Rev E* 88:013015

Lai SK, Wang YY, Hanes J (2009) Mucus-penetrating nanoparticles for drug and gene delivery to mucosal tissues. *Adv Drug Deliver Rev* 61:158-171

Lam RHW, Weng S, Lu W, Fu J (2012) Live-cell subcellular measurement of cell stiffness using a microengineered stretchable micropost array membrane. *Integr Biol* 4:1289–1298

Land JA, Evers JLH (2003) Risks and complications in assisted reproduction techniques: Report of an ESHRE consensus meeting. *Hum Reprod* 18:455-457

Lauga E (2007) Propulsion in a viscoelastic fluid. *Phys Fluids* 19:083104

Lauga E, Powers TR (2009) The hydrodynamics of swimming microorganisms. *Rep Prog Phys* 72:096601

Leiderman K, Bouzarth EL, Cortez R, Layton AT (2013) A regularization method for the numerical solution of periodic Stokes flow. *J Comput Phys* 236:187-202

Levinson G, Keyvanfar K, Wu JC, Fugger EF, Fields RA, Harton GL, Palmer FT, Sisson ME, Starr KM, Dennison-Lagos L, Calvo L, Sherins RJ, Bick D, Schulman JD, Black SH (1995) Genetics and human conception: DNA-based X-enriched sperm separation as an adjunct to preimplantation genetic testing for the prevention of X-linked disease. *Hum Reprod* 10:979-982

Lewpiriyawong N, Kandaswamy K, Yang C, Ivanov V, Stocker R (2011) Microfluidic characterization and continuous separation of cells and particles using conducting poly (dimethyl siloxane) electrode induced alternating current-dielectrophoresis. *Anal Chem* 83:9579-9585

Lewpiriyawong N, Yang C (2012) AC-dielectrophoretic characterization and separation of submicron and micron particles using sidewall AgPDMS electrodes *Biomicrofluidics* 6:012807

Lewpiriyawong N, Yang C (2014) Dielectrophoresis field-flow fractionation for continuous-flow separation of particles and cells in microfluidic devices. In *Advances in Transport Phenomena 2011* (pp. 29-62). *Springer International Publishing*

Li G, Tam L-K, Tang JX (2008) Amplified effect of Brownian motion in bacterial near-surface swimming. *Proc Natl Acad Sci USA* 105:18355-18359

Li G, Tang JX (2009) Accumulation of microswimmers near a surface mediated by collision and rotational Brownian motion. *Phys Rev Lett* 103:078101

Li G, Karimi A, Ardekani A (2014) Effect of solid boundaries on swimming dynamics of microorganisms in a viscoelastic fluid. *Rheol Acta* 53:911-926

Liaw A, Wiener M (2002) Classification and regression by randomForest. *R news* 2:18-22

Lighthill J (1975) Mathematical biofluiddynamics. *Society for Industrial and Applied Mathematics*

Lighthill J (1976) Flagellar hydrodynamics. *SIAM Rev* 18:161-230

Liu B, Powers TR, Breuer KS (2011) Force-free swimming of a model helical flagellum in viscoelastic fluids. *Proc Natl Acad Sci USA* 108:19516-19520

Lopes S, Jurisicova A, Sun JG, Casper RF (1998) Reactive oxygen species: potential cause for DNA fragmentation in human spermatozoa. *Hum Reprod* 13:896-900

Malo AF, Garde JJ, Soler AJ, García AJ, Gomendio M, Roldan ERS (2005) Male fertility in natural populations of red deer is determined by sperm velocity and the proportion of normal spermatozoa. *Biol Reprod* 72:822-829

Malter HE, and Cohen J (2002) Intracytoplasmic sperm injection: technical aspects. Current Practices and Controversies in Assisted Reproduction. *Geneva World Health Organisation* 126-133

Manzur A, Cárdenas I, Macaya R, Almendra C, Gajardo G, Bianchi M, Durruty G (2004) Unbalanced sex ratio in newborns obtained by intrauterine inseminations. *Int Congr Ser* 1271:341-344

Marchesi DE, Biederman H, Ferrara S, Hershlag A, Feng HL (2010) The effect of semen processing on sperm DNA integrity: comparison of two techniques using the novel Toluidine Blue Assay. *Eur J Obstet Gynecol Reprod Biol* 151:176-180

Marcos, Fu HC, Powers TR, Stocker R (2012) Bacterial rheotaxis. *Proc Natl Acad Sci USA* 109:4780-4785

Martin RH, Rademaker A (1988) The relationship between sperm chromosomal abnormalities and sperm morphology in humans. *Mutat Res Lett* 207:159-164

Matsuda Y, Tobari I (1988) Chromosomal analysis in mouse eggs fertilized in vitro with sperma exposed to ultraviolet light (UV) and methyl and ethyl methanesulfonate (MMS and EMS). *Mutat Res-Fund Mol M* 198:131-144

Menkveld R, Kruger TF (1995) Advantages of strict (Tygerberg) criteria for evaluation of sperm morphology. *Int J Androl* 18:36-42

Menkveld R, Stander FS, Kotze TJ, Kruger TF, van Zyl JA (1990) The evaluation of morphological characteristics of human spermatozoa according to stricter criteria. *Hum Reprod* 5:586-592

Menkveld R, Wong WY, Lombard CJ, Wetzels AM, Thomas CM, Merkus HM, Steegers-Theunissen RP (2001) Semen parameters, including WHO and strict criteria morphology, in a fertile and subfertile population: an effort towards standardization of in-vivo thresholds. *Hum Reprod* 16:1165-1171

Michalski RS, Carbonell JG, Mitchell TM (2013) Machine learning: An artificial intelligence approach. *Springer Science & Business Media*

Miki K, Clapham DE (2013) Rheotaxis guides mammalian sperm. *Curr Biol* 23:443-452

Ministry of Health, Singapore. https://www.moh.gov.sg/content/moh_web/home.html Accessed 08 August 2017

Moncada-Hernández H, Lapizco-Encinas B H (2010) Simultaneous concentration and separation of microorganisms: insulator-based dielectrophoretic approach. *Anal Bioanal Chem* 396:1805-1816

Moore LR, Rodriguez AR, Williams PS, McCloskey K, Bolwell BJ, Nakamura M, Chalmers JJ, Zborowski M (2001) Progenitor cell isolation with a high-capacity quadrupole magnetic flow sorter. *J Magn Magn Mater* 225:277-284

Mortimer D (1994) Sperm recovery techniques to maximize fertilizing capacity. *Reprod Fert Develop* 6:25-31

Mortimer D (2000) Sperm Preparation Methods. *J Androl* 21:357-366

Mortimer D, Pandya IJ, Sawers RS (1986) Relationship between human sperm motility characteristics and sperm penetration into human cervical mucus in vitro. *J Reprod Fertil* 78:93-102

Mortimer D, Serres C, Mortimer ST, Jouannet P (1988) Influence of image sampling frequency on the perceived movement characteristics of progressively motile human spermatozoa. *Gamete Res* 20:313-327

Mortimer ST, Swan MA (1995) Variable kinematics of capacitating human spermatozoa. *Hum Reprod* 10:3178-3182
Munné S (1994) Human sperm sex selection Flow cytometry separation of X and Y spermatozoa could be detrimental for human embryos. *Hum Reprod* 9:758-758
Musa H, Saidu I, Waziri MY (2010) A simplified derivation and analysis of fourth order Runge Kutta method. *Int J Comp Appl* 9:51-55
Nallella KP, Sharma RK, Aziz N, Agarwal A (2006) Significance of sperm characteristics in the evaluation of male infertility. *Fertil Steril* 85:629-634
Nascimento JL, Botvinick EL, Shi LZ, Durrant B, Berns MW (2006) Analysis of sperm motility using optical tweezers. *J Biomed Opt* 11:044001
Nasseri S, Phan-Thien N (1997) Hydrodynamic interaction between two nearby swimming micromachines. *Comput Mech* 20:551-559
National University Hospital Woman's Centre Singapore. http://www.nuhgynae.com.sg Accessed 04 June 2018
Nguyen NT (2012) Micromixers: fundamentals, design and fabrication. *Elsevier, Oxford*
Nguyen H, Cortez R, Fauci L (2014) Computing flows around microorganisms: slender-body theory and beyond. *Am Math Mon* 121:810-823
Normand T and Lauga E (2008) Flapping motion and force generation in a viscoelastic fluid. *Phys Rev E* 78:061907
Oehninger S, Franken DR, Ombelet W (2014) Sperm functional tests. *Fertil Steril* 102:1528-1533
Olson CK, Keppler-Noreuil KM, Romitti PA, Budelier WT, Ryan G, Sparks AE, & Van Voorhis BJ (2005) In vitro fertilization is associated with an increase in major birth defects. *Fertil Steril* 84:1308-1315
Ombelet W, Deblaere K, Bosmans E, Cox A, Jacobs P, Janssen M, Nijs M (2003) Semen quality and intrauterine insemination. *Reprod Biomed Online* 7:485-92
Ombelet W, Dhont N, Thijssen A, Bosmans E, Kruger T (2014) Semen quality and prediction of IUI success in male subfertility: a systematic review. *Reprod Biomed Online* 28:300-309
Owen DH, Katz DF (2005) A review of the physical and chemical properties of human semen and the formulation of a semen simulant. *J Androl* 26:459-469
Paasch U, Grunewald S, Fitzl G, Glander HJ (2003) Deterioration of plasma membrane is associated with activated caspases in human spermatozoa. *J Androl* 24: 246-252
Pak OS, Gao W, Wang J, Lauga E (2011) High-speed propulsion of flexible nanowire motors: Theory and experiments. *Soft Matter* 7:8169-8181
Pedley T, Kessler J (1992) Hydrodynamic phenomena in suspensions of swimming microorganisms. *Annu Rev Fluid Mech* 24:313-358
Pedregosa F, Varoquaux G, Gramfort A, Michel V, Thirion B, Grisel O, Blondel M, Prettenhofer P, Weiss R, Dubourg V, Vanderplas J (2011) Scikit-learn: Machine learning in Python. *Journal of Machine Learning Research* 12:2825-2830
Pethig R (2010) Dielectrophoresis: status of the theory, technology, and applications. *Biomicrofluidics* 4:022811
Peyman SA, Kwan EY, Margarson O, Iles A, Pamme N (2009) Diamagnetic repulsion – a versatile tool for label-free particle handling in microfluidic devices. *J Chromatog A* 1216:9055-9062
Pinto SG, Rodríguez SP, Torcal JM (1997) On the numerical solution of stiff IVPs by Lobatto IIIA Runge-Kutta methods. *J Comput Appl Math* 82:129-148
Purcell EM (1977) Life at low Reynolds number. *Am J Phys* 45:3-11

Qi H, Moran MM, Navarro B, Chong JA, Krapivinsky G, Krapivinsky L, Kirichok I, Ramsey S, Quill TA, Clapham DE (2007) All four CatSper ion channel proteins are required for male fertility and sperm cell hyperactivated motility. *Proc Natl Acad Sci USA* 104:1219-1223

Ramia M, Tullock D, Phan-Thien N (1993) The role of hydrodynamic interaction in the locomotion of microorganisms. *Biophys J* 65:755

Rawe VY, Boudri HU, Sedó CA, Carro M, Papier S, Nodar F (2010) Healthy baby born after reduction of sperm DNA fragmentation using cell sorting before ICSI. *Reprod Biomed Online* 20:320-323

Riedel-Kruse IH, Hilfinger A, Howard J, Jülicher F (2007) How molecular motors shape the flagellar beat. *HFSP J* 1:192-208

Riffell JA, Zimmer RK (2007) Sex and flow: the consequences of fluid shear for sperm–egg interactions. *J Exp Biol* 210:3644-3660

Risopatron J, Sanchez R, Sepulveda N, Peña P, Villagran E, Miska W (1996) Migration/sedimentation sperm selection method used in bovine in vitro fertilization: comparison with washing/centrifugation. *Theriogenology* 46:65-73

Rodenborn B, Chen CH, Swinney HL, Liu B, Zhang H (2013) Propulsion of microorganisms by a helical flagellum. *Proc Natl Acad Sci USA* 110:E338-E347

Romanczuk P, Bär M, Ebeling W, Lindner B, Schimansky-Geier L (2012) Active brownian particles. *Eur Phys J - Spec Top* 202:1-162

Roosen-Runge EC (1977) The process of spermatogenesis in animals (Vol. 5). *CUP Archive*

Rosales-Cruzaley E, Cota-Elizondo PA, Sánchez D, Lapizco-Encinas BH (2013) Sperm cells manipulation employing dielectrophoresis. *Bioproc Biosyst Eng* 36:1353-1362

Rose GA, Wong A (1998) Experiences in Hong Kong with the theory and practice of the albumin column method of sperm separation for sex selection. *Hum Reprod* 13:146-149

Said TM, Agarwal A, Zborowski M, Grunewald S, Glander HJ, Paasch U (2008) Andrology Lab Corner: Utility of magnetic cell separation as a molecular sperm preparation technique. *Journal of Andrology* 29:134-142

Said TM, Grunewald S, Paasch U, Rasch M, Agarwal A, Glander HJ (2005) Effects of magnetic-activated cell sorting on sperm motility and cryosurvival rates. *Fertil Steril* 83:1442-1446

Sakkas D, Manicardi GC, Tomlinson M, Mandrioli M, Bizzaro D, Bianchi PG, Bianchi U (2000) The use of two density gradient centrifugation techniques and the swim-up method to separate spermatozoa with chromatin and nuclear DNA anomalies. *Hum Reprod* 15:1112-1116

Sarkar S (1984) Human sperm swimming in flow. *Differentiation* 27:126-132

Schamel D, Mark AG, Gibbs JG, Miksch C, Morozov KI, Leshansky AM, Fischer P (2014) Nanopropellers and their actuation in complex viscoelastic media. *ACS Nano* 8:8794-8801

Schnelle T, Müller T, Fiedler S, Fuhr G (1999) The influence of higher moments on particle behaviour in dielectrophoretic field cages. *J Electrostat* 46:13-28

Schieve LA, Meikle SF, Ferre C, Peterson HB, Jeng G, Wilcox LS (2002) Low and very low birth weight in infants conceived with use of assisted reproductive technology. *New Engl J Med* 346:731-737

Schuster TG, Cho B, Keller LM, Takayama S, Smith GD (2003) Isolation of motile spermatozoa from semen samples using microfluidics. *Reprod Biomed Online* 7:75-81

Schwimmer WB, Ustay KA, Behrman SJ (1967) An evaluation of immunologic factors of infertility. *Fertil Steril* 18:167-180

Senftle FE, Hambright WP (1969) Magnetic susceptibility of biological materials. In *Biological effects of magnetic fields* pp. 261-306. Springer, Boston, MA

Seo DB, Agca Y, Feng ZC, Critser JK (2007) Development of sorting, aligning, and orienting motile sperm using microfluidic device operated by hydrostatic pressure. *Microfluid Nanofluid* 3:561-570

Serres C, Escalier D, David G (1984) Ultrastructural morphometry of the human sperm flagellum with a stereological analysis of the lengths of the dense fibres. *Biol Cell* 49:153-161

Shao B, Shi LZ, Nascimento JM, Botvinick EL, Ozkan M, Berns MW, Esener SC (2007) High-throughput sorting and analysis of human sperm with a ring-shaped laser trap. *Biomed Microdevices* 9:361-369

Shampine LF, Gladwell I, Thompson S (2003) Solving ODEs with matlab. *Cambridge University Press*

Shampine LF, Kierzenka J, Reichelt MW (2000) Solving boundary value problems for ordinary differential equations in MATLAB with bvp4c. From http://www.mathworks.com/

Shampine LF, Reichelt MW (1997) The Matlab ode suite. *SIAM J Sci Comput* 18:1-22

Shapiro HM (2005) Practical flow cytometry. *John Wiley & Sons*

Sharpe JC, Evans KM (2009) Advances in flow cytometry for sperm sexing. *Theriogenology* 71:4-10

Sharma RK, Sabanegh E, Mahfouz R, Gupta S, Thiyagarajan A, Agarwal A (2010) TUNEL as a test for sperm DNA damage in the evaluation of male infertility. *Urology* 76:1380-1386

Shen XN, Arratia PE (2011) Undulatory swimming in viscoelastic fluids. *Phys Rev Lett* 106:208101

Shi L, Shao B, Chen T, Berns M (2009) Automatic annular laser trapping: a system for high‐throughput sperm analysis and sorting. *J Biophotonics* 2:167-177

Singapore Department of Statistics. http://www.singstat.gov.sg/statistics. Accessed 08 Aug 2017

Singleton J, Mielke CH, Migliori A, Boebinger GS, Lacerda AH (2004) The national high magnetic field laboratory pulsed-field facility at Los Alamos National Laboratory. *Physica B* 346:614-617

Smith DJ, Gaffney EA, Blake JR, Kirkman-Brown JC (2009) Human sperm accumulation near surfaces: a simulation study. *J Fluid Mech* 621:289-320

Smith DJ, Gaffney EA, Gadélha H, Kapur N, Kirkman-Brown JC (2009) Bend propagation in the flagella of migrating human sperm, and its modulation by viscosity. *Cell Motil Cytoskel* 66:220-236

Smith JS (2000) High density, low parasitic direct integration by fluidic self assembly (FSA). In: *Electron Devices Meeting, 2000. Technical Digest. International* 201-204. IEEE

Smith S, Pfeifer SM, Collins JA (2003) Diagnosis and management of female infertility. *Jama* 290:1767-1770

Spagnolie SE, Liu B, Powers TR (2013) Locomotion of helical bodies in viscoelastic fluids: enhanced swimming at large helical amplitudes. *Phys Rev Lett* 111:068101

Spehr M, Schwane K, Riffell JA, Barbour J, Zimmer RK, Neuhaus EM, Hatt H (2004) Particulate adenylate cyclase plays a key role in human sperm olfactory receptor-mediated chemotaxis. *J Biol Chem* 279:40194-40203

Stoer J, Bulirsch R (2013) Introduction to numerical analysis, Volume 12. *Springer Science & Business Media*

Suarez SS, Katz DF, Owen DH, Andrew JB, Powell RL (1991) Evidence for the function of hyperactivated motility in sperm. *Biol Reprod* 44: 375-381

Subramani E, Basu H, Thangaraju S, Dandekar S, Mathur D, Chaudhury K (2014) Rotational dynamics of optically trapped human spermatozoa. *The Scientific World J* 2014:154367

Suh TK, Schenk JL, Seidel GE (2005) High pressure flow cytometric sorting damages sperm. *Theriogenology* 64:1035-1048

Summers KE, Gibbons IR (1971) Adenosine triphosphate-induced sliding of tubules in trypsin-treated flagella of sea-urchin sperm. *Proc Natl Acad Sci USA* 68:3092-3096

Sutcliffe AG, Ludwig M (2007) Outcome of assisted reproduction. *The Lancet* 370:351-359

Sznitman J, Shen X, Sznitman R, Arratia PE (2010) Propulsive force measurements and flow behavior of undulatory swimmers at low Reynolds number. *Phys Fluids* 22:121901

Takeda N, Yoshii N, Hoshino Y, Tanemura K, Sato E, Odawara Y (2012) A new human spermatozoon selection method based on penetration of cervical mucus for intracytoplasmic sperm injection. *J Mamm Ova Res* 29:65-74

Taylor G (1951) Analysis of the swimming of microscopic organisms. *P Roy Soc Lond A* 209:447-461

Tea NT, Jondet M, Scholler R (1984) A 'migration-gravity sedimentation' method for collecting motile spermatozoa from human semen. In: *In Vitro Fertilization, Embryo Transfer and Early Pregnancy, Springer Netherlands*, pp 117-120

Teran J, Fauci L, Shelley M (2010) Viscoelastic fluid response can increase the speed and efficiency of a free swimmer. *Phys Rev Lett* 104:038101

Thaler CD, Cardullo RA (1996) The initial molecular interaction between mouse sperm and the zona pellucida is a complex binding event. *J Biol Chem* 271:23289-23297

Tomlinson MJ, Lewis S, Morroll D (2013) Sperm quality and its relationship to natural and assisted conception: British Fertility Society Guidelines for practice. *Hum Fertil* 6:175-193

Tournus M, Kirshtein A, Berlyand L, Aranson IS (2015) Flexibility of bacterial flagella in external shear results in complex swimming trajectories. *J Roy Soc Interface* 12:20140904

Underhill PT, Hernandez-Ortiz JP, Graham MD (2008) Diffusion and spatial correlations in suspensions of swimming particles. *Phys Rev Lett* 100:248101

Utsuno H, Oka K, Yamamoto A, Shiozawa T (2013) Evaluation of sperm head shape at high magnification revealed correlation of sperm DNA fragmentation with aberrant head ellipticity and angularity. *Fertil Steril* 99:1573-1580

Van der Ven HH, Jeyendran RS, Al-Hasani S, Tünnerhoff A, Hoebbel K, Diedrich K, Krebs D, Perez-Pelaez S (1988) Glass wool column filtration of human semen: relation to swim-up procedure and outcome of IVF. *Hum Reprod* 3:85-88

Van Montfoort AP, Dumoulin JC, Land JA, Coonen E, Derhaag JG, Evers JL (2005) Elective single embryo transfer (eSET) policy in the first three IVF/ICSI treatment cycles. *Hum Reprod* 20:433-436

Van Steirteghem A (2002) Intracytoplasmic sperm injection: micromanipulation in assisted fertilization. Current practices and controversies in assisted reproduction. *Geneva: World Health Organisation* 134-141

Verheyen G, Tournaye H, Staessen C, De Vos A, Vandervorst M, Van Steirteghem A (1999) Controlled comparison of conventional in-vitro fertilization and intracytoplasmic sperm injection in patients with asthenozoospermia. *Hum Reprod* 14:2313-2319

Voldman J (2006) Electrical forces for microscale cell manipulation. *Annu Rev Biomed Eng* 8:425-454

Voldman J, Braff RA, Toner M, Gray ML, Schmidt MA (2001) Holding forces of single-particle dielectrophoretic traps. *Biophys J* 80:531-542

Volpe G, Gigan S, Volpe G (2014) Simulation of the active Brownian motion of a microswimmer. *Am J Phys* 82:659-664

Wang MM, Tu E, Raymond DE, Yang JM, Zhang H, Hagen N, Dees B, Mercer EM, Forster AH, Kariv I, Marchand PJ, Butler WF (2005) Microfluidic sorting of mammalian cells by optical force switching. *Nat Biotechnol* 23:83-87

Washizu M, Jones TB (1996) Dielectrophoretic interaction of two spherical particles calculated by equivalent multipole-moment method. *IEEE Trans Ind Appl* 32:233-242

Watarai H, Namba M (2002) Capillary magnetophoresis of human blood cells and their magnetophoretic trapping in a flow system. *J Chromatogr A* 961:3-8

Welch GR, Waldbieser GC, Wall RJ, Johnson LA (1995) Flow cytometric sperm sorting and PCR to confirm separation of X- and Y-chromosome bearing bovine sperm. *Anim Biotechnol* 6:131-139

Winet H, Bernstein G, Head J (1984) Observations on the response of human spermatozoa to gravity, boundaries and fluid shear. *J Reprod Fertil* 70:511-523

Wolf DP, Blasco L, Khan MA, Litt M (1978) Human cervical mucus. IV. Viscoelasticity and sperm penetrability during the ovulatory menstrual cycle. *Fertil Steril* 30:163-169

World Health Organization (1991) Infertility: a tabulation of available data on prevalence of primary and secondary infertility

World Health Organization (2010) WHO laboratory manual for the examination and processing of human semen

Wu CFJ (1986) Jackknife, bootstrap and other resampling methods in regression analysis. *Ann Stat* 14:1261-1295

Wu JM, Chung Y, Belford KJ, Smith GD, Takayama S, Lahann J (2006) A surface-modified sperm sorting device with long-term stability. *Biomed Microdevices* 8:99-107

Yan J, Feng HL, Chen ZJ, Hu J, Gao X, Qin Y (2006) Influence of swim-up time on the ratio of X-and Y-bearing spermatozoa. *Eur J Obstet Gyn R B* 129:150-154

Younglai EV, Holt D, Brown P, Jurisicova A, Casper RF (2001) Sperm swim-up techniques and DNA fragmentation. *Hum Reprod* 16:1950-1953

Yu TS, Lauga E, Hosoi AE (2006) Experimental investigations of elastic tail propulsion at low Reynolds number. *Phys Fluids* 18:091701

Zayed F, Lenton EA, Cooke ID (1997) Comparison between stimulated in-vitro fertilization and stimulated intrauterine insemination for the treatment of unexplained and mild male factor infertility. *Hum Reprod* 12:2408-2413

Zhao C, Yang C (2009) Exact solutions for electro-osmotic flow of viscoelastic fluids in rectangular micro-channels. *Appl Math Comput* 211:502-509

Zhu J, Barratt CL, Lippes J, Pacey AA, Cooke ID (1994) The sequential effects of human cervical mucus, oviductal fluid, and follicular fluid on sperm function. *Fertil Steril* 61:1129-1135

Appendices

Appendix A – Derivations

A.1 Derivation of the force-velocity relation in Resistive Force Theory

This section shows the mathematical procedures leading to the coefficients used in Resistive Force Theory (Lighthill 1976). The preceeding steps leading to the Stokes equation, as well as intermediate steps which Lighthill have omitted, likely to provide a concise paper targeted at experts in the field, are worked out and presented here.

First, the continuity equation will be derived. By the principle of mass conservation, the time rate of change of mass of a material region Ω is zero:

$$\frac{dM_\Omega}{dt} = \frac{d}{dt}\int_{\Omega(t)} \rho \, dV = 0 . \tag{A.1}$$

By Leibnitz's Theorem,

$$\frac{dM_\Omega}{dt} = \int_V \frac{\partial \rho}{\partial t} \, dV + \int_S n_i u_i \, \rho \, dS , \tag{A.2}$$

where the last term represents the mass flux out of the surface, ρ is density and n_i is the unit surface vector. By Gauss' Theorem, the volume integral of the divergence of a tensor is equal to the surface integral of the out flux of that tensor:

$$\int_S n_i \, \rho u_i \, dS = \int_V \partial_i \left(\rho u_i \right) dV . \tag{A.3}$$

Therefore, equation (A.1) becomes

$$\int_V \frac{\partial \rho}{\partial t} \, dV + \int_V \partial_i \left(\rho u_i \right) dV = 0 . \tag{A.4}$$

Since the integral holds for any arbitrary volume V,

$$\frac{\partial \rho}{\partial t} + \partial_i \left(\rho u_i \right) = 0 . \tag{A.5}$$

Applying chain rule,

$$\frac{\partial \rho}{\partial t} + u_i \, \partial_i \, \rho + \rho \, \partial_i \, u_i = \frac{D\rho}{Dt} + \rho \, \partial_i \, u_i = 0 . \tag{A.6}$$

Rearranging the equation and expressing in vector notation,

$$\frac{1}{\rho}\frac{D\rho}{Dt} + \partial_i u_i = 0 . \tag{A.7}$$

For an incompressible fluid, $\frac{D\rho}{Dt} = 0$ and hence the continuity equation is expressed, in tensor notation and vector form respectively, as

$$\partial_i u_i = 0 , \tag{A.8}$$

$$\nabla \bullet \mathbf{u} = 0 . \tag{A.9}$$

Having derived the continuity equation, the Navier-Stokes equation shall be derived starting from momentum balance. On a material region, the time rate of change of momentum is equal to the sum of body and surface forces on that region:

$$\frac{\partial}{\partial t}\int_{\Omega(t)} \rho u_i \, dV = \int_{\Omega(t)} \rho f_i \, dV + \int_S R_i \, dS , \tag{A.10}$$

where f_i is the body force per unit mass, and R_i is the surface force per unit area. The left-hand side of equation (A.10) can be expressed as

$$\frac{\partial}{\partial t}\int_{\Omega(t)} \rho u_i \, dV = \int_{\Omega(t)} \left[\frac{\partial}{\partial t}\left(\rho u_i\right) + \partial_j \left(\rho u_i u_j\right) \right] dV . \tag{A.11}$$

This leads to

$$\int_{\Omega(t)} \left[\frac{\partial}{\partial t}\left(\rho u_i\right) + \partial_j \left(\rho u_i u_j\right) \right] dV = \int_{\Omega(t)} \rho f_i \, dV + \int_S \tau_{ij} \, n_j \, dS , \tag{A.12}$$

where τ_{ij} is the stress tensor. Rearranging the equation, and using Gauss' theorem,

$$\int_{\Omega(t)} \left[\frac{\partial}{\partial t}\left(\rho u_i\right) + \partial_j \left(\rho u_i u_j\right) - \rho f_i - \partial_j \tau_{ij} \right] dV = 0 . \tag{A.13}$$

Since the integral holds for any arbitrary volume *V*,

$$\frac{\partial}{\partial t}\left(\rho u_i\right) + \partial_j \left(\rho u_i u_j\right) - \rho f_i - \partial_j \tau_{ij} = 0 . \tag{A.14}$$

Applying chain rule,

$$u_i \frac{\partial \rho}{\partial t} + \rho \frac{\partial u_i}{\partial t} + u_i \partial_j \left(\rho u_j\right) + \rho u_j \partial_j u_i - \rho f_i - \partial_j \tau_{ij} = 0 . \tag{A.15}$$

Since

$$u_i\left[\frac{\partial \rho}{\partial t}+\partial_j\left(\rho u_j\right)\right]=0, \tag{A.16}$$

equation (A.15) becomes

$$\rho\left[\frac{\partial u_i}{\partial t}+u_j\partial_j u_i\right]-\rho f_i-\partial_j\tau_{ij}=0, \tag{A.17}$$

which is

$$\rho\frac{Du_i}{Dt}=\rho f_i+\partial_j\tau_{ij}. \tag{A.18}$$

For an incompressible Newtonian fluid, the stress tensor is

$$\tau_{ij}=-p\,\delta_{ij}+\mu\left(\partial_j u_i+\partial_i u_j\right), \tag{A.19}$$

where δ_{ij} is the Kronecker delta and μ is the dynamic viscosity. Substituting the above relation back into (A.19),

$$\begin{aligned}\rho\frac{Du_i}{Dt}&=\rho f_i+\partial_j\left[-p\,\delta_{ij}+\mu\left(\partial_j u_i+\partial_i u_j\right)\right]\\&=\rho f_i-\partial_j p+\mu\partial_j\partial_j u_i+\mu\,\partial_j\partial_i u_j\end{aligned}. \tag{A.20}$$

Therefore, the Navier-Stokes equation, in tensor notation and vector form respectively, is

$$\rho\frac{Du_i}{Dt}=\rho f_i-\partial_j p+\mu\partial_j\partial_j u_i, \tag{A.21}$$

$$\rho\frac{D\mathbf{u}}{Dt}=\rho\mathbf{f}-\nabla p+\mu\nabla^2\mathbf{u}. \tag{A.22}$$

In the regime of low Reynolds number, the Navier-Stokes equation can be simplified into the Stokes equation, by applying dimensional analysis from the Navier-Stokes equation:

$$\rho\left[\frac{\partial\mathbf{u}}{\partial t}+\mathbf{u}\bullet\nabla\mathbf{u}\right]=\rho\mathbf{f}-\nabla p+\mu\nabla^2\mathbf{u}. \tag{A.23}$$

The pressure, force per unit mass, velocity, time and space terms shall be non-dimensionalised as follows:

$$\tilde{p} = \frac{p}{(\mu U/L)},\ \tilde{\mathbf{f}} = \frac{\mathbf{f}}{(\mu UL/\rho L^3)},\ \tilde{\mathbf{u}} = \frac{\mathbf{u}}{U},\ \tilde{t} = \frac{t}{T},\ \tilde{\mathbf{x}} = \frac{\mathbf{x}}{L}. \tag{A.24}$$

The dimensionless gradient operator, Reynolds number and Strouhal number are

$$\tilde{\nabla} = L\nabla,\ \mathrm{Re} = \frac{\rho UL}{\mu},\ \mathrm{St} = \frac{(1/T)L}{U}. \tag{A.25}$$

Multiplying equation (A.23) by $L^2/\mu U$,

$$\frac{\rho UL}{\mu}\left[\frac{(1/T)L}{U}\frac{\partial(\mathbf{u}/U)}{\partial(t/T)} + \frac{\mathbf{u}}{U}\bullet(L\nabla)\frac{\mathbf{u}}{U}\right] = \frac{\mathbf{f}}{(\mu UL/\rho L^3)} - (L\nabla)\frac{p}{(\mu U/L)} + (L\nabla)^2\frac{\mathbf{u}}{U}, \tag{A.26}$$

which can be expressed in dimensionless form as

$$\mathrm{Re}\left[\mathrm{St}\frac{\partial\tilde{\mathbf{u}}}{\partial\tilde{t}} + \tilde{\mathbf{u}}\bullet\tilde{\nabla}\tilde{\mathbf{u}}\right] = \tilde{\mathbf{f}} - \tilde{\nabla}\tilde{p} + \tilde{\nabla}^2\tilde{\mathbf{u}}. \tag{A.27}$$

In the limit where Re approaches zero,

$$0 = \tilde{\mathbf{f}} - \tilde{\nabla}\tilde{p} + \tilde{\nabla}^2\tilde{\mathbf{u}}. \tag{A.28}$$

Hence, the dimensional form of Stokes equation, in vector form and tensor notation, is

$$\rho\mathbf{f} - \nabla p + \mu\nabla^2\mathbf{u} = 0, \tag{A.29}$$

$$\rho f_i - \partial_j p + \mu\,\partial_j\partial_j u_i = 0. \tag{A.30}$$

RFT stems from the Stokes equation. Lighthill (1976) begins his derivation of RFT by considering the presence of a Stokeslet, which is a concentrated point force **F** acting on the fluid that introduces a delta function into the governing equation. In low Reynolds number, equation (A.29) becomes

$$-\nabla p + \mu\nabla^2\mathbf{u} + \mathbf{F}\delta(\mathbf{r}) = 0. \tag{A.31}$$

The velocity field due to a Stokeslet in a fluid can be written as

$$\mathbf{u} = \frac{\mathbf{F}}{6\pi\mu r} + \frac{1}{4} r^2 \nabla \left(\nabla \bullet \left(\frac{\mathbf{F}}{6\pi\mu r} \right) \right). \tag{A.32}$$

The above vector equation, in indicial notation, is

$$\begin{aligned} u_i \boldsymbol{e}_i &= \frac{F_i}{6\pi\mu r} \boldsymbol{e}_i + \frac{r^2}{4} \partial_j \boldsymbol{e}_j \left(\partial_k \boldsymbol{e}_k \bullet \frac{F_i}{6\pi\mu r} \boldsymbol{e}_i \right) \\ &= \frac{F_i}{6\pi\mu r} \boldsymbol{e}_i + \frac{r^2}{4} \partial_j \delta_{ij} \boldsymbol{e}_i \left(\partial_i \frac{F_i}{6\pi\mu r} \right) \end{aligned} . \tag{A.33}$$

Since $r = \sqrt{x_1^{\,2} + x_2^{\,2} + x_3^{\,2}} = \sqrt{x_i x_i}$, the equation can be expressed as

$$\begin{aligned} u_i \boldsymbol{e}_i &= \frac{F_i}{6\pi\mu r} \boldsymbol{e}_i + \frac{r^2}{4} \partial_j \delta_{ij} \left(\frac{F_i}{6\pi\mu} \partial_i \frac{1}{\sqrt{x_i x_i}} \right) \boldsymbol{e}_i \\ &= \frac{F_i}{6\pi\mu r} \boldsymbol{e}_i + \frac{r^2}{4} \partial_j \left(\frac{F_j}{6\pi\mu} \partial_i \left(x_i x_i \right)^{-1/2} \right) \boldsymbol{e}_i \\ &= \frac{F_i}{6\pi\mu r} \boldsymbol{e}_i + \frac{r^2}{4} \partial_j \left(\frac{F_j}{6\pi\mu} \left(\frac{-x_i}{\left(x_i x_i \right)^{3/2}} \right) \right) \boldsymbol{e}_i \\ &= \frac{F_i}{6\pi\mu r} \boldsymbol{e}_i + \frac{r^2}{4} \partial_j \left(\frac{-F_j x_i}{6\pi\mu r^3} \right) \boldsymbol{e}_i \end{aligned} . \tag{A.34}$$

Applying product rule to the second term above,

$$\begin{aligned} u_i \boldsymbol{e}_i &= \frac{F_i}{6\pi\mu r} \boldsymbol{e}_i + \frac{r^2}{4} \left(\frac{-F_j \delta_{ij}}{6\pi\mu r^3} + x_i \partial_j \left(\frac{-F_j}{6\pi\mu r^3} \right) \right) \boldsymbol{e}_i \\ &= \frac{F_i}{6\pi\mu r} \boldsymbol{e}_i + \frac{r^2}{4} \left(\frac{-F_i}{6\pi\mu r^3} + \frac{-F_j x_i}{6\pi\mu} \partial_j \left(x_j x_j \right)^{-3/2} \right) \boldsymbol{e}_i \\ &= \frac{F_i}{6\pi\mu r} \boldsymbol{e}_i + \frac{r^2}{4} \left(\frac{-F_i}{6\pi\mu r^3} + \frac{-F_j x_i}{6\pi\mu} \left(\frac{-3x_j}{\left(x_j x_j \right)^{5/2}} \right) \right) \boldsymbol{e}_i \\ &= \left(\frac{F_i}{6\pi\mu r} - \frac{F_i r^2}{24\pi\mu r^3} + \frac{F_j r^2 x_i x_j}{8\pi\mu r^5} \right) \boldsymbol{e}_i \\ &= \frac{1}{8\pi\mu r^3} \left(F_i r^2 + F_j x_j x_i \right) \boldsymbol{e}_i \end{aligned} . \tag{A.35}$$

Converting the indicial notation back into vector notation, we get another expression for describing the velocity field due to a Stokeslet:

$$\mathbf{u} = \frac{r^2\mathbf{F} + (\mathbf{F} \bullet \mathbf{r})\mathbf{r}}{8\pi\mu r^3} . \tag{A.36}$$

The fluid velocity field due to the motion of a flagellum of a small radius, a, can be represented by a distribution of Stokeslets, each of strength $\mathbf{f}(s)$ being the force per unit length, along the centreline (Lighthill 1976). Using equation (A.36), the velocity field due to the tangential Stokeslet distribution f_x is

$$\int_{-q}^{q} \frac{f_x}{8\pi\mu} \begin{bmatrix} 1/r + (x-X)(x-X)/r^3 \\ (x-X)\,y/r^3 \\ (x-X)\,z/r^3 \end{bmatrix} dX , \tag{A.37}$$

where q is a large multiple of the flagellum radius but a small fraction of the flagellum wavelength (Lighthill 1976), and r is the distance from a Stokeslet at (X, 0, 0) to a point (x, y, z) of interest:

$$r = \sqrt{(x-X)^2 + y^2 + z^2} . \tag{A.38}$$

At the surface of the cross-section at $x = 0$,

$$r = \sqrt{(0-X)^2 + y^2 + z^2} = \sqrt{X^2 + a^2} . \tag{A.39}$$

Therefore, equation (A.37) becomes

$$\int_{-q}^{q} \frac{f_x}{8\pi\mu} \begin{bmatrix} \frac{1}{r} + \frac{X^2}{r^3} \\ \frac{-Xy}{r^3} \\ \frac{-Xz}{r^3} \end{bmatrix} dX . \tag{A.40}$$

Applying the mathematical procedures as presented in Appendix A.2, the velocity field due to the tangential Stokeslet distribution f_x can be computed to be

$$\frac{f_x}{8\pi\mu} \begin{bmatrix} 4\ln(2q/a) - 2 \\ 0 \\ 0 \end{bmatrix} . \tag{A.41}$$

The velocity field generated by the Stokeslet distribution f_y is

$$\int_{-q}^{q} \frac{f_y}{8\pi\mu} \begin{bmatrix} \frac{(x-X)y}{r^3} \\ \frac{r^2+y^2}{r^3} \\ \frac{yz}{r^3} \end{bmatrix} dX \,. \tag{A.42}$$

This would result in a velocity that varies along the circumference of a cross-section, which is unphysical. Therefore, a distribution of dipole of strength $-a^2 f_y / 4\mu$ is added, such that the velocity field due to the Stokeslet and dipole distribution is

$$\int_{-q}^{q} \frac{f_y}{8\pi\mu} \begin{bmatrix} \frac{(x-X)y}{r^3} + \frac{1}{2}a^2\left(\frac{-3(x-X)y}{r^5}\right) \\ \frac{r^2+y^2}{r^3} + \frac{1}{2}a^2\left(\frac{r^2-3y^2}{r^5}\right) \\ \frac{yz}{r^3} + \frac{1}{2}a^2\left(\frac{-3yz}{r^5}\right) \end{bmatrix} dX \,. \tag{A.43}$$

At $x = 0$, the above integral is

$$\frac{f_y}{8\pi\mu} \begin{bmatrix} -y\left(\int_{-q}^{q} \frac{X}{r^3}\, dX\right) + \frac{3a^2 y}{2}\left(\int_{-q}^{q} \frac{X}{r^5}\, dX\right) \\ \left(\int_{-q}^{q} \frac{1}{r}\, dX\right) + \left(y^2 + \frac{a^2}{2}\right)\left(\int_{-q}^{q} \frac{1}{r^3}\, dX\right) - \frac{3a^2 y^2}{2}\left(\int_{-q}^{q} \frac{1}{r^5}\, dX\right) \\ yz\left(\int_{-q}^{q} \frac{1}{r^3}\, dX\right) - \frac{3a^2 yz}{2}\left(\int_{-q}^{q} \frac{1}{r^5}\, dX\right) \end{bmatrix}. \tag{A.44}$$

Solving for the integrals as presented in Appendix A.2, the velocity field due to the normal Stokeslet distribution f_y and the accompanying dipole distribution can be computed to be

$$\frac{f_y}{8\pi\mu} \begin{bmatrix} 0 \\ 2\ln(2q/a) + 1 \\ 0 \end{bmatrix}. \tag{A.45}$$

Taking a vector addition of equations (A.41) and (A.45), the velocity field as generated by a flagellum modelled using a distribution of Stokeslets and dipoles become

$$\begin{bmatrix} \left(f_x/2\pi\mu\right)\left[\ln\left(2q/a\right)-0.5\right] \\ \left(f_y/4\pi\mu\right)\left[\ln\left(2q/a\right)+0.5\right] \\ 0 \end{bmatrix}. \tag{A.46}$$

Consequently, we see that the force per unit length f_x relates to the tangential component of the velocity field as

$$f_x = u_x \frac{2\pi\mu}{\ln\left(2q/a\right)-1/2}. \tag{A.47}$$

This leads to the tangential resistive force coefficient

$$K_T = \frac{2\pi\mu}{\ln\left(2q/a\right)-1/2}. \tag{A.48}$$

Similarly, the force per unit length f_y relates to the normal component of the velocity field as

$$f_y = u_y \frac{4\pi\mu}{\ln\left(2q/a\right)+1/2}. \tag{A.49}$$

This leads to the normal resistive force coefficient

$$K_N = \frac{4\pi\mu}{\ln\left(2q/a\right)+1/2}. \tag{A.50}$$

The resistive force coefficients given by equations (A.48) and (A.50) depends on the choice of q. Considering the hydrodynamics of spiral flagellar motions, we shall see that $q = 0.09\Lambda$ gives an accurate approximation of (A.50), while (A.48) needs to be modified if the same value of q is to be selected. For cells which exhibit spiral flagellar motion with a constant pitch and radius, the flagellar centreline, given an inextensible flagellum and no translation or rotation, follows the geometry of a helix:

$$x = \alpha s,\ y = b\cos\left[k\left(s-ct\right)\right],\ z = b\sin\left[k\left(s-ct\right)\right]. \tag{A.51}$$

where s is the distance measured along the flagellum. Since

$$\left(\frac{\partial x}{\partial s}\right)^2 + \left(\frac{\partial y}{\partial s}\right)^2 + \left(\frac{\partial z}{\partial s}\right)^2 = 1, \tag{A.52}$$

it leads to the relation

$$\alpha^2 + b^2 k^2 = 1. \tag{A.53}$$

At an instance, say $t = 0$, a point on the centreline of the flagellum has a position vector

$$\mathbf{r} = \begin{bmatrix} \alpha s \\ b\cos ks \\ b\sin ks \end{bmatrix}. \tag{A.54}$$

The unit tangential vector of the flagellum is therefore

$$\mathbf{e_t} = \begin{bmatrix} \alpha \\ -bk\sin ks \\ bk\cos ks \end{bmatrix}. \tag{A.55}$$

Each point on the flagellum has a velocity equal to the time-derivative of each respective component:

$$\mathbf{w} = \begin{bmatrix} \partial x/\partial t \\ \partial y/\partial t \\ \partial z/\partial t \end{bmatrix} = \begin{bmatrix} 0 \\ bkc\sin ks \\ -bkc\cos ks \end{bmatrix}. \tag{A.56}$$

The velocity can also be written as a function of the cell swimming velocity as well as velocity $\boldsymbol{\omega}_\mathbf{E} \times \mathbf{r}$ due to the spiral undulation:

$$\mathbf{w} = \begin{bmatrix} -U \\ 0 \\ 0 \end{bmatrix} + \begin{bmatrix} -\omega_E \\ 0 \\ 0 \end{bmatrix} \times \begin{bmatrix} \alpha s \\ b\cos ks \\ b\sin ks \end{bmatrix} = \begin{bmatrix} -U \\ \omega_E b\sin ks \\ -\omega_E b\cos ks \end{bmatrix}. \tag{A.57}$$

with

$$\omega_E = \omega - \Omega = kc - \Omega, \tag{A.58}$$

where Ω is the opposing rotation about the x-axis due to hydrodynamic force acting on the flagellum. Relative to the wave propagation velocity $\mathbf{V} = V\mathbf{i}$, each point on the flagellar has a tangential motion of constant speed c:

$$\mathbf{w} - \begin{bmatrix} V \\ 0 \\ 0 \end{bmatrix} = c \begin{bmatrix} \alpha \\ -bk\sin ks \\ bk\cos ks \end{bmatrix}. \tag{A.59}$$

An invariant force $\mathbf{f}(s)$ per unit length which the flagellum induces on the fluid is introduced:

$$\mathbf{f}(s) = \begin{bmatrix} 0 \\ h\sin ks \\ -h\cos ks \end{bmatrix}. \tag{A.60}$$

This force distribution has a tangential component of

$$\begin{aligned} \mathbf{f}_\mathbf{t}(s) &= \left(\mathbf{f}(s)\bullet\mathbf{e}_\mathbf{t}\right)\mathbf{e}_\mathbf{t} \\ &= \left(\begin{bmatrix} 0 \\ h\sin ks \\ -h\cos ks \end{bmatrix} \bullet \begin{bmatrix} \alpha \\ -bk\sin ks \\ bk\cos ks \end{bmatrix}\right)\begin{bmatrix} \alpha \\ -bk\sin ks \\ bk\cos ks \end{bmatrix}, \\ &= -hbk\begin{bmatrix} \alpha \\ -bk\sin ks \\ bk\cos ks \end{bmatrix} \end{aligned} \tag{A.61}$$

as well as a normal component of

$$\begin{aligned} \mathbf{f}_\mathbf{n}(s) &= \mathbf{f}(s) - \mathbf{f}_\mathbf{t}(s) \\ &= \begin{bmatrix} 0 \\ h\sin ks \\ -h\cos ks \end{bmatrix} + hbk\begin{bmatrix} \alpha \\ -bk\sin ks \\ bk\cos ks \end{bmatrix} \\ &= \begin{bmatrix} hbk\alpha \\ h\left(1-b^2k^2\right)\sin ks \\ -h\left(1-b^2k^2\right)\cos ks \end{bmatrix} = h\alpha\begin{bmatrix} bk \\ \alpha\sin ks \\ -\alpha\cos ks \end{bmatrix} \end{aligned} . \tag{A.62}$$

According to Lighthill (1976), the fluid velocity field **u** can be represented by a distribution of Stokeslets with a force per unit length of $\mathbf{f}(s)$ and dipoles of strength $-a^2 f_n(s)/4\mu$ along the flagellum centreline. At $s = s_0$, the flagellum has a similar velocity to that of the fluid field:

$$\mathbf{w}(s_0) = \frac{\mathbf{f}_\mathbf{n}(s)}{4\pi\mu} + \int_{r_0>\delta} \frac{r_0^2\mathbf{f}(s) + \left[\mathbf{f}(s)\bullet\mathbf{r}_0\right]\mathbf{r}_0}{8\pi\mu r_0^3}\,ds, \tag{A.63}$$

where $\delta = 0.5a\sqrt{e}$, in which e is the base of the natural logarithm, and $\mathbf{r}_0$ is the position vector of the point $s = 0$ on the flagellum centreline with respect to s as determined by equation (A.54):

$$\mathbf{r}_0 = \begin{bmatrix} -\alpha s \\ b - b\cos ks \\ -b\sin ks \end{bmatrix}. \tag{A.64}$$

Substituting equations (A.57) and (A.62) into (A.63), with $U = U_0$ and $s_0 = 0$,

$$\begin{aligned} \begin{bmatrix} -U_0 \\ \omega_E b\sin(0) \\ -\omega_E b\cos(0) \end{bmatrix} &= \frac{h\alpha}{4\pi\mu}\begin{bmatrix} bk \\ \alpha\sin(0) \\ -\alpha\cos(0) \end{bmatrix} \\ &+ \int_{r_0>\delta} \frac{1}{8\pi\mu r_0^3}\left\{ r_0^2 \begin{bmatrix} 0 \\ h\sin ks \\ -h\cos ks \end{bmatrix} + \left(\begin{bmatrix} 0 \\ h\sin ks \\ -h\cos ks \end{bmatrix} \bullet \mathbf{r}_0 \right)\mathbf{r}_0 \right\} ds \end{aligned} \tag{A.65}$$

which is

$$\begin{aligned} \begin{bmatrix} -U_0 \\ 0 \\ -\omega_E b \end{bmatrix} &= \frac{h\alpha}{4\pi\mu}\begin{bmatrix} bk \\ 0 \\ -\alpha \end{bmatrix} \\ &+ \int_{r_0>\delta} \frac{1}{8\pi\mu r_0^3}\begin{bmatrix} -h\alpha bs\sin ks \\ r_0^2 h\sin ks + hb^2\sin ks(1-\cos ks) \\ -r_0^2 h\cos ks - hb^2\sin^2 ks \end{bmatrix} ds \end{aligned}. \tag{A.66}$$

Taking the dot product of the unit vector in the x-direction with equation (A.66),

$$\begin{aligned} -U_0 &= \frac{h\alpha bk}{4\pi\mu} + \int_{r_0>\delta} \frac{-h\alpha bs\sin ks}{8\pi\mu r_0^3} ds \\ &= \frac{h\alpha bk}{4\pi\mu} - \frac{h\alpha b}{4\pi\mu}\int_{r_0>\delta} \frac{s\sin ks}{2\left[\alpha^2 s^2 + 2b^2(1-\cos ks)\right]^{3/2}} ds \end{aligned}. \tag{A.67}$$

Using the substitution $\theta = ks$,

$$\begin{aligned} U_0 &= -\frac{h\alpha bk}{4\pi\mu} + \frac{h\alpha b}{4\pi\mu}\int_{\varepsilon=k\delta}^{\infty} \frac{(\theta/k)\sin\theta}{2\left[\alpha^2(\theta/k)^2 + 2\left(\left(1-\alpha^2\right)/k^2\right)(1-\cos\theta)\right]^{3/2}} \frac{d\theta}{k} \\ &= -\frac{h\alpha bk}{4\pi\mu} + \frac{h\alpha bk}{4\pi\mu}\int_{\varepsilon=k\delta}^{\infty} \frac{\theta\sin\theta}{2\left[\alpha^2\theta^2 + 2\left(1-\alpha^2\right)(1-\cos\theta)\right]^{3/2}} d\theta \\ &= \frac{h\alpha bk}{4\pi\mu}\left[-1-\ln\varepsilon + A_1(\alpha)\right] \end{aligned}. \tag{A.68}$$

Taking the dot product of the unit vector in the z-direction with equation (A.66),

$$
\begin{aligned}
-\omega_E b &= -\frac{h\alpha^2}{4\pi\mu} + \int_\varepsilon^\infty \frac{-r_0^{\,2} h\cos ks - hb^2 \sin^2 ks}{8\pi\mu r_0^{\,3}}\, ds \\
&= -\frac{h\alpha^2}{4\pi\mu} - \int_\varepsilon^\infty \frac{h\cos ks}{8\pi\mu\left[\alpha^2 s^2 + 2b^2\left(1-\cos ks\right)\right]^{1/2}}\, ds \,. \\
&\quad -\int_\varepsilon^\infty \frac{hb^2 \sin^2 ks}{8\pi\mu\left[\alpha^2 s^2 + 2b^2\left(1-\cos ks\right)\right]^{3/2}}\, ds
\end{aligned}
\tag{A.69}
$$

Using the substitution $\theta = ks$,

$$
\omega_E = \frac{h\alpha^2}{4\pi\mu b} + \frac{h}{4\pi\mu b}\left\{\begin{array}{l}
\displaystyle\int_\varepsilon^\infty \frac{\cos\theta}{2\left[\alpha^2\theta^2 + 2\left(1-\alpha^2\right)\left(1-\cos\theta\right)\right]^{1/2}}\, d\theta \\
\displaystyle +\int_\varepsilon^\infty \frac{\left(1-\alpha^2\right)\sin^2\theta}{2\left[\alpha^2\theta^2 + 2\left(1-\alpha^2\right)\left(1-\cos\theta\right)\right]^{3/2}}\, d\theta
\end{array}\right\}. \tag{A.70}
$$

The integrals in (A.70) can be expressed as a function of $A_1(\alpha)$ and $A_2(\alpha)$ whose values with respect to α^2 are plotted by Lighthill (1976). Therefore,

$$
\begin{aligned}
\omega_E &= \frac{h}{4\pi\mu b}\left\{\begin{array}{l}
\alpha^2 + \left[-\ln\varepsilon + \alpha^2 A_1(\alpha) + \left(1-\alpha^2\right)A_2(\alpha) - 1\right] \\
+\left(1-\alpha^2\right)\left[-\ln\varepsilon + A_2(\alpha)\right]
\end{array}\right\} \\
&= \frac{h}{4\pi\mu b}\left[\left(\alpha^2-1\right) - \left(2-\alpha^2\right)\ln\varepsilon + \alpha^2 A_1(\alpha) + 2\left(1-\alpha^2\right)A_2(\alpha)\right]
\end{aligned}
\,. \tag{A.71}
$$

The resistive force coefficients linearly relate the force per unit length to the velocity in the respective normal and tangential directions:

$$
f_n = K_N V_{normal}\,, \tag{A.72}
$$

$$
f_t = K_T V_{tangential}\,. \tag{A.73}
$$

The normal and tangential velocity on an element of a flagellum undergoing spiral undulation is

$$
V_{normal} = \begin{bmatrix} -U_0 \\ \omega_E b\sin ks \\ -\omega_E b\cos ks \end{bmatrix} \bullet \begin{bmatrix} bk \\ \alpha\sin ks \\ -\alpha\cos ks \end{bmatrix} = -U_0 bk + \omega_E b\alpha\,, \tag{A.74}
$$

$$
V_{tangential} = \begin{bmatrix} -U_0 \\ \omega_E b\sin ks \\ -\omega_E b\cos ks \end{bmatrix} \bullet \begin{bmatrix} \alpha \\ -bk\sin ks \\ bk\cos ks \end{bmatrix} = -U_0\alpha - \omega_E b^2 k\,. \tag{A.75}
$$

From equation (A.62), the magnitude of the force per unit length in the normal direction is $h\alpha$, and therefore the normal resistive force coefficient can be expressed as

$$K_N = \frac{h\alpha}{-U_0 bk + \omega_E b\alpha}. \tag{A.76}$$

Substituting equations (A.68) and (A.71) into the above, the denominator of K_N is

$$\begin{aligned} -U_0 bk + \omega_E b\alpha &= -\frac{h\alpha b^2 k^2}{4\pi\mu}\left[-1-\ln\varepsilon + A_1(\alpha)\right] \\ &\quad + \frac{hb\alpha}{4\pi\mu b}\left[\left(\alpha^2-1\right)-\left(2-\alpha^2\right)\ln\varepsilon + \alpha^2 A_1(\alpha) + 2\left(1-\alpha^2\right)A_2(\alpha)\right] \\ &= \frac{h\alpha}{4\pi\mu}\left\{\begin{array}{l} -\left(1-\alpha^2\right)\left[-1-\ln\varepsilon + A_1(\alpha)\right] \\ +\left(\alpha^2-1\right)-\left(2-\alpha^2\right)\ln\varepsilon + \alpha^2 A_1(\alpha) + 2\left(1-\alpha^2\right)A_2(\alpha) \end{array}\right\} \\ &= \frac{h\alpha}{4\pi\mu}\left[-\ln\varepsilon + \left(2\alpha^2-1\right)A_1(\alpha) + 2\left(1-\alpha^2\right)A_2(\alpha)\right] \end{aligned}. \tag{A.77}$$

Therefore, the normal resistive force coefficient is

$$\begin{aligned} K_N &= \frac{h\alpha}{\frac{h\alpha}{4\pi\mu}\left[-\ln\varepsilon + \left(2\alpha^2-1\right)A_1(\alpha) + 2\left(1-\alpha^2\right)A_2(\alpha)\right]} \\ &= \frac{4\pi\mu}{-\ln\varepsilon + \left(2\alpha^2-1\right)A_1(\alpha) + 2\left(1-\alpha^2\right)A_2(\alpha)} \end{aligned}. \tag{A.78}$$

In a similar manner, using equation (A.61), the tangential resistive force coefficient is

$$K_T = \frac{-hbk}{-U_0\alpha - \omega_E b^2 k}. \tag{A.79}$$

Substituting equations (A.68) and (A.71) into the above, the denominator of K_T is

$$\begin{aligned} -U_0\alpha - \omega_E b^2 k &= -\frac{h\alpha^2 bk}{4\pi\mu}\left[-1-\ln\varepsilon + A_1(\alpha)\right] \\ &\quad - \frac{hb^2 k}{4\pi\mu b}\left[\left(\alpha^2-1\right)-\left(2-\alpha^2\right)\ln\varepsilon + \alpha^2 A_1(\alpha) + 2\left(1-\alpha^2\right)A_2(\alpha)\right] \\ &= -\frac{hbk}{4\pi\mu}\left\{\begin{array}{l} \alpha^2\left[-1-\ln\varepsilon + A_1(\alpha)\right] + \left(\alpha^2-1\right) \\ -\left(2-\alpha^2\right)\ln\varepsilon + \alpha^2 A_1(\alpha) + 2\left(1-\alpha^2\right)A_2(\alpha) \end{array}\right\} \\ &= -\frac{hbk}{4\pi\mu}\left[-1-2\ln\varepsilon + 2\alpha^2 A_1(\alpha) + 2\left(1-\alpha^2\right)A_2(\alpha)\right] \end{aligned}. \tag{A.80}$$

Therefore, the tangential resistive force coefficient is

$$K_T = \frac{-hbk}{-\frac{hbk}{4\pi\mu}\left[-1-2\ln\varepsilon+2\alpha^2 A_1(\alpha)+2\left(1-\alpha^2\right)A_2(\alpha)\right]} = \frac{2\pi\mu}{-\ln\varepsilon-1/2+\alpha^2 A_1(\alpha)+\left(1-\alpha^2\right)A_2(\alpha)} \quad \text{(A.81)}$$

Equations (A.78) and (A.81) allow the resistive coefficients to be computed as a function of α, which is dependent on the flagellum amplitude. Equations (A.48) and (A.50), on the other hand, allows the resistive coefficients to be computed as a function of q, which is approximately 0.09 times (Lighthill 1976) the flagellum length. Setting equations (A.50) and (A.78), both of which gives an approximate value for the normal resistive force coefficient, to be equal,

$$\frac{4\pi\mu}{\ln(2q/a)+1/2} = \frac{4\pi\mu}{-\ln\varepsilon+\left(2\alpha^2-1\right)A_1(\alpha)+2\left(1-\alpha^2\right)A_2(\alpha)}. \quad \text{(A.82)}$$

Comparing the denominator on both sides,

$$\ln(2q/a)+1/2 = -\ln\varepsilon+\left(2\alpha^2-1\right)A_1(\alpha)+2\left(1-\alpha^2\right)A_2(\alpha). \quad \text{(A.83)}$$

With $\varepsilon = k\delta$ as introduced during the integration by substitution in equation (A.68), and $\delta = 0.5a\sqrt{e}$ as introduced in equation (A.63), this leads to

$$\ln(2q/a)+\ln\left(ka\sqrt{e}/2\right) = -1/2+\left(2\alpha^2-1\right)A_1(\alpha)+2\left(1-\alpha^2\right)A_2(\alpha), \quad \text{(A.84)}$$

$$\ln\left(\frac{2\pi q}{\Lambda}\right) = \left(2\alpha^2-1\right)A_1(\alpha)+2\left(1-\alpha^2\right)A_2(\alpha)-1. \quad \text{(A.85)}$$

Therefore, to satisfy the equality in equation (A.82),

$$\frac{q}{\Lambda} = \frac{1}{2\pi}\exp\left[\left(2\alpha^2-1\right)A_1(\alpha)+2\left(1-\alpha^2\right)A_2(\alpha)-1\right]. \quad \text{(A.86)}$$

For $\alpha \in [0.5, 1]$, $q \approx 0.09\Lambda$ which concludes that $K_N = \frac{4\pi\mu}{\ln(2q/a)+1/2}$ with $q = 0.09\Lambda$ gives a 'suboptimal representation' of the flagellar dynamics in the normal direction. Moving on to the tangential component, it is found that equations (A.48) and (A.81), both of which gives an approximate value for the tangential resistive force coefficient,

will not be consistent if q is chosen to take the value of 0.09Λ. Instead, good agreement is obtained if the $-1/2$ term in (A.48) is removed, such that

$$\frac{2\pi\mu}{\ln\left(2q/a\right)} = \frac{2\pi\mu}{-\ln\varepsilon - 1/2 + \alpha^2 A_1\left(\alpha\right) + \left(1-\alpha^2\right)A_2\left(\alpha\right)}. \tag{A.87}$$

Comparing the denominator on both sides,

$$\ln\left(2q/a\right) = -\ln\varepsilon - 1/2 + \alpha^2 A_1\left(\alpha\right) + \left(1-\alpha^2\right)A_2\left(\alpha\right), \tag{A.88}$$

which leads to

$$\ln\left(2q/a\right) + \ln\left(ka\sqrt{e}/2\right) = -1/2 + \alpha^2 A_1\left(\alpha\right) + \left(1-\alpha^2\right)A_2\left(\alpha\right), \tag{A.89}$$

$$\ln\left(\frac{2\pi q}{\Lambda}\right) = \alpha^2 A_1\left(\alpha\right) + \left(1-\alpha^2\right)A_2\left(\alpha\right) - 1. \tag{A.90}$$

Therefore, to satisfy the equality in equation (A.87),

$$\frac{q}{\Lambda} = \frac{1}{2\pi}\exp\left[\alpha^2 A_1\left(\alpha\right) + \left(1-\alpha^2\right)A_2\left(\alpha\right) - 1\right]. \tag{A.91}$$

For $\alpha \in [0.5, 1]$, $q \approx 0.09\Lambda$ which concludes that $K_T = \dfrac{2\pi\mu}{\ln\left(2q/a\right)}$ with $q = 0.09\Lambda$ gives a 'suboptimal representation' of the flagellar dynamics in the tangential direction. This leads to the conclusion of Lighthill (1976) that the tangential and normal resistive force coefficients are

$$K_T = \frac{2\pi\mu}{\ln\left(2\left(0.09\Lambda\right)/a\right)},\ K_N = \frac{4\pi\mu}{\ln\left(2\left(0.09\Lambda\right)/a\right) + 0.5}. \tag{A.92}$$

A.2 Mathematical procedures used to derive equations in Appendix A.1

A.2.1 Procedure to solve $\int_{-q}^{q} \frac{1}{r}\,dX$, $\int_{-q}^{q} \frac{1}{r^3}\,dX$ and $\int_{-q}^{q} \frac{1}{r^5}\,dX$ in (A.40) and (A.43)

The first integral can be solved by introducing a substitution variable u such that

$$X = a\tan(u) \longleftrightarrow u = \arctan\left(X/a\right), \tag{A.93}$$

$$dX = a\sec^2(u)\,du\,. \tag{A.94}$$

Using the substitution as defined in (A.93), the integral $\int_{-q}^{q} \frac{1}{r}\,dX$ is

$$\begin{aligned}\int_{-q}^{q} \frac{1}{r}\,dX &= \int_{-q}^{q} \frac{1}{\sqrt{X^2+a^2}}\,dX \\ &= \int_{-q}^{q} \frac{1}{\sqrt{a^2\tan^2(u)+a^2}}\;a\sec^2(u)\,du \\ &= \int_{-q}^{q} \frac{a\sec^2(u)}{a\sec(u)}\;du \\ &= \int_{-q}^{q} \sec(u)\,du\end{aligned}\,. \tag{A.95}$$

Adding a common factor to both the numerator and denominator,

$$\begin{aligned}\int_{-q}^{q} \frac{1}{r}\,dX &= \int_{-q}^{q} \frac{\sec(u)\left[\sec(u)+\tan(u)\right]}{\sec(u)+\tan(u)}\;du \\ &= \int_{-q}^{q} \frac{\sec^2(u)+\sec(u)\tan(u)}{\tan(u)+\sec(u)}\;du\,. \\ &= \left[\ln\left(\sec(u)+\tan(u)\right)\right]_{-q}^{q}\end{aligned} \tag{A.96}$$

After replacing the substitution variable u with the original variables,

$$\begin{aligned}\int_{-q}^{q} \frac{1}{r}\,dX &= \left[\ln\left(\frac{\sqrt{X^2+a^2}}{a}+\frac{X}{a}\right)\right]_{-q}^{q} \\ &= \ln\left(\frac{\sqrt{q^2+a^2}}{a}+\frac{q}{a}\right)-\ln\left(\frac{\sqrt{q^2+a^2}}{a}-\frac{q}{a}\right) \\ &= \ln\left(\frac{q}{a}\sqrt{1+\left(\frac{a}{q}\right)^2}+\frac{q}{a}\right)-\ln\left(\frac{q}{a}\sqrt{1+\left(\frac{a}{q}\right)^2}-\frac{q}{a}\right)\end{aligned}\,. \tag{A.97}$$

For $(a/q)^2 = \varepsilon \to 0$, with Binomial expansion, the integral becomes

$$\begin{aligned}\int_{-q}^{q} \frac{1}{r}\,dX &= \ln\left(\frac{q}{a}\sqrt{1+\varepsilon}+\frac{q}{a}\right)-\ln\left(\frac{q}{a}\left(1+\frac{1}{2}\left(\frac{a}{q}\right)^2\right)-\frac{q}{a}\right)\\ &= \ln\left(\frac{q}{a}+\frac{q}{a}\right)-\ln\left(\frac{q}{2a}\left(\frac{a}{q}\right)^2\right)\\ &= \ln\left(\frac{2q}{a}\right)-\ln\left(\frac{a}{2q}\right)\\ &= 2\ln\left(\frac{2q}{a}\right)\end{aligned} \quad . \tag{A.98}$$

Using the same substitution as defined in (A.93), the integral $\int_{-q}^{q} \frac{1}{r^3}\,dX$ is

$$\begin{aligned}\int_{-q}^{q} \frac{1}{r^3}\,dX &= \int_{-q}^{q} \frac{1}{\left(X^2+a^2\right)^{3/2}}\,dX\\ &= \int_{-q}^{q} \frac{1}{\left(a^2\tan^2(u)+a^2\right)^{3/2}}\; a\sec^2(u)\,du\\ &= \int_{-q}^{q} \frac{a\sec^2(u)}{\left(a^2\sec^2(u)\right)^{3/2}}\; du\\ &= \frac{1}{a^2}\int_{-q}^{q} \frac{1}{\sec(u)}\,du\\ &= \frac{1}{a^2}\left[\sin(u)\right]_{-q}^{q}\end{aligned} \quad . \tag{A.99}$$

After replacing the substitution variable u with the original variables:

$$\begin{aligned}\int_{-q}^{q} \frac{1}{r^3}\,dX &= \frac{1}{a^2}\left[\frac{X}{\sqrt{X^2+a^2}}\right]_{-q}^{q}\\ &= \frac{1}{a^2}\frac{2q}{\sqrt{q^2+a^2}}\\ &= \frac{1}{a^2}\frac{2}{\sqrt{1+\left(a/q\right)^2}}\end{aligned} \quad . \tag{A.100}$$

For $(a/q)^2 = \varepsilon \to 0$,

$$\int_{-q}^{q} \frac{1}{r^3}\,dX = \frac{2}{a^2\sqrt{1+\varepsilon}} \approx \frac{2}{a^2}\,. \tag{A.101}$$

Moving on, the integral $\int_{-q}^{q} \frac{1}{r^5} dX$ is solved using the same substitution in (A.93):

$$\begin{aligned}
\int_{-q}^{q} \frac{1}{r^5} dX &= \int_{-q}^{q} \frac{1}{\left(X^2 + a^2\right)^{5/2}} dX \\
&= \int_{-q}^{q} \frac{1}{\left(a^2 \tan^2(u) + a^2\right)^{5/2}} \, a \sec^2(u) \, du \\
&= \int_{-q}^{q} \frac{a \sec^2(u)}{\left(a^2 \sec^2(u)\right)^{5/2}} \, du \\
&= \frac{1}{a^4} \int_{-q}^{q} \frac{1}{\sec^3(u)} du \\
&= \frac{1}{a^4} \int_{-q}^{q} \cos^3(u) \, du
\end{aligned} \quad . \qquad \text{(A.102)}$$

Using trigonometric identities,

$$\begin{aligned}
\int_{-q}^{q} \frac{1}{r^5} dX &= \frac{1}{a^4} \int_{-q}^{q} \left(\frac{3}{4}\cos(u) + \frac{1}{4}\cos(3u) \right) dX \\
&= \frac{1}{a^4} \left[\frac{3}{4}\sin(u) + \frac{1}{12}\sin(3u) \right]_{-q}^{q} \\
&= \frac{1}{a^4} \left[\sin(u) - \frac{1}{3}\sin^3(u) \right]_{-q}^{q}
\end{aligned} \quad . \qquad \text{(A.103)}$$

After replacing the substitution variable u with the original variables,

$$\begin{aligned}
\int_{-q}^{q} \frac{1}{r^5} dX &= \frac{1}{a^4} \left[\frac{X}{\sqrt{X^2 + a^2}} - \frac{1}{3}\left(\frac{X}{\sqrt{X^2 + a^2}} \right)^3 \right]_{-q}^{q} \\
&= \frac{2}{a^4} \left[\frac{q}{\sqrt{q^2 + a^2}} - \frac{1}{3} \frac{q^3}{\left(q^2 + a^2\right)^{3/2}} \right] \\
&= \frac{2}{a^4} \left[\frac{1}{\sqrt{1^2 + (a/q)^2}} - \frac{1}{3} \frac{1}{\sqrt{1^2 + (a/q)^2}} \right]
\end{aligned} \quad . \qquad \text{(A.104)}$$

With $(a/q)^2 = \varepsilon \to 0$,

$$\int_{-q}^{q} \frac{1}{r^5} dX = \frac{2}{3a^4} \frac{1}{\sqrt{1+\varepsilon}} \approx \frac{2}{3a^4} . \qquad \text{(A.105)}$$

A.2.2 Procedure to solve $\int_{-q}^{q} \frac{X^2}{r^3} dX$ in (A.40)

Since $r = \sqrt{X^2 + a^2}$, the integral above can be solved using integration by parts.

$$\begin{aligned}
\int_{-q}^{q} \frac{X^2}{r^3} dX &= \int_{-q}^{q} \frac{X^2}{\left(X^2 + a^2\right)^{3/2}} dX \\
&= \int_{-q}^{q} \left(-X\right) d\left(\left(X^2 + a^2\right)^{-1/2}\right) \\
&= \left[\left(-X\right)\left(X^2 + a^2\right)^{-1/2}\right]_{-q}^{q} - \int_{-q}^{q} \left(X^2 + a^2\right)^{-1/2} \left(-dX\right) \\
&= \left[-\frac{X}{\sqrt{X^2 + a^2}}\right]_{-q}^{q} + \int_{-q}^{q} \frac{1}{r} dX \\
&= -\frac{2q}{\sqrt{q^2 + a^2}} + \int_{-q}^{q} \frac{1}{r} dX \\
&= \int_{-q}^{q} \frac{1}{r} dX - \frac{2}{\sqrt{1 + \left(a/q\right)^2}}
\end{aligned} \quad . \qquad \text{(A.106)}$$

For $(a/q)^2 = \varepsilon \to 0$, solving $\int_{-q}^{q} \frac{1}{r} dX$ by the approach presented in equation (A.98),

$$\begin{aligned}
\int_{-q}^{q} \frac{X^2}{r^3} dX &= 2\ln\left(\frac{2q}{a}\right) - \frac{2}{\sqrt{1+\varepsilon}} \\
&\approx 2\ln\left(\frac{2q}{a}\right) - 2
\end{aligned} \quad . \qquad \text{(A.107)}$$

A.2.3 Procedure to solve $\int_{-q}^{q} \frac{X}{r^3} dX$ and $\int_{-q}^{q} \frac{X}{r^5} dX$ in (A.43)

Both integrals can be solved using integration by substitution. Introduce a substitution variable u such that

$$u = X^2 + a^2 \longleftrightarrow X = \sqrt{u - a^2}\,, \qquad \text{(A.108)}$$

$$du = 2X\,dX\,. \qquad \text{(A.109)}$$

Using the substitution defined above, the integral $\int_{-q}^{q} \frac{X}{r^3} dX$ is

$$\begin{aligned}
\int_{-q}^{q} \frac{X}{r^3}\,dX &= \int_{-q}^{q} \frac{X}{\left(X^2+a^2\right)^{3/2}}\,dX \\
&= \frac{1}{2}\int_{-q}^{q} \frac{1}{u^{3/2}}\,du \\
&= \frac{1}{2}\left[-\frac{2}{\sqrt{u}}\right]_{-q}^{q} \\
&= \left[-\frac{1}{\sqrt{X^2+a^2}}\right]_{-q}^{q} \\
&= -\frac{1}{\sqrt{q^2+a^2}} + \frac{1}{\sqrt{q^2+a^2}} \\
&= 0
\end{aligned} \quad . \qquad \text{(A.110)}$$

Using the same substitution in (A.108), the integral $\int_{-q}^{q} \frac{X}{r^5}\,dX$ is

$$\begin{aligned}
\int_{-q}^{q} \frac{X}{r^5}\,dX &= \int_{-q}^{q} \frac{X}{\left(X^2+a^2\right)^{5/2}}\,dX \\
&= \frac{1}{2}\int_{-q}^{q} \frac{1}{u^{5/2}}\,du \\
&= \frac{1}{2}\left[-\frac{2}{3u^{3/2}}\right]_{-q}^{q} \\
&= \left[-\frac{1}{3\left(X^2+a^2\right)^{3/2}}\right]_{-q}^{q} \\
&= -\frac{1}{3\left(q^2+a^2\right)^{3/2}} + \frac{1}{3\left(q^2+a^2\right)^{3/2}} \\
&= 0
\end{aligned} \quad . \qquad \text{(A.111)}$$

Appendix B – Solving Differential Equations

B.1 Time dependence of flagellum waveform

This section provides the rationale for modelling the time dependency of the flagellum waveform using a complex exponential. The method of separation of variables is used to convert a partial differential equation into an ordinary differential equation. Consider the following fourth order partial differential equation, where the dependent variable y is a function of space s and time t, and C is a constant:

$$\frac{\partial^4 y}{\partial s^4} + C\frac{\partial y}{\partial t} = 0. \tag{B.1}$$

Assuming separation of variables lead to a solution, y can be expressed as a product of a space-dependent function $F(s)$ and a time-dependent function $G(t)$.

$$y = F(s)\cdot G(t). \tag{B.2}$$

Substituting equation (B.2) into equation (B.1),

$$F''''G + CF\dot{G} = 0, \tag{B.3}$$

where F'''' is the fourth-order space derivative of F, and $\dot{G}$ is the first order time derivative of G. Rearranging the equation such that all space-dependent terms are on the opposite side of the equation as the time-dependent terms,

$$\frac{F''''}{F} = -C\frac{\dot{G}}{G}. \tag{B.4}$$

Since the left and right side of equation (B.4) are independent of time and space, respectively, they can be equated to a constant β^4. The space-dependent part of the above equation can hence be expressed as

$$F'''' - \beta^4 F = 0, \tag{B.5}$$

which has a solution of the form

$$F = \kappa_1 e^{\beta_1 s} + \kappa_2 e^{\beta_2 s} + \kappa_3 e^{\beta_3 s} + \kappa_4 e^{\beta_4 s}. \tag{B.6}$$

For the time-dependent part of equation (B.4), we have

$$\dot{G} + \frac{\beta^4}{C} G = 0 , \tag{B.7}$$

which has a solution of the form

$$G = \sigma \exp\left(-\frac{\beta^4}{C} t \right). \tag{B.8}$$

If the above exponential is raised to a real power, the solution y will either decay exponentially to zero or increase exponentially as time progresses. Therefore, the argument of the exponential function in equation (B.8) must be complex:

$$\begin{aligned} G &= \sigma e^{(a-ib)t} \\ &= \sigma e^{a} \cdot e^{-ibt} \\ &= \xi \left(\cos bt - i \sin bt \right) \end{aligned} . \tag{B.9}$$

Next, we know that b governs the period of y, and hence it must necessarily be related to the flagellum wiggling frequency. The above equation can be expressed as

$$\begin{aligned} G &= \xi \left(\cos \omega t - i \sin \omega t \right) \\ &= \xi e^{-i\omega t} \end{aligned} . \tag{B.10}$$

This shows that the solution $y(s, t)$ to the partial differential equation in (B.1) can be expressed as $h(s)\, e^{-i\omega t}$, where $h(s) = \xi F(s)$ can be found by solving the corresponding ordinary differential equation.

B.2 Methods for solving ordinary differential equations

B.2.1 Explicit First-Order (Forward Euler) Runge-Kutta method

The Runge-Kutta method allows the solution to a first-order ordinary differential equation (ODE) to be solved, using initial conditions (if the independent variable is time) or boundary conditions (if the independent variable is space) at the start of the solution domain. While only applicable to a first-order ODE, the method can be used to solve higher orders linear ODE, since the problem can be reframed to reduce the order of the ODE (Hydon 2000). Consider a general third-order ODE of the form:

$$\frac{d^3 y}{ds^3} + a(s) \frac{d^2 y}{ds^2} + b(s) \frac{dy}{ds} + c(s)\, y = f(s) , \tag{B.11}$$

where all coefficient can be normalised with respect to the coefficient of the highest-order derivative. By introducing a new vector variable **z** with as many elements as the order of the ODE,

$$\mathbf{z} = \begin{bmatrix} z_1 \\ z_2 \\ z_3 \end{bmatrix} = \begin{bmatrix} y \\ y' \\ y'' \end{bmatrix}, \tag{B.12}$$

the original ODE can be re-expressed as a system of first-order ODE relating **z** to its derivative $\mathbf{z}'$:

$$\begin{aligned} \begin{bmatrix} z_1' \\ z_2' \\ z_3' \end{bmatrix} = \begin{bmatrix} y' \\ y'' \\ y''' \end{bmatrix} &= \begin{bmatrix} z_2 \\ z_3 \\ f(s) - a(s)z_3 - b(s)z_2 - c(s)z_1 \end{bmatrix} \\ &= \begin{bmatrix} 0 & 1 & 0 \\ 0 & 0 & 1 \\ -c(s) & -b(s) & -a(s) \end{bmatrix} \begin{bmatrix} z_1 \\ z_2 \\ z_3 \end{bmatrix} + \begin{bmatrix} 0 \\ 0 \\ f(s) \end{bmatrix}. \end{aligned} \tag{B.13}$$

Having seen how a first-order ODE may be obtained from any linear ODE in general, consider the following differential equation with s as the independent variable:

$$\frac{dy(s)}{ds} - f(y(s), s) = 0. \tag{B.14}$$

If the initial condition $y(s_0)$ is known, where the solution domain is s $\in$ [s_0, s_{end}], an approximate value $y^*(s_0 + ds)$ at the next step ds from the starting point s_0 is

$$y^*(s_0 + ds) = y(s_0) + k_1\, ds, \tag{B.15}$$

where k_1 is the derivative as obtained from the governing ODE and is a function of the independent variable s. In equation (B.15), this derivative at $s = s_0$ is

$$k_1 = \frac{dy(s_0)}{ds} = f(y(s_0), s_0). \tag{B.16}$$

However, except at $s = s_0$, the solution $y(s)$ and its derivative is unknown everywhere else. Therefore, the derivative at each new step has to be approximated, using the estimated solution $y^*(s)$ obtained in the previous step:

$$k_1 \approx f(y^*(s), s). \tag{B.17}$$

The general solution for a first-order Runge-Kutta method (Butcher 1987) will therefore begin with equation (B.15) and proceed stepwise, from $s = s_a$ to $s = (s_a + ds)$ sequentially, as follows:

$$y^*(s_a + ds) = y^*(s_a) + f(y^*(s_a), s_a)\, ds\ . \tag{B.18}$$

In this first order Runge-Kutta method, the error involved in each step is of the order ds, because Taylor expansion of the exact and approximate solution gives

$$\begin{aligned} y(s_a + ds) &= y(s_a) + y'(s_a)\, ds + y''(s_a)\, \frac{ds^2}{2} + \ldots \\ &= y(s_a) + y'(s_a)\, ds + O\left(ds^2\right) \end{aligned} \tag{B.19}$$

and

$$y^*(s_a + ds) = y^*(s_a) + k_1\, ds + O\left(ds^2\right), \tag{B.20}$$

respectively. The error builds up with each step taken, and the total number of steps over the whole interval is of the order $1/ds$. Therefore, the solution of this first-order method has an overall error of $O(ds^2)\cdot O(1/ds) = O(ds)$.

B.2.2 Explicit Higher-order Runge-Kutta method

In the first-order Runge-Kutta method, when moving from $y(s_a)$ to $y(s_a + ds)$ the slope is calculated at the beginning of each step and held constant until the end of the step. The error in this approximation increases as the distance from s_a increases. Therefore, with a given step ds, a more accurate approach, as apparent in Figure B-1, is to use a slope parallel to the tangent at the mid-point of the interval.

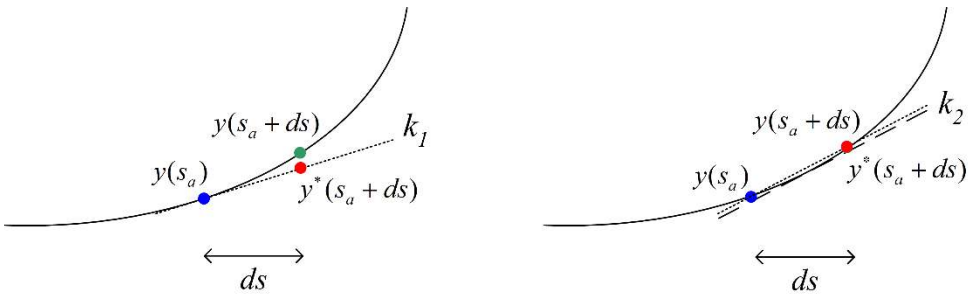

Figure B-1 – Solution $y(s)$ to some ODE, as represented by the solid black curve. The blue dot denotes the value $y(s_a)$ at the beginning of the step, while the green dot denotes the actual solution $y(s_a+ds)$ after the independent variable s is incremented by a step of ds. The red dot denotes the estimated solution $y^*(s_a+ds)$, using (Left) first-order RK method with a slope $k_1(s_a)$ and (Right) second-order RK method with a slope $k_2(s_a+ds/2)$ as denoted by the dotted straight line.

The above illustration is one of many possible second-order Runge-Kutta methods (Butcher 1987). Given that the solution $y(s_a + ds/2)$ at half a step away is unknown, the derivative at that point is unknown as well. However, the first-order RK method can be used to estimate $y^*(s_a + ds/2)$ and correspondingly, the ODE can be used to relate the slope k_2 to y^*. Given known initial conditions, the second-order Runge-Kutta method begins with

$$y^*(s_0 + ds/2) = y(s_0) + k_1\, ds/2\,. \tag{B.21}$$

For a linear first-order ODE of the form given in equation (B.14), the tangent at the mid-point of the step interval, which will be used as the slope to increment $y(s_0)$ to $y(s_0 + ds)$, is

$$k_2 = f\left(y^*(s_0 + ds/2),\, (s_0 + ds/2)\right). \tag{B.22}$$

Going back to the beginning of the step, this second-order RK method then moves from $y(s_0)$ to $y^*(s_0 + ds)$ using k_2 as the slope for the step interval:

$$y^*(s_0 + ds) = y(s_0) + k_2 ds\,. \tag{B.23}$$

Although likely to be an intuitive choice for many, computing the slope using the tangent at the mid-point of the step interval is not the only possibility. In general, the slope m across a single step can be a weighted average of two derivatives, that is,

$$m = b_1 k_1 + b_2 k_2\,. \tag{B.24}$$

The derivative k_1 is taken at $s = s_a$,

$$k_1 = f\left(y^*(s_a),\, s_a\right). \tag{B.25}$$

while the other derivative k_2 is taken at $s = s_a + \alpha\, ds$ and the estimated value at that second point $y^*(s_a + \alpha ds) = y^*(s_a) + k_1 \beta ds$:

$$k_2 = f\left(y^*(s_a) + k_1 \beta ds,\, s_a + \alpha\, ds\right). \tag{B.26}$$

This means that moving $\alpha\, ds$ into the step, the estimated y^* at that point is obtained by adding the product of k_1 and βds, leaving open the flexibility of adjusting the steepness of k_1 by a factor of β/α. However, it shall be mathematically demonstrated that α and β has to be equal to minimize the error. In the example given in equations

(B.21) to (B.23), $b_1 = 0$, $b_2 = 1$ and $\alpha = \beta = 1/2$. One may also choose to compute the first-order derivative at the beginning of the step, estimate the derivative at the end of the step, and then set the slope as the mean of these two computed values. In this case, $b_1 = b_2 = 1/2$ and $\alpha = \beta = 1$.

To determine the order of accuracy, consider the Taylor expansion of the exact solution, where the first- and second-order derivatives can be determined from the governing ODE as given in equation (B.14):

$$\begin{aligned} y(s_a + ds) &= y(s_a) + \frac{dy(s_a)}{ds} ds + \frac{d^2 y(s_a)}{ds^2} \frac{ds^2}{2} + \ldots \\ &= y(s_a) + f ds + \left(\frac{\partial f}{\partial y} f + \frac{\partial f}{\partial s} \right) \frac{ds^2}{2} + \ldots \end{aligned} \tag{B.27}$$

Meanwhile, the Taylor expansion of the approximate solution gives

$$\begin{aligned} y^*(s_a + ds) &= y^*(s_a) + \Big(b_1 \cdot \left[f\left(y^*(s_a), s_a \right) \right] \\ &\qquad + b_2 \cdot \left[f\left(y^*(s_a) + k_1 \beta ds,\, s_a + \alpha ds \right) \right] \Big) ds \\ &= y^*(s_a) + \left(b_1 f + b_2 \cdot \left[f + \frac{\partial f}{\partial y} f \beta ds + \frac{\partial f}{\partial s} \alpha ds \right] \right) ds + \ldots \\ &= y^*(s_a) + \left(b_1 + b_2 \right) f ds + b_2 \left(\frac{\partial f}{\partial y} f \beta + \frac{\partial f}{\partial s} \alpha \right) ds^2 + \ldots \end{aligned} \tag{B.28}$$

Comparing equations (B.27) and (B.28), the exact and approximate solutions are consistent to an error of $O(ds^3)$ when the following three constraints are satisfied:

$$b_1 + b_2 = 1\,,\; b_2 \alpha = 1/2\,,\; b_2 \beta = 1/2\,. \tag{B.29}$$

Since this indicates that $\alpha = \beta$, equations (B.24) and (B.26) can be re-expressed as

$$m = \left(1 - \frac{1}{2\alpha} \right) k_1 + \left(\frac{1}{2\alpha} \right) k_2\,, \tag{B.30}$$

$$k_2 = f\left(y^*(s_a) + k_1 \alpha ds,\; s_a + \alpha ds \right). \tag{B.31}$$

In this second order Runge-Kutta method, the error involved in computing $y^*(s_a + ds)$ for each step is $O(ds^3)$, and the solution across the entire interval has an overall error of $O(ds^3) \cdot O(1/ds) = O(ds^2)$.

Numerical solutions to linear ODEs often utilise the fourth-order Runge-Kutta method (Butcher 2016), in which the solution has an overall error of $O(ds^4)$. Similar to the second-order RK method, there is an infinite number of approach in which the weights of the derivatives contributing towards the slope can be adjusted. A popular fourth-order RK method utilises four derivatives evenly-spaced across the step interval with the following weights, with the complete mathematical derivation given by Musa *et al*. (2010):

$$m = \frac{1}{8}k_1 + \frac{3}{8}k_2 + \frac{3}{8}k_3 + \frac{1}{8}k_4, \tag{B.32}$$

where the weights k_1 to k_4 are

$$k_1 = f\left(y^*(s_a), s_a\right), \tag{B.33}$$

$$k_2 = f\left(y^*(s_a) + k_1\frac{ds}{3},\ s_a + \frac{ds}{3}\right), \tag{B.34}$$

$$k_3 = f\left(y^*(s_a) - k_1\frac{ds}{3} + k_2 ds,\ s_a + \frac{2ds}{3}\right), \tag{B.35}$$

$$k_4 = f\left(y^*(s_a) + k_1 ds - k_2 ds + k_3 ds,\ s_a + ds\right). \tag{B.36}$$

B.2.3 Implicit method

In dealing with differential equations which are stiff (Iserles 2009), that is requiring a very small step size otherwise the problem becomes numerically unstable, it is beneficial to use implicit rather than explicit methods. Implicit methods involve solving a system of algebraic equations at each new step, as the solution appears on both sides of the equation. For example, consider the same differential equation in (B.14):

$$\frac{dy(s)}{ds} - f(y(s), s) = 0. \tag{B.37}$$

Moving a step from s_n to s_{n+1}, the exact change in y depends on the derivative continuously across the step interval:

$$y(s_{n+1}) = y(s_n) + \int_{s_n}^{s_{n+1}} f(y(s), s)\, ds. \tag{B.38}$$

Using the trapezoidal rule, the integral is approximately equal to the average of the integrand at the two ends, multiplied by the size of the interval:

$$\int_{s_n}^{s_{n+1}} f(y(s), s)\,ds \approx \frac{1}{2}\left[f(y(s_n), s_n) + f(y(s_{n+1}), s_{n+1})\right] ds\,. \tag{B.39}$$

Therefore, using the solution $y(s_n)$ at the beginning of the step, the estimate solution $y^*(s_{n+1})$ at the end of the step have to be obtained implicitly:

$$y^*(s_{n+1}) = y(s_n) + \frac{1}{2}\left[f\left(y^*(s_{n+1}), s_{n+1}\right) + f\left(y(s_n), s_n\right)\right] ds\,. \tag{B.40}$$

This is actually a simple case of the Lobatto IIIA method (Pinto *et al*. 1997), which is a category of implicit Runge-Kutta methods, used to solve boundary value problems.

B.3 Using MATLAB for numerical solution

In Chapter 6, the flagellum shape of a sperm subjected to hydrodynamic force computed using different models is investigated. MATLAB's solvers are utilised to seek a numerical solution to ordinary differential equations which implicitly relates the position y to the corresponding force distribution as well as its flexural rigidity. The challenges encountered in the process of seeking a numerical solution, as well as the procedures adopted in response to those challenges and the approach taken to assess the results are presented here.

Given that the physics of a swimming sperm imposes boundary conditions on both ends of the flagellum, the model is naturally approached as a BVP, using MATLAB's *bvp4c* solver (Shampine *et al*. 2000, 2003) which uses an implicit Runge-Kutta method that makes use of collocation. It computes a spline on every subinterval of the domain and solves the finite difference equation implicitly at each step, taking into account all prescribed boundary conditions defined in the input function (Kierzenka and Shampine 2001). This algorithm is applied to the simplified RFT model in Koh and Marcos (2015b), where the normal force on the continuous flagellum is expressed analytically as a function of y in accordance with the small amplitude approximation. The resulting numerical solution is consistent with the analytical solution, thus verifying the validity of the written code. However, using the force distribution computed from the SBT model, no solution was found. It is possible that the approximations made, such

as discretizing the flagellum into a finite number of straight segments, resulted in a force distribution that does not capture the entire physics of a swimming sperm.

Without making any hasty conclusions, changes are introduced one at a time to validate the numerical algorithm and assess the feasibility of using SBT to solve for the flagellum waveform. Given that the force distribution computed by SBT is a stepwise-constant function with an undefined force derivative at each interface between adjacent segments, the discontinuity is recognised as a potential source of error in the computation process. To investigate this possibility, the force in the ODE governing the waveform is expressed as a matrix comprising numerical values, while still adhering to the same small amplitude approximation. The flagellum is discretized into over 1,000 infinitesimal elements, clearly satisfying the earlier convergence test in Chapter 4, and the force distribution expressed numerically as a matrix is nearly identical to a continuous force distribution defined analytically in the RFT model. However, no solution was found, even though there were no abrupt discontinuities across the flagellum, except for the inevitable effects of numerical discretization.

To assess the robustness of the solver, a fourth order ODE, $\tilde{y}'''' - 16\pi^4\tilde{y} = 0$, using a known function $\tilde{y} = \sin(2\pi s)$ for $\tilde{s} \in [0, 1]$ is considered. There are eight known boundaries for this equation, namely, the zeroth to third order derivative of $\tilde{y}$ at $\tilde{s} = 0$ and $\tilde{s} = 1$, of which any four will allow the equation to be solved. When the boundary conditions were set to comprise $\tilde{y}|_{\tilde{s}=0}$, $\tilde{y}'''|_{\tilde{s}=0}$, $\tilde{y}''|_{\tilde{s}=1}$, and $\tilde{y}'''|_{\tilde{s}=1}$, as was the case in the RFT or SBT model, the solver was unable to obtain a solution. This was despite the fact that the initial 'guess' of $\tilde{y}$ to $\tilde{y}''''$ used to initialise the solver was the exact expression, and that the flagellum was discretized into 10,000 elements. However, when the boundary conditions were set using lower-order derivatives, a perfect numerical solution was obtained, even under a coarse discretization of 100 elements and an initial guess of the contant **0** vector used to initialise the solver. Different combinations of boundary conditions were tested, and an interesting pattern was observed. When the sum of the derivatives of the four boundary conditions add up to six or less, an accurate numerical solution can be obtained. However, the converse is true when the sum of the derivaties add up to seven or more. The same findings were recorded using MATLAB's *bvp5c* solver. As it is beyond the scope of this thesis to code a new algorithm or modify the existing solvers, a different approach shall be taken.

To circumvent the above-mentioned limitation, one of the four boundary conditions shall be changed to a lower order derivative. Specifically, the moment-free condition at the start of the flagellum is changed to a prescribed slope while all else remains unchanged, that is, the conditions $\left[\tilde{y}|_{\tilde{s}=0};\ \tilde{y}''|_{\tilde{s}=0} + \tilde{f}_m;\ \tilde{y}''|_{\tilde{s}=1};\ \tilde{y}'''|_{\tilde{s}=1} - \tilde{f}_m \right]$ is modified to $\left[\tilde{y}|_{\tilde{s}=0};\ \tilde{y}'|_{\tilde{s}=0} - \gamma;\ \tilde{y}''|_{\tilde{s}=1};\ \tilde{y}'''|_{\tilde{s}=1} - \tilde{f}_m \right]$. Doing so, the RFT model comprising a matrix of numerical values of normal force resulted in a flagellum waveform closely similar to the analytical solution under the small amplitude approximation. However, under the SBT and RFT model comprising N = 15 segments (chosen to satisfy $p \ll \Lambda/2N \ll \Lambda$), the modified boundary conditions led to numerical solutions which diverge to an unrealistic amplitude and fails to satisfy $\tilde{y}''|_{\tilde{s}=0} + \tilde{f}_m = 0$, even thought the slope is prescribed to take a value following the analytical solution. In both cases, adjustments of varying degree are introduced to the prescribed slope, but none of the numerical solutions result in a reasonable amplitude and satisfy the boundary conditions at the same time.

Recognising this limitation, the differential equation will be approached as an IVP. For an n^{th} order differential equation, there has to be n boundary conditions defined. When framed as an IVP, the boundary conditions at the end of the interval will not be incorporated, and instead, all undefined derivatives at the start of the interval have to be guessed. The resulting solution at the end of the interval will then be compared with the known boundary conditions from the original BVP, and the guesses are thereafter refined using the 'shooting algorithm' (Stoer and Bulirsch 2013). An IVP can be conveniently solved by built-in functions such as MATLAB's *ode45* solver, which utilises the Dormand-Prince method (Dormand and Prince 1980; Shampine and Reichelt 1997) – an explicit Runge-Kutta method of fourth-order accuracy.

In order to validate the accuracy of the flagellum shape obtained from this approach, equation (4.26), which is an ODE from the RFT model with approximations, will be used. Thereafter, the numerical results will be compared with known analytical solutions (Koh and Marcos 2015b), plotted as the flagellum waveform in Figure 4-2. The boundary conditions are established from zero displacement and net moment at the start of the flagellum where it is attached to the cell head, as well as zero net force and moment at the free end of the flagellum. Since the initial conditions for only y and y"

are known exactly at the start of the flagellum, y' and y''' have to be guessed in order to apply the Runge-Kutta method and solve the equation as an IVP. However, instead of making wild guesses, the finite difference approximation for y' and y''' at $\tilde{s} = 0$ can be taken from the discretized analytical solution to equation (4.26). Defining $\mathbf{z}$ to be a vector variable comprising the zeroth to third order derivative of y as a function of s,

$$\mathbf{z} = \begin{bmatrix} y \\ y' \\ y'' \\ y''' \end{bmatrix}, \tag{B.41}$$

the following linear vector equation can be formed:

$$\mathbf{z}' = \begin{bmatrix} 0 & 1 & 0 & 0 \\ 0 & 0 & 1 & 0 \\ 0 & 0 & 0 & 1 \\ i\mathrm{Sp}^4 & 0 & 0 & 0 \end{bmatrix} \mathbf{z} + \begin{bmatrix} 0 \\ 0 \\ 0 \\ ik\bar{f}_m e^{ik\tilde{s}} \end{bmatrix}. \tag{B.42}$$

The initial conditions for Sp = 7 and $k = 0$, obtained from the exact analytical equation versus finite difference approximations of fourth-order accuracy (Fornberg 1988), with the imaginary parts ignored, are

$$\mathbf{z}\big|_{\tilde{s}=0}^{analytical} = \begin{bmatrix} -0.0000000 \\ 1.2972757 \\ -14.1000000 \\ 64.8913035 \end{bmatrix}, \quad \mathbf{z}\big|_{\tilde{s}=0}^{FDA} = \begin{bmatrix} -0.0000000 \\ 1.2972782 \\ -14.1000097 \\ 64.8901456 \end{bmatrix}. \tag{B.43}$$

The percentage difference in the initial conditions, where each step is spatially discretized into a hundredth of the flagellum, is

$$\frac{\mathbf{z}\big|_{\tilde{s}=0}^{approx} - \mathbf{z}\big|_{\tilde{s}=0}^{exact}}{\mathbf{z}\big|_{\tilde{s}=0}^{exact}} = \begin{bmatrix} 0.0000\% \\ 0.0002\% \\ 0.0001\% \\ -0.0018\% \end{bmatrix} \tag{B.44}$$

The numerical solutions obtained, using the exact and approximate initial conditions, are plotted in Figure B-2 below. Even though the initial conditions differ by no more than 10^{-5}, the error in the solution is in excess of 1,000%.

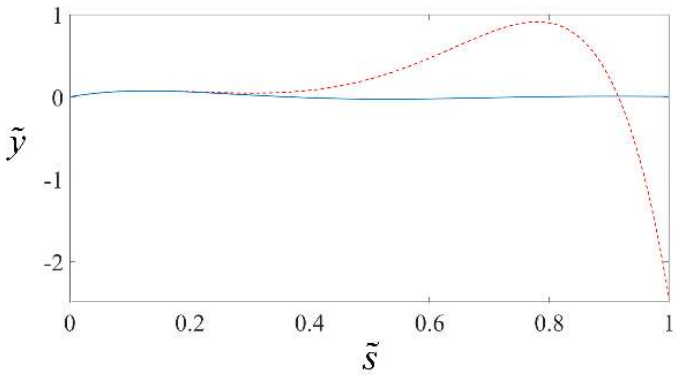

Figure B-2 –Flagellum waveform using real initial conditions obtained from finite difference approximation (dotted red line), with the exact analytical solution (solid blue line).

There is no improvement in the solution even when the flagellum is discretized into finer elements. The reason for this stark inaccuracy, despite what appears to be negligible errors in the initial conditions, stems from the fact that the analytical solution to equation (4.26) is complex, but the imaginary terms in the solution are dropped and only the real part of the solution is retained when plotting the waveform. Given that the governing differential equation is complex, it is inaccurate to obtain the initial boundary conditions from the finite difference approximation of the physical waveform which comprises only the real part of y.

Moving forward, the Runge-Kutta method is once again applied to solve the ODE as an IVP, where the initial conditions are defined by the finite difference approximation of the complex analytical solution. The force distribution in the governing equation is expressed as a matrix of numerical values, thereby validating the robustness of the model with regard to discretization. The numerical solutions, using initial conditions obtained from the finite difference approximation with varying degrees of accuracy, are presented in Figure B-3. There is negligible error with respect to the analytical solution when the initial conditions are obtained from the fourth-order finite difference approximation, even when a coarse discretization is used. If the discretization is refined, initial boundary conditions of second-order finite difference approximation are sufficient to give numerical results which are nearly identical to the analytical solution.

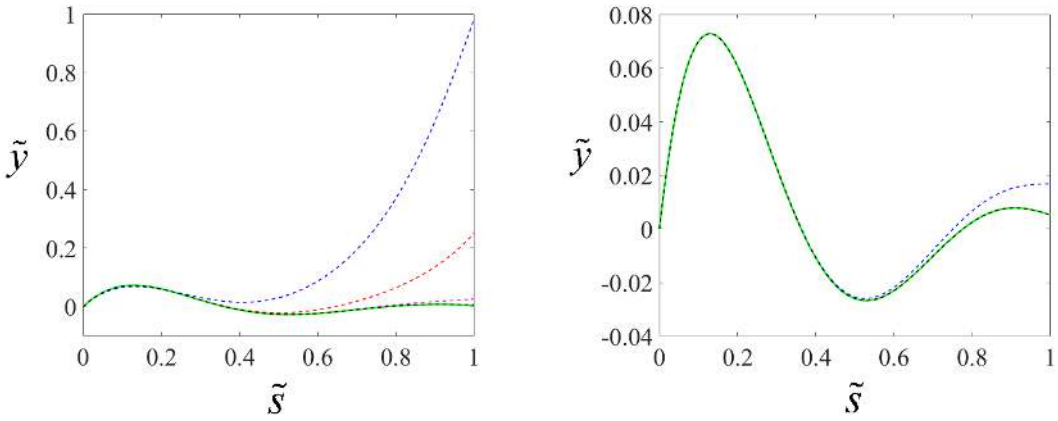

Figure B-3 – Flagellum waveform obtained using initial conditions obtained from finite difference approximation with first-order (dotted blue line), second-order (dotted red line), third-order (dotted pink line) and fourth-order (dotted black line) accuracy, plotted against the exact analytical solution (bold green line), for a discretization of (Left) 100 steps and (Right) 10,000 steps. [Note: For a discretization of 10,000 steps, there is no discernible difference between the exact solution and the initial conditions obtained from finite difference approximation of second-order accuracy or better.]

The numerical results are significantly dependent on the prescribed initial conditions. Moreover, using the derivatives of each new solution as initial conditions for each subsequent round of iteration causes the results to deviate further from the analytical solution. Without knowing the 'true' solution beforehand, the legitimacy of the computed flagellum waveform will have to be ascertained by computing the force and moment as well as comparing with experimental observations.